

DESIGN OF A NUMERICAL SOLAR DYNAMO MODEL

by

CHARLES TONY GORDON

B.S., University of Chicago
(1964)

SUBMITTED IN PARTIAL FULFILLMENT OF THE
REQUIREMENTS FOR THE DEGREE OF
DOCTOR OF PHILOSOPHY

at the

MASSACHUSETTS INSTITUTE OF TECHNOLOGY

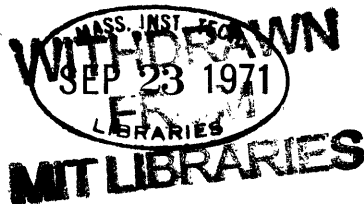
November, 1970 (i.e. Feb 21)

Signature of Author.....
Department of Meteorology

Certified by.....
Thesis Supervisor

Accepted by.....
Chairman, Departmental Committee
on Graduate Students

Lindgren





Room 14-0551
77 Massachusetts Avenue
Cambridge, MA 02139
Ph: 617.253.5668 Fax: 617.253.1690
Email: docs@mit.edu
<http://libraries.mit.edu/docs>

DISCLAIMER OF QUALITY

Due to the condition of the original material, there are unavoidable flaws in this reproduction. We have made every effort possible to provide you with the best copy available. If you are dissatisfied with this product and find it unusable, please contact Document Services as soon as possible.

Thank you.

Due to the poor quality of the original document, there is some spotting or background shading in this document.

DESIGN OF A NUMERICAL SOLAR DYNAMO MODEL

by

Charles Tony Gordon

Submitted to the Department of Meteorology on November 30, 1970
partial fulfillment of the requirements for the
degree of Doctor of Philosophy

ABSTRACT

Observations and theories of the solar differential rotation and of large scale solar magnetic fields are reviewed. The fluid dynamo approach is emphasized for the maintenance of magnetic fields. A numerical, hydromagnetic dynamo model is then formulated. It has two layers and is baroclinically driven. Its principal new features for a model of this type are thin shell spherical geometry, a Robert (equivalent to a spherical harmonic) spectral representation on spherical surfaces, and "primitive" hydro-magnetic equations. Magnetic fields are allowed to penetrate across the upper boundary.

A time averaged, zonally averaged angular momentum balance is achieved locally, only if the angular momentum equations (A.M.E.) are "correctly truncated". This is attributed to both the spectral representation and low model resolution. In contrast, the surface integral of the A.M.E. and the energy integrals derived for the model are preserved by the orthogonal truncation process.

Numerical integration of the low resolution model yields computationally stable solutions. The model is applied to the sun. For two of five thermal forcing profiles examined in the nonmagnetic case, a horizontal differential rotation of the required strength develops and is maintained by horizontal eddy transports. The streamline patterns are usually tilted upstream away from the relative velocity jet. Fultz's dishpan experiments and Ward's sunspot statistics lend credence to the above results.

For four of the thermal forcing profiles, analogous magnetic runs are made to study, qualitatively, magnetic feedback upon the flow. In this context, two magnetic production runs are discussed in detail for the case of approximate equipartition of kinetic and magnetic energy. In neither run do the magnetic fields reverse the sign of the horizontal eddy transport of angular momentum. Nevertheless, the strong magnetic feedback has several consequences including weaker eddy transports and a somewhat stronger meridional circulation. In addition, the horizontal shear of the vertically averaged angular velocity profile is almost totally destroyed. The horizontal axisymmetric Reynolds and Maxwell stresses play very important roles in the vertically averaged angular momentum balance.

At the upper level, the horizontal differential rotation has the correct sign in both magnetic production runs. Thus, in P.R. 1, i.e., the production run with warm equator-cold pole thermal forcing, the horizontal shear has reversed sign there, but is too weak by a factor of ~ 6 , when strong magnetic fields have developed. The horizontal shear decreases, yet remains of the correct order of magnitude in magnetic P.R. 2, i.e., the

production run with warm pole-cold equator forcing. A crude determination of the Rossby-Hadley regime boundary is made for P.R. 2.

Regarding magnetic induction, magnetic fields are generated and then sustained by dynamo action, provided the magnetic Reynolds number exceeds a critical value. This value apparently varies with the type of thermal forcing profile and with model resolution. Illustrations are given of magnetic field patterns, mainly for both production runs. In a very crude sense, the vertical magnetic eddies may be identified with solar magnetic active regions. But except during the first 12 years of P.R. 1, they do not generally tilt persistently in the proper sense.

In the attempted simulation of the solar magnetic cycle, the reversals of axisymmetric poloidal (and toroidal) magnetic fields is an encouraging result. For the run having the less realistic angular velocity profile at the upper level, i.e., P.R. 1, the mean reversal time of 11 to 12 years is in rather good agreement with the presumed solar value. But the reversals are irregular. For P.R. 2, the mean reversal time of 1 to 2 years is about an order of magnitude too small.

The energetics of both magnetic runs and their implications for the maintenance of the dynamo are discussed. In its grossest aspects, the reversal process appears to resemble Gilman's, except that poloidal fields are stretched into toroidal fields by the vertical shear of the differential rotation. Some other phenomena related to the magnetic reversals are briefly described for our model. It is found that the generalized Spörer's law for the equatorward migration of the zone of maximum solar magnetic activity is not obeyed.

A critique of our results and suggestions for future numerical research are given.

Thesis Supervisor: Victor P. Starr
Title: Professor of Meteorology

TABLE OF CONTENTS

CHAPTER I. THE EQUATORIAL JET AND MAGNETIC FIELDS IN THE SOLAR ATMOSPHERE	11
1.1. Introduction	11
1.2. Solar Observations	11
1.2.1. A rough view of the sun	11
1.2.2. Observational length and time scales	12
1.2.3. Observational evidence for the existence and maintenance of the equatorial jet	14
1.2.4. Observations of large scale magnetic fields	21
1.3. Theories of the Solar Differential Rotation	28
1.3.1. Axisymmetric theories	29
1.3.2. Asymmetric theories	36
1.4. Theories of Magnetic Fields	47
1.4.1. Fluid dynamos	48
1.4.2. Maintenance of the observed solar magnetic field	59
1.5. Characteristics of our Dynamo Model	70
1.6. Summary of the Other Chapters	74
CHAPTER II. FORMULATION OF THE SPHERICAL HYDROMAGNETIC DYNAMO MODEL WITH BAROCLINIC HEATING	77
2.1. Introduction	77
2.2. Basic Assumptions	77
2.3. The Equations	82
2.4. The MHD Approximation	88
2.5. Further Refinements and Simplifications	91
2.5.1. The "primitive" equations	91
2.5.2. The thermodynamics	101
2.6. Boundary Conditions	103

TABLE OF CONTENTS (continued)

CHAPTER III. THE NUMERICAL TWO LAYER SPECTRAL MODEL	110
3.1. Introductory Remarks	110
3.2. Representation of Vertical Variation by Two Layers	110
3.3. Interior Equations for the Two Layer Model	113
3.4. The Spectral Representation	122
3.4.1. The correspondence between spherical harmonics and Robert functions	123
3.4.2. Details of the Robert spectral method	126
3.5. The Time Differencing Scheme	137
3.6. Sequence of Equations to be Solved	138
CHAPTER IV. FORMULATION OF A "CORRECTLY TRUNCATED" ANGULAR MOMENTUM BALANCE	143
4.1. Introduction	143
4.2. The Angular Momentum Equations	143
4.3. Inconsistencies in the Untruncated Angular Momentum Balance	149
4.4. Analysis of the "Correctly Truncated" Angular Momentum Balance	150
CHAPTER V. FORMULATION OF THE ENERGY BALANCE	164
CHAPTER VI. NUMERICAL RESULTS	181
6.1. Introduction	181
6.2. Simulation of the Terrestrial Atmosphere — Test Run 1	182
6.3. Summary of Runs and Parameters for the Solar Model	185
6.4. The Effects of Thermal Forcing Profile Type and Magnetic Fields upon the Angular Velocity Profile	188
6.5. General Circulation Statistics for Production Runs 1 and 2	199
6.5.1. Production Run 1	200
6.5.2. Production Run 2	209

TABLE OF CONTENTS (continued)

6.6. The Search for Dynamo Solutions	220
6.7. Basic Structure of the Magnetic Field Solutions	223
6.7.1. Solutions for Production Run 1	224
6.7.2. Solutions for Production Run 2	231
6.8. Magnetic Field Reversals and Dynamo Maintenance	238
6.8.1. Observations and Other Theories of Solar Magnetic Reversals	238
6.8.2. Simulation of Magnetic Reversals by our Model	239
6.8.3. The Energetics of the Model and Its Implications for Dynamo Maintenance	243
6.8.4. Further Discussion of Dynamo Maintenance	252
6.8.5. Spörer's Law and Possibly Related Phenomena	253
CHAPTER VII. CONCLUSIONS AND SUGGESTIONS FOR FUTURE RESEARCH	261
APPENDIX A. POLOIDAL AND TOROIDAL VECTOR SPHERICAL HARMONICS	269
APPENDIX B. PROGRAMMING THE NUMERICAL INTEGRATION	271
APPENDIX C. ENERGY INTEGRALS FOR A CONTINUOUS, QUASI- BOUSSINESQ MODEL	272
BIBLIOGRAPHY	277
ACKNOWLEDGEMENTS	286
BIOGRAPHICAL NOTE	287

LIST OF FIGURES

Fig. 1.1.	Synoptic chart of line of sight solar magnetic fields (from Bumba and Howard (1965b)).	25
Fig. 3.1.	Schematic diagram of two layer model.	113
Fig. 4.1.	Effect of truncation on coriolis torque for P.R. 2.	160
Fig. 4.2.	Effect of truncation on coriolis torque for P.R. 1.	161
Fig. 5.1a.	Energy diagram for the generalized magnetic case.	179
Fig. 5.1b.	Energy diagram for the nonmagnetic case.	179
Fig. 5.2a.	Energy diagram for toroidal motion anti-dynamo.	179
Fig. 5.2b.	Energy diagram for axisymmetric anti-dynamo.	179
Fig. 6.1.	General circulation statistics for terrestrial atmosphere test run.	186
Fig. 6.2.	Four types of thermal forcing profiles. These profiles have been quasi-normalized.	190
Fig. 6.3a.	Absolute angular velocity $\bar{\pi}_{abs}$ profiles for test run 7.	196
Fig. 6.3b.	Perturbation potential temperature and thermal forcing profiles for test run 7.	196
Fig. 6.4.	Some general circulation statistics for P.R. 1.	203
Fig. 6.5.	Comparison of absolute angular velocity profiles of magnetic P.R. 1 with observations.	205
Fig. 6.6.	Vertically averaged angular momentum balance of magnetic P.R. 1.	206
Fig. 6.7.	Vertically averaged horizontal Reynolds stresses and Maxwell stresses of magnetic P.R. 1.	207
Fig. 6.8.	Some general circulation statistics for P.R. 2.	212
Fig. 6.9.	Comparison of absolute angular velocity profiles of magnetic P.R. 2 with observations.	214

LIST OF FIGURES (continued)

Fig. 6.10.	Vertically averaged angular momentum balance of magnetic P.R. 2.	215
Fig. 6.11.	Vertically averaged horizontal Reynolds stresses and Maxwell stresses of magnetic P.R. 2.	216
Fig. 6.12.	Crude determination of the Rossby regime-Hadley regime boundary for nonmagnetic P.R. 2.	219
Fig. 6.13.	Time evolution of horizontal magnetic field \underline{B}_{H_2} for P.R. 1, at intervals of 10 solar rotations.	227
Fig. 6.14.	\underline{B}_{H_2} for P.R. 1.	229
Fig. 6.15.	B_2^z for P.R. 1.	229
Fig. 6.16.	Stream function $\psi_{\sqrt{2}}$ for P.R. 1 at $t=0.69$ yrs., i.e. before significant dynamo action occurs.	229
Fig. 6.17.	Sample solutions for P.R. 1 at $t=8.20$ yrs.	230
Fig. 6.18.	Time evolution of horizontal magnetic field \underline{B}_{H_2} for P.R. 2 at intervals of 10 solar rotations.	233
Fig. 6.19.	Sample solutions for P.R. 2 at $t=24.60$ yrs.	235
Fig. 6.20.	Vertical magnetic fields for P.R. 2 at $t=28.08$ yrs.	236
Fig. 6.21.	Stream function $\psi_{\sqrt{2}}$ for test run 7 at $t=1.11$ yrs., i.e. before significant dynamo action occurs.	237
Fig. 6.22.	Horizontal magnetic field \underline{B}_{H_2} for test run 7 at 3.89 yrs.	237
Fig. 6.23.	Magnetic fields for test run 12 ($R_m = 500$) at $t=21.75$ yrs.	237
Fig. 6.24.	Time reversal of polar magnetic fields for P.R. 1.	241
Fig. 6.25.	Time reversal of polar magnetic fields for P.R. 2.	242
Fig. 6.26.	Energy diagram for magnetic P.R. 1.	244
Fig. 6.27.	Energy diagram for magnetic P.R. 2.	245

LIST OF FIGURES (continued)

Fig. 6.28.	Meridional-time cross section of axisymmetric toroidal and vertical magnetic fields for P.R. 1.	256
Fig. 6.29.	Meridional-time cross section of axisymmetric toroidal and vertical magnetic fields for P.R. 2.	257
Fig. 6.30a.	Superposition of regions of strong vertical eddy motions upon the meridional-time cross section of $\langle B_2^{\wedge} \rangle$ of Fig. 6.28a for P.R. 1.	258
Fig. 6.30b.	Superposition of regions of strong vertical eddy motions upon the meridional-time cross section of $\langle B_2^{\wedge} \rangle$ of Fig. 6.29a for P.R. 2.	258
Fig. 6.31a.	Meridional-time cross section of the <u>vertically averaged</u> zonal wind $\langle u_2 \rangle$ in P.R. 2.	259
Fig. 6.31b.	Time evolution of the square of the Alfvén number.	259

LIST OF TABLES

Table 1.1.	Latitude Distribution of Sunspots as a Function of Time (from Ward (1964)).	20
Table 4.1.	Catalogue of Terms in the Angular Momentum Balance Equations.	146
Table 4.2.	Useful Properties of Some Low Order Legendre Polynomials.	154
Table 6.1.	Specified Parameters for the Earth and Sun.	183
Table 6.2.	Catalogue of Test Runs and Production Runs for Solar Model.	189
Table 6.3.	Qualitative Effects of the Ω_* Profile on Velocity Shear for Nonmagnetic and Magnetic Cases.	192
Table 6.4.	Dynamo Behavior for Different Runs.	222

CHAPTER I. THE EQUATORIAL JET AND MAGNETIC FIELDS
IN THE SOLAR ATMOSPHERE

1.1. Introduction.

The existence and maintenance of the solar equatorial jet and the large scale solar magnetic fields will be a central theme of this study. In Chapter I, the basic observational evidence relating to the equatorial jet and to large scale magnetic fields will first be reviewed. The discussion then turns to various possible physical mechanisms for maintaining the jet. As for the maintenance of the magnetic fields, the self-sustaining fluid dynamo approach is emphasized. In this connection, a survey of the literature on dynamo theory has revealed certain basic properties of fluid dynamos.

In the concluding part of Chapter I, a self-consistent model which contains various essential ingredients already enumerated, is proposed. In principle, the model is capable of dynamo generation and maintenance. The chief departures from a recent numerical dynamo study by Gilman (1968) include the adoption of the "primitive" hydromagnetic equations and thin shell spherical geometry. When these modifications are coupled with suitably adjusted baroclinic thermal forcing, an equatorial acceleration is possible.

1.2. Solar Observations.

1.2.1. A rough view of the sun.

The basic solar data consists of continuum emission, absorption lines, and emission lines. This radiation reflects the local values of wind, temperature, density, magnetic field strength, composition, and

state of ionization averaged along the line of sight. The most serious observational limitation is due to the opacity of the solar disk. Even in white light, only its uppermost few hundred kilometers are visible.

A rough picture of the solar interior has emerged, however, from stellar model calculations of Schwarzschild (1958) and others.¹ Thus the sun probably has a convective envelope, and a radiative core in which a thermonuclear core is imbedded. Denoting the solar radius by R_{\odot} , the radiative core-convection zone interface lies between $0.8 R_{\odot}$ and $0.9 R_{\odot}$, while the upper boundary of the convection zone lies just beneath the visible surface. The observed photospheric "granulation" would then represent small scale convection which has penetrated this upper boundary. Speculation on the more detailed temperature structure within the convection zone is deferred until later.

The 5×10^3 °K photosphere is separated from the overlying 1.5×10^6 °K corona by a sharp transition region known as the chromosphere. The continuum emission originates mainly from the photosphere and lower chromosphere. Absorption lines are also formed there, while emission lines are formed predominantly in the corona and upper chromosphere.

1.2.2. Observational length and time scales.

Solar observations reveal hydrodynamic and magnetic phenomena over a broad range of time and space scales. Near the short end of the spectrum is the granulation. An individual granule has a characteristic size of 700 km and a lifetime of 8 minutes (Zirin, 1966). These scales are

¹The method is summarized by Zirin (1966) on pp. 279-280.

small compared to the sun's radius ($R_{\odot} \approx 6.95 \times 10^5$ km) and observed mean rotation period ($\tau_{\odot} \approx 25.4$ sidereal days). Photospheric cellular horizontal motion patterns, dubbed supergranules, have a diameter of about 3×10^4 km and a mean lifetime of 20 hours (Simon and Leighton, 1964). Supersupergranulation, i.e., convective cells with a characteristic dimension of several hundred thousand kilometers may have been observed (Bumba, 1967). Horizontal eddy motions of similar size are implied by Ward's (1964) and later studies.

A very large sunspot group may encompass 0.3% of the solar disk area (Zirin, 1966), which is roughly supergranular size. But spots are imbedded in active regions having lateral dimensions of up to 2×10^5 km (Bumba and Howard, 1965b). Comparably large scale magnetic fields having intensities of several gauss are another manifestation of active regions (Bumba and Howard, 1965b). These magnetic fields as well as active regions and large sunspots may persist for several rotations. A polarity reversal of the leader and follower spot magnetic fields is a feature of the double sunspot cycle². The large scale, axisymmetric poloidal field, i.e., the axisymmetric component in meridional planes, also seems to undergo such a reversal. The average length of the double sunspot cycle is 22 years. Finally, an equatorial jet is a quasi-permanent feature, and not just a statistical remnant of the solar general circulation. Of chief interest to us will be phenomena having large length and time scales.

²The various characteristics of the sunspot cycle are conveniently summarized by Babcock (1961).

1.2.3. Observational evidence for the existence and maintenance of the equatorial jet.

"Observations" of the Differential Rotation.

Three methods of observing motions in the solar atmosphere are (1) tracing sunspot displacements, (2) tracing other definable features such as filaments and (3) measuring Doppler line shifts. Sunspot data is the most comprehensive. Since 1874, sunspot group positions (in tenths of degrees of latitude and longitude) have been extracted and tabulated once each day, from photographs taken principally at the Greenwich or Cape Observatories.

Newton and Nunn (1951) measured the time interval between successive central meridian passages of longlived, generally large sunspots from recurrent³ sunspot data for the period 1878-1944. By a least squares technique, they obtained the angular velocity profile

$$\mathcal{N}_0 = 14.38^\circ - 2.77^\circ \sin^2 \varrho \quad \text{longitude per day} \quad (1.1)$$

ϱ being the latitude.

As an alternative to Newton and Nunn's procedure, Ward (1964) computed displacements of shortlived and longlived spots. His angular velocity profile agreed with equation (1.1) to within a few percent. Ward (1966) noted that the daily motions of small spots predict an angular rotation rate slightly larger than equation (1.1) near the equator and 2% larger at 30°. Moreover, elongated spots seemed to move up to 2%

³ Recurrent sunspots reappear at least once on the east limb (looking toward the sun) of the solar disk.

faster than circularly shaped spots.

An auto-correlation analysis of the local magnetic polarity in active regions has recently been performed by Wilcox and Howard (1970) based upon roughly seven years of data. A mean differential rotation qualitatively similar to equation (1.1) may be inferred from the sharp peaks at 26 to 29 synodic days in the auto-correlation curves for different latitudes.

Filaments can be found at more poleward latitudes than sunspots, tend to be elongated, and are of chromospheric rather than of photospheric origin (Zirin, 1966). The angular velocity profile determined from filament displacements by M. and L. d'Azambuja (1948) agrees qualitatively with (1.1) but the angular velocities are slightly larger.

Since 1966, Dr. Howard has obtained Doppler shift measurements at 11,000 points over nearly the whole disk on an almost daily basis. Howard and Harvey (1970) comment in fact that "the analysis of the 1st day's observation combined more individual measures of rotation Doppler line shifts than were collected in all such previous endeavors". Obtaining a least squares fit to their data, they found

$$\mathcal{N}_\theta = 13.76^\circ - 1.74^\circ \sin^2 \varphi - 2.19^\circ \sin^4 \varphi \quad \text{per day.} \quad (1.2)$$

Note that the equatorial value is some 4% less than in (1.1). It also happens to be in fairly good agreement with other recent spectroscopic determinations. Secondly, the shear is less pronounced in (1.2) than in (1.1) at sunspot latitudes. The probable errors of the coefficients in (1.2) were estimated to be of order 0.1%, 10%, and 10%, respectively.

Based upon a small sample of Doppler measurements, Flaskett (1962) found

a maximum angular velocity at $\varphi = 22^\circ$, although his equatorial value agreed with (1.2).

Unlike sunspot heights, the heights of different spectral line formation can be estimated. Thus, Doppler measurements could be useful to help determine height variations in \mathcal{N}_o . In a review article, Bumba (1967) cites Aslanov's results on the variation of (zonally-averaged) solar equatorial zonal velocity, u_o . From optical depth .111 to .010, (a 210 km thick layer) u_o increases monotonically with height by 12%, whereas from optical depth .125 to .111, u_o decreases with height. Comparison of the filament and sunspot rotation laws suggests \mathcal{N}_o increases with height, but the primary effect could be the shape of the filaments rather than their location in the chromosphere.

Mean Meridional Velocities

Ward (1964) attempted to compute the space-time mean meridional velocity $\{v\}$ from daily displacements of sunspots. But the 5% confidence limits exceeded the magnitude of the computed $\{v\}$'s everywhere except in the $0^\circ - 5^\circ N$ latitude belt. Within the sunspot latitude belt, the largest possible magnitude for $\{v\}$ consistent with the confidence limits was slightly under 20 m/sec.

Even earlier, Plaskett (1962) attempted to determine $\{v\}$ from line of sight spectroscopic measurements. Unfortunately, the sign of the meridional velocity depended upon which wavelength standard was adopted. Nevertheless he felt that the 'observed' meridional velocity was equatorward. No similar attempt has been made yet with Howard's 1966-1969 data. In principle, coefficients of a $\{v\}$ profile and their probable errors

could be estimated from his spectroscopic data.

Horizontal Eddy Motions and Eddy Momentum Transports

Ward (1964) has computed the space-time covariance $\{u'v'\} = \{uv\} - \{u\}\{v\}$ and the associated correlation coefficients from the daily sunspot displacements. The zonal velocity u and meridional velocity v are measured in the Greenwich reference frame whose rotation rate is 14.184° per day. Space-time averaging (denoted by $\{ \}$) weights each spot group equally and is appropriate considering the nature of the data. The u and v components are significantly correlated so that faster rotating spots tend to move towards the equator. If streamlines could be drawn, the trough and ridge lines would probably tilt northwest-southeast (in the northern hemisphere). The eddy momentum transport is up the angular velocity gradient. Ward (1964) estimated the decay time of the differential rotation at just a few rotations if the eddy momentum transport were cut off and not replaced. Starr and Gilman (1965a) showed that Ward's results implied a systematic conversion by horizontal eddies of eddy kinetic energy into kinetic energy of the mean zonal flow at sunspot latitudes.

Hart (1956) demonstrated that observed fluctuations of the Doppler line of sight velocity V_L were above the noise level and coherent for at least an hour. The fluctuations had a weak spectral peak near 2.6×10^4 km and an RMS value of $O(100 \text{ m/sec})$. Howard and Harvey (1970) thought they detected fluctuations with a comparable length scale and a time scale of several days, in addition to a much longer secular variation of \mathcal{N}_\odot .

It may even be possible to construct a zeroth order approximation of the large scale flow pattern from Howard's V_L data by retrieving the eddy motions from the residual velocities defined by Howard and Harvey (1970). One would assume (1) the large scale velocity field is horizontal and nondivergent, i.e., can be specified by a stream function ψ_r , and (2) the equator is a streamline (at least as an initial guess). Then a linear first order partial differential equation in ψ_r relates ψ_r to the observed V_L values integrated (numerically) by the method of characteristics. A necessary condition for assumption (1) to be valid is that V_L be small near the center of the disk. Hopefully, the streamline patterns would be tilted in a manner consistent with Ward's (1964) results.

Ambiguities in the Observational Data

There are certain ambiguities in the interpretation of the data mentioned thus far. A very crucial assumption is that sunspots are good tracers of the large scale flow. An interesting indirect check was made by MacDonald (1966) who used migratory cyclones and anticyclones as tracers of the angular velocity and eddy motions in the terrestrial atmosphere. The predicted eddy momentum transport was only 1/3 the observed transport. Nevertheless, the predicted shapes of both the eddy momentum transport and absolute angular velocity profiles agree fairly well with the (vertically averaged) observations, except near the equator where cyclone and anticyclone data was scarce. MacDonald reasoned that if the migratory cyclones and anticyclones were satisfactory tracers, then by analogy, sunspots could be too.

It has already been noted that size and shape and life expectancy of sunspots affect how fast they move. Spots also move faster in the incipient as compared to later stages of development (Ward, 1966). In addition, the equivalent height of the circulation traced out by sunspots is not clear. Sunspots are thought to be manifestations of hydro-magnetic disturbances in the convection zone. Ward (1964) speculated that spots of greatest vertical extent (which might include the large recurrent spots) move the slowest.

Even assuming that sunspots (groups) are good tracers, positional errors of sunspots (center of gravity of groups) might seriously affect the results. For example, sunspot positions are least accurately known near the edges of the disk due to foreshortening. Ward (1964) counteracted this difficulty by discarding sunspot data close to the disk edges. Even worse, the birth of a new sunspot and death of an old one between observations or change in structure of a sunspot group could be misinterpreted as sunspot motion. Suspicions were advanced that Ward's (1964) eddy correlations might be due largely to systematic errors in the center of gravity position of sunspot groups along the spot group axis, which was preferentially tilted NW-SE (NE-SW) in the northern (southern) hemisphere. But Ward (1965b) refuted the brunt of this argument by obtaining significant correlations from displacements of single spots. Also, the correlations basically held up when sunspot displacements exceeding critical longitude and/or latitude values were screened out (Ward, 1964).

Table 2 of Ward (1964) reproduced as Table 1.1 shows that the

Table 1.1. Latitude distribution of sunspots as a function of time (from Ward (1964)).

Table 2
Number of Observations
 (Cutoff: 1.0° Lat., 1.5° Long.)

Year	North						South						Total		
	≥ 30	30-25	25-20	20-15	15-10	10-5	5-0	0-5	5-10	10-15	15-20	20-25		25-30	≥ 30
1935	16	76	115	40	25	0	5	2	4	23	102	93	78	47	626
1936	23	44	129	188	138	18	0	0	33	149	229	160	89	74	1276
1937	58	52	179	225	367	179	9	1	106	226	204	141	56	24	1827
1938	3	69	128	142	255	137	50	29	251	220	188	120	65	12	1669
1939	2	59	74	158	178	167	41	41	241	233	238	67	2	9	1510
1940	0	2	20	90	176	168	26	33	239	233	90	22	1	0	1100
1941	0	1	5	46	204	113	68	68	137	78	27	0	0	0	747
1942	0	0	4	21	98	132	12	36	101	105	1	0	0	0	510
1943	0	0	0	9	47	86	38	26	22	12	1	8	2	1	252
1944	4	7	21	9	1	11	9	0	14	0	0	50	17	7	150
1935-44	108	310	675	928	1489	1011	258	236	1148	1279	1080	661	310	174	9667
1935-44	282	620	1336	2008	2768	2159	494	(9667) North and South Total (Cutoff: 1.0°, 1.5°)							
1935-44	335	753	1569	2361	3203	2519	574	(11 314) North and South Total (Cutoff: 2.0°, 3.0°)							
1935-44	350	777	1635	2464	3333	2595	596	(11 750) North and South Total (no cutoff)							

-50-

latitude distribution and total number of sunspots varies dramatically over the sunspot cycle. Thus a formula like (1.1) might reflect a time variation as well as latitudinal variation of the solar rotation. The reduction of spectroscopic data of Livingston (1969) and of Howard and Harvey (1970) suggests that whereas a positive solar equatorial jet is present on most days, the profile does vary with time.

It may be noted that the Doppler line shift measurements contain various systematic and random errors. The orbital motion and rotation of the earth must be subtracted out as well as the red shift at the limb (~ 340 m/sec). Also, the arbitrary zero reference may shift from day to day or even during the 90 minute scan of the disk. A pressure fluctuation of only 0.13 mb will produce a 60 m/sec shift. These and other sources of error including scattering by the terrestrial atmosphere and optics involved are discussed by Howard and Harvey (1970).

As techniques are improved and more Doppler measurements made, our knowledge of the large scale solar circulation will be refined. Nevertheless, the basic quantities mentioned in this section are probably of the correct order of magnitude and the differential rotation should be accurate to within 20%. At this stage, it would be gratifying if the numerical model we construct could reproduce the large scale solar circulation even qualitatively.

1.2.4. Observations of large scale magnetic fields.

Methods of Observation

In the presence of a magnetic field, solar spectral lines split approximately into a classical Zeeman triplet. Two components, σ_1

and σ_2 are shifted $\pm \Delta\lambda$ relative to the center of the undisturbed π component. The formula for the wavelength splitting in A^0 is (Zirin, 1965)

$$\Delta\lambda = 4.7 \times 10^{-13} G \lambda^2 H. \quad (1.3)$$

Here the nondimensional Landé factor G depends upon the atomic transition, λ is the wavelength in A^0 of the undisturbed line, and H is the magnetic field in gauss. Except in very strong magnetic fields, e.g. sunspot fields of over 1000 gauss, the splitting is too small to measure directly.

Line of sight magnetic field components in the photosphere (or chromosphere) slightly weaker than 1 gauss can be detected, however, by the solar magnetograph, a sensitive photoelectric instrument devised by Horace Babcock in 1952.⁴ The magnetograph actually measures the splitting $\Delta\lambda$ in equation (1.4). The observed splitting is usually so small that the shape of the line profile responds as a linear function of $\Delta\lambda$ (Bumba and Howard, 1965c). Secondly, the magnetograph subtracts out almost all the instrumental errors which would otherwise be detrimental. A magnetogram is produced by scanning the disk.⁵ Synoptic isogauss contour maps of the line of sight magnetic field can be constructed daily from magnetograms (Bumba and Howard, 1956b). Then over each solar rota-

⁴A good description of the magnetograph may be found in Zirin (1966), pp.105-106 and pp. 367-370, or in Bumba and Howard (1965c).

⁵Utilizing the basic principles of the magnetograph, Leighton (1959) devised a photographic subtraction technique for obtaining an instantaneous picture of solar magnetic fields. This method is quicker but less sensitive than photoelectric scanning. Astronomers at the Crimean Observatory have measured strong magnetic fields transverse to the line of sight (Severny, 1965).

tion, data near (if possible) the central meridian on successive daily maps may be transferred to a mean synoptic chart whose abscissa is time. Assuming large scale features are longlived, the abscissa may be converted to longitude using the mean solar rotation rate. Bumba and Howard (1956b) argue that such mean synoptic charts help facilitate the study of large scale magnetic features. There is of course some tradeoff. The final product is not a time mean (i.e., averaged over one rotation) map in the usual sense, but a collage. Alternatively, significant inhomogeneities between central meridian vs. limb data as well as foreshortening effects are avoided. In any event, rather coherent, large scale contour patterns appear on many of Bumba and Howard's (1965b) mean synoptic charts. Secondly, features on one mean synoptic chart can often be identified on the next.

Magnetograph Resolution

Babcock's original magnetograph had an angular resolution of 70" of arc while resolution close to 1" has since been achieved (Livingston, 1967).⁶ With the development of the higher resolution magnetographs, increasingly fine structure magnetic fields have been reported. Bumba and Howard (1965b) noted that weaker features and finer structures could be detected with a magnetograph having 23" compared to 70" resolution. Severny (1965) plotted H vs. position in an active region, at two resolutions. Again, finer structure was revealed at the higher resolution. The greatest magnitude of H was about 35 gauss at both resolutions however. Livingston (1966) also reported little variation in range of intensity (as

⁶The solar disk subtends 31'59" of arc while a characteristic granule dimension is roughly 0.5" of arc.

opposed to fineness of structure) when his magnetograph resolution was improved thirtyfold to 1.8" of arc.

In contrast, Severny (1965) did observe a marked variation of maximum magnetic field intensity near latitude 60° as a function of angular resolution. At 5" arc resolution, the maximum intensity was nearly 30 gauss, about ten times the value at 50" resolution. ~~Second~~, Severny (1965) could identify only 50% of the magnetic elements on two successive 5" resolution magnetograms of the polar region. Unfortunately, he did not indicate how short the time interval was between successive magnetograms. A rather short lifetime for features having a characteristic angular dimension of approximately 5" could contribute to the observed incoherency.

Bumba (1967) has attributed apparent discrepancies in reported results to factors like differences in seeing conditions and differences in sensitivity or resolution amongst magnetographs. In contrast, the general validity of the magnetograph measurements has been challenged by Alfvén (1965). He postulated that numerous dark pores called microspots, which are small compared to the magnetograph resolution, could be imbedded in the background medium. Supposedly, magnetic fields would be very strong inside microspots and weak elsewhere. Moreover, magnetographs would fail to adequately compensate for saturation effects due to the intense field strength and reduced light emission within microspots. Thus, magnetograph measurements would bear little resemblance to large scale magnetic field patterns if, in fact, any even exist. At best, they could indicate the level of microspot activity.

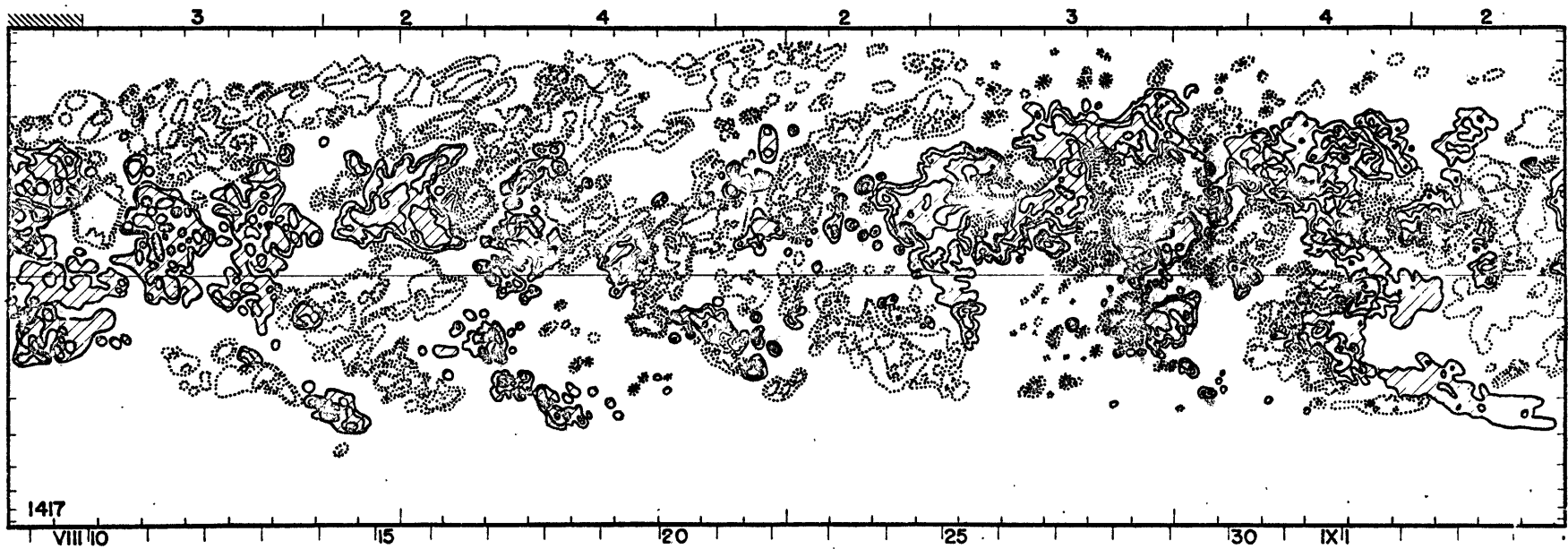


FIG. 1.—Synoptic chart of solar magnetic fields for rotation No. 1417 (August, 1959). Solid lines and hatching represent positive polarity, and dotted lines and shading represent negative polarity. Iso-gauss lines are for 2, 6, 10, 15, 25 gauss. Dates are given below with marks representing 10° intervals of longitude. The equator is drawn, and every 10° in latitude is marked at the sides. The numbers at the top give an indication of the quality of the magnetograms from which the synoptic chart was drawn, with 4 the best. The hatching represents an area which had to be drawn more than 40° from the central meridian of the magnetogram.

Fig. 1.1. Synoptic chart of line of sight solar magnetic fields (from Bumba and Howard (1965b)).

Of course, tiny microspots cannot be observed. There are also some counter arguments to Alfvén's. First of all, consider the measurements of Bumba and Howard (1965b) taken with a 23" angular resolution instrument. The noticeable regularity of the contour patterns on a given chart and the persistence of features (mostly active regions) from one chart to the next lend plausibility to the measurements. At higher resolution, there is more fine structure as already mentioned. But eyeball smoothing suggests qualitatively similar patterns to those observed at lower resolution.

Second, a sector structure in the interplanetary magnetic field has been measured by magnetometers aboard orbiting satellites (Wilcox, 1966). The predominant polarity of the interplanetary magnetic field varied from + to - to + to - (corresponding to wave number two) for each solar rotation. This polarity was correlated with that of the large scale photospheric field. A subjective smoothing was applied to some mean synoptic magnetic charts for this purpose. A cross correlation of 0.8 was achieved at a time lag of four to five days, a reasonable transit time for solar wind plasma.

Observational Results

We will take the view that the magnetograph basically responds to the line of sight magnetic field. The character of the magnetic observations is revealed in Fig. 1.1 which is a reproduction of a mean synoptic magnetic chart of Bumba and Howard (1965b). The contour patterns are typical for the more active phases of the sunspot cycle, when measurable fields cover over 50% of the disk. Smoothing over the fine scale struc-

ture, a dominant feature equatorward of 40° is extensive regions (bipolar magnetic regions) of predominantly one magnetic polarity flanked on either side by analogous regions of predominantly opposite polarity. These regions are preferentially elongated as if stretched out by the differential rotation. Thus the elongated axis is tilted NW-SE (NE-SW) in the northern (southern) hemisphere⁷. Maximum field strengths of 25 gauss and large areas with field strengths between 2 and 6 gauss are typical when active regions are present. On a small magnetograph data sample covering seven solar rotations, Bumba, Howard, Kopecky, and Kuklin (1969) performed an auto-correlation analysis. The significance of various bumps in the auto-correlation curve may be questionable. But it is interesting perhaps, that there are peaks corresponding to longitudinal wave numbers 6 and 2. The more extensive auto-correlation analysis by Wilcox and Howard (1970) reveals peaks corresponding to wave numbers 1, 2, 3, 4, 6, and others. The wave number one peak, which reflects the persistence of active regions over a solar rotation, is sharpest, most persistent, and most coherent.

The synoptic chart also reveals unipolar and ghost unipolar magnetic regions. The leading portion of a unipolar region merges with the bipolar field of the same polarity equatorward of 40° . The tail portion is poleward of 40° and is more spread out in longitude, usually over 100° . At times, these unipolar regions show up virtually as a wave number one feature on the auto-correlation curves of Wilcox and Howard (1970) poleward of 40° . Typically, the tail portion is weaker than the

⁷ Reflect the chart about its left boundary and take longitude, increasing to the right, as the abscissa.

leading portion, has the opposite polarity as the net polar field, and migrates towards the nearest pole. Compared to unipolar tails, the ghost unipolar tails have the reverse polarity and are weaker by at least a factor of two. (Bumba and Howard, 1965b).

Bumba (1967) believes that all magnetic fields observed on the sun probably originate in active regions during the first few days of development. A field could evolve through the combined action of advection, stretching by differential motions, and magnetic diffusion. During periods of strong activity, active regions overlap. Preferential longitude zones of activity could be only partially explained by persistence.

Despite fine scale structure and nonuniformity, the concept of a net space-averaged polar field is apparently valid. Severny (1965) remarked that the observed (line of sight) net polar field was rather constant with latitude instead of decaying as the pole is approached. The implication is that even the net large scale polar magnetic field is not like a pure dipole. The rapid oscillations in the fine structured fields are not necessarily incompatible with the slow secular changes in polarity of the net field either. For the past two cycles, polarity reversals have been observed, not quite simultaneously, at the two poles, around the time of maximum sunspot activity. Also, a poleward migration of poloidal magnetic flux has been noted by Bumba and Howard (1965b).

1.3. Theories of the Solar Differential Rotation.

A systematic review of theories on the differential rotation was given by Gilman(1966). We plan to reiterate only a few essentials of the earlier work while emphasizing the more recent ideas. The various theories could be categorized as to mode (i.e., axisymmetric or eddy),

ultimate driving mechanism (e.g., convective, baroclinic or unspecified process), or dependence, if any, upon magnetic fields. Some physical mechanisms seem more plausible than others. But the question of which mechanisms actually dominate is unresolved mainly because they tend to apply to deep regions hidden from view. Often, one is forced to assume the surface observations are linked to conditions below the surface in "comparing" theory and observations. Moreover, even if a theory makes a prediction for the visible surface layers, the nature of the data may make direct comparisons difficult.

1.3.1. Axisymmetric theories

The idea that an axisymmetric circulation in meridional planes might maintain the differential rotation was put forth by Eddington (1925) and Bjerknes (1926). In principle such a circulation could transport either (1) so-called \mathcal{L} angular momentum or (2) relative angular momentum up the angular velocity gradient (Lorenz, 1967). The first type could be associated with either a significant mass transport or a variation of radius within the fluid layer. Mass ejection by the solar wind is itself too slow to cause a significant mass transport at photospheric or convection zone levels. The radius variation effect requires a deep layer. Roxburgh (1969) suggested that this effect might take place in the convection zone. The meridional cell would be characterized by rising motion near the poles, a descending branch near the equator, equatorward transport near the top, and poleward transport near the bottom. A net horizontal transport of relative angular momentum by mean meridional motions would require a vertical shear of angular velocity, if the net mass transport and variation of radius effects were neglected.

There are a few general criticisms of axisymmetric theories. Observationally, large scale, time varying eddy patterns of photospheric line of sight velocities appear on Howard's recent dopplergrams. The presence of large scale horizontal eddies may also be inferred from Ward's (1964) sunspot statistics. Secondly, eddy motions are probably required for dynamo maintenance of the magnetic fields, as discussed later. Third, mathematical solutions which are axisymmetric could possibly be unstable to small perturbations.

Energy Sources for Axisymmetric Models

An energy source is an essential ingredient of any self-consistent theory of the differential rotation which includes dissipation. Also, it now seems quite plausible that small scale turbulent dissipation predominates by several orders of magnitude over molecular dissipation (e.g. see Ward (1964) or Cocke (1967)). In the present context, the question is then what drives a large scale axisymmetric meridional circulation.

Baroclinic Energy Sources

Until roughly 20 years ago, the core had been regarded as convective and the envelope as in radiative equilibrium, in opposition to current thinking. Von Zeipel's theorem predicted negative energy generation near the surface of a barotropic star in radiative equilibrium. Rejecting this conclusion, Eddington (1925) suggested the sun might be baroclinic. But as Gilman (1966) mentioned, the deduced Eddington meridional currents were later shown to be only of order 10^{-9} cm/sec, much too small

to affect the angular momentum balance. Krogdahl (1944) showed that in principle, a baroclinic star, but not a barotropic one, could have non-uniform rotation in the equilibrium state despite isotropic friction.

The verification of large scale meridional temperature gradients would promote the cause of baroclinic theories, whether they be of the axisymmetric or eddy mode type. As noted by Gilman (1966), various measurements of pole to equator temperature gradient are in disagreement. Polar temperatures warmer, the same as, and colder than the equatorial temperature have been reported. In one case the pole was found to be warmer than the equator, with a temperature minimum at middle latitudes. Measurement uncertainties are such that temperature differences of a few tens of degrees of either sign cannot be precluded at the surface and larger temperature differences could exist deeper down. Even if photoelectric techniques increase the sensitivity of measurements, there is still the problem of knowing for certain whether they are being made along geopotential surfaces.

One early justification for the existence of baroclinicity was given by Randers (1942). He suggested parcels would rise preferentially along the axis of rotation, movements perpendicular to the axis being constrained by centrifugal stability. The implication was that the poles would be warmer than the equator. More recent work by Chandrasekhar (1961) and Busse (1970) indicates a tendency at least for asymmetric convection parallel to the rotation axis to be inhibited by rotation. More will be said qualitatively on the plausibility of the baroclinitic hypothesis, in

connection with asymmetric baroclinic instability theories.

Anisotropic Viscosity as an Energy Source

Kippenhahn (1963) studied steady state, axisymmetric motions in a spherical shell of incompressible, barotropic fluid with anisotropic viscosity and stress-free boundaries. The frictional force was derived from Wasiutynski's (1946) anisotropic turbulent stress tensor. The anisotropic viscosity was parameterized by the ratio S of the horizontal to radial constant diffusivities. Kippenhahn thought the anisotropic viscosity might help explain the solar differential rotation. We shall attempt to clarify the significance of his work.

The following notation will be used: the absolute angular velocity $W^{(k)}$, the stream function $\psi^{(k)}$ for axisymmetric motions in meridional planes, the velocity vector $\underline{v}^{(k)}$, isotropic friction $\underline{f}^{(k)}$, the anisotropic correction $\underline{f}'^{(k)}$ to $\underline{f}^{(k)}$, the azimuthal unit vector $\hat{\lambda}$, the radial coordinate r , the latitude φ , and the integral $\int d\tau$ over the fluid volume. The "0" or "1" subscript on $W^{(k)}$ or $\psi^{(k)}$ denotes a zeroth or first order correction, respectively.

Two equations, i.e., the azimuthal components of (1) the vector equation of motion and (2) its curl, contain only inertial and frictional terms and hence constitute a closed set for $W^{(k)}$ and $\psi^{(k)}$. Biermann (1958) had demonstrated that (nontrivial) solid body rotation ($W^{(k)} = \text{constant}$, $\psi^{(k)} = 0$) is not a solution to the hydrodynamic equations if $S \neq 1$. Kippenhahn assumed $W_0^{(k)}(r) \propto r^{2(S-1)}$ and $\psi_0^{(k)} = 0$. This zero order solution failed to satisfy the second of the above two equations for the anisotropic case $S \neq 1$. First order

corrections were obtained by a method of successive approximations.

Kippenhahn felt this order of approximation would suffice qualitatively but not quantitatively for the sun. The nonlinear self-interaction of $W_0^{(k)}$ in the second, i.e., unbalanced equation gave a meridional circulation $\psi_1^{(k)}$. In turn $\psi_1^{(k)}$ interacted with $W_0^{(k)}$ in the first equation to give a differential rotation $W_1^{(k)}(r, \alpha) = W_{10}^{(k)}(r) + W_{12}^{(k)}(\alpha) (1 - 3 \sin^2 \alpha)$.

For $S > 1$, the meridional circulation was characterized by one cell in each hemisphere with rising motions near the poles and descending motions near the equator. As $W_{12}(r)$ was positive so was the equatorial acceleration. Finally, the meridional circulation even transported angular momentum up the gradient of $W_1^{(k)}$ but down the gradient of $W_0^{(k)}$. It may be noted that a meridional circulation with the same sign could result from heating the poles baroclinically (see Chapter VI). Also,

$dW_{10}(r)/dr < 0$, which is consistent with the thermal wind relation.

Whereas the meridional circulation, $dW_0^{(k)}/dr$, and $W_{12}(r)$ all reverse sign if $S < 1$, Kippenhahn (1963) argued that $S > 1$ could be reasonable for the solar convection zone.

The vertical shear of $W_0^{(k)}$ rather than the anisotropic viscosity is apparently the true energy source. The basic criticism of Kippenhahn's (1963) model is that he has failed to show that anisotropic viscosity (or any other process for that matter) maintains $W_0^{(k)}$. The energy equation for Kippenhahn's steady state model should reduce to $\int (\underline{f}^{(k)} + \underline{f}'^{(k)}) \cdot \underline{v}^{(k)} d\tau = 0$ because the kinematic boundary condition prevents any flux of kinetic, internal, or potential energy across the boundaries. Since isotropic friction is a well known energy sink, i.e., since $\int \underline{f}^{(k)} \cdot \underline{v}^{(k)} d\tau < 0$,

there is an inconsistency unless $\int \underline{F}'^{(\kappa)} \cdot \underline{V}^{(\kappa)} d\tau > 0$. We verified that $\int (\underline{F}'^{(\kappa)} \cdot \hat{\lambda})(W_o^{(\kappa)} r \cos \theta) d\tau < 0$, so that anisotropic friction does not maintain $W_o^{(k)}$. The inequality $\int \underline{F}'^{(\kappa)} \cdot \underline{V}^{(\kappa)} d\tau < 0$ probably holds for the deep atmosphere case, since it holds for the thin spherical shell case. But even if anisotropic viscosity were an energy source, there would have to be a negative viscous effect which might be better understood by explicitly retaining turbulent eddies. What Kippenhahn has really shown is that an axisymmetric meridional circulation which is driven by a rather nebulously defined energy source could maintain a differential rotation.

Axisymmetric Magnetic Theories

Differential rotation in a (thin) spherical shell containing magnetic fields has been studied by Nakagawa and Trehan (1968) and by Nakagawa and Swartztrauber (1969). Neither model really explains the observed differential rotation however, because it is imposed as a condition at the top boundary. In both, solid body rotation ω_o is also imposed at the lower boundary.

Nakagawa and Trehan (1968) seek steady state, axisymmetric, toroidal velocity and poloidal magnetic field solutions in an inviscid, perfectly conducting fluid. Thus Ferraro's law of rotation holds throughout, i.e. the angular velocity ω is a function of the poloidal magnetic stream function ψ_{mp} in meridional planes. They choose a simple relationship of the form $\omega^2 = a \psi_{mp} + b$, where a , and b , are constants.

This formula is imposed as a constraint in the Nakagawa-Swartztrauber (1969) model at both boundaries. However, such a constraint may violate the physical boundary condition that currents be confined to

the spherical shell. The axisymmetric toroidal magnetic field (which does not identically vanish) is correctly set to zero at both boundaries. But judging by the kinks in their figures 3a, 4a, 5a, and 6a, $\partial\psi_{m_p}/\partial r$ is discontinuous at the boundaries. Yet, as shown in Chapter II, all magnetic field components and hence $\partial\psi_{m_p}/\partial r$ (as well as ψ_{m_p}) should be continuous there. In any case, the magnetic field plays a strong role even though the Maxwell stresses are insignificant. Thus, as in the first model, ω_0 equals the angular velocity of the pole at the top boundary and $b_1 = \omega_0$.

The Nakagawa-Trehan (1968) model is not relevant to the question of maintenance of a differential rotation, since viscous dissipation is absent. There are no Reynolds stresses nor Maxwell stresses, and none are needed. The maintenance of Nakagawa and Swarztrauber's (1969) differential rotation is of interest however, since their model includes a meridional circulation, toroidal magnetic field, and viscous (as well as ohmic) dissipation. The differential rotation within their spherical shell is directly maintained against frictional dissipation mainly by axisymmetric Reynolds stresses, which can be inferred from their figures 3b and 3d. Curiously enough, the cellular patterns and sense of the meridional circulation agree qualitatively with Kippenhahn's for his $S > 1$ case. The ultimate energy source is of course the imposed differential rotation at the upper boundary.

The horizontal angular velocity profile exhibits a smooth transition with height between the profiles at the top and bottom boundaries, suggestive of frictional coupling. In contrast, in the first model,

the angular velocity profile depends upon an arbitrary constant surface current at the upper boundary. An intense positive jet just below the surface or a negative equatorial jet in the center of the shell are possible.

1.3.2. Asymmetric Theories

A Modified Barotropic Model

Thus far the discussion has focused upon axisymmetric theories of the solar differential rotation. But in Nickel's (1966) modified barotropic model, the differential rotation was maintained by asymmetric processes. The flow was assumed to be two-dimensional and was characterized by a stream function $\Psi = \sum_{m=0}^{12} \sum_{n=0}^{12} \tilde{\Psi}_{m+n}^n Y_{m+n}^n(\lambda, \omega)$, where the $\tilde{\Psi}_{m+n}^n(\lambda)$ are complex spectral coefficients and the Y_{m+n}^n are spherical harmonics. The barotropic vorticity equation was modified by including horizontal frictional coupling, parameterizing vertical frictional coupling, and infusing energy into one or more source modes $\tilde{\Psi}_{m+n}^n$ at a constant rate. This rate was governed by the decay time τ_3^0 of the differential rotation. The model was integrated numerically in time.

The following source modes were considered: $\tilde{\Psi}_7^6$ alone; $\tilde{\Psi}_{13}^{12}$ alone; $\tilde{\Psi}_{13}^6$ alone; $\tilde{\Psi}_{13}^9$ alone; $\tilde{\Psi}_2^k, k=6, \dots, 12$ equally weighted; and $\tilde{\Psi}_8^k, k=1, 2, \dots, 8$ equally weighted. With $\tilde{\Psi}_3^0$ very small initially, a large amplitude quasi-steady differential rotation developed only for the source modes $\tilde{\Psi}_7^6$ or $\tilde{\Psi}_{13}^{12}$. The higher energy input required by source mode $\tilde{\Psi}_{13}^{12}$ as compared to $\tilde{\Psi}_7^6$ probably reflects the greater frictional dissipation of $\tilde{\Psi}_{13}^{12}$.

Eddy transport of relative angular momentum up the angular velocity gradient is the only mechanism which can maintain the differential rotation against frictional dissipation. This is achieved through energy flow from the source mode to lower modes. The best qualitative results were achieved with source mode $\tilde{\Psi}_7^6$ and $\tau_3^0 \sim 10^7$ seconds, a decay time comparable to Ward's (1964) estimate. While modes with $n=1$ and $n=2$ had sizable amplitudes, the dominant eddy momentum transport was by source mode type waves ($n=6$). Angular momentum convergence occurred equatorward of 25° . In this region, the streamlines were tilted NW-SE (SW-NE) in the northern (southern) hemisphere. The differential rotation and eddy transports were only a factor of two greater than indicated by the observational data.

Unfortunately perhaps, a negative differential rotation or even an antisymmetric one could be maintained given different initial conditions. Presumably, the quasi-barotropic model lacks sufficient physical constraints to insure independence of the average differential rotation from the initial conditions. In a sense, the behavior of Lorenz's (1960a) maximum simplification "dishpan" model is analogous.

His unsuccessful attempts with other source modes led Nickel to speculate that a small upper bound on m could be a prerequisite of suitable source modes. Such a result would be interesting in view of recent findings by Busse (1970). Although Nickel's energy source lacks an explicit physical mechanism, his energetics are self-consistent.

Magnetic Braking

According to Starr and Gilman (1965b), horizontal eddy Maxwell

(magnetic) stresses might oppose the action of the horizontal eddy Reynolds stresses on the differential rotation. Such magnetic braking could occur if the large scale horizontal magnetic streamline pattern were tilted systematically in the same sense as Nickel's (1966) velocity streamline pattern. The line of sight contours on mean synoptic magnetic charts do tilt this way. From these charts, Starr and Gilman (1965b) have inferred that the horizontal eddy Maxwell stresses could be about 25% as strong as the Reynolds stresses. An RMS value of roughly 7 gauss for the horizontal eddy magnetic field would suffice at photospheric levels (150 gauss at $r=0.98 R_{\odot}$), assuming similar correlation coefficients for the Maxwell and Reynolds stresses.

Of course, there is no guarantee that charts of horizontal magnetic field patterns resemble the contours on mean synoptic magnetic charts. After all, the functional relationship between the line of sight component and the radial, meridional, and zonal magnetic field components depends upon the disk coordinates of the original magnetograph measurements.⁸ But suppose the large scale photospheric field were shown to pass a known consistency check for approximately horizontally nondivergent vectors. Then the magnetic stream function Ψ_m (analogous to Ψ_v) could probably be estimated by the method of characteristics. In this case, one could obtain a better estimate of magnetic braking by horizontal eddy Maxwell stresses.

⁸The line of sight magnetic field is approximately radial near the disk center, zonal near the east and west limbs, and meridional near the poles. Inclination of the plane of the ecliptic to the solar equatorial plane adds complications.

Convective Energy Source

As already implied, a convectively unstable lapse rate in a portion of the sun is predicted by stellar models and suggested from observations of cellular patterns of various sizes. It is capable of locally generating convective motions, some of which penetrate into the visible photosphere. The effects of rotation and possibly spherical geometry could be important in solar convection. For a sphere of Boussinesq fluid containing an axisymmetric distribution of heat sources, Roberts' (1968) linear theory predicts that asymmetric convective modes are the most unstable except for the smallest Taylor numbers. Asymmetric motions also tend to occur in rotating dishpan experiments or numerical simulations of them. An implication is that asymmetric motions may be characteristic of (rapidly) rotating fluids whether the motions are convectively or baroclinically driven.

Very recently, some important theoretical work relating to the maintenance of the differential rotation by convective motions has been carried out by Busse (1970) and Davies-Jones (1969). Busse solved the Bénard convection problem with dissipation, heat conduction, and rotation for a spherical shell of Boussinesq fluid. The nondimensional variables and Rayleigh number were expanded in terms of two small parameters ϵ_B and λ_B which are measures of convection amplitude and rotation, respectively. The mean temperature gradient was a linear function of radius.

Unlike the nonrotating case, oscillatory convection set in at the onset, when rotation was present. The convective waves propagated in the opposite direction as the rotation, and the dispersion relationship

was rather like the one for conventional Rossby waves on a sphere. The most unstable mode corresponded to the spherical harmonic Y_{ℓ}^{ℓ} ($Y_{\ell+i}^{\ell}$ was the most successful energy source mode in Nickel's modified barotropic model). As in previous investigations, rotation inhibited the onset of convection in Busse's model. The known solutions of $\mathcal{O}(\varepsilon_a)$ entered into the nonlinear terms of the $\mathcal{O}(\varepsilon_b^2)$ equations. A very important result was that the $\mathcal{O}(\varepsilon^2)$ nonlinear terms generated a vertically averaged differential rotation. We do not know if the differential rotation was positive at all heights, however.

Although Busse claimed his results should carry over for large λ_B , corresponding to the solar case, he did not prove this. Also he did not give the ratio of horizontal to vertical scale of the unstable modes for the spherical geometry. But he seemed to have in mind very large scale modes corresponding to the postulated supersupergranulation. As Busse recognized himself, compressibility should really be included for such modes since the vertical scale is $\mathcal{O}(10^{-1} R_{\odot})$. Despite the above shortcomings, Busse's theory must be considered as a plausible, self-consistent explanation of the differential rotation. It would be interesting to see of course, if large amplitude eddy angular momentum transports by supersupergranules could establish and maintain the sun's differential rotation.

Davies-Jones (1969) considered the effects of linear horizontal velocity shear and uniform rotation separately and together upon convection in an infinitely long channel. The treatment was simpler mathematically than Busse's, due largely to the cartesian geometry. The mean

temperature structure was characterized by a constant unstable lapse rate. Generally speaking, the fluid was assumed ideal. But for the case of linear horizontal shear, a fluid with frictional dissipation and finite thermal conductivity was also studied. In the ideal fluid case, attention was focused on the lowest latitudinal modes because they interact most strongly with the shear flow, although they had the lowest growth rates. But the largest scale modes could be made the most unstable in a real fluid.

The closest analogue to Busse's model was the case of rotation with no shear. However the fluid was ideal, had side boundaries, and no β effect. Davies-Jones found that the eddy Reynolds stress could have the same sign throughout the channel. Moreover, among various unstable modes including those having the same latitudinal and longitudinal wave numbers and growth rates not fast compared to the rotation period, the Reynolds stress and rotation had opposite signs. These modes do not exactly correspond to the Y_ℓ^{ℓ} modes of Busse, except for $\ell = 1$.

With no rotation, the convection interacted with the shear in an ideal fluid as follows: (a) For latitudinal mode 0, disturbances with all longitudinal wave numbers gave up energy to the mean flow. For latitudinal modes 1 and 2, the shorter wavelength disturbances also delivered energy to the mean flow while the longer wavelengths extracted energy from it.

With rotation and shear, up the gradient momentum transport could still occur. For example, if the rotation and shear had opposite signs, such a transport was accomplished by waves whose ratios of longitu-

dinal to latitudinal wave number⁹ and rotation rate to growth rate were not small. Conversely, axisymmetric cells transported momentum down the gradient. Increasing the rotation rate served to decrease the growth rate of latitudinal mode 1 type disturbances and make the horizontal flow more parallel to the isobars. The latter effect is reminiscent of geostrophic flow.

The results of Davis-Jones indicate that the dynamical effects of sphericity, more specifically the β effect is not crucial for up gradient momentum transports. The validity of an extrapolation for conditions in the sun is not fully established. Regarding the channel as an annulus, the outer rim is a kinematically rigid side wall boundary. The region adjacent to the outer rim would correspond to the solar equatorial region. But the latter presumably plays a role in the equatorial acceleration and is not flanked by any side boundaries. On the other hand, Davies-Jones work does lend plausibility to a convective theory of the differential rotation.

Baroclinic Energy Source Reconsidered

Whether of symmetric or asymmetric origin, a baroclinic theory in its simplest form requires the existence of a large scale meridional temperature gradient in a convectively stable layer. The only relevant temperature measurements available are in the surface layers. But their uncertainty is so great that at best they give an estimate of the upper bound of horizontal temperature differences. Although the surface layers

⁹The result applies basically to latitudinal mode 1. Higher modes were not discussed.

are convectively stable, the radiation relaxation time based upon photospheric opacity estimates (Allen, 1963) is only of the order of minutes. Radiation processes would attempt to destroy slowly varying large scale, horizontal photospheric temperature differences.

No observations are available of course, inside the convection zone say at $r=0.98R_{\odot}$. Stellar evolution models now in use preclude horizontal temperature differences anywhere, as all variables depend by assumption only upon radius. They also do not permit subadiabatic lapse rates to be imbedded in the middle of the convective zone, although the positive departure from adiabatic can be made small there. On the other hand, such models do provide estimates of the opacity in the convective zone. From these, one may infer radiative relaxation times $\geq \mathcal{O}(10 \text{ years})$ at $r=0.93R_{\odot}$, a very tolerable value. This radiative relaxation is less of an obstacle at that depth for baroclinic theories. But can a large scale meridional temperature gradient be imbedded inside a "stable" layer of the convective zone? Gilman (1967, 1969) was the first to argue that this could be a plausible condition based upon the work of Veronis (1966) and Gille (1967). We shall now elaborate on these arguments.

Veronis's (1966) numerical-spectral model of two dimensional, nonlinear, asymmetric Bénard convection in a nonrotating fluid with stress-free boundaries is relevant here. The initial lapse rate was linear and unstable, and the system of equations ultimately approached a steady state. The final lapse rate was slightly stable over much of the region away from the top and bottom boundaries and very unstable near them in many instances. More specifically, this behavior occurred over

the wide range of Prandtl numbers tried, and for Rayleigh numbers of order 10 times the critical value. The overshooting did not occur for low supercritical Rayleigh numbers and was confined to small boundary-interior transition regions for very high supercritical Rayleigh numbers. Temperature reversals in boundary-interior regions were also reported by Herring (1964). Likewise, Deardorff (1965) obtained a slight reversal for a Rayleigh number of 6.75×10^5 . For small Prandtl numbers, Veronis argued that a region of stable stratification for a fully turbulent fluid with three dimensional motions should not exist. He was not sure what to expect for larger Prandtl numbers.

On the experimental end, temperature reversals had been observed to be present prior to 1967, but were either not recognized as significant or else were regarded as spurious. By means of an interferometric technique, Gille (1967) successfully measured in a laboratory model the horizontally averaged lapse rate at 20 levels of air between two plates roughly 2 cm apart. The differential heating between the plates corresponded to a superadiabatic lapse rate. As the ratio of actual to critical Rayleigh number increased, the mean temperature profile became steeper near the boundaries and more nearly adiabatic away from them. Finally, at a ratio of 16, the mean temperature profile was subadiabatic by roughly 1 part in 100 in about the middle third of the air layer. Gille attributed Deardorff's failure to observe a temperature reversal experimentally to the Rayleigh number (1.5×10^6) being slightly too high, i.e. being characteristic of the fully turbulent regime. Estimates of the Rayleigh number for solar convection could vary over several orders of magnitude. But adopting $4 \times 10^{13} \text{ cm}^2/\text{sec}$ as the

eddy viscosity and eddy thermal conductivity, 10^{-4} as the mean positive departure from adiabatic of the lapse rates, and 10^{10} cm as the depth, then the Rayleigh number is $\mathcal{O}(10^4)$. Thus a region of subadiabatic lapse rate in the solar convection zone is plausible. Buoyant convective elements could penetrate into the overlying unstable layer thereby transporting heat upwards through the stable layer, i.e. up the potential temperature gradient (refrigerator effect).

Secondly, would a meridional temperature gradient be possible within the convection zone? Now in Weiss's (1964) cellular model of convection, the superadiabatic lapse rate depends among other things upon whether the rotation and gravity vectors are (1) parallel or (2) mutually perpendicular. If the respective vertical heat fluxes $F_{(1)}$ and $F_{(2)}$ were equal, then the lapse rate for case (1) would be steeper by 4×10^{-8} °K/cm. As noted by Roxburgh (1967) this could imply a 300° horizontal temperature difference near the top of the solar convection zone, the pole being colder. If $F_{(2)} - F_{(1)}$ were gradually increased from zero, this temperature difference would first decrease and ultimately change sign. A latitude-varying heat flux at certain levels might be related to the inhibiting effects of rotation upon convection noted by Chandrasekhar (1953), Busse (1970) and others. In particular, Busse's most unstable mode (for marginally unstable convection) is proportional to $\cos \vartheta$ and hence dies off rapidly near the poles. Does this mean that the vertical heat flux would be inhibited near the poles within the convection zone? If so, a vertical convergence of heat would occur in polar regions, assuming the vertical heat flux at the radiative core-convection zone interface were radially symmetric. Horizontal heat transports towards the equator and a

relatively warm pole might then develop at certain levels. The warm pole could radiate more strongly, without complete compensation for the reduced vertical convective heat flux.

In the above scheme, energy generated in the thermonuclear core and transported upwards would first be transformed into convection energy. A small fraction of the latter would then be converted to available potential energy which could be released baroclinically.

Nickel (1966, 1969) estimated the rate of kinetic energy released by granulation and available potential energy released from baroclinic processes, comparing them to his required source mode energy input. Although the granulation released energy at a much more rapid rate than required, probably only a small fraction would cascade up and be available to modes of source mode size. There was a marginally adequate amount of available potential energy, for a horizontal temperature difference of 100° K.

Judging from results of Busse (1970) mentioned earlier, rotation has similar dynamical effects upon large scale convective waves and conventional Rossby waves despite their different sources of energy. These two types of waves could possibly even coexist. If so, an intriguing question is whether both or just one type would deliver energy to the solar differential rotation. Ward (1964) suggested that the solar atmosphere has a Rossby regime (in the general sense) as opposed to a symmetric regime. Given the observed mean solar rotation, a pole to equator temperature difference of 100° K, and a Reynolds number of $O(10)$, a Rossby regime could exist in the solar atmosphere (see Chapter VI).

Recently, Davies-Jones and Gilman (1970) have evaluated hor-

horizontal and vertical heat transports as well as other second order quantities for Davies-Jones's (1969) model. The effect upon the 0th order temperature structure was then computed. The upper (lower) half of the fluid was warmed (cooled) by vertical heat transports, at both high and low Prandtl number. In contrast, a significant 0th order horizontal temperature gradient was set up by horizontal heat transports at low Prandtl number only. As the model was linear, these computations were made at slightly supercritical Rayleigh number. A nonlinear numerical study of large scale convection in a rotating fluid having a moderately high supercritical Rayleigh number would be valuable. It might answer the question: Can a significant horizontal temperature gradient exist in a stably stratified layer within a convection zone?

If magnetic fields are present, baroclinic instability can still occur (Gilman, 1967), provided the ratio of inertial to magnetic forces is not small. But there are complications. In particular, the question arises to what extent the magnetic fields would modify the time-averaged differential rotation. (See Chapter VI.)

1.4. Theories of Magnetic Fields.

A fundamental question is how the solar magnetic fields are maintained. According to Mestel (1967) the three most popular classes of stellar magnetism theories are (a) primeval theories, (b) battery theories, and (c) dynamo theories.

Cowling (1957a) gave molecular magnetic diffusivity estimates of $10^8 \text{ cm}^2/\text{sec}$ and $10^2 \text{ cm}^2/\text{sec}$ for the photosphere and radiative core, respectively. On the other hand, the magnetic diffusivity outside the radiative core should probably be characterized by a much larger eddy

coefficient. (See Elsasser (1956) and Leighton (1964)). Eddy decay times are just too short for the observed solar magnetic field to be a remnant of some primeval photospheric field. Moreover, polarity reversals are difficult to reconcile with a theory based upon primeval fields in the radiative core.

The so-called battery term, i.e. the last term in equation (2-22) could convert thermal energy directly into magnetic energy. A qualitative description of a battery process was given in Mestel's (1967) review article. Consider a fluid in which axisymmetric conditions prevail and the pressure gradient is balanced by gravitational and centrifugal forces. If the rotation rate is uniform or a function only of distance from the rotation axis, no currents are generated. But for a more complicated rotation, the fluid is baroclinic and the battery term has a nonvanishing curl. This provides an EMF which generates an axisymmetric toroidal (zonal) magnetic field associated with currents in meridional planes. Neither asymmetries nor any fluid motions relative to the basic rotation are required.

1.4.1. Fluid Dynamos

Another possibility is that fluid motions could maintain finite amplitude magnetic fields and associated currents indefinitely, through induction, against ohmic dissipation. Such a fluid system may be loosely termed a (self-sustaining) fluid dynamo. Dynamo action could generate large magnetic fields from a small, seed magnetic field originally created by the battery process.

Two subclasses of fluid dynamo problems are the kinematic and

hydromagnetic types. For a kinematic dynamo, the problem is to find a magnetic field \underline{B} given the velocity field \underline{V} . The magnetic induction equation (3-36) is linear in \underline{B} . For hydromagnetic dynamos, the feedback of the Lorentz force upon the motion is taken into account. In addition, the problem is nonlinear in both \underline{V} and \underline{B} . If frictional dissipation is present, the Lorentz force cannot indefinitely maintain motions so that a new energy source, e.g. thermal energy is required. But induction is still assumed to be the only source of magnetic energy. In a homogeneous fluid dynamo, the fluid has homogeneous density. The homogeneous kinematic fluid dynamo is the simplest and most often treated case. In a reversing dynamo, the polarity of the magnetic field oscillates with time. Geophysical or astrophysical dynamo models usually have simply connected, e.g. spherical, geometry and frequently contain exterior current free regions. For a long time, there was considerable controversy whether a homogeneous fluid dynamo could exist. In fact, several anti-dynamo theorems were proved before any existence proofs were constructed. Historically, the idea of a steady state dynamo seemed rather intriguing.

The rotating disk dynamo is an example of a successful laboratory dynamo constructed from rigid moving parts. In contrast, there are no successful experimental fluid dynamos, to our knowledge. The dimensions of electrically conducting fluids in the laboratory are so small that magnetic induction evidently cannot overcome ohmic dissipation.

Anti-Dynamo Theorems

Cowling (1934) showed that magnetic fields cannot be maintained under steady state, axisymmetric conditions with the magnetic and velocity fields confined to meridional planes. Backus and Chandrasekhar

(1956) proved that Cowling's theorem still holds even if the magnetic and velocity fields are not confined to meridional planes. Braginskii (1964) showed rather elegantly that no axisymmetric dynamo exists, even if conditions are unsteady.

Another theorem states that dynamo maintenance is impossible if the velocity field is toroidal, i.e. can be expressed in terms of a horizontal stream function alone. Utilizing a vector spherical harmonic representation, Bullard and Gellman (1954) proved this for steady state conditions. But the proof holds even for unsteady conditions. The crucial point is that there is no way to regenerate poloidal from toroidal magnetic fields without poloidal motions. Thus, all magnetic fields ultimately die out, even if poloidal fields are initially stretched out into strong toroidal fields.

Finally, a steady state dynamo in which the variables are functions of only two cartesian coordinates cannot exist. Cowling (1957b) devised a general technique to prove this anti-dynamo theorem and the others in which steady state conditions were assumed.

Analytic Dynamos

The Backus (1958) existence proof applies to a spherical non-steady, asymmetric, three dimensional, homogeneous fluid dynamo. Both poloidal and toroidal fluid motions and magnetic fields are allowed. The energy source which drives the motions is apparently not specified. The only restrictions on the velocity are that it be solenoidal, be bounded, be continuously differentiable everywhere for all time, and vanish on the outer surface.

The actual motions which maintain the dynamo are somewhat

peculiar in that there are time intervals when stasis occurs, i.e. the fluid is at rest. Backus's motions cannot be identified with convection cells or Rossby waves. But Backus (1958) claims that "the magnetic effect of any motion can be approximated with arbitrary accuracy by replacing it by a series of rapid jerks interspersed with periods of rest." The dynamo works as follows. Initially, a strong axisymmetric shear flow converts an axisymmetric poloidal (dipole) field of unit energy into a strong axisymmetric toroidal field. Some contamination fields are also present. By shutting off the motion, the small contamination fields decay more rapidly, leaving mostly the axisymmetric toroidal field. By switching on asymmetric poloidal motions for a short time, the axisymmetric toroidal field are converted to the original dipole field plus other unwanted components. The latter fields decay faster than the dipole field when the motion is switched off again. To the extent the original starting point is reached, the process is periodic. Notice that the desired main field is a pure dipole.

The setup for the Herzenberg (1958) dynamo model consists of two rapidly rotating electrically conducting, rigid spheres of radius "a" imbedded in a stationary conducting fluid medium. Their centers are separated by a distance $R > a$. While each sphere rotates at the same angular velocity, their respective rotation axes are oriented in different directions. The magnetic Reynolds number is $R_m \gg 1$ and a steady state is quickly attained.

The dynamo works on the following principle. A magnetic field is created by mutual induction in the first sphere. The rotation of the second sphere acts upon this field to generate a second magnetic field

component. Likewise, the rotation of the first sphere acts on the latter magnetic field to produce the original magnetic field. Energy must of course be supplied externally to keep the spheres rotating at the desired rate. For the dynamo to work, both spheres must rotate in the same sense about their respective axes.

Mathematically, a set of homogeneous equations are solved for which the magnetic Reynolds number is an eigenvalue. There is the possibility of R_m being small but imaginary, which is unphysical. Various remedies exist to guarantee that R_m be positive, such as surrounding the two spheres at a large distance from them with an insulator. The theory predicts a value of $R_m=24.5$ if the rotation axes of the two spheres form a 90° angle and both axes are also inclined at 45° to the line joining the centers of the two spheres.

The Herzenberg (1958) dynamo model is not a good analogue to the sun of course. One of its virtues is that the theory is mathematically rigorous. Also, Lowes and Wilkinson (1967) have demonstrated experimentally that a Herzenberg-like dynamo works even if R_m and R/a are not large.

A very important analytic study of homogeneous kinematic dynamos has been carried out by Braginskii (1964). Some of his basic ideas were foreshadowed by Parker (1955b). But Parker's dynamo was partially based upon heuristic arguments and lacked a completely self-consistent expansion scheme (P.H. Roberts, 1967).

In Braginskii's (1964) theory, the velocity is assumed to have the form $\underline{v} = \langle \underline{v}_0 \rangle + \underline{v}'_1 + \langle \underline{v}_2 \rangle$. Here $\langle \underline{v}_0 \rangle$ is the axisymmetric toroidal (zonal) velocity, \underline{v}'_1 is the total eddy velocity of $\mathcal{O}(\langle \underline{v}_0 \rangle R_m^{-1/2})$,

and $\langle V_2 \rangle$ is the zonally averaged poloidal velocity of $\mathcal{O}(\langle V_0 \rangle R_m^{-1})$. The symbol R_m is the magnetic Reynolds number and $\langle V_0 \rangle$ is the magnitude of $\langle V_0 \rangle$, etc. Similarly, $\underline{B} = \langle B_0 \rangle + \langle B_2 \rangle + \sum_{n=1}^{\infty} \underline{B}'_n$ where $\langle B \rangle$ is the zonally averaged toroidal magnetic field, \underline{B}'_n is the total eddy magnetic field of $\mathcal{O}(\langle B_0 \rangle R_m^{-n/2})$, and $\langle B_2 \rangle$ is the zonally averaged poloidal field of $\mathcal{O}(\langle B_0 \rangle R_m^{-1})$. The Braginskii theory is valid in the asymptotic limit as $R_m \rightarrow \infty$. Clearly, the axisymmetric toroidal velocity and magnetic fields are much larger than corresponding poloidal fields and asymmetric fields in this limit.

Braginskii considers the induction of poloidal magnetic fields $\langle B_2 \rangle$ using the $\hat{\lambda}$ component equation for the magnetic vector potential $\langle A_2 \rangle$, where $\text{curl}(\langle A_2 \rangle \hat{\lambda}) = \langle B_2 \rangle$, $\langle A_2 \rangle = \hat{\lambda} \cdot \langle A_2 \rangle$, and $\hat{\lambda}$ is a unit azimuthal vector. The induction equation for $\langle B_0 \rangle$ is retained. Secondly, Braginskii introduces "effective quantities" $\langle A_2 \rangle_e$ and $\langle V_2 \rangle_e$ into the equations mentioned above. They reduce to $\langle A_2 \rangle$ and $\langle V_2 \rangle$ for the axisymmetric case.

Following this procedure, the zonally averaged $\langle B_0 \rangle$ induction equation has the same form in cylindrical coordinates for both the axisymmetric and asymmetric cases. This is also true of the zonally averaged $\langle A_2 \rangle_e$ induction equation with one crucial exception. There is a new term containing asymmetric effects, i.e. the generation term $\langle \mathcal{E} \rangle = \sum_{n=2}^{\infty} \langle \mathcal{E}_n \rangle$ which depends upon eddy correlations involving functions of V'_1 and B'_n . Braginskii shows that $\langle \mathcal{E}_2 \rangle = \langle \mathcal{E}_3 \rangle = 0$, while $\langle \mathcal{E}_4 \rangle = \Gamma_2 \langle B_0 \rangle$, where $\Gamma_2 \sim \mathcal{O}(R_m^{-2})$ does not vanish. This result is consistent with the diffusive time scaling and the scaling for $\langle A_2 \rangle$. Now Γ_2 can be expressed as a function of C'_m 's and S'_m 's of the spectral expansion

$V_{1\rho}' = \langle V_0 \rangle \sum_{m=1}^{\infty} (C_m \cos m\lambda + S_m \sin m\lambda)$ for the poloidal part $V_{1\rho}'$ of the asymmetric velocity $V_{1\rho}'$. This follows from the relation $B_{1\rho}' = \frac{\langle B_0 \rangle}{\langle V_0 \rangle} V_{1\rho}'$ for the first order asymmetric poloidal magnetic field and a more complicated expression for $B_{2\rho}'$ in terms of functions of $\langle V_0 \rangle$ and $V_{1\rho}'$. Carrying out the expansion to the next highest order in $R_m^{-n/2}$, the equations quite remarkably retain the same form (Tough and Gibson, 1969)¹¹. The only modifications are that Γ_2 is replaced by $\Gamma_2 + \Gamma_3$ and the "effective quantities" are more complicated.

The generation term $\langle \mathcal{E}_4 \rangle$ is crucial to the net production of axisymmetric poloidal fields $\langle B_2 \rangle$. The following conditions must be met if Γ_2 and $\langle \mathcal{E}_4 \rangle$ are not to vanish. First, neither the zonally asymmetric poloidal velocity $V_{1\rho}'$ nor the asymmetric poloidal magnetic field $B_{1\rho}' + B_{2\rho}'$ may vanish. From the formulae for $\langle \mathcal{E}_4 \rangle$ and Γ_2 (plus $V_{1\rho}'$, $B_{1\rho}'$ and $B_{2\rho}'$), $\langle B_0 \rangle \neq 0$ and $\langle V_0 \rangle \neq 0$ as well. Second, the phases of at least one C_m, S_m pair in the spectral representation of $V_{1\rho}'$ must be nonuniform, i.e. $C_m \times S_m \neq 0$ for some value of m .

In turn, the $\langle B_2 \rangle$ fields are twisted into axisymmetric toroidal fields $\langle B_0 \rangle$. This link is vital to the dynamo process, due to the explicit dependence of $\langle \mathcal{E}_4 \rangle$ upon $\langle B_0 \rangle$. But twisting cannot occur if a Ferraro's law type of configuration is present, i.e. if the surfaces of constant $\tilde{\omega} \langle A_2 \rangle$ and $\langle V_0 \rangle / \tilde{\omega}$ coincide, where $\tilde{\omega}$ is the cylindrical radius.

The boundary layers in the Braginskii kinematic dynamo theory are passive, i.e. the interior solution can be obtained without reference

¹¹ They even speculate that this could be true for expansions of arbitrarily high order in $R_m^{-n/2}$.

to the boundary layer solution. However the boundary layer is as important a source of induction as the interior.

Braginskii (1964) and Tough and Gibson (1969) actually obtained kinematic dynamo solutions. The geometry was cylindrical and the specified velocity field steady, whereas the solution for the magnetic field was time variable. This does not prove that a hydromagnetic fluid dynamo with a steady velocity field is possible.

The Braginskii theory illustrates quite elegantly the necessary conditions for dynamo maintenance. It is perhaps noteworthy that poloidal velocity eddies and large scale toroidal magnetic fields are common to the Backus (1958) and Braginskii (1964) dynamos. Although the latter is probably more realistic for solar applications, since it requires no jerky motions, it is not conducive to solar magnetic reversals, as noted by P.H. Roberts (1967). He speculates that magnetic reversals might be restricted to hydromagnetic type dynamos.

Irregular magnetic reversals are predicted by Rikitake's (1958) relatively simple double disk (hydromagnetic) dynamo theory. Of course, the conducting medium is not a fluid. But the electromagnetic feedback upon the angular velocities of the rotors is apparently crucial to the reversal process.

As a final example of analytical dynamo work, Childress (1969) examines a general class of time-dependent hydromagnetic dynamos. He expands variables in powers of a small parameter $\delta^{1/2}$ (instead of $R_m^{-1/2}$), where δ is the ratio of the characteristic small to large length scales. Large scale effects and the spacial average of small scale effects are in-

cluded in the magnetic induction equation. However the magnetic body forces in the momentum equation are of only the latter type.

Numerical Dynamos

The numerical study of Bullard and Gellman (1954) is rather well known. Their model applies to a homogeneous, kinematic, steady state (and hence nonreversing) dynamo. The geometry is spherical and the fluid is surrounded by an exterior insulating region. A spherical harmonic spectral representation with radially dependent spectral coefficients is employed.

Bullard and Gellman's velocity is specified by the toroidal harmonic $T_1^{0,c} = -Er^3$ or $-Er^2(1-r)$ and a poloidal harmonic such as $S_2^{2,c} = r^3(1-r)^2$ for the nondimensional radius $r, 0 \leq r \leq 1$. The $T_1^{0,c}$ harmonic represents an axisymmetric angular velocity which varies with radius only and whose mean is $E/2$ or $E/10$. Also, the $S_2^{2,c}$ harmonic simulates convective eddies and E measures the ratio of the toroidal flow to the poloidal eddies.

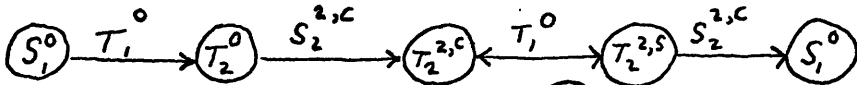
Equations in the spectral domain are obtained from the orthogonality relations on the sphere of ordinary spherical harmonics, toroidal vector spherical harmonics, and poloidal vector spherical harmonics.¹² Having computed the required Gaunt and Elsasser interaction integrals, Bullard and Gellman (1954) evaluate various nonlinear products. If A_α, B_β , and C_γ are spectral coefficients and $I_{\alpha\beta\gamma}$ is an interaction integral, then a typical nonlinear product has the form $C_\gamma = \sum_\alpha \sum_\beta I_{\alpha\beta\gamma} A_\alpha B_\beta$. Fortunately most of the $I_{\alpha\beta\gamma}$'s vanish according to the "selection rules".

¹² Poloidal vectors, toroidal vectors, and vector spherical harmonics are all defined in Appendix A.

These include low order orthogonal truncation, in which only a small number of harmonics are retained.

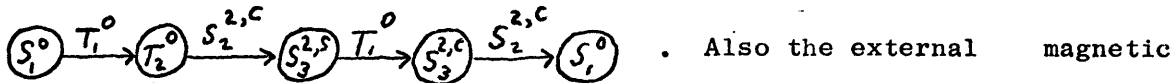
In the computations, the radial dependence of spectral coefficients is approximated numerically. The problem is then to determine the eigenvalue R_m for which solutions can exist. A dynamo solution appears to be physically plausible because positive real values of R_m can be found. For a particular level of truncation, i.e. $m+n \leq 2$ the following interactions in the dynamo are most important: (i) An axisymmetric dipole magnetic field S_1^0 is twisted by the axisymmetric toroidal velocity field T_1^0 into an axisymmetric toroidal magnetic field T_2^0 antisymmetric about the equator. (ii) The T_2^0 magnetic field interacts with the eddy convection mode $S_2^{2,C}$ to produce an eddy toroidal magnetic field $T_2^{2,C}$. (iii) In turn, the $T_2^{2,C}$ magnetic field and the T_1^0 motion interact to produce another eddy toroidal magnetic field $T_2^{2,S}$. (iv) To complete the cycle, the $T_2^{2,S}$ magnetic field and $S_2^{2,C}$ motion interact to produce S_1^0 magnetic fields.

This closed cycle has the schematic representation



The double arrow between $T_2^{2,C}$ and $T_2^{2,S}$ indicates sufficient back coupling occurs to reduce dynamo action unless R_m is increased significantly. With

$m+n \leq 3$, more closed loops are possible including the chain



Also the external magnetic field has opposite signs for the two cases $m+n \leq 2$ vs. $m+n \leq 3$

(Bullard and Gellman, 1954).

A controversial question is whether they obtained a true numerical dynamo solution. To a purist, a dynamo solution is convincing only if it remains essentially unchanged, beyond some level of truncation. Now

Bullard and Gellman (1954) retained the first q interactions starting with T_1^0 and $S_2^{2,c}$ harmonics for \underline{V} and an S_1^0 harmonic for \underline{B} . They let $q=4, 7, \text{ and } 12$, ie, retained all spherical harmonics up to Y_2^2, Y_3^2 , and Y_4^4 , respectively. The dynamo seemed convincing to many people at first because R_m did not vary much.

However, a more systematic investigation by Gibson, Roberts, and Scott (1969) of the effect of the level of truncation upon R_m proved more discouraging. They let $q=4, 5, 7, 8, 10, 12, 13, 15$, and 17 so that spherical harmonics of degree up to $m+n=5$ were retained for the cases $q=15$ and $q=17$. Unfortunately, whereas $R_m(q)$ was bounded by $63 \leq R_m \leq 75$ for the cases $q=4, 5, 7, 8, 10, 12$ and 13, $R_m(q=15) \sim 112$ and $R_m(q=17) \sim 139$, suggesting no convergence. Now perhaps $R_m(q)$ would begin to converge at higher values of q . But if the above trend continued, then with an infinite number of harmonics, dynamo action might not be possible for a finite value of R_m . They also found incidentally that convergence to the model solution $R_m(q)$ required greater vertical resolution as q and hence the horizontal resolution increased.

The Bullard and Gellman (1954) dynamo has been criticized on other grounds also. Their dynamo may be compared to the Braginskii dynamo for the asymptotic limits $E \rightarrow \infty, R_m \rightarrow \infty$ and $R_m^{-1/2}/E^{-1} \rightarrow$ finite limit (P.H. Roberts, 1967). Although the Bullard and Gellman dynamo violates the hypotheses of the so-called anti-dynamos and even has an asymmetric poloidal velocity $\underline{V}_{1,\rho}'$, the phase of $\underline{V}_{1,\rho}'$ is uniform ($\underline{S}_m=0$). Hence $\Gamma_2=0$ and in fact, $\Gamma_3=0$.

Another steady state numerical spherical dynamo investigation was carried out by Stevenson and Wolfson (1966). The levels of horizon-

tal and vertical low order resolution were comparable. Spherical harmonics and Bessel functions were the expansion functions for the spectral representations tangent to and normal to the sphere, respectively. The most significant departures from the Bullard and Gellman study are (1) the dynamo was of the hydromagnetic type (2) a thermodynamics equation was added, and (3) the ultimate energy source for the system was a volume distribution of heat sources. Unfortunately their only physically meaningful solutions, i.e. with positive joule heating, were axisymmetric and thus incapable of dynamo action. This result has obvious implications for the Bullard and Gellman (1954) dynamo too. In the final analysis, some physical mechanism is needed to generate and hence justify large scale steady, but asymmetric motions.

1.4.2. Maintenance of the observed solar magnetic field

Several theories have been proposed to explain the maintenance of large scale solar magnetic fields and/or aspects of the sunspot cycle. Generally speaking, they borrow elements from dynamo theories described heretofore, but are less rigorous.

A classic example is Babcock's (1961) theory. Initially the large scale magnetic field \underline{B} is axisymmetric and poloidal and is confined to the region $r \geq \theta(0.9)$. In fact \underline{B} is a pure dipole, although the large scale poloidal magnetic field on the sun is more complex, as noted previously.

Now the "Babcock term" $\frac{\langle B^{\theta} \rangle}{r} \frac{\partial}{\partial \varphi} (\langle \omega_{\theta} \rangle r \cos \varphi)$ in the magnetic induction equation twists the poloidal field $\langle B^{\theta} \rangle$ into an axisymmetric toroidal field $\langle B^{\lambda} \rangle$.¹³ From the shape of the observed differential rota-

¹³ cf. with Bullard and Gellman (1954) and Braginskii (1964).

tion $\langle \omega \rangle, \langle B^A \rangle$ is antisymmetric about the equator, with $\langle B^A \rangle > 0$ in the northern hemisphere. The toroidal field amplifies linearly with time and with $\frac{d}{dt}(\sin^2 \varphi)$ for $|\varphi| \leq 30^\circ$, extracting energy from the differential rotation. Also, the stronger the differential rotation, the more rapidly the amplification process proceeds.

Next, strands of amplifying toroidal magnetic field are twisted locally into ropes, enhancing the local field intensity by up to a factor of 10. If the large scale toroidal field reaches the critical intensity of $B_c \sim 264$ gauss at a given latitude φ_c , $|\varphi_c| \leq 30^\circ$, then the flux ropes can form loops. These loops are supposed to rise due to magnetic buoyancy¹⁴, emerging at the surface as bipolar magnetic regions (BMR's) or as sunspots (imbedded inside BMR's). The convective motions which carry flux loops upward are asymmetric and poloidal. Babcock's formula for the critical latitude as a function of time agrees rather well with the observed equatorward migration of sunspot activity zones. Sunspots and BMR's form randomly for some time after the critical field intensity is attained. The net toroidal field intensity begins to decay after enough magnetic flux loops rise to the surface, and decay even more when toroidal fields of opposite signs are produced somewhat later.

A rising loop of magnetic flux has a positive and a negative polarity branch which may be identified with two sunspots of opposite

¹⁴Parker (1955a) considered a local parcel of ideal gas containing magnetic flux. If the parcel had the same temperature and total (i.e. gas plus magnetic) pressure as its flux-free surroundings, its density was less. On the other hand, if such a parcel were cooler than its surroundings, its buoyancy would be less positive or perhaps even negative.

polarity. By definition, the \mathcal{P} spot of a group is closer to the equator while the f spot is farther away. In the northern hemisphere, a loop is tilted relative to a meridian such that the \mathcal{P} spot has the same polarity and the f spot the opposite polarity as the original poloidal field. As noted by Leighton (1964), the observed tilts of sunspot group axes are much larger however, than predicted by Babcock's theory. In any case, p spots or f spots have opposite polarities in the two hemispheres, because the corresponding tilts of flux loops are mirror images about a meridian.

In the final phase of the cycle, axisymmetric, meridional currents at middle latitudes could transport f spot fields (or follower portions of BMR's) poleward to first neutralize and then reverse the poloidal field. Similarly, equatorward currents at low latitudes could help promote cancelation of p spots (or corresponding leader portions of BMR's) from the two hemispheres. The amount of ohmic dissipation would govern the time interval for achieving a polarity reversal. Since much more flux is available than required, considerable dissipation is evidently present. Of course, axisymmetric meridional motions have not been conclusively observed.

After another cycle, the original dipole field is retrieved. During the double cycle, the direction of the horizontal magnetic field rotates counterclockwise (clockwise) in the northern (southern) hemisphere.

Although Babcock's (1961) arguments are quite heuristic, he stimulated considerable further research. His ideas on the role of the differential rotation in converting poloidal into toroidal magnetic fields and on the meridional transport of magnetic fields have been incorporated,

generalized, or modified in more sophisticated models.

For example, Leighton (1964) accepts Babcock's idea that the reversal of the dipole field results from migrations of f spot magnetic fields towards the poles and p spot fields towards the equator. But he proposes a new mechanism to achieve this. In effect, he solves the vertical component magnetic induction equation (3-38c), retaining only the horizontal dissipation term $\eta \nabla_H^2 B^z$ for a thin spherical shell. In this expression, B^z is the vertical magnetic field and ∇_H^2 the Laplacian operator on a spherical surface. Also, $\eta \sim \mathcal{O}(\frac{1}{2} L_{SG}^2 / \tau_{SG})$ is an eddy coefficient of ohmic dissipation, where L_{SG} is the radius and τ_{SG}^{-1} the reciprocal life time of a supergranule. The characteristic decay time is $\tau_0 = R_0^2 / \eta \sim \mathcal{O}(20 \text{ years})$.

Leighton (1964) argues heuristically that supergranules are good dispersing agents assuming their quasi-horizontal motions are well coupled with the magnetic fields in the heart of the convection zone. He cites the preferred location of strong magnetic fields at supergranular cell boundaries found by Simon and Leighton (1964) as evidence of such coupling.

As his most complicated example, Leighton considers the dispersal of a time-latitude dependent distribution of ring doublet magnetic field sources. These are supposed to simulate the longitudinally averaged sunspot distribution. At time $t=3$ years, the polarity reverses within the 25° to 40° latitude belt of both hemispheres, creating an octopole magnetic field configuration. The region of reversed polarity expands towards both the equator and the pole. This occurs even if only an instantaneous, localized doublet source is specified, suggesting that the tilt of a sunspot

group axis or doublet source plays a key role here. In the continuous source distribution case, the equatorward expansion of the reversed polarity region is also aided by the equatorward movement of the sources. In any case, the ratio of decay times of the octapole over dipole moments is only $1/6$ and by time $t=11$ years, a new dipole field of reversed polarity is established. The neutral line closer to the pole progresses poleward at a rate comparable to the observed migration of quiescent prominences (filaments) which are thought to lie along the neutral line. Advection of magnetic fields by the average differential rotation does not affect their northward or southward migration. The differential rotation does deform expanding regions however. The fields at high latitudes would be elongated and hence weakened the most.

In a more elaborate model, Leighton (1969) tries to simulate the entire sunspot cycle. Poloidal magnetic fields are twisted into toroidal fields by an angular velocity profile that varies with latitude and depth. When the toroidal field β^{λ} reaches a preassigned critical value β_c , a source eruption term for a ring doublet vertical magnetic field is switched on. No twisting of toroidal fields into magnetic ropes is required. Two important parameters in the source term are the time constant T_m for eruptions of toroidal flux tubes and a parameter F which measures the tilt of the doublet moment. There is a corresponding sink term in the equation for toroidal fields. As in Leighton's earlier model, ohmic dissipation on the supergranule scale leads to a polarity reversal of the β^{λ} fields formed by eruptions. The meridional magnetic field component β^{μ} is obtained from magnetic continuity.

Besides T_M and F , the model effectively contains three other parameters, i.e. α , β and n . These permit various angular velocity profiles of the form $\Omega = \langle \omega_0 \rangle + (\alpha + \beta \cos^n \omega)(R_0 - r)/H$ to be tested. In this formula, $\langle \omega_0 \rangle$ is the observed surface differential rotation relative to the polar rate, H is the depth of the layer, and the radial coordinate r satisfies the inequality $R_0 - H \leq r \leq R_0$. As n is increased, flux eruptions occur closer to the equator. Therefore it takes more time for the polarity reversal to reach the pole. For fixed α , β , and n , Leighton could usually adjust F and T_M to obtain a 22 year double cycle. Large values of F are undesirable as they would imply too great a tilt. Conversely, if F does not exceed a minimum value, an oscillatory solution is not possible.

The most realistic results are achieved for the case $\alpha = 0$, $\beta = 10$, and $n = 8$, corresponding to a $\partial\Omega/\partial r < 0$ type profile with the sharpest drop off near the equator. With $\alpha = 1000$, $\beta = -18$, and $n = 2$, corresponding to a core-convection zone interface in very rapid solid body rotation, the results are unrealistic. Perhaps the most interesting result is that the radial variation of Ω is more crucial than its latitudinal variation. In particular, the B^1 and hence B^2 magnetic field maximum drifts towards the equator in agreement with the Maunder Butterfly diagram only if $\partial\Omega/\partial r < 0$.

The following comments may be made about Leighton's kinematic model. The conversion of B^1 into B^2 fields is parameterized by an eruption term. The true induction equation for B^2 is not utilized for this crucial link. Also, the parameterization is such that no asymmetric magnetic fields or poloidal velocity fields explicitly appear. Thus the anti-dynamo

theorems show that Leighton's model is not a true dynamo. While the ohmic diffusion mechanism can cause a polarity reversal, other mechanisms are available. These include meridional transports by supersupergranule (baroclinic) scale eddy motions (Gilman, 1968), and by axisymmetric motions (Nakagawa and Swartztrauber, 1969). Furthermore, there is no feedback on the motion.

On the good side, many of Leighton's results agree qualitatively with various known facts concerning magnetic activity on the sun, whether or not by coincidence. Finally, his work could have implications for the variation of solar angular velocity with depth.

The work of Nakagawa and Swartztrauber (1969) previously discussed in a different context is relevant here. Their model has essentially no feedback on the motion and is incapable of dynamo action since all variables are axisymmetric. However their stated purpose is to investigate only how a toroidal field would evolve from an initial poloidal magnetic field. In contrast to Leighton's (1969) model, the Nakagawa-Swartztrauber (1969) model utilizes the true magnetic induction equation and has a meridional circulation. We recall that the meridional cell consists of rising branches at the poles and a descending equatorial branch.

As the law of isorotation holds initially, the meridional motions must first distort the field lines so that the differential rotation can twist them into toroidal fields. Adopting the Newton and Nunn (1951) profile for the surface angular velocity, toroidal fields form initially at $\varphi = 38^\circ$. Near the surface, the toroidal field is negative as desired and is transported towards the equator by the meridional cell.

The stronger the ohmic dissipation, the deeper the negative toroidal field penetrates. Its maximum intensity of 300 gauss (compared to Leighton's value of several thousand gauss) occurs at $\ell = 25^\circ$. Farther down, the toroidal field is positive and is transported poleward.

Now M. and L. d'Azambuja's profile is only slightly different from Newton and Nunn's. Yet for the former, the first negative toroidal fields appear at 43° , the maximum toroidal field intensity is under 150 gauss, and after a short equatorward drift, the toroidal fields drift poleward.

Nakagawa and Swarztrauber (1969) suggest that these divergent results may correspond to the Maunder butterfly diagram for sunspot migration and to the law of filaments, respectively. But that seems too much to expect. Also, they are in error in claiming that their meridional circulation with a maximum of 200 cm/sec at $\ell = 30^\circ$ is in close agreement with Ward's values. Actually at 30° , Ward could not obtain a statistically significant estimate of the axisymmetric meridional velocity. Finally, we note that their angular velocity is greater at the top than at the bottom boundary in contrast to Leighton's most successful profiles.

The extension of Pedlosky's (1964) linearized baroclinic instability analysis to the magnetic case by Gilman (1967) lays the groundwork for the development of nonlinear baroclinically driven, hydromagnetic dynamo models. His linearized model is quasi-heliostrophic¹⁵, utilizes cartesian geometry, and has two layers. But in addition to a latitude-height dependent zonal wind profile, the basic (axisymmetric) state has

¹⁵This term is the solar equivalent of quasi-geostrophic.

a toroidal magnetic field. Gilman shows how the presence of magnetic fields modifies Pedlosky's growth rates and phase speeds of eddy disturbances and his necessary conditions for instability (integral theorems).

Although the fluid is a perfect conductor (as well as inviscid), the model lacks two crucial ingredients for sustaining dynamo action, as recognized by Gilman. These are (1) a generation term for mean square poloidal magnetic flux and (2) a feedback of the poloidal field upon the toroidal magnetic field. These deficiencies are a consequence of the scaling of the first order terms in a Rossby number expansion. In particular, the velocity and magnetic fields are both assumed to be horizontally nondivergent, i.e. to depend upon (toroidal) velocity and magnetic stream functions alone, to first order.

More recently, Gilman (1968, 1969) has incorporated the two crucial ingredients for dynamo action mentioned above into a nonlinear, quasi-heliospheric two layer hydromagnetic model with baroclinic forcing. The geometry is cartesian, a low order spectral representation is adopted, and the spectral equations are integrated numerically in time. The large amplitude magnetic field reversals are particularly encouraging even though only 18 (or 36) degrees of freedom are retained.

The first link in the induction process is a Babcock type twisting term. It appears because the horizontal poloidal magnetic field is now formally scaled as large as the toroidal magnetic field. Basically, the horizontal shear of the axisymmetric zonal wind twists axisymmetric poloidal into axisymmetric toroidal magnetic fields. Vertical motions then twist toroidal into poloidal magnetic fields. The dominant interaction involves axisymmetric toroidal magnetic fields plus asymmetric

vertical motions and poloidal fields. Finally, asymmetric poloidal magnetic fields are systematically transported towards the northernmost wall by meridional eddy motions of toroidal as opposed to poloidal type. Eventually a polarity reversal occurs. Meanwhile, ohmic dissipation acts to reduce the amplitude of the axisymmetric poloidal magnetic field harmonic.

For horizontal velocity shears comparable to the observed differential rotation, the period for a double reversal is $\mathcal{O}(2)$ years). The observed double sunspot cycle and double reversal of the polar field takes about 22 years. A longer reversal period can be attained by decreasing the Rossby number, but then the differential rotation is too weak. Dynamo action is sustained only above a critical magnetic Reynolds number $R_{mc} \sim 100$. Whereas the "reversal period" is apparently insensitive to the value of $R_m - R_{mc}$, the amplitude of successive peaks begins to fluctuate as $R_m - R_{mc}$ is increased.

As various toroidal harmonics and asymmetric poloidal harmonics are reaching peak field strengths, the dominant axisymmetric poloidal magnetic field harmonic is just changing sign. The peak axisymmetric vertical magnetic field of roughly 40 gauss exceeds the "observed" solar value by somewhat over a factor of ten. This discrepancy can be reduced by choosing the ratio δ of the vertical to horizontal length scale to be $\leq \mathcal{O}(0.1)$ instead of $\delta = 1$. The ratio of magnetic to kinetic energy remains rather small, in agreement with Gilman's (1967) linear study.

Dynamo maintenance within a quasi-heliostrophic framework is possible only by sacrificing some mathematical rigor. This is at least

partially justifiable a posteriori. The generation term for vertical magnetic fields involving vertical motions is formally of $O(R_o^2)$, but in the actual computations is of $O(R_o)$. Other terms in the same induction equation formally of $O(R_o^2)$ vanish anyway in the two layer model due to the boundary conditions on the vertical velocity and vertical magnetic field.

In the absence of thermal forcing and viscous and ohmic dissipation, an invariant "total" energy integral can be obtained, but at a price. Imposing different potential temperatures at the two lateral boundaries, Gilman (1969) must discard all terms which explicitly involve both vertical differentiation and the vertical magnetic field component, in the horizontal momentum and horizontal induction equations. Meanwhile terms of the same order in Rossby number involving horizontal differentiation and horizontal poloidal magnetic field components are retained. Gilman (1969) argues heuristically that the neglected terms would probably not affect the results too much. However, the twisting of vertical magnetic fields by the vertical wind shear could interfere either constructively or destructively, depending upon the selected thermal forcing profile. Also, the vertical shear twisting term was more important in Leighton's (1969) model.

The "total" energy mentioned above is defined as the available potential plus toroidal kinetic plus toroidal magnetic energy. The formal scaling suggests that the energy of the horizontal poloidal magnetic field should not be excluded. A posteriori, the ratio of peak poloidal to peak toroidal energy is only 6%. But the instantaneous ratio is higher since the energy peaks are roughly 90° out of phase.

There are three shortcomings of the model which are especially relevant to the sun. Two of these were discussed by Gilman (1969). First of all, his axisymmetric zonal velocity profile $\langle u_3 \rangle$ at the upper level corresponds more to the terrestrial midlatitude jet than to the observed solar equatorial jet. More specifically, $\langle u_3 \rangle \sim c(t) \sin y$ where $c(t)$ remains positive and y is the nondimensional cartesian coordinate transverse to the channel $0 \leq y \leq \pi$. If the lateral wall $y=0$ corresponded to the equator, an easterly jet ($c < 0$) would be a better analogue to the solar case. Unfortunately, Gilman's Rossby number expansion is not valid, strictly speaking, too close to the equator. Besides, an artificial lateral wall at the equator is not very realistic.

Second, Gilman's magnetic field harmonics do not really correspond to the lowest order harmonics of interest on the sphere. For example, his only axisymmetric poloidal magnetic field harmonic is proportional to $\cos y$. At first glance, this harmonic is analogous to the dipole poloidal magnetic field harmonic $Y_1^0 \propto \sin \vartheta$ where $-\pi/2 \leq \vartheta \leq \pi/2$. However, the channel $0 \leq y \leq \pi$ is confined to a latitude band in the northern hemisphere.

Third, the magnetic fields are confined between the top and bottom boundaries in Gilman's model because both boundaries are perfect conductors. Yet coronal observations suggest that magnetic flux does leak out of the photosphere.

1.5 Characteristics of Our Dynamo Model.

We have formulated another numerical dynamo model. The basic physical processes of the Gilman (1968, 1969) model are retained. Thus ours has various essential ingredients for the generation and maintenance

of a fluid dynamo. These include (1) suitably large fluid dimensions, (2) an energy source, and (3) three dimensional, asymmetric motions. (See Elsasser, 1956).

The dimensions of the sun are inherently large enough so that magnetic induction can, in principle, compete with ohmic dissipation. Despite its possible shortcomings, baroclinic heating does serve as an energy source. Under suitable condition e.g., sufficiently rapid rotation, asymmetric baroclinic disturbances can develop. Also, the conversion of eddy available potential energy into eddy kinetic energy is accomplished through asymmetric, poloidal (vertical) motions. Finally, the model apparently passes the various anti-dynamo theorem tests and in principle satisfies the conditions for a nonvanishing Braginskii type of generation term.

The chief modifications we have introduced are:

- (i) a set of "primitive" hydromagnetic equations
- (ii) more degrees of freedom (126 in all)
- (iii) spherical geometry
- (iv) a Robert spectral representation
- (v) irrotational magnetic fields in a nonconducting region above the fluid region of main interest.

In principle, our model has the capability of making predictions near the equator which Gilman's (1969) model lacks. This feature is desirable because most of the relevant solar observations including those of the equatorial jet are confined to the 30°S - 30°N latitude band. Also, the lowest order odd harmonics of the axisymmetric poloidal magnetic field i.e. the dipole and octapole harmonics are included. These contribute to

the mean hemispheric magnetic polarity.

In formulating the "primitive" equation hydromagnetic model, vertical hydrostatic balance is replaced by vertical magnetohydrostatic balance, i.e. the magnetic pressure is taken into account. In addition, the vertical magnetic field induction equation is discarded and the vertical field is obtained from the magnetic continuity equation. This procedure is dictated by scaling and energetic consistency arguments. Our scaling is more rigorous than Gilman's. Finally, in the absence of dissipation and thermal forcing, an integral invariant can still be found for the "total" energy.

We retain considerably more degrees of freedom than in Gilman (1969). Nevertheless, we would have preferred many more harmonics and more levels for representing even fairly large scale processes within a thin spherical shell. Due to computational limitations, there is only a single positive zonal wave number though, as in Gilman's (1969) model. Zonal wave number $n=6$ seemed suitable because it is baroclinically unstable. Its presence in the solar atmosphere is suggested by Wilcox and Howard's (1970) auto-correlation curves. The Robert functions R_m^n (corresponding to spherical harmonics Y_{m+n}^n) with $n=0, m=1,2,3,4$; and $n=6, m=0,1,2,3,4$ are retained for stream functions, potentials and the temperature.

For a realistic dynamo model, the critical magnetic Reynolds number R_{mc} for dynamo maintenance should not increase without bound as the resolution is increased. This does not mean that the time histories for solutions of two models which were identical except for slight differences in resolution should coincide for all time. Unfortunately, the computations required for testing the convergence of R_{mc} cannot be handled by

present day computers.

We note that the potential field in the nonconducting region is not maintained by any external sources at infinity. The nonconducting region and the underlying atmosphere are coupled by the potential field through equations (3-5b), (3-5c), (3-5d), (3-24c), (3-20b), and (3-20d).

The increased complexity of our model is due mainly to the first three improvements. The effect of more degrees of freedom is obvious. In adopting the "primitive" hydromagnetic equations, the time step must be considerably reduced to prevent computational instability. These equations are also inherently more complicated than Gilman's. But fortunately, the number of distinct bilinear terms T can be substantially reduced by applying the linear Lundquist (1952) transformations¹⁶ to our "primitive" equations. (See Chapter III). In fact, the Lundquist and quasi-heliostrophic equations have comparable values of T in the space domain. Despite the additional linear operations associated with the Lundquist transformations, they give rise to increased computational efficiency.

Spherical geometry introduces complications also, because the equations contain curvature correction terms, and the algorithms for evaluating bilinear products in the spectral domain are more complex. On the other hand, simpler geometry is probably not as physically realistic. For example, an equatorial β -plane primitive equation model would not be valid at "sufficiently high" latitudes. Artificial walls could be inserted at latitudes 30° N and 30° S say. But hydromagnetic disturbances at higher latitudes on the sun might affect the dynamo process or help maintain the equatorial jet. Another approach would be to scale the equations

¹⁶ Elsasser actually deserves the credit for independently discovering these transformations earlier. See Elsasser, W. M., The Hydromagnetic Equations, Phys. Rev. 79, 1950, p. 183.

differently at low and high latitudes. However, a rigorous matching of solutions at some intermediate latitude might be difficult to achieve.

Beyond a certain resolution limit, a grid-point representation would be more efficient than a spectral representation. But a sophisticated grid would be required on the sphere in order to prevent linear and nonlinear instabilities. Two possibilities are the Kurihara-Holloway (1967) box grid or the Williamson (1969) spherical geodesic grid. Experience with these grids is limited to nonmagnetic models and we preferred to avoid working with them if possible.

In any case, we felt that a spectral representation would be well suited to a low order resolution model like ours. No nonlinear aliasing instability of the type illustrated by Phillips (1959) should occur, provided that the truncation is orthogonal. All discarded components are then uncorrelated, in the integral sense, with the retained components (Robert, 1966). Whereas nonorthogonal truncation might lead to instability, orthogonal truncation is simple enough to perform. It turns out that there is some difficulty associated with the truncation process (hopefully for only low order systems) as described in Chapter IV. The spectral representation itself utilizes a set of Robert functions. This representation should be equivalent to a spherical harmonic representation, but is more convenient, as explained in Chapter III.

1.6. Summary of the Other Chapters.

The model assumptions are spelled out in Chapter II. The prognostic and diagnostic equations plus the boundary conditions are then formulated for a model with continuous vertical resolution. In Chapter III, the equations are reformulated for a model with two layers in the vertical,

Following that, the Robert (1965, 1966) spectral method is explained in considerable detail and is applied to these equations. Finally, the sequence of steps for solving the equations is summarized.

The angular momentum balance is formulated in Chapter IV in the space domain, for the two layer model. Using the Robert spectral representation, the truncation process preserves the integrated angular momentum balance on each spherical surface. But a localized angular momentum balance exists for only "correctly truncated" terms. Chapter V contains a formulation of the energetics for the model.

Model solutions are described in Chapter VI while conclusions and suggestions for future research are given in Chapter VII. Angular velocity profiles are obtained for different thermal forcing profiles both in the magnetic and nonmagnetic case. Two angular velocity profiles are in qualitative agreement with solar observations. The "correctly truncated" angular momentum balance is discussed for two production runs.

Magnetic fields may be generated and sustained by dynamo action if the magnetic Reynolds number exceeds a critical value. Irregular magnetic reversals occur for both runs. The energetics help elucidate the reversal process. The characteristic reversal time is of the correct order of magnitude for the run having the less realistic angular velocity profile and too fast for the other run. While our vertical magnetic eddies may be loosely interpreted as active regions, they fail to obey certain laws (such as the generalized Spörer's law) of the solar magnetic cycle. This lack of agreement may be due however to the crude resolution, rather than to the basic thermal drive. When computationally feasible, runs should be made having (1) more horizontal resolution (and possibly more layers), (2) a larger aspect ratio δ , and (3) less magnetic induction,

i.e., a smaller value of $R_m - R_{m_c}$. This would provide a more definitive test of the baroclinic hypothesis. Other modifications include (4) choosing a dipole as the initial seed magnetic field, (5) testing the response of the model to different conditions on the velocity at the lower boundary, and (6) explicitly solving for large scale convective modes.

CHAPTER II. FORMULATION OF THE SPHERICAL HYDROMAGNETIC DYNAMO
MODEL WITH BAROCLINIC HEATING

2.1. Introduction.

It is now appropriate to state explicitly the model assumptions and develop the mathematical formalism. A rather general set of equations governing magnetohydrodynamic flow is simplified by making the "MHD approximation". In effect, this filters out relativistic electromagnetic phenomena. A rather detailed account of the "MHD approximation" has been included for the benefit of readers unfamiliar with it. But the real starting point is the equations for a thin spherical shell of rotating, Boussinesq, conducting, nonrelativistic fluid, heated baroclinically. Some simplification is achieved through scaling arguments and energetic consistency arguments of the sort familiar to meteorologists. Lastly, the boundary conditions are discussed with emphasis placed upon the electromagnetic boundary conditions. Incidentally, cgs electromagnetic units (cgs emu) are adhered to almost exclusively.¹

2.2. Basic assumptions.

At the outset, several basic assumptions are made which are either justifiable for the sun or at least self consistent. The first seven lead to the standard MHD equations. The others or their nonmagnetic analogues should be familiar to meteorologists.

¹In these units, the magnetic permeability μ_0 of free space is unity and the dielectric constant ϵ_0 of free space equals the inverse square of the speed of light. The magnetic induction \mathcal{B} is measured in gauss. Solar magnetic observations are generally reported in gauss.

- (i) The fluid is a single component, fully ionized gas, i.e., contains free electrons and only one species of bare nuclei.
- (ii) The fully ionized gas is a plasma, i.e. is essentially electrically neutral.
- (iii) The fluid may be treated as a continuum.
- (iv) The electron gas is in thermal equilibrium and is nondegenerate.²
- (v) The plasma is of the "high density" type.
- (vi) The gas motions are nonrelativistic.
- (vii) The magnetic permeability and dielectric constant take on the constant values of free space.
- (viii) The dynamo region is a thin spherical shell of rotating fluid about 2400 km thick and centered roughly 0.02 solar radii (14000 km) beneath the surface.
- (ix) The fluid in this shell is approximately Boussinesq.
- (x) The plasma is in magnetohydrostatic balance in the vertical direction. In this generalization of ordinary hydrostatic balance, the relevant pressure is the sum of the hydrodynamic plus "magnetic" pressure.
- (xi) The plasma motions are thermally driven by an externally imposed meridional (potential) temperature gradient.
- (xii) Relaxation towards the imposed gradient predominates over other non-adiabatic heating processes such as Joule or viscous heating in the thermodynamic equation.

²Degeneracy occurs in very dense stars as a consequence of the Pauli exclusion principle. Electrons (and possibly even ions) with low momenta are forced into higher momentum regions of phase space, squaring off the Maxwell-Boltzmann profile. See Schwarzschild (1958).

Let us elaborate further on these assumptions. For the postulated model depth, hydrogen is roughly 95% ionized and its relative abundance is $\mathcal{O}(0.9)$ by mass.³ Thus, as a first approximation, assumption (i) is fairly reasonable.

The potential due to a charged particle is essentially neutralized outside a sphere of radius λ_d (the Debye shielding distance) by the distribution of oppositely charged particles. Roughly speaking, $\lambda_d \sim 4.9(T_0/n_0)^{1/2}$, where n_0 is the average number density of electrons and ions and T_0 is a characteristic temperature. For the postulated dynamo region, $n_0 \sim 10^{18}$ particles/cm³, $T_0 \sim 8 \times 10^4$ °K, and so $\lambda_d \sim 1.4 \times 10^{-6}$ cm. Estimating the characteristic length scale of the large scale flow as $\lambda_0 \sim 1.5 \times 10^{10}$ cm, then $\lambda_d \ll \lambda_0$. Equivalently, the relaxation time for charge neutralization is extremely rapid. Therefore the solar gas is regarded as a plasma.

In a highly ionized plasma, the dominant collision process is weak interactions at a distance between electrons and ions. Based upon the above values of n_0 and T_0 , Jeffrey (1966) offers the crude estimate $\lambda_c \sim 5 \times 10^{-4}$ cm for the effective mean free path of electrons. Clearly, the plasma is collision dominated and can be described by continuum fluid properties.

The condition of thermal equilibrium is adopted as a first approximation, i.e. thermal relaxation processes on the atomic scale are filtered out. A simplification of the thermodynamics is thereby achieved.

³ Helium is mostly singly ionized and has a relative abundance of $\mathcal{O}(0.1)$ at $r \sim 0.98R_\odot$. The heavier elements are not stripped of many electrons, but their abundance is relatively small. The ionization estimates were calculated from a stellar model of Iben (1966).

In any case, there are no bound electrons to excite or ionize and no chemical reactions in a fully ionized, single component gas. From stellar model calculations by Schwarzschild (1958), electron degeneracy may also be neglected in the sun. Then, following Schwarzschild, we can write an ideal gas law as the equation of state for the fully ionized gas.

Suppose the centripetal acceleration and the magnetic part of the Lorentz force acting on an individual electron were in balance. The electron would then circle about the local magnetic lines of force. However, through an aggregate of weak interactions with other charged particles, the test electron would in reality be significantly deflected after traversing a distance of $\mathcal{O}(\lambda_c)$. Denoting the spiral or gyro radius by λ_g , the gyro frequency by ω_g and the effective collision time by τ_c , electron spiraling is inhibited if $\lambda_c \ll \lambda_g$, or $\omega_g \tau_c \ll 1$. In this case, the plasma is a "high density" plasma. The characteristic large scale magnetic field B_0 is most likely bounded by 2.5×10^3 gauss while the characteristic electron density is n_0 . Then from Jeffrey's discussion (1966, p.6) comes the estimate $\lambda_c/\lambda_g \lesssim \mathcal{O}(10^{-1})$ for the solar plasma in the postulated dynamo region.

The characteristic speed v_0 of large scale relative motions in the solar plasma $\sim \mathcal{O}(10^4 \text{ cm/sec})$. As $v_0^2/c^2 \ll 1$, c being the speed of light, the nonrelativistic approximation is valid for our model.⁴

The thermodynamics of an electrically conducting medium is simplified if the magnetic permeability μ and dielectric "constant" ϵ are constants. A plasma is called nonmagnetic if $\mu = \mu_0$. Its effect

⁴Also, the flow is definitely subsonic.

upon magnetic fields is described solely in terms of electric currents. While a conducting fluid could be a dielectric, the bound charges (as well as the free ones) have no dynamic effect in a nonrelativistic plasma, as shown later. Consequently, the actual value of ϵ is not too important. As a first approximation, the free space values μ_0 and ϵ_0 are adopted here. They should not fundamentally alter the physics of the dynamo.

According to the measurements of Dicke and Goldenberg (1967), the surface solar oblateness is only 50 ppm. The ratio of rotational to gravitational potential is very small at the surface and should remain small in the postulated dynamo region centered at $r \sim 0.98 R_\odot$. The rapidly rotating interior postulated by Dicke (1964) would presumably be confined to the radiative core, i.e. to $r < 0.9 R_\odot$. Finally, the convection zone contains only a tiny fraction of the solar mass (Schwarzschild, 1958). Therefore, apparent gravity is approximately a uniform vector directed radially inward within a shallow layer of the convection zone centered at $r \sim 0.98 R_\odot$.

The convection zone is a likely seat of dynamo action, as it has the important ingredient of relative motions. (on various scales). The current speculation is that the magnetic fields do not penetrate much into the radiative core. But the actual thickness $2D$ of the dynamo region is really quite speculative. If the solar horizontal eddy motions were associated with giant convection cells, $2D$ would be comparable to the thickness R_{cz} of the convection zone. Since $R_{cz} \sim 0.1 R_\odot$ to $0.2 R_\odot$, the thin shell approximation would be marginal for $2D/R_{cz} \sim \mathcal{O}(1)$. But it is very good for our choice of $2D \ll R_{cz}$.

The Boussinesq approximation makes the model computations more tractable while filtering out magnetoacoustic waves. In addition, compressibility is not a necessary ingredient of a fluid dynamo. Consistency requires the characteristic vertical scale to be smaller than the local scale height S_H . Although D could be large in the lower convection zone where S_H is large, we chose to consider a region closer to the photosphere.

The assumption of baroclinic thermal forcing is probably the most ad hoc, but is at least internally consistent. We argued heuristically in Chapter I that perhaps the convection could set up and maintain a meridional temperature gradient within a stable layer of the convection zone. To a certain extent, the model results can be used as a further check on the plausibility (as opposed to the validity) of the baroclinic hypothesis. Other possibilities were also mentioned in Chapter I.

The dynamo region is several optical depths beneath the solar surface, where the radiative relaxation time is $\mathcal{O}(10 \text{ yrs})$. Thus, direct radiative heating is small compared to the thermal forcing which is expressed as a Newtonian cooling law. If reliable observations of a meridional temperature gradient are ever made, a model forcing-profile and thermal coefficient could be fit to them. The magnetohydrostatic assumption (x) as well as assumption (xii) will follow from scaling arguments presented in section 2.5.2. To summarize, assumptions (i) through (vii) are probably the most justifiable for the sun. Assumptions (viii) and (xi) tend to be ad hoc but internally consistent, while (ix), (x), and (xii) are reasonable to the extent that (viii) and (xi) are.

2.3. The equations.

In analogy to ordinary fluid dynamics, the behavior of an elec-

trically conducting fluid is described by a set of partial differential equations, identities and boundary conditions. In an inertial coordinate system, the relevant partial differential equations and identities are:

$$\rho_{i_s} \frac{d\underline{v}_i}{dt} = -\nabla(P_i + P_e) + \rho_i \underline{G} + \rho_{i_s} \nabla \nabla^2 \underline{v}_i + \left\{ (z_+ e n_i - e n_e) \underline{E} + (z_+ e n_i \underline{v}_i - e n_e \underline{v}_e) \times \underline{B} \right\} \quad (2-1)$$

$$\left\{ 0 = -\nabla P_e - e n_e (\underline{E} + \underline{v}_e \times \underline{B}) - \frac{n_e m_e}{\tau_c} (\underline{v}_e - \underline{v}_i) \right\} \quad (2-2)$$

$$\nabla \cdot \underline{v} + \frac{1}{\rho} \frac{d\rho}{dt} = 0 \approx \nabla \cdot \underline{v} \quad (2-3)$$

$$c_p T \frac{d \ln \theta}{dt} = Q + Q_{\nu} + \{Q_{\sigma} + Q_i\} \approx Q + Q_{\nu} + \{Q_{\sigma}\} \quad (2-4)$$

$$\ln\left(T \left(\frac{P_{20}}{P}\right)^{R/c_p}\right) - \ln \theta_s = \ln\left(1 + \frac{\theta - \theta_s}{\theta_s}\right) = \left(1 - \frac{R}{c_p}\right) \ln\left(1 + \frac{T - T_s}{T_s}\right) - \frac{R}{c_p} \ln\left(1 + \frac{P - P_s}{P_s}\right) \quad (2-5)$$

$$\left\{ \partial \underline{B} / \partial t = -\nabla \times \underline{E} \right\} \quad (2-6)$$

$$\left\{ \underline{j} = \frac{1}{4\pi} \nabla \times \underline{H} - \frac{1}{4\pi} \frac{\partial \underline{D}}{\partial t} \right\} \quad (2-7)$$

$$\left\{ \nabla \cdot \underline{D} = 4\pi q \right\} \quad (2-8)$$

$$\left\{ \nabla \cdot \underline{B} = 0 \right\} \quad (2-9)$$

$$\left\{ \partial q / \partial t + \nabla \cdot \underline{j} = 0 \right\} \quad (2-10)$$

$$\left\{ \underline{D} = \epsilon_0 \underline{E} + 4\pi \underline{P} \approx \epsilon_0 \underline{E} \right\} \quad (2-11)$$

$$\left\{ \underline{H} = \underline{B}/\mu_0 - 4\pi \underline{M} \approx \underline{B}/\mu_0 \right\} \quad (2-12)$$

The terms in curly brackets are of electromagnetic origin. In order of appearance, the variables and parameters in these equations are:

- ρ_{i_s} , the ion mass density of the resting equilibrium atmosphere
- ρ_i , the ion mass density
- \underline{v}_i , the ion velocity
- p_i , the ion gas partial pressure
- p_e , the electron gas partial pressure
- \underline{G} , total gravity
- ν , the eddy kinematic viscosity
- Z_+ , the number of elementary charges in each ion ($Z_+=1$ for protons)
- e , the elementary charge of an electron (1.6×10^{-20} emu)
- n_i , the ion number density
- n_e , the electron number density
- \underline{E} , the electric field
- \underline{v}_e , the electron velocity
- \underline{B} , the magnetic induction (often referred to as the magnetic field)
- τ_c , the effective mean collision time for electron-ion interactions
- m_e , the mass of an electron
- \underline{v} , the velocity of the mass as a whole (essentially \underline{v}_i)
- ρ , the total mass density

- c_p , the specific heat capacity at constant pressure
 T , the temperature
 θ , the potential temperature
 Q , the Newtonian cooling associated with baroclinic forcing
 Q_v , the viscous heating
 Q_e , the joule heating
 Q_i , the latent heating due to ionization
 P_{oo} , a reference pressure
 p , the gas pressure
 R , the individual gas constant based upon the mean molecular weight
 θ_s , the potential temperature of the equilibrium atmosphere
 T_s , the temperature of the equilibrium atmosphere
 ρ_s , the mass density of the equilibrium atmosphere
 \underline{j} , the total current density (charge per unit area per unit time)
 \underline{H} , the magnetic field
 \underline{D} , the displacement
 q , the charge density (charge per unit volume)
 ϵ_0 , the dielectric constant of free space
 \underline{P} , the electric polarization (vanishes by assumption (vii))
 μ_0 , the magnetic permeability of free space
 \underline{M} , the magnetization (vanishes by assumption (vii))

The differential operators are the total time derivative d/dt , the partial time derivative $\partial/\partial t$, the gradient ∇ , the divergence $\nabla \cdot$, and the curl $\nabla \times$.

Equation (2-1) is the momentum equation for the mass motion,

i.e. electrons plus ions. Equation (2-2) is the momentum equation for electrons alone. The viscous, gravitational, and inertial terms are neglected in (2-2), and $\underline{v} \approx \underline{v}_i$, since the electron to ion mass ratio m_e/m_i is very small. Similarly, $\rho \approx \rho_i \approx \rho_s \approx \rho_s$. The ion drag on the electrons in (2-2) represents the rate of momentum exchange through (weak) interactions between ions and electrons. Assuming the electron drag on the ions is equal and opposite, there is no net ion-electron drag in (2-1).

It is convenient to introduce the following standard definitions for the charge density q , the total current density \underline{J} the conduction current \underline{J} and the convection current \underline{J}_c .

$$q = z_+ e n_i - e n_e \quad (2-13)$$

$$\underline{J} = \underline{J} + \underline{J}_c \quad (2-14)$$

$$\underline{J} = -e n_e (\underline{v}_e - \underline{v}_i) \quad (2-15)$$

$$\underline{J}_c = q \underline{v} \quad (2-16)$$

The law of partial pressures is

$$p = p_i + p_e \quad (2-17)$$

The electrical conductivity is given by

$$\sigma = n_e e^2 \tau_c / m_e \quad (2-18)$$

and the gyro frequency by

$$\omega_g = e B_0 / m_e \quad (2-19)$$

$$\underline{E}^{(rel)} = \underline{E} + \underline{V} \times \underline{B} \quad (2-20)$$

is the electric field measured by an observer moving at the local velocity \underline{v} . The momentum equations now simplify to

$$\frac{d\underline{V}}{dt} = -\frac{1}{\rho_s} \nabla p + \left(\frac{\rho}{\rho_s}\right) \underline{G} + \underline{V} \nabla^2 \underline{V} + \frac{1}{\rho_s} \underline{J} \times \underline{B} + \left[\frac{1}{\rho_s} (\rho \underline{E} + \underline{J} \times \underline{B}) \right] \quad (2-21)$$

$$\underline{J} = \sigma \underline{E}^{(rel)} + \left[\omega_g \tau_c \frac{\underline{J} \times \underline{B}}{B_0} - \frac{\sigma}{n_e e} \nabla p_e \right] \quad (2-22)$$

The terms in square brackets will be discarded shortly.

The usual mass continuity equation (2-3) still holds. Two new terms in the thermodynamic equation (2-4) are joule heating Q_σ and latent heating Q_i of ionization.⁵ The quantity Q_i vanishes in a fully ionized gas, but could be significant in the weakly ionized photosphere.⁶

Equation (2-5) is the equation of state, where ρ_s , T_s , p_s , and ρ_s are the thermodynamic variables in a resting atmosphere. Equations (2-6) through (2-9) are the Maxwell equations. Equation (2-10) expresses charge conservation and follows from (2-7) and (2-8). Since \underline{P} and \underline{M} vanish in the constitutive relations (2-11) and (2-12), \underline{D} and \underline{H} may be eliminated.

⁵If the magnetic permeability or electric permittivity were temperature or density dependent, a magnetization or polarization term would be needed —Chu (1959)

⁶As an added complication in a partially ionized gas, additional equations relate T to n and to the ratio of number densities in adjacent stages of ionization for each element. The Saha equations would be appropriate for local thermodynamic equilibrium.

2.4. The MHD approximation.

MHD theory is really a fusion of ordinary fluid dynamics and preMaxwellian (nonrelativistic) electromagnetic theory. In analogy to meteorological filtering approximations for eliminating sound waves and external gravity waves, the MHD approximation filters out high frequency electromagnetic phenomena.

Let us denote the characteristic magnitudes of \underline{V} , \underline{E} , \underline{B} , q , \underline{J} , \underline{J}_c , and \underline{f} by a zero subscript, the characteristic time scale by τ_0 , and the characteristic length scale by λ_0 . Observing that $\mu_0 = 1$ and $\epsilon_0 = 1/c^2$ in our system of units, the following scaling estimates are made in MHD theory:

$$\tau_0 \sim \lambda_0 / V_0 \quad (2-23)$$

$$E_0 \sim V_0 B_0 \quad (2-24)$$

$$q_0 \sim \epsilon_0 B_0 / 4\pi \tau_0 \quad (2-25)$$

$$J_0 \sim J_c \sim B_0 / 4\pi \mu_0 \lambda_0 \quad (2-26)$$

$$(J_c)_0 \sim q_0 V_0 \quad (2-27)$$

Therefore $\underline{f} \approx \underline{J}$, while all bracketed terms in (2-21), $-\frac{1}{4\pi} \partial \rho / \partial t$ in (2-7), and $\partial q / \partial t$ in (2-10) vanish to $\mathcal{O}(v_0^2/c^2) \ll 1$. To this order of approximation, equation (2-7) simplifies to

$$\underline{J} = \frac{1}{4\pi \mu_0} \nabla \times \underline{B} \quad (2-28)$$

while equation (2-8) may be rewritten as

$$\underline{q} = \frac{1}{4\pi c^2} \nabla \cdot \underline{E} \quad (2-29)$$

Equations (2-6), (2-9), (2-28) and (2-29) are the preMaxwell equations.

The charge continuity equation reduces to $\nabla \cdot \underline{J} = 0$.

Now in equation (2-22), $|B_0^{-1} \omega_g \tau_c \underline{J} \times \underline{B} / \underline{J}| \sim \omega_g \tau_c \ll 1$ while $|-n_e^{-1} e^{-1} \sigma \nabla P_e / \underline{J}| \sim \frac{\omega_g \tau_c}{2} |\nabla P / \underline{J} \times \underline{B}|$. The latter ratio should be small even before significant dynamo action occurs in our model, since $\underline{J} \times \underline{B} \neq 0$ initially. Therefore the traditional approximation of replacing (2-22) by Ohm's law is made,⁷ i.e.

$$\underline{J} = \sigma (\underline{E} + \underline{V} \times \underline{B}) \quad (2-30)$$

Suppose a primed coordinate system moves at uniform velocity \underline{U}_0 with respect to an unprimed system, where $U_0^2/c^2 \ll 1$. Then according to electromagnetic theory, the equations

$$\underline{B}' = \underline{B} - (\underline{U}_0 \times \underline{B})/c^2 \approx \underline{B} \quad (2-31)$$

$$\underline{J}' \approx \underline{J} - \underline{q} \underline{U}_0 \approx \underline{J} \quad (2-32)$$

$$\underline{E}' \approx \underline{E} + \underline{U}_0 \times \underline{B} \quad (2-33)$$

relate the primed to the unprimed field variables. For the more compli-

⁷ If $\omega_g \tau_c \gg \mathcal{O}(1)$, (2-22) is equivalent to $\underline{J}'_{\parallel} = \sigma (\underline{E}'_{\parallel} + \underline{E}'_{\parallel}^{(bat)})$ and $\underline{J}'_{\perp} = \sigma (1 + \omega_g^2 \tau_c^2)^{-1} (\underline{E}_{\perp}^{(rel)} + \underline{E}_{\perp}^{(bat)}) + \sigma \omega_g \tau_c (1 + \omega_g^2 \tau_c^2)^{-1} (\underline{E}_{\perp}^{(rel)} + \underline{E}_{\perp}^{(bat)}) \times \hat{b}$ —Cowling (1957a). \hat{b} is a unit vector parallel to \underline{B} , $\underline{E}^{(bat)} = -\frac{e}{n_e} \nabla P_e$ and \underline{J} , $\underline{E}^{(rel)}$ and $\underline{E}^{(bat)}$ are split up into vectors parallel and transverse to \underline{B} . Note the reduction of currents perpendicular to magnetic field lines and the emergence of Hall currents. These effects are associated with electron spiraling.

cated case in which ϵ or μ are functions of ρ or τ , see Chu (1959). The invariance of the preMaxwell equations (2-6), (2-9), and (2-28) under the Galilean transformation

$$\partial/\partial t' = \partial/\partial t + \underline{u}_0 \cdot \nabla \quad (2-34)$$

is fairly simple to demonstrate (See Shercliff, 1965). However, in order for equation (2-29) to remain invariant,

$$q' = q - \underline{u}_0 \cdot \underline{J}/c^2 \quad (2-35)$$

In contrast, the charge q would be invariant under Lorentz transformation in the nonrelativistic limit.

In MHD theory, the magnetic field \underline{B} may be regarded as the fundamental quantity. The other electromagnetic variables may be eliminated by substituting (2-6) and (2-28) into the curl of (2-30), using the identity $\nabla \times \nabla \times \underline{B} = -\nabla^2 \underline{B} + \nabla(\nabla \cdot \underline{B})$. We thereby obtain the magnetic induction equation

$$\partial \underline{B} / \partial t = \nabla \times (\underline{v} \times \underline{B}) + \eta \nabla^2 \underline{B} \quad (2-36)$$

where $\eta = (4\pi \mu_0 \sigma)^{-1}$ is the eddy magnetic diffusivity or resistivity. Equation (2-9) is still retained.

The current density \underline{J} can be computed from (2-28), then \underline{E} from (2-30). Although equation (2-29) defines q , this equation is not essential to MHD because q is associated with purely irrotational \underline{E} fields and hence has no dynamic effect upon (2-36).

The magnetic induction equation (as well as the preMaxwellian equations) is invariant under a nonrelativistic uniform rotation transformation. This may be proved by analogy of equation (2-36) to the absolute vorticity equation, noting that \underline{B} is virtually the same vector in both the rotating and nonrotating coordinate systems. But as noted by Backus (1958), the boundary conditions for \underline{B} in a finite domain are different from those of $\text{curl } \underline{V}$.

Corresponding to the conventional Reynolds number is the magnetic Reynolds number $R_m = \lambda_0 V_0 / \eta$. We then have $R_m \gg 1$ in the postulated dynamo region of the sun, since λ_0 and σ are large. If R_m were too small, the induction term $\nabla \times (\underline{V} \times \underline{B})$ could not compete with the dissipation term.

2.5. Further refinements and simplifications.

We have already made use of assumptions (i) through (vii), and to some extent (ix). The others will now be incorporated into the equations.⁸

2.5.1. The "primitive" equations.

In a rotating coordinate system, the component equations of motion for a thin spherical shell of Boussinesq fluid are

⁸ Simplification of (2-4) and (2-5) hinges in part on the Boussinesq approximation.

$$\begin{aligned}
 \frac{\partial u}{\partial t} &= -\left(\frac{u}{a \cos \varphi} \frac{\partial}{\partial \lambda} + \frac{v}{a} \frac{\partial}{\partial \varphi} + w \frac{\partial}{\partial z}\right)u + u v \frac{\tan \varphi}{a} \\
 &+ \frac{1}{4\pi\mu_0 \rho_s} \left(\frac{B^\lambda}{a \cos \varphi} \frac{\partial}{\partial \lambda} + \frac{B^\varphi}{a} \frac{\partial}{\partial \varphi} + B^z \frac{\partial}{\partial z}\right)B^\lambda - \frac{B^\lambda B^\varphi}{4\pi\mu_0 \rho_s} \frac{\tan \varphi}{a} \\
 &- \frac{1}{a \cos \varphi} \frac{\partial}{\partial \lambda} \left(\frac{\mathcal{P}'}{\rho_s} + \frac{B^{\lambda^2} + B^{\varphi^2}}{8\pi\mu_0 \rho_s}\right) + 2\mathcal{L} \sin \varphi v \\
 &+ v \Delta^\lambda(u, v) + v \frac{\partial^2 u}{\partial z^2} + \left[-\frac{1}{a \cos \varphi} \frac{\partial}{\partial \lambda} \left(\frac{B^z^2}{8\pi\mu_0 \rho_s}\right)\right]
 \end{aligned} \tag{2-37a}$$

$$\begin{aligned}
 \frac{\partial v}{\partial t} &= -\left(\frac{u}{a \cos \varphi} \frac{\partial}{\partial \lambda} + \frac{v}{a} \frac{\partial}{\partial \varphi} + w \frac{\partial}{\partial z}\right)v - u^2 \frac{\tan \varphi}{a} \\
 &+ \frac{1}{4\pi\mu_0 \rho_s} \left(\frac{B^\lambda}{a \cos \varphi} \frac{\partial}{\partial \lambda} + \frac{B^\varphi}{a} \frac{\partial}{\partial \varphi} + B^z \frac{\partial}{\partial z}\right)B^\varphi + \frac{B^{\lambda^2}}{4\pi\mu_0 \rho_s} \frac{\tan \varphi}{a} \\
 &- \frac{1}{a} \frac{\partial}{\partial \varphi} \left(\frac{\mathcal{P}'}{\rho_s} + \frac{B^{\lambda^2} + B^{\varphi^2}}{8\pi\mu_0 \rho_s}\right) - 2\mathcal{L} \sin \varphi u \\
 &+ v \Delta^\varphi(u, v) + v \frac{\partial^2 v}{\partial z^2} + \left[-\frac{1}{a} \frac{\partial}{\partial \varphi} \left(\frac{B^z^2}{8\pi\mu_0 \rho_s}\right)\right]
 \end{aligned} \tag{2-37b}$$

$$\begin{aligned}
 \left[\frac{\partial W}{\partial t} \right] = & -\frac{1}{\rho_s} \frac{\partial}{\partial z} \left(\rho' + \frac{B^\lambda{}^2 + B^\omega{}^2}{8\pi\mu_0} \right) - \frac{\rho'}{\rho_s} g \\
 & + \left[-\left(\frac{u}{a \cos \varphi} \frac{\partial}{\partial \lambda} + \frac{v}{a} \frac{\partial}{\partial \varphi} + w \frac{\partial}{\partial z} \right) W + \frac{1}{4\pi\mu_0 \rho_s} \left(\frac{B^\lambda}{a \cos \varphi} \frac{\partial}{\partial \lambda} + \frac{B^\omega}{a} \frac{\partial}{\partial \varphi} \right) B^z \right. \\
 & \left. + \nu \left(\nabla_H^2 W + \frac{\partial^2 W}{\partial z^2} \right) \right] \quad (2-37c)
 \end{aligned}$$

$$\begin{aligned}
 \frac{\partial B^\lambda}{\partial t} = & -\left(\frac{u}{a \cos \varphi} \frac{\partial}{\partial \lambda} + \frac{v}{a} \frac{\partial}{\partial \varphi} + w \frac{\partial}{\partial z} \right) B^\lambda \\
 & + \left(\frac{B^\lambda}{a \cos \varphi} \frac{\partial}{\partial \lambda} + \frac{B^\omega}{a} \frac{\partial}{\partial \varphi} + B^z \frac{\partial}{\partial z} \right) u + (u B^\omega - v B^\lambda) \frac{\tan \varphi}{a} \\
 & + \eta \Delta^\lambda(B^\lambda, B^\omega) + \eta \frac{\partial^2 B^\lambda}{\partial z^2} \quad (2-38a)
 \end{aligned}$$

$$\frac{\partial B^{\varrho}}{\partial t} = -\left(\frac{u}{a \cos \varrho} \frac{\partial}{\partial \lambda} + \frac{v}{a} \frac{\partial}{\partial \varrho} + w \frac{\partial}{\partial z}\right) B^{\varrho} + \left(\frac{B^{\lambda}}{a \cos \varrho} \frac{\partial}{\partial \lambda} + \frac{B^{\varrho}}{a} \frac{\partial}{\partial \varrho} + B^z \frac{\partial}{\partial z}\right) v$$

$$+ \eta \Delta^{\varrho} (B^{\lambda}, B^{\varrho}) + \eta \frac{\partial^2 B^{\varrho}}{\partial z^2} \quad (2-38b)$$

$$\left[\frac{\partial B^z}{\partial t} = -\left(\frac{u}{a \cos \varrho} \frac{\partial}{\partial \lambda} + \frac{v}{a} \frac{\partial}{\partial \varrho} + w \frac{\partial}{\partial z}\right) B^z + \left(\frac{B^{\lambda}}{a \cos \varrho} \frac{\partial}{\partial \lambda} + \frac{B^{\varrho}}{a} \frac{\partial}{\partial \varrho} + B^z \frac{\partial}{\partial z}\right) w \right.$$

$$\left. + \eta \left(\nabla_H^2 B^z + \frac{\partial^2 B^z}{\partial z^2} \right) \right] \quad (2-38c)$$

The square brackets in (2-37) and (2-38) indicate that the terms inside will be discarded in the magnetohydrostatic approximation.

The new symbols are

λ , the longitude

ϱ , the latitude

z , the height relative to the lower boundary

r , the radius measured from the center of the sun

$a = r - z \sim 6.8 \times 10^{10} \text{ cm} \sim R_{\odot}$

$\hat{\lambda}$, $\hat{\varrho}$, and \hat{z} , the unit vectors in the λ , ϱ , and z directions

t , the time coordinate

Ω , the uniform rotation $\sim 2.86 \times 10^{-6}$ radians/sec (Greenwich convention)

g , the uniform apparent solar gravity $\sim 2.73 \times 10^4$ cm/sec²

$p' = p - p_s$, the perturbation (i.e. dynamically active) pressure

u , the eastward velocity component

v , the northward velocity component

w , the vertical velocity component

B^λ , the eastward magnetic field component

B^ω , the northward magnetic field component

B^z , the vertical magnetic field component

∇_H^2 , the thin shell horizontal Laplacian operator defined below

$\Delta = \hat{\lambda} \Delta^\lambda + \hat{\omega} \Delta^\omega$, the operation of the horizontal thin shell Laplacian on a horizontal vector in terms of the vector components.

Also, for future reference, we introduce

$\underline{V}_H = u \hat{\lambda} + v \hat{\omega}$, the horizontal velocity

$\underline{B}_H = B^\lambda \hat{\lambda} + B^\omega \hat{\omega}$, the horizontal magnetic field

$\rho' = \rho - \rho_s$, the perturbation density

$T' = T - T_s$, the perturbation temperature

$\theta' = \theta - \theta_s$, the perturbation potential temperature

ψ_v , the velocity stream function

ϕ_v , the velocity potential

ψ_m , the magnetic stream function

ϕ_m , the magnetic potential

and the thin shell differential operators

$\nabla = \frac{\hat{\lambda}}{a \cos \omega} \frac{\partial}{\partial \lambda} + \frac{\hat{\omega}}{a} \frac{\partial}{\partial \omega} + \hat{z} \frac{\partial}{\partial z}$, the gradient

$\nabla_H = \frac{\hat{\lambda}}{a \cos \omega} \frac{\partial}{\partial \lambda} + \frac{\hat{\omega}}{a} \frac{\partial}{\partial \omega}$, the horizontal gradient

$$\nabla \cdot \underline{V} = \frac{1}{a \cos \varphi} \left(\frac{\partial u}{\partial \lambda} + \frac{\partial v \cos \varphi}{\partial \varphi} \right) + \frac{\partial w}{\partial z}, \text{ the divergence (applied to } \underline{v} \text{)}$$

$$\nabla_H \cdot \underline{V} = \frac{1}{a \cos \varphi} \left(\frac{\partial u}{\partial \lambda} + \frac{\partial v \cos \varphi}{\partial \varphi} \right), \text{ the horizontal divergence (applied to } \underline{v} \text{)}$$

$$\hat{z} \cdot \nabla \times \underline{V} = \frac{1}{a \cos \varphi} \left(\frac{\partial v}{\partial \lambda} - \frac{\partial u \cos \varphi}{\partial \varphi} \right), \text{ the horizontal curl (applied to } \underline{v} \text{)}$$

The ∇_H^2 , $\underline{\Delta}$, $\hat{z} \cdot \nabla \times \underline{\Delta}$, and $\nabla_H \cdot \underline{\Delta}$ operators are defined as follows:

$$\nabla_H^2 \psi_v = \frac{1}{a^2 \cos \varphi} \left(\frac{1}{\cos \varphi} \frac{\partial^2 \psi_v}{\partial \lambda^2} + \frac{\partial}{\partial \varphi} \left(\cos \varphi \frac{\partial \psi_v}{\partial \varphi} \right) \right) \quad (2-39a)$$

$$\underline{\Delta}(B^\lambda, B^\varphi) = \hat{\lambda} \left(\nabla_H^2 B^\lambda - \frac{2 \sin \varphi}{a^2 \cos \varphi} \frac{\partial B^\varphi}{\partial \lambda} - \frac{B^\lambda}{a^2 \cos^2 \varphi} \right) + \hat{\varphi} \left(\nabla_H^2 B^\varphi + \frac{2 \sin \varphi}{a^2 \cos \varphi} \frac{\partial B^\lambda}{\partial \lambda} - \frac{B^\varphi}{a^2 \cos^2 \varphi} \right) \quad (2-39b)$$

$$\hat{z} \cdot \nabla \times \underline{\Delta}(B^\lambda, B^\varphi) = \nabla_H^2 (\nabla_H^2 \psi_m) \quad (2-39c)$$

$$\nabla_H \cdot \underline{\Delta}(u, v) = \nabla_H^2 (\nabla_H^2 \phi_v) \quad (2-39d)$$

In accordance with the thin shell approximation (Phillips, 1967), we substituted "a" for r and $\partial/\partial z$ for $\partial/\partial r$ in the various differential operators. Phillips (1966) has remarked that the angular momentum principle is preserved.

The equilibrium atmosphere is defined by the equations

$$\partial p_s / \partial z + \rho_s g = 0 \quad (2-40a)$$

$$p_s = \rho_s R T_s \quad (2-40b)$$

$$\sigma_s = T_s \left(p_{00} / p_s \right)^{R/c_p} \quad (2-40c)$$

where ρ_s , T_s , p_s , and σ_s are all functions of z only. But in the Boussinesq approximation, variations in ρ_s are neglected. In (2-37c), the equilibrium atmosphere contribution was separated out. In (2-37a),

(2-37b) and (2-37c), \underline{J} was expressed in terms of \underline{B} through (2-28), and the bracketed terms of (2-21) were discarded. Observe that the curvature correction terms take a somewhat different form in (2-38) than in (2-37). Yet, when the scalar energy equation $\underline{v} \cdot \partial \underline{v} / \partial t + (4\pi\mu_0 \rho_s)^{-1} \underline{B} \cdot \partial \underline{B} / \partial t = \dots$ is formed, the relevant curvature terms cancel each other. Writing the thin shell vector Laplacian ∇^2 as $-\nabla \times \nabla$ for the solenoidal vectors \underline{v} and \underline{B} gave rise to the dissipation terms which appear in (2-37) and (2-38).

The details of quasi-geostrophic scaling in a baroclinic atmosphere are by now quite familiar and have been reiterated by Gilman (1967). Suppressing the magnetic body force terms, equations (2-37a) and (2-37b) are the standard horizontal momentum equations. For the motions of interest, the Reynolds number for vertical eddy diffusion, the aspect ratio, the ratio of horizontal length scale to the radius, and the (thermal) Rossby number are given respectively by

$$R_e = D^2 \Delta u / \lambda_0 \nu \gtrsim 1 \tag{2-41a}$$

$$\delta = D / \lambda_0 \sim 1 / 50 \tag{2-41b}$$

$$L = \lambda_0 / a \sim 1 / 4 \tag{2-41c}$$

$$R_o = \Delta u / f_0 \lambda_0 \lesssim 1 / 4 \tag{2-41d}$$

In (2-41d), Δu is a characteristic (thermal) wind and f_0 is a characteristic coriolis parameter. Thus, the coriolis term should still provide a good order of magnitude estimate of the perturbation pressure except near the equator. The constraint of strict geostrophic balance to lowest

order is of course relaxed. Numerical results suggest that the divergent part of the motion tends to be rather small. The basic phenomenon of baroclinic instability remains intact. The external thermal forcing sets up a meridional temperature gradient of comparable magnitude. For R_0 sufficiently small, a wavelike (Rossby) regime is established.

Restoring the magnetic terms again, the only direct source of magnetic energy is the velocity field, which links the various stages of the dynamo process. The toroidal magnetic field, for example, extracts its energy from the horizontal or vertical shear of u . The magnetic fields could also inhibit baroclinic instability. Then induction would become weaker and the magnetic energy would decay, allowing the kinetic energy of shearing motions to build up again through thermal processes. At times the $\underline{J} \times \underline{B}$ term could even deliver magnetic energy to the shear flow. Introducing the Alfvén number \mathcal{A} , the formula

$$\mathcal{A}^2 = v_0^2 / (B_0^2 / 4\pi\mu_0\rho_s) \quad (2-41e)$$

gives the ratio of inertial to magnetic terms in (2-37) or the ratio of kinetic to magnetic energy. The case $\mathcal{A}^2 = 1$ corresponds to exact equipartition of magnetic and kinetic energy. Both B_0 and \mathcal{A}^2 are functions of time, strictly speaking, since they are not external parameters. But defining B_0 and hence \mathcal{A}^2 as time averaged values, $\mathcal{A}^2 \ll 1$ would seem unreasonable for a baroclinically driven dynamo. The gist of the above heuristic arguments is that the geostrophic scale factor $\rho_0' \sim \rho_s f_0 v_0 \lambda_0$ is still a good order of magnitude estimate for ρ_0' in the magnetic case.

To justify the magnetohydrostatic approximation, consider the

ratios of terms in (2-37c) for $\delta \sim 1/50$, $Ro \lesssim 1/4$, $a^2 \sim 1$, and $Re \gtrsim 1$. The scale factors for w and B^z are $w_0 \lesssim \delta v_0$ and $b_0 \lesssim \delta B_0$, respectively.

$$\left| \frac{\partial w}{\partial t} / \frac{1}{\rho_s} \frac{\partial p'}{\partial z} \right| \sim \left| \underline{v} \cdot \nabla w / \frac{1}{\rho_s} \frac{\partial p'}{\partial z} \right| \lesssim \delta^2 R_o \ll 1 \quad (2-42a)$$

$$\left| \underline{B}_H \cdot \nabla_H B^z / \frac{1}{\rho_s} \frac{\partial p'}{\partial z} \right| \lesssim \delta^2 R_o a^{-2} \ll 1 \quad (2-42b)$$

$$\left| \underline{v} \nabla^2 w / \frac{1}{\rho_s} \frac{\partial p'}{\partial z} \right| \lesssim \delta^2 R_o Re^{-1} \ll 1 \quad (2-42c)$$

$$\left| \frac{1}{\rho_s} \frac{\partial}{\partial z} \left(\frac{B^{\lambda^2} + B^{\omega^2}}{8\pi \mu_0} \right) / \frac{1}{\rho_s} \frac{\partial p'}{\partial z} \right| \sim \frac{R_o a^{-2}}{2} < 1 \quad (2-42d)$$

Each ratio except the last is extremely small. But even $R_o a^{-2}/2 \sim \mathcal{O}(10^{-1})$, so the buoyancy term should still be significant in the balance of forces. Thus p_{og}'/gD is a good order of magnitude estimate for ρ_o' . All bracketed terms in (2-37) are hence discarded, giving the law of magneto-hydrostatic balance

$$\frac{\partial}{\partial z} \left(\rho' / \rho_s + (B^{\lambda^2} + B^{\omega^2}) / 8\pi \mu_0 \rho_s \right) + (\rho' / \rho_s) g = 0 \quad (2-43)$$

Since $|B^z|^2 / (B^{\lambda^2} + B^{\omega^2}) \sim \delta^2 \ll 1$, the last term of both (2-37a) and (2-37b) is neglected as well.

To preserve energetic consistency in the sense of Lorenz (1960b), the terms $-\underline{v} \cdot \nabla B^z + \underline{B} \cdot \nabla w$ in (2-38c) must be omitted also. Forming an equation for kinetic plus magnetic energy density, the omitted coupled hydromagnetic terms are $-\underline{v}_H \cdot \nabla_H (B^z / 8\pi \mu_0 \rho_s)$ from (2-37a) and

(2-37b), $(w)(4\pi\mu_0\rho_S)^{-1} \underline{B}_H \cdot \nabla B^2$ from (2-37c) and $(B^2)(-\underline{v} \cdot \nabla B^2 + \underline{B} \cdot \nabla w)/4\pi\mu_0\rho_S$

from (2-38c). These terms add up to the divergence expression

$$\nabla_H \cdot \left\{ \frac{B^2}{4\pi\mu_0\rho_S} (w \underline{B}_H - B^2 \underline{v}_H) \right\}, \text{ after differentiation by parts. This}$$

simple result also depends upon the equations of mass continuity and magnetic continuity in the form

$$\nabla_H \cdot \underline{v}_H + \partial w / \partial z = 0 \quad (2-44)$$

$$\nabla_H \cdot \underline{B}_H + \partial B^2 / \partial z = 0 \quad (2-45)$$

Equations (2-38a) and (2-38b) implicitly contain the expressions $(\nabla_H \cdot \underline{v}_H + \partial w / \partial z) B^A$ and $(\nabla_H \cdot \underline{v}_H + \partial w / \partial z) B^E$, respectively. According to (2-44), both terms vanish, as we have assumed for the magnetohydrostatic case. Curiously enough, in the ordinary hydrostatic case, the terms $(\partial w / \partial z) B^A$ and $(\partial w / \partial z) B^E$ would have to be discarded alone in order to preserve energetic consistency. A scaling inconsistency is then unavoidable. To minimize its effect, one could explicitly impose the constraint that the motion be horizontally nondivergent to lowest order as Gilman (1969) did. In the horizontal magnetic induction equation, poloidal motions would still twist toroidal magnetic fields to complete the dynamo process and the magnetic energy would still include a contribution from horizontal poloidal magnetic fields.

Noting that $R_m \gg 1$ for the dynamo, the dissipation terms should also be dropped from (2-38c). In fact, equation (2-38c) may be discarded altogether, provided $B^2 / (8\pi\mu_0\rho_S)$ is excluded from the definition of magnetic energy density. The justification is that $B^2 / |B_H|^2 \approx \delta^2 \ll 1$. Likewise, $w^2/2$ is excluded from the definition of kinetic energy density.

Thus, in the magnetohydrostatic approximation, the two redundant prognostic equations (2-37c) and (2-38c) are replaced by the diagnostic equation (2-43). The redundancies stem from (2-44) and (2-45), i.e., the solenoidal vector fields \underline{v} and \underline{B} are each uniquely determined from two scalars. In terms of the velocity and magnetic stream functions and potentials,

$$\underline{v}_H = \hat{z} \times \nabla_H \psi_v + \nabla_H \phi_v \quad (2-46a)$$

$$w = - \int_0^z \nabla_H^2 \phi_v dz + w(z=0) \quad (2-46b)$$

$$\underline{B}_H = \hat{z} \times \nabla_H \psi_m + \nabla_H \phi_m \quad (2-47a)$$

$$B^z = - \int_0^z \nabla_H^2 \phi_m dz + B^z(z=0) \quad (2-47b)$$

2.5.2. The thermodynamics

Quasi-geostrophic theory predicts p'/p_s , T'/T_s , ρ'/ρ_s and $\theta'/\theta_s \ll 1$. We again argue heuristically that these results should carry over to our primitive equation magnetic model. An empirical upper bound of T'/T_s based upon the strength of the external thermal forcing is $10^2 \text{ }^\circ\text{K}/10^5 \text{ }^\circ\text{K} \sim 10^{-3}$. Hence we retain the linearized equation of state

$$\theta'/\theta_s = (1 - R/c_p) p'/p_s - \rho'/\rho_s = T'/T_s + (R/c_p) p'/p_s \quad (2-48)$$

Substituting equation (2-48) into the law of magnetohydrostatic balance and applying the Boussinesq approximation, we obtain

$$\frac{g \theta'}{\sigma_s} = \frac{\partial}{\partial z} \left(\frac{p'}{\rho_s} + \frac{B^2 + B^2}{8\pi\mu_0\rho_s} \right) \quad (2-49)$$

$$\frac{T'}{T_s} = -\frac{p'}{\rho_s} = \frac{\theta'}{\sigma_s} \quad (2-50)$$

Observing that $R/C_p = 2/5$ for the solar atmosphere, the Boussinesq approximation is valid provided $(3/5)(D/S_H) \ll 1$, where $S_H = P_s/g\rho_s$ is the local scale height. Equations (2-49) and (2-50) are only marginally valid for our model since we chose $D/S_H = 0.5$. Equation (2-50) could be interpreted as the equation of state of a liquid whose coefficient of thermal expansion is T_s^{-1} .

The nonadiabatic terms in equation (2-4) are the external thermal forcing $Q = K(\theta' - \theta_*)/\sigma_s$, viscous heating $Q_v = -\nu(\underline{v} \cdot \nabla^2 \underline{v})/c_p T$, and Joule heating $Q_j = -\eta(\underline{B} \cdot \nabla^2 \underline{B})/(4\pi\mu_0\rho_s c_p T)$. Here K is a thermal forcing coefficient in sec^{-1} and $\theta_*(\omega, z)$ is the specified thermal forcing. Now $Q_v/Q \sim \theta \left(\frac{\nu}{K D^2} \frac{v_0^2}{c_p T_s} \frac{\sigma_s}{\theta_s} \right)$. Guessing that the eddy magnetic Prandtl number $P_r = \nu/(K D^2)$ for vertical diffusion $\sim \theta(1)$ and taking $v_0^2/c_p T_s \sim \theta(10^{-5})$ and $\sigma_s/\theta_s \sim \theta(10^{+3})$, then $Q_v/Q \sim \theta(10^{-2})$. Similarly, Q_j may be neglected if $a^2 \gtrsim \theta(1)$ and the eddy magnetic Prandtl number $P_{r_m} = \nu/\eta \gtrsim \theta(1)$. Thus the thermodynamic equation for the perturbation potential temperature is

$$\begin{aligned} \frac{\partial(\theta'/\sigma_s)}{\partial t} = & -\hat{z} \cdot \nabla_H \psi_v \times \nabla_H (\theta'/\sigma_s) - w \frac{\partial \ln \sigma_s}{\partial z} - \frac{K}{\sigma_s} (\theta' - \theta_*) \\ & + \left[-\nabla_H \phi_v \cdot \nabla_H (\theta'/\sigma_s) - w \frac{\partial}{\partial z} (\theta'/\sigma_s) \right] \quad (2-51) \end{aligned}$$

The terms in square brackets will vanish in the two layer model.

To summarize, the governing equations for the continuous theory are the momentum equations (2-37a) and (2-37b) with terms in square brackets discarded, the magnetic induction equations (2-38a) and (2-38b), the mass continuity equation (2-44), the magnetic continuity equation (2-45), the equation of state (2-49) for vertical magnetohydrostatic balance, and the thermodynamic equation (2-51). The equation of state (2-50) merely defines ρ' and T' in terms of variables already computed.

2.6. Boundary conditions

The boundary conditions complete the formulation of the continuous model. With spherical geometry, there are no artificial lateral boundaries. For a spherical harmonic type representation, no singularities arise at the poles, as explained in section 3.4.

The true boundary conditions on w at the top and bottom of the solar dynamo region are speculative. The small scale vertical oscillations of the photosphere originate in the convection zone. Judging from recent unpublished dopplergrams of Howard's, large scale vertical motions may be weak compared to large scale horizontal motions. In any case, we choose the simplest conditions. The top and bottom boundaries will be regarded as rigid lids, i.e.,

$$w = 0 \quad \text{at} \quad z = 0, z_4 \quad (2-52)$$

where z_4 is the height of the top boundary. If time dependent oscillations were specified for w at the top boundary, the behavior below might

be largely a response to that forcing. However, we wanted to see how the model responds to time-independent baroclinic thermal forcing.

Finally, since such boundary conditions would not filter out external gravity waves, the time step required for computational stability would be prohibitively small.

The boundary conditions on u and v are also somewhat ad hoc. We shall assume a no-slip bottom boundary and a free stress top boundary. Hence

$$u = v = 0 \quad \text{at} \quad z = 0 \quad (2-53a)$$

$$\frac{\partial u}{\partial z} = \frac{\partial v}{\partial z} = 0 \quad \text{at} \quad z = z_4 \quad (2-53b)$$

The magnetic boundary conditions are somewhat more complicated. Three electromagnetic jump conditions must be satisfied at the interface between two fluids, irrespective of the electrical conductivities. These are

$$\int B^n \Gamma = 0 \quad (2-54)$$

$$\lim_{\gamma \rightarrow 0} J_{\text{tan}} = \frac{\int \hat{n} \times \underline{B} \Gamma}{4\pi\mu_0\gamma} \quad (2-55a)$$

$$\hat{n} \times \left(\int \underline{E} + \underline{v} \times \underline{B} \Gamma \right) = 0 \quad (2-56)$$

Here \hat{n} is the local normal to the interface, and γ is the thickness of a slab straddling the interface. Also, the superscript n denotes the vector component parallel to \hat{n} and $\int \Gamma$ is the jump of the enclosed

quantity across the slab. Equation (2-55a) may be regarded as the definition of the current flow $\int \underline{J}_{tan}$ per unit slab length in terms of \underline{B} . Proof of the above jump conditions may be found in Jeffrey (1966).

In a perfectly conducting medium ($\sigma = \infty$),

$$\underline{E} + \underline{v} \times \underline{B} = 0 \quad (2-57)$$

so that \underline{J} is finite. Suppose the fluid region of primary interest lies above $n=z_0$ while the region $n \leq z_0$ is a perfect conductor. Combining (2-56) and (2-57),

$$\lim_{n \rightarrow z_0^+} \hat{n} \times (\underline{E} + \underline{v} \times \underline{B}) = 0 \quad (2-58)$$

where $n \rightarrow z_0^+$ ($n \rightarrow z_0^-$) signifies the limit is approached from above (below). Moreover, taking the fluid region $n > z_0$ as finitely conducting (i.e. $0 \leq \sigma < \infty$), $\lim_{n \rightarrow z_0^+} \hat{n} \times \underline{J} = \sigma \lim_{n \rightarrow z_0^+} \hat{n} \times (\underline{E} + \underline{v} \times \underline{B}) = 0$, by Ohm's law. Invoking (2-28), the correct boundary conditions on the magnetic field at the perfectly conducting boundary $n = z_0$ are equation (2-54) and

$$\lim_{n \rightarrow z_0^+} (\hat{n} \times \nabla \times \underline{B}) = 0 \quad (2-59)$$

At the interface between two finitely conducting fluids (regions 1 and 2) or a finitely conducting fluid (1) and an insulator (2), the boundary conditions on the magnetic field are (2-54) and

$$\int \hat{n} \times \underline{B} \cdot \underline{d}l = 0 \quad (2-55b)$$

Thus \underline{B} is continuous across the interface. As $\hat{n} \cdot \text{curl } \underline{B}$ involves only

tangential derivatives, (2-55b) implies that $\int J^n = 0$. But if region 2 is an insulator, $J^n = 0$ there. In particular, $\lim_{n \rightarrow z_+} J^n = 0$, taking $n=z_4$ at the interface. An immediate consequence is the familiar condition at an insulating boundary

$$\lim_{n \rightarrow z_4^-} J_n = 0 \quad (2-60)$$

The perfectly conducting boundary is the only type that shields the fluid from external electromagnetic fields. Otherwise one must solve for \underline{B} both inside and outside the fluid region of interest, and then match the two solutions at the boundary, i.e. apply (2-54) and (2-55b).

For the special case in which the exterior region acts like an insulator ($\underline{J}=0$, σ finite, and $\underline{E} + \underline{v} \times \underline{B} = 0$; or $\underline{J} = 0, \sigma=0$, and $\underline{E} + \underline{v} \times \underline{B}$ finite), the exterior problem and matching problem are relatively simple. Since \underline{B} is then irrotational as well as solenoidal, the exterior problem consists of the diagnostic equations and boundary conditions

$$\nabla^2 \bar{\Phi}_m = 0 \quad (2-61a)$$

$$\underline{B} = \nabla \bar{\Phi}_m \quad (2-61b)$$

$$\left(\frac{\partial \bar{\Phi}_m}{\partial r} \right)_{r=a+z_+} = \lim_{z \rightarrow z_+} B^z \quad (2-61c)$$

$$\lim_{r \rightarrow \infty} \bar{\Phi}_m \sim O(r^{-2}) \quad (2-61d)$$

Equation (2-61c) follows from (2-61b) and the jump condition (2-54), while (2-61d) guarantees that there are no external sources of magnetic field. The above Neumann boundary value problem has an analytic solution.

If (2-61c) has the spherical harmonic expansion $\sum_{n=0} \sum_{m=0} \tilde{b}_{m+n}^n Y_{m+n}^n$ (where $\tilde{b}_0^0 = 0$), then

$$\Phi_m(\lambda, \varphi, r, t) = \sum_{n=0} \sum_{m=0} -\left(\frac{a+z_4}{m+n+1}\right) \left(\frac{a+z_4}{r}\right)^{m+n+1} \tilde{b}_{m+n}^n(t) Y_{m+n}^n(\lambda, \varphi) \quad (2-62)$$

Here $Y_{m+n}^n(\lambda, \varphi)$ is the complex spherical harmonic of degree $m+n$ and rank n defined by equations (3-30c) and (3-36) while $\tilde{b}_{m+n}^n(t)$ is a corresponding spectral coefficient.⁹ The feedback into the interior region completes the matching problem. Applying the jump condition (2-55b),

$$\underline{B}_H(\lambda, \varphi, z_4, t) = \nabla_H \lim_{r \rightarrow a+z_4^+} \Phi_m(\lambda, \varphi, r, t) \quad (2-63)$$

In this manner, there is no overspecification of variables. Also, the only way to regenerate magnetic fields is through the interior induction process.

Finally, what electromagnetic boundary conditions should be chosen for the solar model? Qualitatively, a perfectly conducting lower boundary and a nonconducting upper boundary of the above type are not too unreasonable. Cowling (1957a) estimates the molecular resistivity is several orders of magnitude smaller in the core than in the photosphere. Likewise, the eddy resistivity could be height-dependent. The transition of conductivity could be fairly sharp corresponding to the rapid increase

⁹We note that m corresponds to the number of nodes from pole to pole while n is the longitudinal wave number.

of ionized particles with depth.¹⁰ We crudely parameterize such a variation of η with depth by subdividing the model into five zones:

(i) an underlying perfectly conducting region in solid body rotation

($\underline{v} = \partial \underline{v} / \partial z = 0$ for $z < 0$) . Since induction is absent from this

region, \underline{B} vanishes for all time if $\underline{B} = 0$ initially.

In particular, $B^z = 0$ for $z < 0$.

(ii) An interface between region (i) and the interior fluid region.

Applying the jump condition (2-54) and noting that $\lim_{z \rightarrow 0^-} B^z = 0$,

$$B^z = 0 \quad \text{at} \quad z = 0 \quad (2-64)$$

Then expanding (2-59),

$$\partial B^x / \partial z = \partial B^y / \partial z = 0 \quad \text{at} \quad z = 0 \quad (2-65)$$

These conditions are analogous to the conditions (2-53b) and (2-52) on $\frac{\partial \underline{v}}{\partial z}$ and \underline{w} at a free stress, rigid lid boundary.

(iii) The interior region in which η is a finite constant. The partial differential equations and identities discussed previously are solved here.

(iv) A nonconducting interface separating the finitely conducting interior region from the insulator or current free exterior region (v). The appropriate boundary conditions are given by equations (2-61c) and (2-63). The matching conditions (2-54) and (2-55b) are analogous to the conditions (2-53a) and (2-52) on \underline{v} at a no-slip, rigid lid. The added complication is the coupling between the interior and exterior regions.

¹⁰ The atoms are also highly ionized in the corona. In the rarified chromosphere and corona, η is a molecular resistivity and η decreases upward through the chromosphere and lower corona due to the sharp increase in ionization.

(v) The exterior region in which Φ_m is determined from (2-62), then \underline{B} from (2-61b) if desired. As far as the interior is concerned though, (2-62) need be evaluated only at $r=a+z_4$.

No boundary conditions are required for \mathcal{O}' since the potential temperature is to be predicted at a single level. Thus the formulation of the partial differential equations, identities, and boundary conditions for the continuous model is now complete. Obviously, analytic solutions (assuming they exist) to the nonlinear model are unknown. Yet as suggested earlier, nonlinearity is probably an important feature of a reversing dynamo. We simulate it by constructing a numerical model in Chapter III.

CHAPTER III. THE NUMERICAL TWO LAYER SPECTRAL MODEL

3.1 Introductory Remarks.

The numerical model combines a two layer vertical representation with a truncated spectral representation on (horizontal) spherical surfaces. In addition to these aspects, the time differencing scheme and the sequence of equations to be integrated are now to be discussed. In view of the available computer time, the model is chosen to contain relatively few degrees of freedom. Nevertheless, it is hoped a crude simulation of physical processes is achieved.

3.2. Representation of Vertical Variation by Two Layers.

The continuous z dependence of interior variables is replaced by a generalized two layer meteorological model. This type of procedure was used by Gilman (1968). A one layer model would lack three dimensional, horizontally divergent motions required for dynamo maintenance.

The interior region is represented by five equispaced levels. Level 0 corresponds to the lower boundary and level 4 to the upper boundary. Level 2 subdivides the interior into a lower and upper layer of thickness D , whose midpoints are respectively at levels 1 and 3.

Henceforth, a numerical subscript on a variable denotes its level. The prognostic variables are $\psi_{v_1}, \phi_{v_1}, \psi_{m_1}, \phi_{m_1}, \psi_{v_3}, \phi_{v_3}, \psi_{m_3}, \phi_{m_3}$, (and hence $Y_{u_1} = u_1 \hat{\lambda} + v_1 \hat{\phi}$, $B_{u_1} = B_1^{\lambda} \hat{\lambda} + B_1^{\phi} \hat{\phi}$, $Y_{u_3} = u_3 \hat{\lambda} + v_3 \hat{\phi}$, and $B_{u_3} = B_3^{\lambda} \hat{\lambda} + B_3^{\phi} \hat{\phi}$), and σ_2' . The diagnostic variables w_2, B_2^z , and B_4^z are computed from the mass and magnetic continuity equations. The only other active diagnostic variables are the pressures P_1' and P_3' . A variable at an intermediate level is taken as the linear average of that variable at adjacent levels.

For example,

$$u_2 = (u_1 + u_3)/2 \quad (3-1a)$$

$$B_2^{\omega} = (B_1^{\omega} + B_3^{\omega})/2 \quad (3-1b)$$

$$W_1 = (W_0 + W_2)/2 \quad (3-1c)$$

$$B_3^z = (B_2^z + B_4^z)/2 \quad (3-1d)$$

Let Λ denote any variable and $(\partial\Lambda/\partial z)_i$ its vertical derivative evaluated at level i . An off-centered difference scheme is always employed at the boundaries so that

$$(\partial\Lambda/\partial z)_0 = (\Lambda_1 - \Lambda_0)/(.5D) \quad (3-2a)$$

$$(\partial\Lambda/\partial z)_4 = (\Lambda_4 - \Lambda_3)/(.5D) \quad (3-2b)$$

In most circumstances, the following difference schemes are applied to the interior:

$$(\partial\Lambda/\partial z)_i = (\Lambda_3 - \Lambda_1)/D, \quad i = 1, 2, 3 \quad (3-2c)$$

$$(\partial^2\Lambda/\partial z^2)_i = (4/D^2)(\Lambda_{i+1} + \Lambda_{i-1} - 2\Lambda_i), \quad i = 1, 3 \quad (3-2d)$$

However, to avoid spurious sources of vertically averaged angular momentum or mean square kinetic and magnetic energy, for our boundary conditions on \underline{B} , we require that

$$(B^z \partial\Lambda/\partial z)_3 = \frac{B_3^z}{2}(\Lambda_3 - \Lambda_1)/D + \frac{B_4^z}{2}(\Lambda_4 - \Lambda_3)/(.5D) \quad (3-3)$$

Here $\Lambda = \underline{B}_H$ or \underline{V}_H , although $\underline{V}_{H_4} - \underline{V}_{H_3}$ will vanish due to (3-4b).

No nonlinear instabilities should develop due to the vertical differencing scheme, i.e. formulae (3-2) and (3-3).

The boundary conditions for the two layer model are

$$(u_0, v_0, w_0) = (0, 0, 0) \quad (3-4a)$$

$$(u_4, v_4, w_4) = (u_3, v_3, 0) \quad (3-4b)$$

$$(B_0^\lambda, B_0^\varphi, B_0^z) = (B_1^\lambda, B_1^\varphi, 0) \quad (3-5a)$$

$$\left(\frac{\partial \Phi_m}{\partial r}\right)_{r=a+z_4} = B_4^z \quad (3-5b)$$

$$B_4^\lambda = \frac{1}{(a+z_4) \cos \varphi} \frac{\partial}{\partial \lambda} \left(\lim_{r \rightarrow a+z_4^+} \Phi_m \right) \quad (3-5c)$$

$$B_4^\varphi = \frac{1}{(a+z_4)} \frac{\partial}{\partial \varphi} \left(\lim_{r \rightarrow a+z_4^+} \Phi_m \right) \quad (3-5d)$$

The conditions (3-4a) through (3-5a) are substituted directly into the two layer model prognostic and diagnostic equations at levels 1, 2, and 3. The exterior magnetic potential Φ_m is the solution to (2-62), in which the \tilde{b}_{m+n}^n are spectral coefficients of B_4^z , while B_4^λ and B_4^φ are obtained from (3-5c) and (3-5d). In the perfectly conducting region below level 0, $\mathbf{V} = \mathbf{B} = 0$. The two layer model is obviously too crude to resolve boundary layers. In a continuous model, the vertical currents at $z=z_3$ would form loops to satisfy (2-60) i.e. $\lim_{z \rightarrow z_4^-} J^z = 0$.

The nonmagnetic case corresponds to the conventional two layer model of meteorology. The basic features of the generalized two layer

hydromagnetic model are summarized in Fig. 3.1.

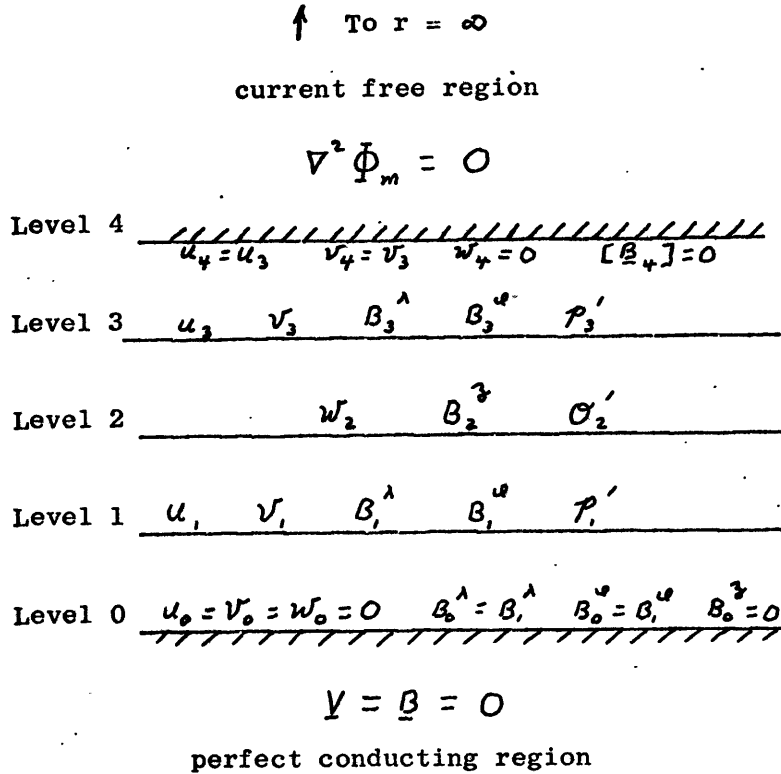


Fig. 3.1. Schematic diagram of the two layer model.

3.3. Interior Equations for the Two Layer Model.

In the interest of efficiency, the Lundquist (1952) linear transformations of hydromagnetic variables and equations are adopted here. While apparently providing no new physical insights, these transformations reduce the number of distinct bilinear products in a Boussinesq model. A net savings of CPU (central processing unit) computer time is thereby achieved. Even with the transformations, roughly 50% of the CPU time was devoted to bilinear multiplication.

Following Lundquist (1952), the variable transformations are

$$\underline{B}_* = (4\pi\mu_0\rho_s)^{-1/2} \underline{B} \quad (3-6)$$

$$\underline{V}^\pm = \underline{V}_H^\pm + \omega^\pm \hat{z} = \underline{V}^\pm \pm \underline{B}_* \quad (3-7a)$$

$$\underline{\psi}^\pm = \underline{\psi}_v^\pm (4\pi\mu_0\rho_s)^{-1/2} \underline{\psi}_m \quad (3-7b)$$

$$\underline{\phi}^\pm = \underline{\phi}_v^\pm (4\pi\mu_0\rho_s)^{-1/2} \underline{\phi}_m \quad (3-7c)$$

Each of equations (3-7a), (3-7b), and (3-7c) is really two equations in one for the variables $\underline{V}^+, \underline{V}^-$; $\underline{\psi}^+, \underline{\psi}^-$; and $\underline{\phi}^+, \underline{\phi}^-$ respectively. Thus $\underline{V}^\pm = \underline{V} \pm \underline{B}_*$ means $\underline{V}^+ = \underline{V} + \underline{B}_*$ and $\underline{V}^- = \underline{V} - \underline{B}_*$, etc. This notation is used throughout this section. The inverse transformations are

$$\underline{V} = .5(\underline{V}^+ + \underline{V}^-) \quad (3-8a)$$

$$\underline{B} = .5(4\pi\mu_0\rho_s)^{1/2}(\underline{V}^+ - \underline{V}^-) \quad (3-8b)$$

$$\underline{\psi}_v = .5(\underline{\psi}^+ - \underline{\psi}^-) \quad (3-8c)$$

$$\underline{\psi}_m = .5(4\pi\mu_0\rho_s)^{1/2}(\underline{\psi}^+ - \underline{\psi}^-) \quad (3-8d)$$

$$\underline{\phi}_v = .5(\underline{\phi}^+ + \underline{\phi}^-) \quad (3-8e)$$

$$\underline{\phi}_m = .5(4\pi\mu_0\rho_s)^{1/2}(\underline{\phi}^+ - \underline{\phi}^-) \quad (3-8f)$$

The Lundquist transformation of the λ and ω component hydromagnetic equations may be written symbolically as

$$\{(2-37a); (2-38a)\} \rightarrow \{(2-37a) \pm (4\pi\mu_0\rho_s)^{-1/2} \cdot (2-38a)\} \quad (3-9a)$$

$$\{(2-37b); (2-38b)\} \rightarrow \{(2-37b) \pm (4\pi\mu_0\rho_s)^{-1/2} \cdot (2-38b)\} \quad (3-9b)$$

In particular, (3-9) gives us prognostic equations for u^+ , u^- , v^+ , and v^- at levels 1 and 3.

Applying (3-8) and (3-9) to the time derivative terms of (2-37a), (2-37b), (2-38a) and (2-38b), we have

$$\left\{ \frac{\partial u}{\partial t}; \frac{\partial B^\lambda}{\partial t} \right\} \rightarrow \left\{ \frac{\partial u}{\partial t} \pm (4\pi\mu_0\rho_s)^{-1/2} \frac{\partial B^\lambda}{\partial t} \right\} = \left\{ \frac{\partial u^\pm}{\partial t} \right\} \quad (3-10a)$$

$$\left\{ \frac{\partial v}{\partial t}; \frac{\partial B^\omega}{\partial t} \right\} \rightarrow \left\{ \frac{\partial v}{\partial t} \pm (4\pi\mu_0\rho_s)^{-1/2} \frac{\partial B^\omega}{\partial t} \right\} = \left\{ \frac{\partial v^\pm}{\partial t} \right\} \quad (3-10b)$$

The corresponding transformations for the curvature correction terms are

$$\left\{ \frac{\tan \omega}{a} (uv - \frac{B^\lambda B^\omega}{4\pi\mu_0\rho_s}); \frac{\tan \omega}{a} (uB^\omega - vB^\lambda) \right\} \rightarrow \left\{ \pm (u^-v^+ - u^+v^-) \frac{\sin \omega}{a \cos \omega} + v^\mp u^\pm \frac{\sin \omega}{a \cos \omega} \right\} \quad (3-11a)$$

$$\left\{ \frac{\tan \omega}{a} \left(\frac{B^\lambda{}^2}{4\pi\mu_0\rho_s} - u^2 \right); 0 \right\} \rightarrow \left\{ \begin{matrix} + \\ + \end{matrix} \left[-\frac{2}{a} (\epsilon^N - \epsilon^M) \frac{\sin \omega}{\cos \omega} + \frac{v^-v^+ \sin \omega}{a \cos \omega} \right] \right\} \quad (3-11b)$$

The symbols \mathcal{E}^K and \mathcal{E}^M denote the kinetic and magnetic energy density respectively, i.e.

$$\mathcal{E}^K = (u^2 + v^2)/2 \quad (3-12a)$$

$$\mathcal{E}^M = (B^{\lambda^2} + B^{\omega^2}) / (8\pi\mu_0\rho_s) \quad (3-12b)$$

Introducing the variable

$$\rho = p'/\rho_s \quad (3-13)$$

the horizontal gradient of total pressure has the transformation

$$\left\{ -\nabla_H \left(\frac{p'}{\rho_s} + \frac{(B^{\lambda^2} + B^{\omega^2})}{8\pi\mu_0\rho_s} \right); 0 \right\} \rightarrow \left\{ -\nabla_H (\rho + \mathcal{E}^M) \right\} \quad (3-14)$$

A considerable simplification is achieved by transforming the remaining nonlinear terms:

$$\left\{ -\underline{v} \cdot \nabla \underline{v}_H + \frac{\underline{B} \cdot \nabla \underline{B}_H}{4\pi\mu_0\rho_s}; -\underline{v} \cdot \nabla \underline{B}_H + \underline{B} \cdot \nabla \underline{v}_H \right\} \rightarrow \left\{ -\underline{v}_H^{\pm} \cdot \nabla \underline{v}_H^{\pm} - w^{\pm} \frac{\partial \underline{v}_H^{\pm}}{\partial z} \right\} \quad (3-15)$$

Taking into account (3-2c) and (3-3), we can evaluate the last terms on the right hand side of equation (3-15) at levels 1 and 3 of the two layer model. Thus,

$$-(w^{\pm} \frac{\partial \underline{v}_H^{\pm}}{\partial z})_1 = -w_2^{\pm} (\underline{v}_{H_3}^{\pm} - \underline{v}_{H_1}^{\pm}) / 2D \quad (3-16a)$$

$$-(w^{\pm} \frac{\partial \underline{v}_H^{\pm}}{\partial z})_3 = -(w^{\pm} \frac{\partial \underline{v}_H^{\pm}}{\partial z})_1 + B_{*4}^{\pm} (\underline{B}_{H*4} - \underline{B}_{H*3}) / D \quad (3-16b)$$

From equations (3-11) and (3-15),

$$-\frac{V^{\pm}}{a} \frac{\partial V_H^{\pm}}{\partial \varphi} + \frac{V^{\pm} V_H^{\pm} \sin \varphi}{a \cos \varphi} = -\frac{V^{\pm}}{a \cos \varphi} \frac{\partial (V_H^{\pm} \cos \varphi)}{\partial \varphi} \quad (3-17)$$

Decomposing the coefficients of eddy viscosity and eddy resistivity into vertical and horizontal coefficients,

$$V_{(z)}^{\pm} = 4D^{-2} V \quad (3-18a)$$

$$\eta_{(z)}^{\pm} = 4D^{-2} \eta \quad (3-18b)$$

$$V_{(H)}^{\pm} = V \quad (3-18c)$$

$$\eta_{(H)}^{\pm} = \eta \quad (3-18d)$$

$V_{(z)}^{\pm}$ and $\eta_{(z)}^{\pm}$ are the vertical eddy coefficients in units of inverse time, whereas the horizontal coefficients $V_{(H)}^{\pm}$ and $\eta_{(H)}^{\pm}$ have the same units as V and η . The latter two equations are valid under isotropic conditions, implicitly assumed to exist up to now.¹ It is also convenient to introduce

$$V_{(H)}^{\pm} = .5 (V_{(H)}^{\pm} \pm \eta_{(H)}^{\pm}) \quad (3-19)$$

Utilizing the above formulas, the hydromagnetic equations for the two layer model are written as

¹ Later on, $\eta_{(H)}^{\pm}$ and $V_{(H)}^{\pm}$ are enhanced to promote selective damping of the higher harmonics of V and B . Otherwise the horizontal dissipation terms are negligible since $D^2/a^2 \ll 1$.

$$\begin{aligned}
 \frac{\partial u_i^\pm}{\partial t} &= -\frac{u_i^\mp}{a \cos \varphi} \frac{\partial u_i^\pm}{\partial \lambda} - \frac{v_i^\mp}{a \cos \varphi} \frac{\partial (u_i^\pm \cos \varphi)}{\partial \varphi} \pm (u_i^- v_i^+ - u_i^+ v_i^-) \frac{\sin \varphi}{a \cos \varphi} \\
 &\quad - \frac{w_2^\mp}{2D} (u_3^\pm - u_1^\pm) - \frac{1}{a \cos \varphi} \frac{\partial}{\partial \lambda} (\rho_i + \varepsilon_i^M) + 2\mathcal{N} \sin \varphi v_i \\
 &\quad + v_{(3)}^\pm (u_3 - 3u_i) \pm \eta_{(3)}^\lambda (B_{x_3}^\lambda - B_{x_i}^\lambda) + v_{(H)}^\pm \Delta^\lambda (u_i^+, v_i^+) \\
 &\quad + v_{(H)}^\mp \Delta^\lambda (u_i^-, v_i^-)
 \end{aligned} \tag{3-20a}$$

$$\begin{aligned}
 \frac{\partial u_3^\pm}{\partial t} &= -\frac{u_3^\mp}{a \cos \varphi} \frac{\partial u_3^\pm}{\partial \lambda} - \frac{v_3^\mp}{a \cos \varphi} \frac{\partial (u_3^\pm \cos \varphi)}{\partial \varphi} \pm (u_3^- v_3^+ - u_3^+ v_3^-) \frac{\sin \varphi}{a \cos \varphi} \\
 &\quad - \frac{w_2^\mp}{2D} (u_3^\pm - u_1^\pm) + \frac{B_{x_4}^\mp}{D} (B_{x_4}^\lambda - B_{x_3}^\lambda) - \frac{1}{a \cos \varphi} \frac{\partial}{\partial \lambda} (\rho_3 + \varepsilon_3^M) \\
 &\quad + 2\mathcal{N} \sin \varphi v_3 + v_{(3)}^\pm (u_1 - u_3) + \eta_{(3)}^\lambda (B_{x_1}^\lambda - 3B_{x_3}^\lambda + 2B_{x_4}^\lambda) \\
 &\quad + v_{(H)}^\pm \Delta^\lambda (u_3^+, v_3^+) + v_{(H)}^\mp \Delta^\lambda (u_3^-, v_3^-)
 \end{aligned} \tag{3-20b}$$

$$\begin{aligned}
 \frac{\partial v_1^\pm}{\partial x} &= -\frac{u_1^\mp}{a \cos \omega} \frac{\partial v_1^\pm}{\partial \lambda} - \frac{v_1^\mp}{a \cos \omega} \frac{\partial (v_1^\pm \cos \omega)}{\partial \omega} - \frac{2}{a} (\varepsilon_1^K - \varepsilon_1^M) \frac{\sin \omega}{\cos \omega} \\
 &\quad - \frac{w_2^\mp}{2D} (v_3^\pm - v_1^\pm) - \frac{1}{a} \frac{\partial}{\partial \omega} (\rho_1 + \varepsilon_1^M) - 2\mathcal{N} \sin \omega u_1 \\
 &\quad + V_{(3)} (v_3 - 3v_1) \pm \eta_{(3)} (B_{x_3}^\omega - B_{x_1}^\omega) + V_{(H)}^\pm \Delta^\omega(u_1^\pm, v_1^\pm) \\
 &\quad + V_{(H)}^\mp \Delta^\omega(u_1^\mp, v_1^\mp)
 \end{aligned} \tag{3-20c}$$

$$\begin{aligned}
 \frac{\partial v_3^\pm}{\partial x} &= -\frac{u_3^\mp}{a \cos \omega} \frac{\partial v_3^\pm}{\partial \lambda} - \frac{v_3^\mp}{a \cos \omega} \frac{\partial (v_3^\pm \cos \omega)}{\partial \omega} - \frac{2}{a} (\varepsilon_3^K - \varepsilon_3^M) \frac{\sin \omega}{\cos \omega} \\
 &\quad - \frac{w_2^\mp}{2D} (v_3^\pm - v_1^\pm) + \frac{B_{x_4}^\omega}{D} (B_{x_4}^\omega - B_{x_3}^\omega) - \frac{1}{a} \frac{\partial}{\partial \omega} (\rho_3 + \varepsilon_3^M) \\
 &\quad - 2\mathcal{N} \sin \omega u_3 + V_{(3)} (v_1 - v_3) \pm \eta_{(3)} (B_{x_1}^\omega - 3B_{x_3}^\omega + 2B_{x_4}^\omega) \\
 &\quad + V_{(H)}^\pm \Delta^\omega(u_3^\pm, v_3^\pm) + V_{(H)}^\mp \Delta^\omega(u_3^\mp, v_3^\mp)
 \end{aligned} \tag{3-20d}$$

Each of the above is really two equations in one. The notation was previously explained in the discussion of equation (3-7a).

From equations (2-44), (2-46a), (3-2c), and (3-4), conservation of mass in the two layer model requires that²

$$\nabla_H \cdot \underline{V}_{H_1} + \frac{W_2}{D} = \nabla_H \cdot \underline{V}_{H_3} - \frac{W_2}{D} = 0 \quad (3-21a)$$

$$W_2 = -D \nabla_H^2 \Phi_{V_1} \quad (3-21b)$$

These equations then imply

$$\nabla_H^2 (\Phi_{V_1} + \Phi_{V_3}) = 0 \quad (3-22a)$$

We may express Φ_{V_1} and Φ_{V_3} in terms of a finite number of spherical harmonics Y_{m+n}^n defined by equation (3-30c). Since

$\nabla_H^2 Y_{m+n}^n = -\frac{(m+n)(m+n+1)}{\alpha^2} Y_{m+n}^n$, then $\Phi_{V_1} + \Phi_{V_3}$ is an arbitrary unphysical constant. Therefore,

$$\Phi_{V_3} = \Phi_{V_1} \quad (3-22b)$$

$$\Phi_3^- = -(\Phi_1^+ + \Phi_3^+ + \Phi_1^-) \quad (3-22c)$$

$$\Phi_{V_2} = 0 \quad (3-23a)$$

$$\underline{V}_{H_2} = \hat{z} \times \nabla_H \Psi_{V_2} \quad (3-23b)$$

The continuity of magnetic fields in the two-layer model is described by

$$\nabla_H \cdot \underline{B}_{H_1} + \frac{B_2^z}{D} = \nabla_H \cdot \underline{B}_{H_3} + \frac{(B_4^z - B_2^z)}{D} = 0 \quad (3-24a)$$

²For our purposes, it is convenient not to work exclusively with the \underline{V}^\pm variables.

$$B_2^z = -D \nabla_H^2 \Phi_{m_1} \quad (3-24b)$$

$$B_4^z = B_2^z - D \nabla_H^2 \Phi_{m_3} = -D \nabla_H^2 (\Phi_{m_1} + \Phi_{m_3}) \quad (3-24c)$$

According to (3-23), only the nondivergent part of the motion advects potential temperature σ_2' at level 2, in the thermodynamic equation. To be energetically consistent, the vertical advection of σ_2' should be suppressed. Fortunately the $w \frac{\partial \sigma_2'}{\partial z}$ term vanishes anyway, if potential temperature is predicted at only one level. Consequently, the thermodynamics is governed by the prognostic equation

$$\begin{aligned} \frac{\partial \sigma_2'}{\partial t} = & \frac{1}{a^2 \cos \varphi} \left(\frac{\partial \sigma_2'}{\partial \lambda} \frac{\partial \psi_{r_2}}{\partial \varphi} - \frac{\partial \sigma_2'}{\partial \varphi} \frac{\partial \psi_{r_2}}{\partial \lambda} \right) \\ & - \left(\frac{\partial \sigma_s}{\partial z} \right)_{z=z_2} w_2 - K (\sigma_2' - \sigma_{x_2}') \end{aligned} \quad (3-25)$$

The diagnostic equation of vertical magnetohydrostatic balance is

$$p_3 - p_1 = \frac{gD}{\sigma_s} \sigma_2' + \epsilon_1^M - \epsilon_3^M \quad (3-26)$$

From the nondivergence condition, i.e., (3-23b), one can compute

$\nabla_H^2 (\rho_1 + \rho_3)$. Inverting this expression and using (3-26), ρ_1 and ρ_3 and hence p_1' and p_3' are determined. The perturbation density and temperature play a passive role in the model, i.e.,

$$\frac{T_2'}{T_s} = \frac{\sigma_2'}{\sigma_s} = -\frac{p_2'}{p_s} \quad (3-27)$$

In the special case $\underline{B} = 0$,

$$\underline{v}^+ = \underline{v}^- = \underline{v} \quad (3-28a)$$

$$\underline{B}_x = 0 \quad (3-28b)$$

$$\psi^+ = \psi^- = \psi_r \quad (3-28c)$$

$$\phi^+ = \phi^- = \phi_r \quad (3-28d)$$

at all levels, while

$$\bar{\Phi}_m = 0 \quad (3-29)$$

Also the set of equations (3-20) would reduce to four (nonmagnetic) primitive equations.

3.4. The Spectral Representation.

Based upon their mathematical properties on the sphere, spherical harmonics are a logical class of orthogonal spectral functions for our spherical model. However we have chosen to work with an equivalent set of nonorthogonal functions called Robert functions.³ One advantage is that the interaction coefficients are much simpler. Computational efficiency is an even more important consideration.

Unfortunately, the spherical harmonic spectral method of Bullard and Gellman (1954) suitable for their kinematic dynamo model cannot be extended in an efficient manner to our hydromagnetic equations. Some of their spectral equations are derived directly from the vertical

³The following references contain useful background material on properties of spherical harmonics or Robert spectral functions, nonlinear spectral multiplication (interactions), and/or applications to fluids problems: Bullard and Gellman (1954), Platzman (1960), and Robert (1965, 1966).

component of the magnetic induction equation, which we do not retain. In our model, explicit scalar equations for the horizontal divergence of magnetic field (and velocity) would play a corresponding role. The number of nonlinear terms would clearly increase due to the term by term differentiation required to obtain these equations.⁴ The spherical harmonic expansion of the meteorological vorticity and horizontal divergence equations by Kubota (1959) is inefficient a priori.

The spectral method of Robert (1966) may be applied to the horizontal projections of the primitive hydromagnetic vector equations. Since the curl and horizontal divergence operate on the sum of terms in the horizontal primitive hydromagnetic equations, additional nonlinear terms are not explicitly generated. Orthogonal truncation is a relatively efficient linear operation. Roundoff errors are potentially more serious for the Robert representation as the resolution is increased. However, they were very manageable thanks to the relatively low order spectral resolution and the 60 bit CDC-6600 word length.

3.4.1. The correspondence between spherical harmonics and Robert functions.

Ordinary spherical harmonics may be expressed as a series of trigonometric functions:

$$\left\{ \begin{aligned} Y_{m+n}^{n,c}(\lambda, \varphi) &= \left(\sum_{l=0}^{\binom{m}{2}} y_{m-2l,m}^n \sin^{m-2l} \varphi \right) \cos^n \varphi \cos n\lambda = P_{m+n}^n \cos n\lambda \\ Y_{m+n}^{n,s}(\lambda, \varphi) &= \left(\sum_{l=0}^{\binom{m}{2}} y_{m-2l,m}^n \sin^{m-2l} \varphi \right) \cos^n \varphi \sin n\lambda = P_{m+n}^n \sin n\lambda \end{aligned} \right. \quad \left. \begin{array}{l} (3-30a) \\ (3-30b) \end{array} \right\} \quad n, m \geq 0$$

⁴In a convective model, the magnetohydrostatic approximation should be dropped. But the gas pressure still has to be eliminated by applying the $\hat{r} \cdot \text{curl}$ curl operator to the vector angular momentum equation, for example.

$$Y_{m+n}^n(\lambda, \varphi) = \sum_{i=0}^{(\frac{m}{2})_T} y_{m-2i, m}^n \sin^{m-2i} \varphi \cos^{i|n|} \varphi e^{in\lambda} = P_{m+n}^n e^{in\lambda}, m \geq 0 \quad (3-30c)$$

Here $i = \sqrt{-1}$, m and n are integers, $(m/2)_T$ is the integer part of $m/2$, P_{m+n}^n is the associated Legendre polynomial of degree $m+n$ and rank m , and the $y_{m-2i, m}^n$ are (normalized) constants. In many studies, the name spherical harmonic is reserved for the Y_{m+n}^n . In analogy, the $Y_{m+n}^{n, c}$ and $Y_{m+n}^{n, s}$ could be called cosine and sine spherical harmonics, respectively. But collectively, all three functions will be referred to as spherical harmonics. These functions are related to the nonorthogonal "Robert" harmonic functions

$$\left\{ \begin{array}{l} R_m^{n, c} = \sin^m \varphi \cos^n \varphi \cos n\lambda \\ R_m^{n, s} = \sin^m \varphi \cos^n \varphi \sin n\lambda \end{array} \right\} n, m \geq 0 \quad (3-31a)$$

$$(3-31b)$$

$$R_m^n = \sin^m \varphi \cos^{i|n|} \varphi e^{in\lambda}, m \geq 0 \quad (3-31c)$$

There is in fact a one-to-one correspondence between the Y's and R's, provided m takes on all values in the range $0, 2, 4, \dots, M$ and/or $1, 3, 5, \dots, M-1$, where M is even. Equation (3-30) expresses spherical harmonic functions in terms of Robert functions. The inverse transformation is

$$\sin^m \varphi \cos^n \varphi = \sum_{j=0}^{(\frac{m}{2})_T} A_{m, m-2j}^n P_{m-2j+n}^n, n, m \geq 0 \quad (3-32)$$

or since the summation is over J only,⁵

$$R_m^{n, (s)} = \sum_{J=0}^{\binom{m}{2}_T} A_{m, m-2J}^n Y_{m-2J+n}^{n, (s)} \quad n, m \geq 0. \quad (3-33)$$

If the formula for the $y_{m-2I, m}^n$ coefficients is known, the $A_{m, m-2J}^n$ can be generated from the $y_{m-2I, m}^n$.

From (3-32) and (3-30),

$$\left\{ \sum_{I=0}^{\binom{m}{2}_T - J} \sum_{J=0}^{\binom{m}{2}_T} (A_{m, m-2J}^n y_{m-2(I+J), m-2J}^n \cdot \sin^{m-2(I+J)} \omega) - \sin^m \omega \right\} \cos^n \omega = 0 \quad (3-34)$$

The only combination of I and J contributing to $\sin^m \omega$ is $I=J=0$. Hence

$$A_{m, m}^n = 1 / y_{m, m}^n \quad (3-35a)$$

In addition, $\sum_{I=0}^{\binom{m}{2}_T - J} \leftrightarrow \sum_{J=0}^{\binom{m}{2}_T} A_{m, m-2J}^n y_{m-2(I+J), m-2J}^n = 0$, where $\sum_I \leftrightarrow \sum_J$ denotes summation over all I, J pairs such that $I+J = K = \text{constant}$ and $1 \leq K \leq \binom{m}{2}_T$.

In general, the recursion formula

$$A_{m, m-2K}^n = - \left(\sum_{J=0}^{K-1} y_{m-2K, m-2J}^n A_{m, m-2J}^n \right) / y_{m-2K, m-2K}^n \quad (3-35b)$$

is valid for $K=1, 2, 3, \dots, \binom{m}{2}_T$. For $K=1$,

$$A_{m, m-2}^n = - y_{m-2, m}^n / (y_{m, m}^n y_{m-2, m-2}^n) \quad (3-35c)$$

⁵The $\binom{c}{s}$ notation here is analogous to the \pm notation of section 3.

Only (3-35a) is needed if $m=0$ or $m=1$. To obtain the y coefficients of

(3-30), express P_ℓ^n as the product of the normalization factor $[2(2\ell+1)(\ell-n)!/(\ell+n)!]^{1/2}$ and Rodrigues's formula $(2^\ell \ell!)^{-1} (-1)^\ell (1-z^2)^{\ell/2} d^{\ell+n} (1-z^2)^\ell / dz^{\ell+n}$. Expanding $(1-z^2)^\ell$ in a binomial series,

$$d^{\ell+n} (1-z^2)^\ell / dz^{\ell+n} = \sum_{k=(\ell+n)/2}^{\ell} \left\{ \frac{(-1)^k \ell!}{k! (\ell-k)!} \right\} \frac{(2k)!}{(2k-\ell-n)!} z^{2k-\ell-n}$$

Finally, setting $\ell = m + n$, $z = \sin \varphi$, and $I = \ell - k$,

$$y_{m-2I, m}^n = \left\{ \frac{2[2(n+m)+1]m!}{(2n+m)!} \right\}^{1/2} \frac{(-1)^I}{2^{n+m}} \left\{ \frac{[2(m+n-I)]!}{(m-2I)!(m+n-I)! I!} \right\} \quad (3-36)$$

where $n, m, I \geq 0$. The A and y coefficients play an important role in the orthogonal truncation of the Robert representation.

3.4.2. Details of the Robert spectral method.

Let us now consider the details of the Robert (1965, 1966) spectral method. All potentials, stream functions and thermodynamic scalars are represented by a Robert polynomial of the type

$$Z = \sum_n \sum_{m=0}^M (\bar{Z}_m^{n,c} \cos n\lambda + \bar{Z}_m^{n,s} \sin n\lambda) \sin^m \varphi \cos^n \varphi \quad (3-37)$$

The Robert spectral harmonics $\bar{Z}_m^{n,c}$ and $\bar{Z}_m^{n,s}$ are functions of t only. In our model, $M=4$ and $n=0$ or 6 . Since $\bar{Z}_m^{0,s}$ has no physical meaning, we take $\bar{Z}_m^{0,s} = 0$ for all m . Also, $\bar{Z}_0^{0,c} = 0$ for stream functions and potentials. Thus fourteen nontrivial harmonics are left. For convenience, we introduce the variable \bar{Z}_m^n , where

$$Z = \sum_n \sum_{m=0}^M \bar{Z}_m^n \sin^m \varphi \cos^n \varphi \quad (3-38)$$

$$\bar{z}_m^n(\lambda, t) = \hat{z}_m^{n,c} \cos n\lambda + \hat{z}_m^{n,s} \sin n\lambda \quad (3-39)$$

Each vector field, i.e. \underline{B} , \underline{V} , \underline{V}^+ , and \underline{V}^- is derivable from a potential and a stream function. Equation (3-37) is also valid for vertical vector components. But horizontal vector components have expansions like

$$S = \frac{1}{\cos^2 \varphi} \sum_n \sum_{m=0}^{M+1} (\hat{S}_m^{n,c} \cos n\lambda + \hat{S}_m^{n,s} \sin n\lambda) \sin^m \varphi \cos^n \varphi \quad (3-40)$$

Robert (1965) designated Z type variables as true scalars and S type variables as pseudoscalars. At certain stages of the calculations, Robert series of the form

$$U = \frac{1}{\cos^2 \varphi} \sum_n \sum_{m=0}^{M_1} (\hat{U}_m^{n,c} \cos n\lambda + \hat{U}_m^{n,s} \sin n\lambda) \sin^m \varphi \cos^n \varphi \quad (3-41)$$

may appear, with $M_1 > M$. U can be transformed to a Z type polynomial however in which m is summed from 0 to $M_2 > M$. Also, S type polynomials in which m is summed up to $M_3 > M$ are generated. Ultimately, truncation of m harmonics leads to a new series of the form (3-37).

Keeping track of $\cos^{-1} \varphi$ factors, each Robert series may be described by a spectral coefficient matrix. Most of these matrices are stored in the computer as 3x40x2 arrays and a few as 3x10x2 arrays. The first index corresponds to n, the second to m, and the third distinguishes the "c" from the "s" superscript. Schematically, one can think of a typical 3x40x2 coefficient matrix as a 6x40 matrix:

$$\{Z\} = \begin{pmatrix} \hat{Z}_{23}^{0,c} & \hat{Z}_{23}^{6,c} & 0 & 0 & \hat{Z}_{23}^{6,s} & 0 \\ \hat{Z}_{23}^{0,c} & \hat{Z}_{23}^{6,c} & 0 & 0 & \hat{Z}_{23}^{6,s} & 0 \\ \vdots & \vdots & \vdots & \vdots & \vdots & \vdots \\ \hat{Z}_{23}^{0,c} & \hat{Z}_{23}^{6,c} & 0 & 0 & \hat{Z}_{23}^{6,s} & 0 \\ \vdots & \vdots & \vdots & \vdots & \vdots & \vdots \\ 0 & 0 & 0 & 0 & 0 & 0 \end{pmatrix} \quad (3-42)$$

The fourth column contains the trivial coefficients $\hat{Z}_m^{0,s}$. The third and sixth columns may be ignored unless an additional longitudinal wave number is permitted. In practice, $\hat{Z}_{24}^{0,c}, \hat{Z}_{25}^{0,c}, \dots, \hat{Z}_{39}^{0,c}; \hat{Z}_{12}^{6,c}, \hat{Z}_{13}^{6,c}, \dots, \hat{Z}_{39}^{6,c}$; and $\hat{Z}_{12}^{6,s}, \hat{Z}_{13}^{6,s}, \dots, \hat{Z}_{39}^{6,s}$ remain dormant too. These locations were kept to allow enhanced resolution with a bare minimum of program modifications.

The effect of each mathematical operation is to transform one array of spectral coefficients into another array. The notation $Z \rightarrow Z'$ will denote a transformation from the spectral coefficient array $\{Z\}$ of Z to the array $\{Z'\}$ of Z' . $Z \rightarrow Z'/\cos \omega$ would indicate the new Robert polynomial Z' is to be formally divided by $\cos \omega$.

Armed with the following transformation algorithms for the various operators, one can solve the model equations. These algorithms are equivalent to the ones given by Robert (1966) except for (x) . We discuss them here for the sake of completeness.

- (i) addition: Like array elements are added as in ordinary matrix addition.
- (ii) scalar multiplication: Each element of the spectral coefficient array is multiplied by the scalar.
- (iii) $\frac{1}{a \cos \omega} \frac{\partial}{\partial \lambda}$ differentiation: The transformation is of the type

$Z \rightarrow Z'/\cos \varrho$. Clearly,

$$\left(\hat{Z}'\right)_m^{n,c} = \frac{n}{a} \hat{Z}_m^{n,s} \quad (3-43a)$$

$$\left(\hat{Z}'\right)_m^{n,s} = -\frac{n}{a} \hat{Z}_m^{n,c} \quad (3-43b)$$

(iv) $\frac{1}{a} \frac{\partial}{\partial \varrho}$ differentiation: The transformation is also of the type

$Z \rightarrow Z'/\cos \varrho$. After applying $\frac{1}{a} \frac{\partial}{\partial \varrho}$ to (3-38), rearranging terms, and noting that $\bar{z}_{-1}^n = \bar{z}_{M+1}^n = \bar{z}_{M+2}^n = 0$, we obtain

$$\left(\hat{Z}'\right)_m^{n,(s)} = \frac{(1-\delta_{m,M})(1-\delta_{m,M+1})(m+1)\hat{Z}_{m+1}^{n,(s)} - (1-\delta_{m,0})(m+n-1)\hat{Z}_{m-1}^{n,(s)}}{a} \quad (3-44)$$

$m=0$ to $M+1$. $\delta_{m_1, m_2} = \begin{cases} 0, & m_1 \neq m_2 \\ 1, & m_1 = m_2 \end{cases}$ is the Kronecker delta.

(v) Vertical differentiation: Using the finite difference operators, this is just a combination of matrix addition and scalar multiplication.

(vi) The Laplacian ∇_H^2 : Applying (2-39a) to a particular term of the Robert polynomial (3-38), we obtain

$$\frac{\bar{z}_m^n}{a^2} \left(m(m-1) \sin^{m-2} \varrho (1 - \sin^2 \varrho) - [\eta^2 + (n+2)m + (m+1)n] \sin^m \varrho \right) \cos^n \varrho .$$

After all contributions are added, a new Robert polynomial Z^I is defined by

$$\begin{aligned} \left(\hat{Z}'\right)_m^{n,(s)} &= -\frac{1}{a^2} (m+n)(m+n+1) \hat{Z}_m^{n,(s)} \\ &+ \frac{1}{a^2} (m+1)(m+2)(1-\delta_{m,M})(1-\delta_{m,M-1}) \hat{Z}_{m+2}^{n,(s)} \end{aligned} \quad (3-45)$$

The factor $\cos^{-2} \varrho$ in the Laplacian operator is effectively removable.

(vii) The inverse Laplacian $(\nabla_H^2)^{-1}$: Interchanging the role of the primed and unprimed coefficients in (3-45) yields the recursion formula

$$\begin{aligned} (\hat{Z}')_m^{n,(s),c} &= \frac{(m+1)(m+2)(1-\delta_{m,M})(1-\delta_{m,M-1})}{(m+n)(m+n+1)} (\hat{Z}')_{m+2}^{n,(s),c} \\ &- \frac{a^2}{(m+n)(m+n+1)} \hat{Z}_m^{n,(s),c} \end{aligned} \quad (3-46)$$

$m=0$ to M , $m+n \neq 0$, for $(\nabla_H^2)^{-1}$. $(\hat{Z}')_M^{n,(s),c}$ is calculated first and m is successively decremented by one. Since Z' is either a stream function or potential, $(\hat{Z}')_0^{0,c}$ is an unphysical, arbitrary constant. To avoid a singularity in (3-46) for $m+n = 0$, $(\hat{Z}')_0^{0,c}$ is set equal to zero.

(viii) Bilinear multiplication of two Robert series: Let the two polynomials be X and Z , and the product Z' .

$$\begin{aligned} Z' = Z \cdot X &= \sum_{l=0}^{\infty} \sum_{k=0}^{\infty} \sum_{n=0}^{\infty} \sum_{m=0}^{\infty} \left(\hat{Z}_m^{n,c} \cos n\lambda + \hat{Z}_m^{n,s} \sin n\lambda \right) \\ &\cdot \left(\hat{X}_k^{l,c} \cos l\lambda + \hat{X}_k^{l,s} \sin l\lambda \right) \sin^{m+k} \omega \cos^{n+l} \omega \end{aligned} \quad (3-47)$$

For generality, no restrictions are placed upon the upper summation limits.

From well-known trigonometric identities,

$$\begin{aligned} & \left(\hat{Z}_m^{n,c} \cos n\lambda + \hat{Z}_m^{n,s} \sin n\lambda \right) \cdot \left(\hat{X}_k^{l,c} \cos l\lambda + \hat{X}_k^{l,s} \sin l\lambda \right) \\ &= \frac{1}{2} \left[W_{m+k}^{n+l,c} \cos(n+l)\lambda + W_{m+k}^{n+l,s} \sin(n+l)\lambda \right. \\ & \left. + W_{m+k}^{n-l,c} \cos(n-l)\lambda + W_{m+k}^{n-l,s} \sin|n-l|\lambda \right] \end{aligned} \quad (3-48)$$

where we have introduced

$$W_{m+k}^{n+l,c} = \hat{Z}_m^{n,c} \hat{X}_k^{l,c} - \hat{Z}_m^{n,s} \hat{X}_k^{l,s} \quad (3-49a)$$

$$W_{m+k}^{n+l,s} = \hat{Z}_m^{n,c} \hat{X}_k^{l,s} + \hat{Z}_m^{n,s} \hat{X}_k^{l,c} \quad (3-49b)$$

$$W_{m+k}^{n-l,c} = \hat{Z}_m^{n,c} \hat{X}_k^{l,c} + \hat{Z}_m^{n,s} \hat{X}_k^{l,s} \quad (3-49c)$$

$$W_{m+k}^{n-l,s} = \text{sgn}(n,l) \left(-\hat{Z}_m^{n,c} \hat{X}_k^{l,s} + \hat{Z}_m^{n,s} \hat{X}_k^{l,c} \right) \quad (3-49d)$$

$$\text{sgn}(n,l) = \begin{cases} 1, & n > l \\ 0, & n = l \\ -1, & n < l \end{cases} \quad (3-50)$$

In order to obtain a Robert series of the correct form, the power of $\cos \varrho$ must equal the longitudinal wave number for each term. Fortunately,

$$\cos^{n+l} \varrho = \cos^{|n-l|} \varrho \sum_{i=0}^{\min(n,l)} b_{2i} \sin^{2i} \varrho \quad (3-51)$$

where $b_{2i}^{\min(n,l)}$ are coefficients of the binomial expansion of $(1 - \sin^2 \varrho)^{\min(n,l)}$ and

$$\min(n,l) = \begin{cases} l, & n \geq l \\ n, & n < l \end{cases} \quad (3-52)$$

Hence the product is

$$\begin{aligned} Z' = & \frac{1}{2} \sum_{l=0}^{\infty} \sum_{n=0}^{\infty} \sum_{k=0}^{\infty} \sum_{m=0}^{\infty} \left[W_{m+k}^{n+l,c} \cos(n+l)\lambda \right. \\ & \left. + W_{m+k}^{n+l,s} \sin(n+l)\lambda \right] \sin^{m+k} \varrho \cos^{n+l} \varrho \\ & + \frac{1}{2} \sum_{i=0}^{\min(n,l)} \sum_{l=0}^{\infty} \sum_{n=0}^{\infty} \sum_{k=0}^{\infty} \sum_{m=0}^{\infty} \left[W_{m+k}^{n-l,c} \cos(n-l)\lambda \right. \\ & \left. + W_{m+k}^{n-l,s} \sin|n-l|\lambda \right] b_{2i}^{\min(n,l)} \sin^{m+k+2i} \varrho \cos^{|n-l|} \varrho \quad (3-53) \end{aligned}$$

The new coefficients of the transformation $Z \cdot X \rightarrow Z'$ are

$$\begin{aligned}
 \left(\frac{\hat{A}}{\hat{Z}}\right)_m^{n',c,(s)} &= \frac{1}{2} \sum_{k=m'-m} \sum_{m=0} \sum_{\substack{\ell=n-n' \\ 0 \leq \ell}} \sum_{n=0} W_{m+k}^{n+l,(s)} \\
 &+ \frac{1}{2} \sum_{\substack{k=m' \\ -(m+2i)}} \sum_{m=0} \sum_{i=0}^{\min(n,l)} \sum_{\substack{\ell=n \pm n' \\ 0 \leq \ell \leq n}} \sum_{n=0} W_{m+k}^{n-l,(s)} b_{2i}^{\min(n,l)} \quad (3-54)
 \end{aligned}$$

If either Z or X has any factor of $\cos \varphi$ in the denominator, Z' will be divided by the product of such factors.

Bilinear multiplication is the most time consuming computer operation. Certain simplifications are possible. Each product in (3-49) appears twice but need be computed only once, and any product involving $Z_m^{l,0,s}$ or $X_k^{l,0,s}$ may be discarded. Then too, it is more efficient to compute just $W_{m+k}^{n+l,c}$ than $\frac{1}{2}(W_{m+k}^{n+l,c} + W_{m+k}^{n-l,c})$ when $n+l = 0$. The factor 0.5 can be incorporated into the binomial coefficients to save more time. Finally, truncation over n can be imposed as a selection rule since the Robert harmonics are orthogonal with respect to n over the sphere. More specifically, if $n' = n + l$ or $n' = |n - l|$ is not in the system, terms which would contribute to these harmonics are discarded.

In our model, $n=0$ and $n=6$ are the only longitudinal wave numbers. The self-interaction of two longitudinally symmetric modes ($n=l=0$) generates another symmetric mode. Similarly, the self-interaction of two $n=6$ harmonics modifies the symmetric modes. The contribution $n+l=12$ is discarded in accordance with the truncation selection rule. Finally, the interaction of an $n=0$ harmonic with an $n=6$ harmonic affects wave number 6.

(IX) Division by $\cos^2 \varphi$ in nonlinear products: Consider the generalized horizontal advection terms, (e.g. $\frac{u^-}{a \cos \varphi} \frac{\partial u^+}{\partial \lambda} + \frac{v^-}{a \cos \varphi} \frac{\partial (u^+ \cos \varphi)}{\partial \varphi}$) and curvature correction

terms in (3-20) plus the horizontal advection of potential temperature in (3-25). These nonlinear terms can be decomposed into a combination of Jacobians and scalar products multiplied by a constant or by $\sin \varrho$. For example⁶, $\underline{V}_2 \cdot \nabla \phi_2' = J_{\lambda, \varrho}(\psi_{v_2}, \phi_2')$ and $\epsilon_1^k \frac{\sin \varrho}{a} = \frac{(u_1^2 + v_1^2)}{2a} \sin \varrho$

$$= \left[\nabla_H \frac{\phi_{v_1}}{2a} \cdot \nabla_H \phi_{v_1} + \nabla_H \frac{\psi_{v_1}}{2a} \cdot \nabla_H \psi_{v_1} + J_{\lambda, \varrho} \left(\frac{\psi_{v_1}}{a}, \phi_{v_1} \right) \right] \sin \varrho$$

Symbolically, each member of the decomposition has the form $Z''/\cos^2 \varrho$, where

$$\bar{Z}'' = \sum_n \sum_{m=0}^n \left[(\hat{Z}'')_m^{n,c} \cos n\lambda + (\hat{Z}'')_m^{n,s} \sin n\lambda \right] \sin^m \varrho \cos^n \varrho \quad (3-55)$$

is a true scalar. Robert (1966) proved that

$$\bar{Z}''/\cos^2 \varrho = \bar{Z}' \quad (3-56)$$

\bar{Z}' being another true scalar. Since (3-56) holds for each Jacobian or scalar product, it also holds for a sum of them. It is more efficient to group nonlinear terms as an implicit sum of scalar products and Jacobians, i.e., a sum of \bar{Z}' 's. Denoting such a sum by Z ,

$$\bar{Z}/\cos^2 \varrho \rightarrow \bar{Z}' \quad (3-57)$$

Whenever (3-57) holds for a variable Z , Z is said to be "exactly divisible" by $\cos^2 \varrho$. Division by $\cos^2 \varrho$ is equivalent to multiplication by the infinite binomial series $(1 + \sin^2 \varrho + \sin^4 \varrho + \dots)$.

The transformation algorithm is

$$\left(\hat{Z}' \right)_m^{n,(s)} = \sum_{i=0}^{\lfloor \frac{m}{2} \rfloor} \hat{Z}_{m-2i}^{n,(s)} \quad (3-58)$$

⁶ $J_{\lambda, \varrho}$ is the Jacobian operator in spherical coordinates, not to be confused with the current vector $\underline{J} = (J^\lambda, J^\varrho, J^\vartheta)$.

m=0 to MAX. A necessary and sufficient condition for exact divisibility by $\cos^2 \varrho$ is

$$\sum_{i=0}^{\left(\frac{\text{MAX}}{2}\right)_T} \hat{Z}_{2i}^{n,(S)} = \sum_{i=0}^{\left(\frac{\text{MAX}-1}{2}\right)_T} \hat{Z}_{2i+1}^{n,(S)} = 0 \quad (3-59)$$

Otherwise, an infinite number of $\hat{Z}_m^{n,(S)}$ coefficients would be generated. Program checks confirmed the validity of (3-59) to 12 decimal places on the CDC-6600 computer, when transformation (3-58) was applied.

(X) Orthogonal truncation of Robert harmonics: Due to the mutual orthogonality of spherical harmonic functions over the sphere, truncation over m and n is automatically orthogonal. For Robert functions, this is true for truncation over n only. Whereas

$$\int_{\text{unit sphere}} R_m^{n,c} R_k^{l,s} dS = 0 \text{ for all } n, l, m, \text{ and } k, \text{ we have}$$

$$\int_{\sigma_s} R_m^{n,(s)} R_k^{l,(s)} dS \propto \int_{n,l} \int_{-\pi/2}^{\pi/2} \sin^{m+k} \varrho \cos^{n+l} \varrho d\varrho \neq 0$$

if $n \neq l$ and $m+k$ is even. The only operator to generate new n harmonics is bilinear multiplication. These are discarded. To make the truncation orthogonal over m:

(a) Evaluate the right side of (3-25) and the set (3-20), retaining the generated array elements for $n=0, 6$ and all m.

(b) Apply the $\hat{\mathcal{J}} \cdot \nabla_H \times$ and $\nabla_H \cdot$ operators⁷ to the set (3-20). This produces equations for the true scalars $\nabla_H^2 \psi_1^+, \nabla_H^2 \psi_3^+, \dots, \nabla_H^2 \phi_3^-$.

⁷The transformations for these operators are a combination of (3-43) (3-44) and (3-58). Exact divisibility by $\cos^2 \varrho$ was verified.

- (c) Transform the Robert representation of the right side of these equations and of (3-25) to a spherical harmonic representation, using (3-32) and (3-35). The projection of Robert functions onto $Y_m^{n,c}$ or $Y_m^{n,s}$ are retained only for $0 \leq m \leq M$, invoking the mutual orthogonality of the Y 's.
- (d) Transform the truncated spherical harmonic series back to a Robert series using (3-30) and (3-36).

The above truncation requires relatively little CPU time because it is carried out only at the very end. The actual procedure was to compute the y coefficients from (3-36) and then the A 's from (3-35) once and for all, and read them into the computer as data. The computations were performed on the CDC-6600 computer in double precision to guarantee accuracy of the first 60 bits. As a check on these coefficients, an arbitrary set of Robert coefficients was transformed without truncation to a set of spherical harmonic coefficients. Then the inverse transformation was taken. The result was the original set of coefficients. Some of the lower order transformations were hand calculated as a second check.⁸

Thirdly, the global mean of an arbitrary true scalar in the Robert representation proved to be invariant under orthogonal truncation as it should. In particular, this is true for the mean square magnetic energy, vorticity or for each term in the vorticity equation.

Incidentally, checks of the various other operators were made also. Sample arrays along with their transformations were supplied by André Robert, although for somewhat different values of m and n . Some hand-calculations and the identity transformation $(\nabla_H^2)^{-1} \{ \nabla_H^2 \}$ were likewise performed.

⁸Inadvertently, $\int_{\sigma_s} (y_{m+n}^{n,c})^2 dS = 8\pi$ rather than 4π , for $n=0$. But this does not affect the validity of the truncation technique.

Despite the $\cos^{-1}\varrho$ factor, the Robert series (3-40) for horizontal vector components has no singularities at the poles. Due to the $\cos^n \varrho$ factor in the numerator, only the $n=0$ harmonics could possibly be singular. Now the vector components are obtained by differentiation of stream functions and potentials with respect to λ and ϱ . Observing from (3-43) that the $\frac{1}{a \cos \varrho} \frac{\partial}{\partial \lambda}$ operator generates no contribution to the zonal average $\langle S \rangle$ of S ,

$$\langle S \rangle = \frac{1}{\cos \varrho} \sum_{m=0}^{M+1} \left[(1 - \delta_{m,M}) (1 - \delta_{m,M+1}) (m+1) \hat{Z}_{m+1}^{0,c} - (1 - \delta_{m,0}) (m-1) \hat{Z}_{m-1}^{0,c} \right] \frac{\sin^m \varrho}{a} \quad (3-60)$$

according to (3-44). At the poles, $\sin \varrho = \pm 1$ for all m . The series (3-60) can be decomposed into a summation over even m and over odd m there. It could be shown that each of these summations and hence the whole series for $\langle S \rangle \cos \varrho$ vanishes. Then by application of LaHospitale's rule, $\langle S \rangle = 0$ at $\varrho = \pm 90^\circ$. Likewise $\langle \frac{1}{a} \frac{\partial S}{\partial \varrho} \rangle$ is finite and the $n=1$ component of $\frac{1}{a} \frac{\partial S}{\partial \varrho}$ vanishes at the poles. More generally, no explicit boundary conditions are needed there, for either the Robert or spherical harmonic representations. Taking stream functions and potentials as the fundamental variables, the vectors derived from them behave properly at the poles.

To summarize the Robert procedure, the evaluation of the equations consists of a sequence of transformations on spectral coefficients. The operators are applied directly to the equations of section 3. Before time differentiation, each equation takes the form

$$\sum_n \sum_{m=0} \left\{ \left(\overset{(0)}{Z}_m^{\wedge n, c} - \overset{(1)}{Z}_m^{\wedge n, c} \right) \cos n\lambda + \left(\overset{(0)}{Z}_m^{\wedge n, s} - \overset{(1)}{Z}_m^{\wedge n, s} \right) \sin n\lambda \right\} \\ \cdot \cos^n \varrho \sin^m \varrho = 0 \quad (3-61)$$

The symbol (0) corresponds to either the time derivative of a prognostic spectral coefficient or a diagnostic spectral coefficient on the left side of an equation. The symbol (1) denotes summation over all terms on the right side of the equation. By the linear independence of Robert functions, the spectral equation analogue of (3-61) drops out effortlessly, i.e.,

$$\overset{(0)}{Z}_m^{\wedge n, (S)} = \overset{(1)}{Z}_m^{\wedge n, (S)}, \quad 0 \leq m \leq 4; \quad n = 0, 6 \quad (3-62)$$

In particular, each ordinary differential equation contains the time derivative of but a single spectral coefficient.

3.5. The Time Differencing Scheme.

There are 9 prognostic variables and 15 spectral coefficients per variable (including the $n=0, m=0$ coefficient). Hence a set of 135 coupled ordinary differential equations are to be solved simultaneously. The equations are integrated in time numerically.

Lilly (1965) tested various explicit finite time differencing schemes on a four component set of nonlinear hydrodynamic spectral equations. The expansion functions were elementary sines and cosines, appropriate to cartesian geometry. As to stability characteristics, the Adams-Bashforth two-step procedure ranked high, being decidedly superior to the centered difference scheme. Furthermore, of the leading contenders, it was the simplest. Incidentally, Gilman (1969) had good success with

the Adams-Bashforth scheme for a hydromagnetic dynamo problem. On these grounds, it is employed in this investigation.

The Adams-Bashforth algorithm for integrating the ordinary differential equation $dX/dt = F$ is

$$X_{j+1} = X_j + \frac{1}{2} \Delta t (3F_j - F_{j-1}) \quad (3-63)$$

Here $j=1,2,3,\dots,n,\dots$, Δt is the time step, and the subscript j denotes evaluation at time $t=j \Delta t$. For $j=0$, the single step Euler forward differencing scheme

$$X_1 = X_0 + \Delta t F_0 \quad (3-64)$$

is used. The storage requirements of the integration procedure are not very demanding, and (3-63) uses relatively little computer time compared to nonlinear multiplication. In practice, X is an array of $Z_m^{(0),n,(5)}$ coefficients.

The actual choice of Δt was governed by the phase speed of the fastest propagating wave. Of all the wave types not filtered out, internal gravity waves apparently have the edge. An estimate of their phase speed is $c_g \sim \sqrt{gD} \left(D \frac{\partial \ln \sigma_s}{\partial z} \sim 10^{-4} \right) \sim 2.6 \times 10^4$ cm/sec. Heuristic arguments based upon the magnitude of σ'_* and anticipated magnitude of the Alfvén number suggest hydromagnetic waves propagate slower. $\Delta t = \frac{1}{25} \left(\frac{2\pi}{\Omega} \right)$ was rather close to the cutoff between computationally stable and unstable solutions. Therefore, we set $\Delta t = \frac{1}{50} \left(\frac{2\pi}{\Omega} \right)$, corresponding to 50 time steps per rotation.

3.6. Sequence of Equations to be Solved.

To conclude this chapter, we outline in effect how the problem was posed.

A. Nonmagnetic case

- (i) Set $\underline{B} = 0$ to let a **nonmagnetic** flow to develop.
- (ii) Prior to $t=0$, $\psi_{v_1} = \psi_{v_3} = \phi_{v_1} = \phi_{v_3} = \sigma_2' = 0$
- (iii) At $t=0$, specify various required constants and nondimensional parameters. Then inject small (random) perturbations ($n=6$) into σ_2' .
- (iv) Solve (3-22b), i.e. set $\phi_{v_3} = -\phi_{v_1}$
- (v) Evaluate u_1, v_1, u_3, v_3, u_2 , and v_2 from (2-46a). They are initially zero.
- (vi) Compute ϵ_1^k and ϵ_3^k from (3-12a). Initially $\epsilon^k = 0$.
- (vii) Solve (3-21b) for w_2 . $w_2 = 0$ at $t=0$.
- (viii) Solve (3-26) with $\epsilon_1^M \equiv \epsilon_3^M \equiv 0$ for the (truncated) true scalar $\sigma_3 - \sigma_1$. Initially, $\nabla_H \sigma$ will be the only non-vanishing term in (3-20). After time $t = \Delta t$, rotational motions will be generated also.
- (ix) Apply the ∇_H^2 operator to $\sigma_3 - \sigma_1$.
- (x) Solve the **nonmagnetic** version of the equation set (3-20), making the substitutions (3-28a) through (3-28d).

- a. Compute each term on the right except the horizontal pressure gradient term and the horizontal viscous dissipation term.
- b. For each equation, add all the computed terms.
- c. Apply the $\hat{z} \cdot \nabla_H^*$ and $\nabla_H \cdot$ operators to (3-20), incorporating $\nabla_{(H)} \nabla_H^2 (\nabla_H^2 \psi_{v_1}), \nabla_{(H)} \nabla_H^2 (\nabla_H^2 \psi_{v_3}), \nabla_{(H)} \nabla_H^2 (\nabla_H^2 \phi_{v_1})$ and $\nabla_{(H)} \nabla_H^2 (\nabla_H^2 \phi_{v_3})$.
- d. Orthogonally truncate the spectral coefficients. Analogous to (3-62) is a set of spectral equations

$$\begin{aligned} \left(\begin{matrix} (0) \wedge n, (s) \\ \underline{z}_m \end{matrix} \right)_{j+1} &= \left(\begin{matrix} (0) \wedge n, (s) \\ \underline{z}_m \end{matrix} \right)_j + \frac{1}{2} \Delta t \\ &\bullet \left\{ 3 \left(\begin{matrix} (1) \wedge n, (s) \\ \underline{z}_m \end{matrix} \right)_j - \left(\begin{matrix} (1) \wedge n, (s) \\ \underline{z}_m \end{matrix} \right)_{j-1} \right\}, \quad j \geq 1 \quad (3-62)' \end{aligned}$$

e. The condition $\nabla_H \cdot \mathbf{V}_{H_2} = 0$ is equivalent to the initial value problem

$$\omega = \nabla_H^2 (\phi_{v_1} + \phi_{v_3}) \quad (3-65a)$$

$$\partial\omega/\partial t = 0 = \nabla_H^2 (\sigma_1 + \sigma_3) + \dots \quad (3-65b)$$

$$\omega = 0 \quad \text{at} \quad t = 0 \quad . \quad (3-65c)$$

Equation (3-65c) is satisfied by our initial conditions. Equation (3-65b) is obtained by adding the divergence equations at levels 1 and 3, and is solved for $\nabla_H^2 (\sigma_1 + \sigma_3)$. With the aid of step (ix), truncated expressions for $\nabla_H^2 \sigma_1$ and $\nabla_H^2 \sigma_3$ are obtained.

f. The spectral differential equations for $\nabla_H^2 \psi_{v_1}$, $\nabla_H^2 \psi_{v_3}$ and $\nabla_H^2 \phi_{v_1}$ are marched ahead one time step. For each of the three equations in the space domain, arrays of truncated spectral coefficients $z_m^{(1) n, (s)}$ of (3-62) are needed for time steps j and $j-1$. The redundant equation for $\nabla_H^2 \phi_{v_3}$ is discarded.

(xi) Solve the thermodynamic equation (3-25). Since σ_2' is a true scalar, the terms on the right are first evaluated, then added, and finally truncated.

(xii) Invert the Laplacians to obtain ψ_{v_1} , ψ_{v_3} , and ϕ_{v_1} at $t=(j+1)\Delta t$. p_1' and p_3' could also be retrieved, if desired. Return to step (iv) and recycle.

B. Magnetic case⁹

(i) After baroclinic disturbances and self-consistent mean flow patterns

⁹The numbering of steps in the magnetic and nonmagnetic cases corresponds as much as possible.

for specified thermal forcing profiles have developed, small magnetic perturbations are introduced into ψ_1^+ , ψ_1^- , ψ_3^+ , and ψ_3^- . These perturbations should affect ψ_m but not ψ_r . Alternatively, a small zonally symmetric magnetic field may be introduced. Resume integration.

(ii)-----

(iii) -----

(iv) Solve the equation $\phi_3^- = -(\phi_1^+ + \phi_1^- + \phi_3^+)$.

(v) From (2-46a), (2-47a), (3-1) and (3-8), evaluate u_1^+ , u_3^+ , u_1^- , u_3^- , v_1^+ , v_1^- , v_3^+ , v_3^- , u_1 , u_2 , u_3 , v_1 , v_2 , v_3 , B_1^λ , B_3^λ , B_1^ω , B_3^ω , B_{*1}^λ , B_{*3}^λ , B_{*1}^ω and B_{*3}^ω .

(vi) Compute \mathcal{E}^κ and \mathcal{E}^M from (3-12) at levels 1 and 3.

(vii) With assistance from the inverse Lundquist transformations (3-8), solve (3-21b) for w_2 , (3-24b) for B_2^z , and (3-24c) for B_4^z . Initially $B_2^z = B_4^z = 0$ since $\phi_m = \phi_{m_3} = 0$. w_2, B_2^z and B_4^z are all truncated true scalars. Next, convert B_4^z to a spherical harmonic representation. In terms of spherical harmonics, the solution to the Neumann boundary value problem for the exterior region, i.e. to equations (2-61a), (3-5b), and (2-61d) is

$$\bar{\Phi}_m = -\sum_{n=0, \delta}^M \sum_{m=0}^M (\tilde{B}_4^z)^n (a+z_4) \left(\frac{a+z_4}{r}\right)^{m+n+1} Y_{m+n}^{n, (s)} \quad (3-66)$$

Here, $(\tilde{B}_4^z)^n_{m+n}$ is the cosine (sine) spherical harmonic spectral coefficient of degree $m+n$ and rank n . After transforming $\lim_{r \rightarrow a+z_4^+} \bar{\Phi}_m$ to a Robert representation, B_4^λ and B_4^ω may be computed from (3-5c) and (3-5d).

(viii) Solve (3-26) with the magnetic terms left in for $\sigma_3 - \sigma_1$.

(ix) Compute $\nabla_H^2(\sigma_3 - \sigma_1)$.

- (x) Use the same basic procedure as in the nonmagnetic case on the eight Lundquist equations of (3-20). In step (x)-a., there are now two horizontal dissipation terms. In step (x)-c., add the horizontal dissipation terms $\nabla_{(H)}^+ \nabla_H^2 (\nabla_H^2 \psi_1^+)$, and $\nabla_{(H)}^- \nabla_H^2 (\nabla_H^2 \phi_3^-)$. In step (x)-e., $\omega = \nabla_H^2 (\phi_1^+ + \phi_3^+ + \phi_1^- + \phi_3^-)$. Equation (3-65b) is now the sum of four equations. In step (x)-f., the spectral differential equations for $\nabla_H^2 \psi_1^+$, $\nabla_H^2 \psi_1^-$, $\nabla_H^2 \psi_3^+$, $\nabla_H^2 \psi_3^-$, $\nabla_H^2 \phi_1^+$, $\nabla_H^2 \phi_1^-$ and $\nabla_H^2 \phi_3^+$ are marched ahead one time step. The redundant equation for $\nabla_H^2 \phi_3^-$ is discarded.
- (xi) Solve (3-25) for σ_2' exactly as in the nonmagnetic case.
- (xii) Invert the above Laplacians. ψ_1^+ , ψ_1^- , ψ_3^+ , ψ_3^- , ϕ_1^+ , ϕ_1^- and ϕ_3^+ are then known at the new time $(j+1)\Delta t$. Return to step (iv) and recycle.

CHAPTER IV. FORMULATION OF A "CORRECTLY TRUNCATED" ANGULAR MOMENTUM BALANCE.

4.1. Introduction.

An "angular momentum balance" is useful for describing the maintenance of model angular velocity profiles. With this motivation, we formulate the zonally averaged angular momentum equations (A.M.E.). When the truncated spectral representation is introduced, the time averaged A.M.E. do not balance prior to truncation. Also, if these equations are truncated directly, implicit boundary conditions at the poles could be violated. This effect is related to the recursion relationships for the derivatives of Legendre functions (spherical harmonics). In practice, inadequate resolution is a necessary condition for imbalance here. The implicit boundary conditions and hence a self-consistent local angular momentum balance are restored by "correct truncation". This is in accord with the method of truncation at each time step. It consists of differentiating the A.M.E., orthogonally truncating the resulting vorticity equation, and then integrating. The surface integrals of the time averaged A.M.E. do balance and the balance is invariant under "correct truncation" as shown by Robert (1970). In our low resolution model, local phase distortion due to truncation can be severe, for some terms.

4.2. The Angular Momentum Equations.

The instantaneous zonally averaged angular momentum equations at level 1 and 3 of our spherical, thin shell, two layer model are

$$\begin{aligned}
 \frac{\partial m_1}{\partial t} &= (2\mathcal{N} \sin \varphi)(a \cos \varphi \langle v_1 \rangle) + \frac{1}{a \cos \varphi} \frac{\partial}{\partial \varphi} \left(\frac{\langle B_1^\lambda \rangle \langle B_1^\varphi \rangle a \cos^2 \varphi}{4\pi \mu_0 \rho_s} \right) \\
 &\quad (1a) \qquad (2a) \\
 &+ \frac{1}{a \cos \varphi} \frac{\partial}{\partial \varphi} \left(\frac{\langle B_1^{\lambda*} B_1^{\varphi*} \rangle a \cos^2 \varphi}{4\pi \mu_0 \rho_s} \right) + \frac{a \cos \varphi}{4\pi \mu_0 \rho_s D} \langle B_2^\lambda \rangle \langle B_2^{\lambda'} \rangle \\
 &\quad (3a) \qquad (4) \\
 &+ \frac{a \cos \varphi}{4\pi \mu_0 \rho_s D} \langle B_2^{\lambda*} B_2^{\lambda'*} \rangle - \frac{1}{a \cos \varphi} \frac{\partial}{\partial \varphi} (\langle u_1 \rangle \langle v_1 \rangle a \cos^2 \varphi) \\
 &\quad (5a) \qquad (6a) \\
 &- \frac{1}{a \cos \varphi} \frac{\partial}{\partial \varphi} (\langle u_1^* v_1^* \rangle a \cos^2 \varphi) - \frac{a \cos \varphi}{D} \langle u_2^* w_2^* \rangle - \frac{a \cos \varphi}{D} \langle u_2 \rangle \langle w_2 \rangle \\
 &\quad (7a) \qquad (8) \qquad (9) \\
 &+ \mathcal{V}_{(3)} (\langle u_3 \rangle - 3 \langle u_1 \rangle) a \cos \varphi + \mathcal{V}_{(4)} \Delta^\lambda (\langle u_1 \rangle, 0) a \cos \varphi \quad (4-1) \\
 &\quad (10a) \qquad (11a)
 \end{aligned}$$

$$\begin{aligned}
 \frac{\partial m_3}{\partial t} &= (2\mathcal{N} \sin \varphi)(a \cos \varphi \langle v_3 \rangle) + \frac{1}{a \cos \varphi} \frac{\partial}{\partial \varphi} \left(\frac{\langle B_3^\lambda \rangle \langle B_3^\varphi \rangle a \cos^2 \varphi}{4\pi \mu_0 \rho_s} \right) \\
 &\quad (1b) \qquad (2b) \\
 &+ \frac{1}{a \cos \varphi} \frac{\partial}{\partial \varphi} \left(\frac{\langle B_3^{\lambda*} B_3^{\varphi*} \rangle a \cos^2 \varphi}{4\pi \mu_0 \rho_s} \right) - \frac{a \cos \varphi}{4\pi \mu_0 \rho_s D} \langle B_2^\lambda \rangle \langle B_2^{\lambda'} \rangle \\
 &\quad (3b) \qquad (4) \\
 &- \frac{a \cos \varphi}{4\pi \mu_0 \rho_s D} \langle B_2^{\lambda*} B_2^{\lambda'*} \rangle + \frac{a \cos \varphi}{4\pi \mu_0 \rho_s D} \langle B_4^{\lambda*} B_4^{\lambda'*} \rangle \\
 &\quad (5a) \qquad (5b) \\
 &- \frac{1}{a \cos \varphi} \frac{\partial}{\partial \varphi} (\langle u_3 \rangle \langle v_3 \rangle a \cos^2 \varphi) - \frac{1}{a \cos \varphi} \frac{\partial}{\partial \varphi} (\langle u_3^* v_3^* \rangle a \cos^2 \varphi) \\
 &\quad (6b) \qquad (7b) \\
 &+ \frac{a \cos \varphi}{D} \langle u_2^* w_2^* \rangle + \frac{a \cos \varphi}{D} \langle u_2 \rangle \langle w_2 \rangle \\
 &\quad (8) \qquad (9) \\
 &+ \mathcal{V}_{(3)} (\langle u_1 \rangle - \langle u_3 \rangle) a \cos \varphi + \mathcal{V}_{(4)} \Delta^\lambda (\langle u_3 \rangle, 0) a \cos \varphi \quad (4-2) \\
 &\quad (10b) \qquad (11b)
 \end{aligned}$$

Here the symbol $\langle \rangle$ denotes the zonal average $\frac{1}{2\pi} \int_0^{2\pi} () d\lambda$

while the asterisk * denotes a departure from the zonal average.

$\mathcal{M}_i = \langle u_i \rangle a \cos \varphi$ is the zonally averaged angular momentum at level i . To obtain equations (4-1) and (4-2), we first multiply the two layer model analogue of equation (2-37a) by $a \cos \varphi$ and take the zonal average. We then differentiate by parts, utilizing the top and bottom boundary conditions in the usual manner.

All terms in equations (4-1) and (4-2) have been labeled. The same label was assigned to terms which appear in both equations, but with opposite signs. Those terms cancel out in the vertically averaged angular momentum balance

$$\begin{aligned} \frac{\partial \mathcal{M}_2}{\partial t} = & \frac{1}{a \cos \varphi} \frac{\partial}{\partial \varphi} \left[\frac{(\langle B_1^\lambda \rangle \langle B_1^\varphi \rangle + \langle B_3^\lambda \rangle \langle B_3^\varphi \rangle) a \cos^2 \varphi}{8\pi \mu_0 \rho_5} \right] \\ & + \frac{1}{a \cos \varphi} \frac{\partial}{\partial \varphi} \left[\frac{\langle B_1^{\lambda*} B_1^{\varphi*} + B_3^{\lambda*} B_3^{\varphi*} \rangle a \cos^2 \varphi}{8\pi \mu_0 \rho_5} \right] \\ & + \frac{a \cos \varphi}{8\pi \mu_0 \rho_5 D} \langle B_4^{\lambda*} B_4^{\varphi*} \rangle - \frac{1}{2a \cos \varphi} \frac{\partial}{\partial \varphi} \left[(\langle u_1 \rangle \langle v_1 \rangle + \langle u_3 \rangle \langle v_3 \rangle) a \cos^2 \varphi \right] \\ & - \frac{1}{2a \cos \varphi} \frac{\partial}{\partial \varphi} \left[\langle u_1^* v_1^* + u_3^* v_3^* \rangle a \cos^2 \varphi \right] - V_{(2)} \langle u_i \rangle a \cos \varphi \\ & + V_{(H)} \left[\nabla_H^2 (\langle u_2 \rangle a \cos \varphi) - 2 \sin \varphi \nabla_H^2 \langle \psi_{v_2} \rangle \right] \quad (4-3) \end{aligned}$$

for $\mathcal{M}_2 = (\mathcal{M}_1 + \mathcal{M}_3) / 2$.

The various terms in equations (4-1) and (4-2) are summarized in Table 4.1. Most of the nonmagnetic terms are quite familiar to meteorologists. For example, at midlatitudes in the terrestrial atmosphere, a sizable percentage of the net angular momentum transport

Table 4.1 Catalogue of Terms in the Angular Momentum Balance Equations

<u>Category</u>	<u>Subclass</u>	<u>Label</u>
A. Coriolis Torque		(1a), (1b)
B. Maxwell stresses		
	horizontal, axisymmetric	(2a), (2b)
	horizontal, eddy ¹	(3a), (3b)
	vertical, axisymmetric	(4)
	vertical, eddy	(5a), (5b)
C. Reynolds stresses		
	horizontal, axisymmetric	(6a), (6b)
	horizontal, eddy	(7a), (7b)
	vertical, eddy	(8)
	vertical, axisymmetric	(9)
D. Frictional torque		
	vertical coupling	(10a), (10b)
	horizontal coupling	(11a), (11b)

¹The notation "eddy" indicates that the zonal average is taken of a product of asymmetric factors.

across latitude circles is accomplished by horizontal eddy motion, i.e. by term (7b). Incidentally, the vertically averaged coriolis torque vanishes because $\langle v_1 \rangle = -\langle v_3 \rangle$.

There are two possible sources or sinks of angular momentum for the fluid region $0 \leq z \leq z_4$. The first is a net frictional torque T_F per unit mass equal to 1/2 the sum of terms (10a), (10b), (11a), and (11b). Thus

$$T_F = \frac{1}{2} \int_{-\pi/2}^{\pi/2} \left\{ v_{(3)} (\langle u_3 \rangle - 3\langle u_1 \rangle) + v_{(3)} (\langle u_1 \rangle - \langle u_3 \rangle) + v_{(H)} \Delta^{\wedge}(\langle u_1 \rangle, 0) + v_{(H)} \Delta^{\wedge}(\langle u_3 \rangle, 0) \right\} a^3 \cos^2 \varphi d\varphi \quad (4-4)$$

where $v_{(H)}$ has the same units as $v = D^2 v_{(3)} / 4$. With the help of equation (3-39),

$$\Delta^{\wedge}(\langle u \rangle, 0) = \Delta^{\wedge}(\langle u \rangle, \langle v \rangle) = \frac{1}{a^2} \frac{\partial}{\partial \varphi} \left[\frac{1}{\cos \varphi} \frac{\partial}{\partial \varphi} (\langle u \rangle \cos \varphi) \right] \quad (4-5)$$

Then substituting equation (4-5) into (4-4) and integrating the last two terms by parts,

$$T_F = -\frac{4v}{D^2} \int_{-\pi/2}^{\pi/2} a^2 (\langle u_1 \rangle a \cos \varphi) \cos \varphi d\varphi - \frac{v_{(H)}}{a^2} \int_{-\pi/2}^{\pi/2} a^2 (\langle u_1 \rangle a \cos \varphi) \cos \varphi d\varphi - \frac{v_{(H)}}{a^2} \int_{-\pi/2}^{\pi/2} a^2 (\langle u_3 \rangle a \cos \varphi) \cos \varphi d\varphi \quad (4-6)$$

The first term on the right side of (4-6) is usually associated with the net external torque (per unit mass) exerted by the rigidly rotating lower

boundary at $z=0$ upon the fluid region $z > 0$. The last two terms are due to the spherical (thin shell) geometry and resemble the first in form. They vanish only if the horizontal dissipation is neglected. Of course for the isotropic case ($v_{(H)} = V$), the second term is clearly negligible compared to the first, whereas the third term is small provided

$|\int \langle u_3 \rangle \cos^2 \varphi d\varphi / \int \langle u_1 \rangle \cos^2 \varphi d\varphi| \ll a^2/D^2$. For either the highly anisotropic case ($v_{(H)} \gg V$), or the deep atmosphere case ($D^2 \sim a^2$), T_F could conceivably be the small difference of larger terms. The long term mean of T_F should be small unless the fluid layer is systematically slowing down or speeding up.

The second possible source or sink of angular momentum for the fluid region $0 \leq z \leq z_4$ is the eddy Maxwell stress term (5b), i.e.

$$T_B(z) = (4\pi\mu_0\rho_s)^{-1} \langle B_4^\lambda B_4^{z*} \rangle a \cos \varphi \quad (4-7)$$

Formally, this magnetic braking term is not spurious since an analogous term would occur in a model with continuous vertical variation. If the vertical integration were extended to the nonconducting region $z > z_4$, then $\lim_{z \rightarrow \infty} T_B = 0$ due to boundary condition (2-6ld).

The axisymmetric counterpart to (4-7) vanishes because

$\langle B_4^\lambda \rangle = 0$. We also discovered that T_B was negligible in the numerical computations even though neither $B_4^{\lambda*}$ nor B_4^{z*} vanished. It turns out that $B_4^{z*} \ll B_2^{z*}$ in the production runs. Also, $B^\lambda \sim \theta(B^z)$ in the region $z \geq z_4$ which causes another reduction by a factor of at least $\delta \sim D/L$. Furthermore, we note that no magnetic braking

if $B_y^2 = 0$ as at a perfectly conducting boundary. Finally, the motion in the nonconducting region $z > z_y$ is not affected by local magnetic fields there, since $\underline{J} \equiv 0$.

4.3. Inconsistencies in the Untruncated Angular Momentum Balance.

To reiterate, in the course of the original numerical integrations of the Lundquist equations, various hydromagnetic variables were written on a history tape once every rotation, i.e. every 50th time step. From this information, we could reconstruct equations (4-1) and (4-2) at time $t = t_0 + j\Delta t$, $j = 0, 1, 2, \dots, J-1$. The arithmetic average of these equations formally yields the time averaged, zonally averaged angular momentum balance.

According to the Adams-Bashforth finite difference scheme, the arithmetic average of the differential equation $dX^{(m)}/dt = \sum_{k=1} F^{(k,m)}$ over the time interval $t_0 \leq t \leq t_0 + (J-1)\Delta t$ is approximated by

$$X_J^{(m)} = X_0^{(m)} + J\Delta t \sum_{k=1} \overline{F^{(k,m)}} + .5\Delta t \sum_{k=1} \left(F_{J-1}^{(k,m)} - F_{-1}^{(k,m)} \right) \quad (4-8a)$$

where $\overline{F^{(k,m)}}$ is the arithmetic time average $\frac{1}{J} \sum_{j=0}^{J-1} F_j^{(k,m)}$. The quantity $X^{(m)}$ could represent the mth spectral coefficient of the angular momentum $\eta = \langle u \rangle a \cdot \cos \vartheta$. Similarly, $F^{(k,m)}$ could represent the mth spectral coefficient of the kth term on the right hand side of equations (4-1) or (4-2).

For a typical "production run", $J \sim 35000$. Thus the edge effects in (4-8a) can be neglected, i.e.

$$X_J^{(m)} = X_0^{(m)} + J\Delta t \sum_{k=1} \overline{F^{(k,m)}} \quad (4-8b)$$

Generally speaking, no drastic long term trend would be expected for \mathcal{M} . Direct computations confirmed that $\mathcal{M}_m \sim O(\mathcal{M}_0)$. Consistency requires that

$$\left| \frac{\sum_{k=1} \overline{F^{(k,m)}}}{\sum_{k=1} F_j^{(k,m)}} \right| \ll 1, \quad (4-9)$$

for a typical value of $F_j^{(k,m)}$. But our computations failed to satisfy this inequality for the untruncated equations. In the present usage, untruncated means that the forbidden harmonics generated by products like $\langle u \rangle \langle v \rangle$ or $\langle B^{\lambda*} B^{\varphi*} \rangle$ were not discarded. Of course the history tape data, i.e. $\langle u \rangle, \langle v \rangle, B^{\lambda*}, B^{\varphi*}$, etc. that went into the above products were of truncated form.

Programming errors and roundoff errors were quickly ruled out as causes of the inconsistency. Also, our estimations of the $\overline{F^{(k,m)}}$ coefficients were probably not very biased because J is large and the relevant characteristic periods are longer than one rotation.

4.4. Analysis of the "Correctly Truncated" Angular Momentum Balance.

The above inconsistency disappeared when the truncation procedure used for the original numerical integrations was in effect adopted here. First, the $\frac{1}{a \cos \vartheta} \frac{\partial}{\partial \vartheta}$ differential operator was applied to an angular momentum equation, but term by term. Second, the resulting vorticity equation was orthogonally truncated term by term. Third, the $\int_{-\pi/2}^{\pi/2} (\) \cos \vartheta d\vartheta$ operator was applied to the truncated vorticity equation to obtain a "correctly truncated" angular momentum balance. Our computations for the "correctly truncated" angular

momentum balance provided an indirect check on the Lundquist transformations.² Further numerical and analytical investigation revealed that the $\frac{1}{a \cos \vartheta} \frac{\partial}{\partial \vartheta}$ and orthogonal truncation operators are not commutative on the sphere.

We shall now analyze the truncation process. The various terms in the time averaged balance at levels 1 or 3 were evaluated in the Robert representation. Symbolically, the net angular momentum balance is given by

$$\frac{m_J - m_0}{J \Delta t} = \sum_{k=1}^{\infty} \left(\sum_{m=0}^{M(k)} \overline{F^{(k,m)}} \sin^m \vartheta \right), \quad J \gg 1 \quad (4-10)$$

Here $M(k) \leq 2l$ for all k , while m_j is the angular momentum in the space domain at time $t = t_0 + j \Delta t$.

For the present analysis, the right hand side of equation (4-10) is rewritten in equivalent spherical harmonic representation. Accordingly, each array $\overline{F^{(k,m)}}$, $m = 0, 1, \dots, M(k)$ of Robert spectral coefficients is transformed into an array $\overline{S^{(k,m)}}$, $m = 0, 1, \dots, M(k)$ of spherical harmonic coefficients. Without loss of generality, we set the radius $a=1$, $M(k)=2l$ for all k , and $\overline{S^{(k_R, m)}} = S_m$ for one of the values k_R of k . Similarly, the orthogonal but unnormalized Legendre polynomials P_m found in Abramowitz and Stegun (1965) may be used. These

²We also numerically integrated the standard hydromagnetic equations for a few rotations. The results agreed to several decimal places with those obtained by the Lundquist transformation method.

have the desirable property of being +1 or -1 at the poles, just like $\sin^m \varphi$. In the spherical harmonic representation,

$$\frac{m_J - m_0}{J \Delta t} = \sum_{m=0}^{2l} S_m P_m(\varphi) + \dots, \quad (J \gg 1) \quad (4-11)$$

Now there are two constraints on the $F^{(k,m)}$ and on the S_m coefficients as noted by Robert (1970), which hold even in the instantaneous case $J=1$. More specifically,

$$\sum_{m=0}^{10} \overline{F^{(k,2m)}} = 0 \quad (4-12a)$$

$$\sum_{m=0}^{10} \overline{F^{(k,2m+1)}} = 0 \quad (4-12b)$$

for all k , since each term in equations (4-1) and (4-2) vanishes together with $\langle u \rangle$, $\langle v \rangle$, $\langle B^A \rangle$, and $\langle B^W \rangle$ at the poles. In turn, the constraints

$$S_0 + S_2 + S_4 + S_6 + \dots + S_{20} = 0 \quad (4-13a)$$

$$S_1 + S_3 + S_5 + S_7 + \dots + S_{21} = 0 \quad (4-13b)$$

may be inferred from (4-12). Incidentally, if the P_m are normalized Legendre functions, $P_m(\varphi = \pi/2) \cdot S_m$ replaces S_m in equations (4-13a) and (4-13b). The actual numerical computations satisfied the constraints (4-12).

Differentiating equation (4-11) yields the net rate of change of zonally averaged vorticity, i.e.

$$\frac{I_J - I_0}{J \Delta t} = -\frac{1}{a \cos \varrho} \frac{\partial}{\partial \varrho} \left(\frac{m_J - m_0}{J \Delta t} \right)$$

$$= -\sum_{m=0}^{21} S_m \left(\frac{1}{\cos \varrho} \frac{dP_m}{d\varrho} \right) + \dots = \sum_{m=0}^{20} T_m P_m + \dots, (J \gg 1). \quad (4-14)$$

The $\frac{1}{\cos \varrho} \frac{dP_m}{d\varrho}$ polynomials have been expressed in terms of the P_m polynomials in Table 4.2. With the aid of this table, the first set of equalities in (4-15) are obtained below. Robert (1970) obtained the second set of equalities by invoking the constraints (4-13a) and (4-13b). They help to further clarify the effects of truncation upon the angular momentum balance. Also, equation (4-16) below represents the orthogonal truncation of equation (4-14). So

$$T_0 = -(S_1 + S_3 + S_5 + \dots + S_{21}) = 0 \quad (4-15a)$$

$$T_1 = -3(S_2 + S_4 + S_6 + \dots + S_{20}) = 3S_0 \quad (4-15b)$$

$$T_2 = -5(S_3 + S_5 + \dots + S_{21}) = 5S_1 \quad (4-15c)$$

$$T_3 = -7(S_4 + S_6 + \dots + S_{20}) = 7(S_0 + S_2) \quad (4-15d)$$

$$T_4 = -9(S_5 + \dots + S_{21}) = 9(S_1 + S_3) \quad (4-15e)$$

$$T_m = 0, \quad 5 \leq m \leq 21 \quad (4-16)$$

Table 4.2 Useful Properties of Some Low Order Legendre Polynomials³

$$P_0 = 1$$

$$P_1 = \sin \varphi$$

$$P_2 = (3\sin^2 \varphi - 1)/2$$

$$P_3 = (5\sin^3 \varphi - 3\sin \varphi)/2$$

$$P_4 = (35\sin^4 \varphi - 30\sin^2 \varphi + 3)/8$$

$$P_5 = (63\sin^5 \varphi - 70\sin^3 \varphi + 15\sin \varphi)/8$$

$$P_6 = (231\sin^6 \varphi - 315\sin^4 \varphi + 105\sin^2 \varphi - 5)/16$$

$$1 = P_0$$

$$\sin \varphi = P_1$$

$$\sin^2 \varphi = (P_0 + 2P_2)/3$$

$$\sin^3 \varphi = (3P_1 + 2P_3)/5$$

$$\sin^4 \varphi = (8P_4 + 20P_2 + 7P_0)/35$$

$$\sin^5 \varphi = (8P_5 + 28P_3 + 27P_1)/63$$

$$\sin^6 \varphi = (33P_6 + 110P_4 + 72P_2 + 16P_0)/231$$

³Based upon material in Abramowitz and Stegun (1965), p. 798

$$\frac{1}{\cos u} \frac{dP_0}{du} = 0$$

$$\frac{1}{\cos u} \frac{dP_1}{du} = P_0$$

$$\frac{1}{\cos u} \frac{dP_2}{du} = 3P_1$$

$$\frac{1}{\cos u} \frac{dP_3}{du} = P_0 + 5P_2$$

$$\frac{1}{\cos u} \frac{dP_4}{du} = 3P_1 + 7P_3$$

$$\frac{1}{\cos u} \frac{dP_5}{du} = P_0 + 5P_2 + 9P_4$$

$$\frac{1}{\cos u} \frac{dP_6}{du} = 3P_1 + 7P_3 + 11P_5$$

$$\frac{1}{\cos u} \frac{dP_m}{du} = \frac{1}{\cos u} \frac{dP_{m-2}}{du} + (2m-1) P_{m-1}, \quad m \geq 2$$

$$\int_{-\pi/2}^{\pi/2} P_0 \cos u \, du = P_1 + P_0$$

$$\int_{-\pi/2}^{\pi/2} P_1 \cos u \, du = (P_2 - P_0) / 3$$

$$\int_{-\pi/2}^{\pi/2} P_2 \cos u \, du = (P_3 - P_1) / 5$$

$$\int_{-\pi/2}^{\pi/2} P_3 \cos u \, du = (P_4 - P_2) / 7$$

$$\int_{-\pi/2}^{\pi/2} P_4 \cos u \, du = (P_5 - P_3) / 9$$

$$\int_{-\pi/2}^{\pi/2} P_5 \cos u \, du = (P_6 - P_4) / 11$$

$$\int_{-\pi/2}^{\pi/2} P_m \cos u \, du = (P_{m+1} - P_{m-1}) / (2m+1), \quad m \geq 1$$

$$\int_{-\pi/2}^{\pi/2} P_m \cos u \, du = \begin{cases} 2, & m=0 \\ 0, & m \geq 1 \end{cases}$$

We can integrate (4-15) and (4-16) to obtain the net rate of change $(^{(\tau)}m_J - ^{(\tau)}m_0) / J \Delta t$ of the "correctly truncated" angular momentum balance. A boundary condition is needed to determine the constant of integration. We require that no term in the truncated angular momentum balance generates any angular momentum at $\varrho = -\pi/2$ (or $\varrho = +\pi/2$). In effect, this restores a constraint previously satisfied by the truncated angular momentum equations. Mathematically,

$$\begin{aligned} \frac{^{(\tau)}m_J - ^{(\tau)}m_0}{J \Delta t} &= - \int \frac{(f_J - f_0)}{J \Delta t} \cos \varrho d\varrho = - \sum_{m=0}^4 T_m \int_{-\pi/2}^{\varrho} P_m \cos \varrho d\varrho + \dots \\ &= \sum_{m=0}^5 ^{(\tau)}S_m P_m + \dots, \quad (J \gg 1) \end{aligned} \quad (4-17)$$

Obtaining the $\int_{-\pi/2}^{\pi/2} P_m \cos \varrho d\varrho$ integrals from Table 4.2 and utilizing equations (4-15) and (4-16), the "correctly truncated" $^{(\tau)}S_m$ coefficients are given by

$$^{(\tau)}S_m = S_m, \quad 0 \leq m \leq 3 \quad (4-18a)$$

$$^{(\tau)}S_4 = -(S_0 + S_2) \quad (4-18b)$$

$$^{(\tau)}S_5 = -(S_1 + S_3) \quad (4-18c)$$

$$^{(\tau)}S_m = 0, \quad 6 \leq m \leq 21 \quad (4-18d)$$

In contrast, if the angular momentum equations are truncated directly, the resulting $^{(\tau)}S'_m$ coefficients are

$$^{(\tau)}S'_m = S_m, \quad 0 \leq m \leq 5 \quad (4-19a)$$

$${}^{(T)}S_m' = 0, \quad 6 \leq m \leq 21 \quad (4-19b)$$

Clearly ${}^{(T)}S_4 \neq {}^{(T)}S_4'$ and ${}^{(T)}S_5 \neq {}^{(T)}S_5'$ in general.

This means that the linear operations of differentiation and orthogonal truncation on spherical harmonics (Legendre polynomials) are not necessarily commutative. The recursion relationship

$$\frac{1}{\cos \vartheta} \frac{dP_m}{d\vartheta} = \frac{1}{\cos \vartheta} \frac{dP_{m-2}}{d\vartheta} + (2m-1)P_{m-1}, \quad m \geq 2$$

of Table 4.2 is responsible.

Conversely, differentiation and nonorthogonal truncation of the zonally averaged angular momentum equations would be commutative, since $\frac{1}{\cos \vartheta} \frac{dR_m^0}{d\vartheta}$ is a function of only R_{m-1}^0 and m , for $m \geq 1$. However nonorthogonal truncation is undesirable on other grounds as suggested in Chapter III.

Equations (4-18b) and (4-18c) have an interesting interpretation. Now each nonlinear term in equations (4-1) and (4-2) involves a factor which vanishes at the poles. Hence the untruncated nonlinear products also vanish there, as is reflected by the constraints (4-13a) and (4-13b). In essence, equations (4-18b) and (4-18c) are the analogous constraints for the "correctly truncated" angular momentum balance. Physically, they enable the "correctly truncated" nonlinear products to vanish at the poles. In return, up to two of the retained harmonics are modified. Conversely, the directly truncated nonlinear products do not automatically satisfy the correct boundary conditions at the poles.

The above results could be generalized of course for higher resolution models. For example, if all harmonics are discarded for $m > M$,

$$(T) \quad S_m = S_m, \quad 0 \leq m \leq M-2 \quad (4-20a)$$

$$(T) \quad S_{M-1} = -(S_{M-3} + S_{M-5} + \dots + S_0), \quad (M \text{ odd}) \quad (4-20b)$$

$$(T) \quad S_M = -(S_{M-2} + S_{M-4} + \dots + S_1), \quad (M \text{ odd}) \quad (4-20c)$$

$$(T) \quad S_M = 0, \quad m > M \quad (4-20d)$$

The constraints (4-20b) and (4-20c) do not uniquely determine the retained $(T) S_m$ harmonics unless $M \leq 3$, and if $M = 0$ or $M = 1$, only trivial solutions are possible.

For our model, there is considerable distortion of the S_4 and S_5 harmonics. This affects all the Robert harmonics $F^{(k_R, m)}$ for $m \leq 5$ but $\sum_{m=0}^2 F^{(k_R, m)} = \sum_{m=0}^2 F^{(k_R, 2m+1)} = 0$, i.e. they satisfy the correct boundary conditions at the poles.

As an example, consider the distortion of the time averaged coriolis torque $f \langle \overline{v_3} \rangle$, as opposed to $\langle \overline{v_3} \rangle$ itself, caused by the "correct truncation" process. This term appears in equation (4-2) because the motions are not strictly horizontally nondivergent. Multiplication of $\langle \overline{v_3} \rangle$ by $f = 2\Omega \sin \varrho$ generates an S_6 harmonic. Thus truncation is necessary⁴ for only the even harmonics. But in addition to discarding S_6 , S_4 is replaced by $-(S_0 + S_2)$. The constraint $S_1 + S_3 + S_5 = 0$ remains

⁴ Equivalently, in the vorticity equation, the terms $2\Omega a^{-2} \cos \varrho \partial \Phi_{v_3} / \partial \varrho$ and $2\Omega \sin \varrho \nabla_H^2 \Phi_{v_3}$ would require truncation unlike $2\Omega a^{-2} \partial \Psi_v / \partial \lambda$.

in tact.

Both the untruncated and "correctly truncated" forms of $f \langle \overline{v_3} \rangle$ are plotted vs. latitude for the two long production runs in figures 4.1. and 4.2, respectively. The discrepancies between the two forms could arise from the low order spectral resolution. The phase distortion in latitude caused by truncation is worse in Fig. 4.2 than in Fig. 4.1. Observe that $f \langle \overline{v_3} \rangle$ attains a relative minimum (zero) in Fig. 4.2 at the equator if untruncated, but a relative maximum there if truncated. That the P_4 harmonic contributes to the thermal forcing profile for Fig. 4.2 is not particularly desirable since P_4 is the highest retained even parity mode. In contrast, the highest degree harmonic, i.e. P_2 in the thermal forcing profile for Fig. 4.1 is at only half the resolution limit. Now the run corresponding to Fig. 4.2 has a positive equatorial jet at level 4 (or 3) as depicted in Fig. 6.4a. However, it is apparently being maintained by a spurious equatorial convergence of angular momentum associated with the truncated $f \langle \overline{v_3} \rangle$ term in Fig. 4.2b. The situation is better for the other run. Incidentally, the coriolis torque does not affect the vertically averaged angular momentum m_2 .

Although the "correctly truncated" angular momentum balance is locally distorted, the surface integral of the angular momentum balance at any level is not affected by orthogonal truncation. More specifically, application of the last integral formula in Table 4.2 yields the result

$$\int_{-\pi/2}^{\pi/2} \partial m / \partial t \cos \omega d\omega = \int_{-\pi/2}^{\pi/2} \partial [{}^{(T)}m] / \partial t \cos \omega d\omega = 2 S_0 + \dots \quad (4-21)$$

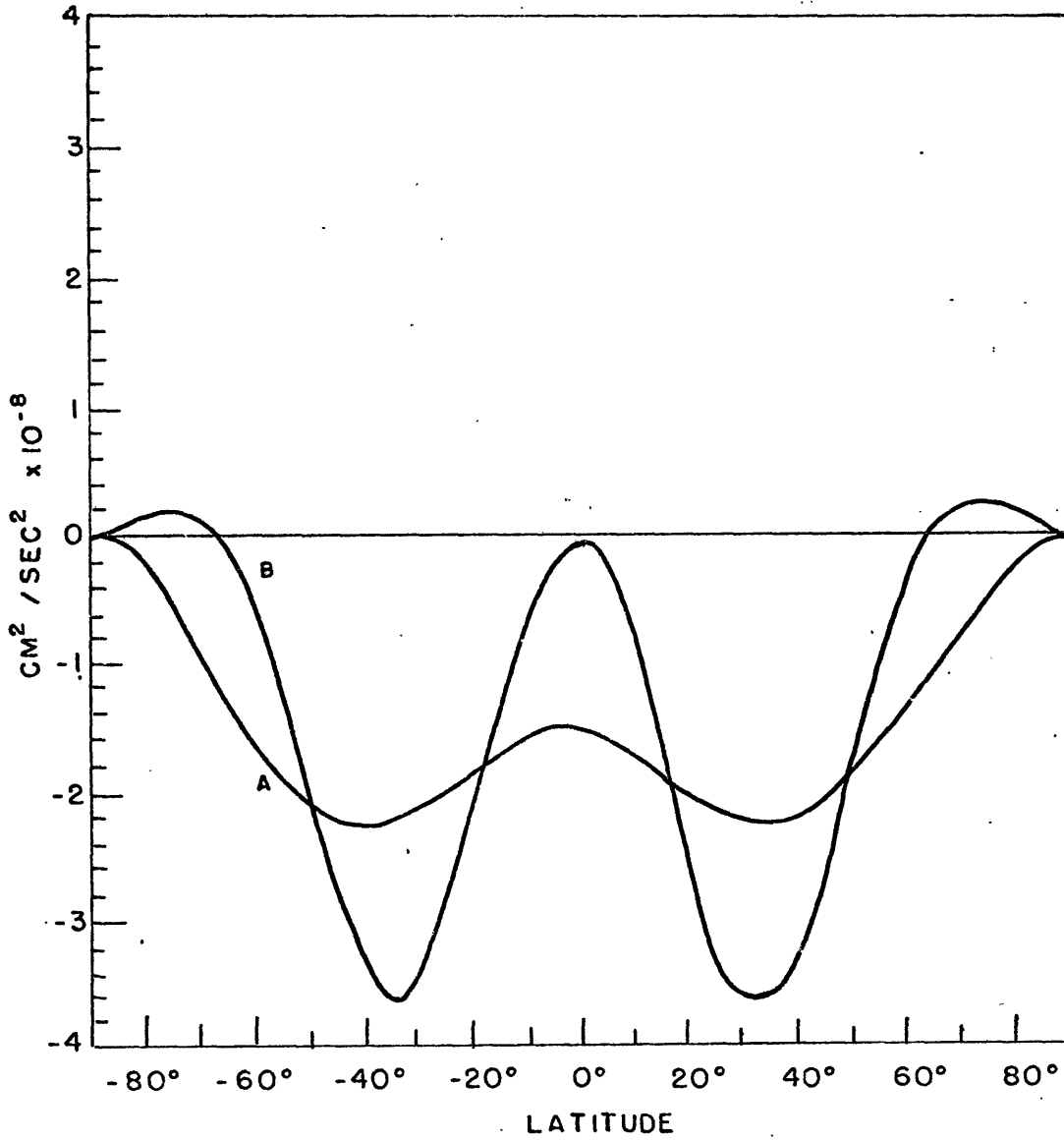


Figure 4.1. Effect of truncation on coriolis torque for P.R. 2.
A-"correctly truncated" coriolis torque.
B-untruncated coriolis torque.

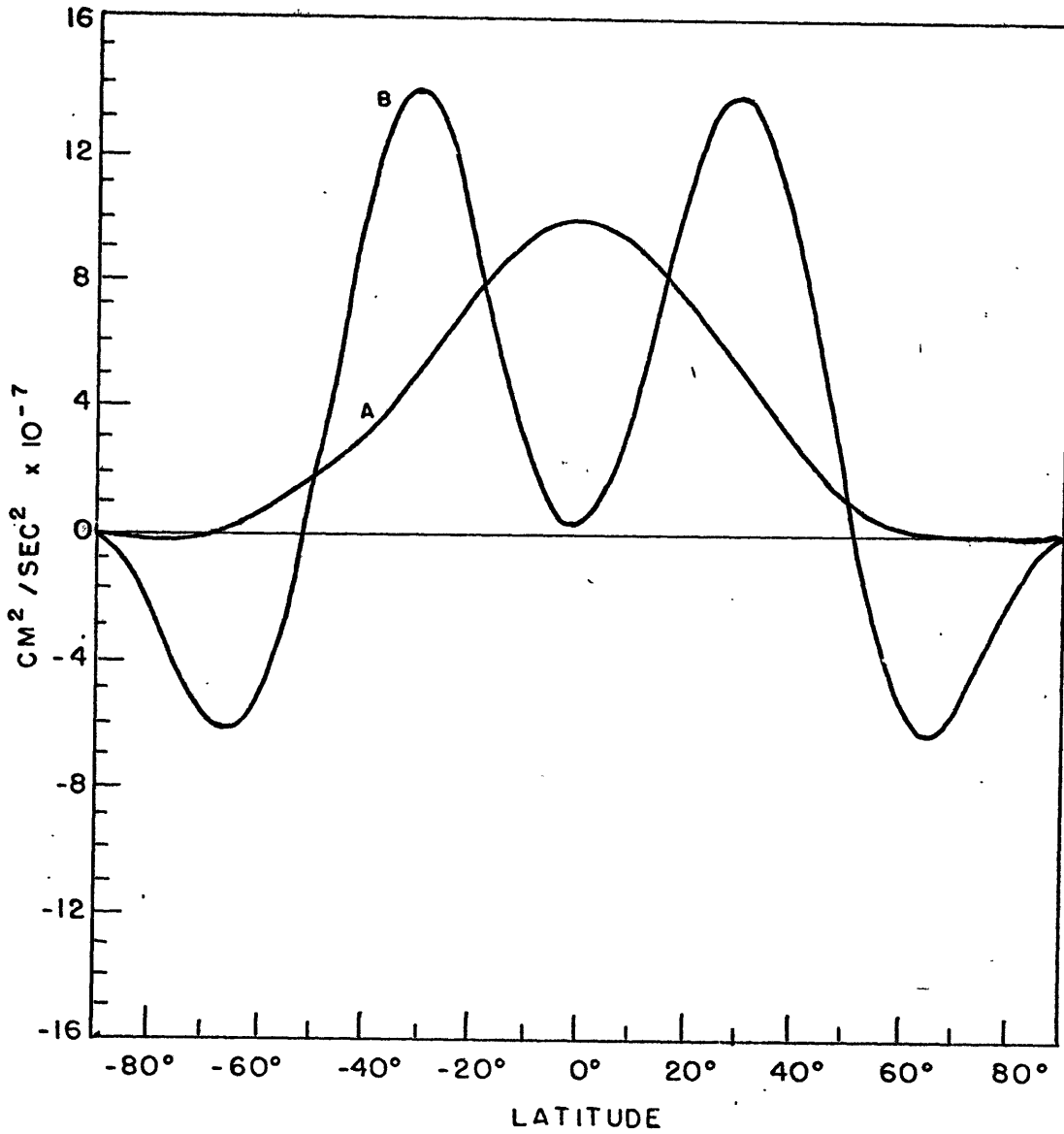


Fig. 4.2. Effect of truncation on coriolis torque for P.R. 1.
A-"correctly truncated" coriolis torque.
B-untruncated coriolis torque.

obtained by Robert (1970). Equation (4-21) states that the untruncated as well as the "correctly truncated" integrated angular momentum balances should be self-consistent, and our numerical computations have confirmed this.

But a self-consistent untruncated angular momentum balance for each spectral harmonic would exist and coincide with the "correctly truncated" and directly truncated balances, only if each $F^{(k,m)}$ or $S^{(k,m)}$ coefficient vanished for $m > M$ ($M = 5$ for our model). It would certainly be desirable to show that the truncation has no significant time averaged effect upon the model's large scale angular momentum balance. Our model resolution was too low to expect this. A consistency check of the untruncated angular momentum balance for higher resolution spherical harmonic models would be worthwhile.

Another constraint might be more easily satisfied by higher resolution models. This is that the sums of even and odd discarded coefficients, e.g. $S_{M+1} + S_{M+3} + \dots$ and $S_{M+2} + S_{M+4} + \dots$ would be smaller than typical individual discarded coefficients. Then S_{M-1} and S_M would approximately satisfy the same constraints, i.e. equations (4-20b) and (4-20c) respectively, as ${}^{(T)}S_{M-1}$ and ${}^{(T)}S_M$. Mathematically, truncation and differentiation would be quasi-commutative. Physically, direct truncation would not significantly upset the boundary conditions at the poles, and "correct truncation" would not significantly distort the retained harmonics.

It is interesting to consider the consequences of setting $M = 6$ instead of $M = 5$, on the "correctly truncated" coriolis torque.

One would discard S_7 , set $S_5 = -(S_1 + S_3)$ and leave the other modes alone. But since $f\langle \overline{v}_3 \rangle$ is approximately an even function of latitude, truncation would barely distort the $f\langle \overline{v}_3 \rangle$ profile. Meanwhile, $f\langle \overline{u}_3 \rangle$ is approximately an odd function. Consequently, $f\langle \overline{u}_3 \rangle$ and hence $\langle \overline{v}_3 \rangle$ itself could be as distorted if not somewhat more so than previously. We did not conduct such an experiment however.

CHAPTER V. FORMULATION OF THE ENERGY BALANCE

It is customary to formulate energy balances for general circulation models. An energy balance serves two useful functions. First its form reveals whether energetic consistency has been achieved in the sense of Lorenz (1960b). Energetic consistency is a desirable property. If the model contains spurious energy sources or sinks, modifications should perhaps be made to eliminate them. Second, an energy balance is another tool for interpreting the model results. In fact, numerous observational studies of the energetics of the earth's atmosphere have been carried out.

An energy balance can also be formulated for an hydromagnetic model. This was done, for example, by Starr and Gilman (1966) in cartesian geometry for a very general set of nonhydrostatic primitive hydromagnetic equations. The energetics for Gilman's (1967) linearized, magnetic model were much simpler. Finally, as previously mentioned, Gilman (1968,1969) verified that his nonlinear numerical dynamo model was energetically consistent, provided the kinetic and magnetic energy were suitably defined. The energy balance for our model most closely resembles that of Starr and Gilman (1966) in form. One simplification is that we assume a vertical magnetohydrostatic balance instead of nonhydrostatic conditions. Conversely, the spherical geometry of our model introduces complications.

The two layer model contains several forms of energy. The kinetic energy is split up into the contributions $\langle K^2 \rangle$ from the

axisymmetric zonal flow, $\langle KM \rangle$ from the axisymmetric meridional flow, and $\langle EKE \rangle$ from the eddy horizontal flow. Thus

$$\langle KZ \rangle = \rho_s D \int_{\sigma_s} \frac{(\langle u_1 \rangle^2 + \langle u_3 \rangle^2)}{2} dS \quad (5-1a)$$

$$\langle KM \rangle = \rho_s D \int_{\sigma_s} \frac{(\langle v_1 \rangle^2 + \langle v_3 \rangle^2)}{2} dS = 2 \rho_s D \int_{\sigma_s} \frac{\langle v_3 \rangle^2}{2} dS \quad (5-1b)$$

$$\langle EKE \rangle = \rho_s D \int_{\sigma_s} \frac{(\langle u_1^{*2} + v_1^{*2} \rangle + \langle u_3^{*2} + v_3^{*2} \rangle)}{2} dS \quad (5-1c)$$

The bracket $\langle \rangle$ still denotes the longitudinal average $(2\pi)^{-1} \int_0^{2\pi} (\) d\lambda$ of a quantity and $*$ the departure from that average. Since the integrands are all independent of latitude, the surface integral $\int_{\sigma_s} dS$ is equivalent to $(2\pi)^{-1} \int_{-\pi/2}^{\pi/2} \cos \varphi d\varphi$. Note that an integral over height has been replaced by a summation over levels 1 and 3. The total zonal kinetic energy is

$$\langle ZKE \rangle = \langle KZ \rangle + \langle KM \rangle \quad (5-1d)$$

Likewise, the magnetic energy of the axisymmetric zonal field, the axisymmetric meridional field, and the eddy horizontal field are respectively

$$\langle MZ \rangle = \rho_s D \int_{\sigma_s} \frac{(\langle B_1^\lambda \rangle^2 + \langle B_3^\lambda \rangle^2)}{8\pi \mu_0 \rho_s} dS \quad (5-2a)$$

$$\langle MM \rangle = \rho_s D \int_{\sigma_s} \frac{(\langle B_1^\varphi \rangle^2 + \langle B_3^\varphi \rangle^2)}{8\pi \mu_0 \rho_s} dS \quad (5-2b)$$

$$\langle EME \rangle = \rho_s D \int_{\sigma_s} \frac{(\langle B_1^{\lambda*2} + B_1^{\psi*2} \rangle + \langle B_3^{\lambda*2} + B_3^{\psi*2} \rangle)}{8\pi\mu_0 \rho_s} dS \quad (5-2c)$$

whereas the total zonal magnetic energy is

$$\langle ZME \rangle = \langle MZ \rangle + \langle MM \rangle \quad (5-2d)$$

Both $\langle KZ \rangle$ and $\langle MZ \rangle$ are purely toroidal, while $\langle KM \rangle$ and $\langle MM \rangle$ are purely poloidal.¹ But $\langle EKE \rangle$, $\langle ZKE \rangle$, $\langle EME \rangle$ and $\langle ZME \rangle$ are combinations of poloidal and toroidal components. The electrical energy has been filtered out by the MHD approximation.

Meanwhile, the zonal available potential energy is

$$\langle ZPE \rangle = \rho_s D \int_{\sigma_s} \frac{\langle \Phi \rangle^2}{2} dS \quad (5-3a)$$

and the eddy available potential energy is

$$\langle EPE \rangle = \rho_s D \int_{\sigma_s} \frac{\langle \Phi^{*2} \rangle}{2} dS \quad (5-3b)$$

In these equations, the thermodynamic variable Φ is defined as

$$\Phi = [g(\partial \ln \sigma_s / \partial z)^{-1}]^{1/2} \sigma_2' / \sigma_s \quad (5-4)$$

The usual approach for deriving the energy balance is adopted here. The horizontal primitive hydromagnetic equations

¹The vertical components of motion and magnetic field do not enter into $\langle KM \rangle$ or $\langle MM \rangle$, as discussed in Chapter 2.

(rather than the Lundquist equations) at levels 1 and 3 are first decomposed into zonally averaged and eddy equations. The next step is to form the energy density equations

$$\langle u_1 \rangle \frac{\partial \langle u_1 \rangle}{\partial t} + \langle u_3 \rangle \frac{\partial \langle u_3 \rangle}{\partial t} = \dots \quad (5-5a)$$

$$\langle v_1 \rangle \frac{\partial \langle v_1 \rangle}{\partial t} + \langle v_3 \rangle \frac{\partial \langle v_3 \rangle}{\partial t} = \dots \quad (5-5b)$$

$$\left\langle u_1^* \frac{\partial u_1^*}{\partial t} + v_1^* \frac{\partial v_1^*}{\partial t} + u_3^* \frac{\partial u_3^*}{\partial t} + v_3^* \frac{\partial v_3^*}{\partial t} \right\rangle = \dots \quad (5-5c)$$

$$\frac{\langle B_1^\lambda \rangle}{4\pi\mu_0\rho_s} \frac{\partial \langle B_1^\lambda \rangle}{\partial t} + \frac{\langle B_3^\lambda \rangle}{4\pi\mu_0\rho_s} \frac{\partial \langle B_3^\lambda \rangle}{\partial t} = \dots \quad (5-5d)$$

$$\frac{\langle B_1^\varphi \rangle}{4\pi\mu_0\rho_s} \frac{\partial \langle B_1^\varphi \rangle}{\partial t} + \frac{\langle B_3^\varphi \rangle}{4\pi\mu_0\rho_s} \frac{\partial \langle B_3^\varphi \rangle}{\partial t} = \dots \quad (5-5e)$$

$$\left\langle \frac{B_1^{\lambda*}}{4\pi\mu_0\rho_s} \frac{\partial B_1^{\lambda*}}{\partial t} + \frac{B_1^{\varphi*}}{4\pi\mu_0\rho_s} \frac{\partial B_1^{\varphi*}}{\partial t} + \frac{B_3^{\lambda*}}{4\pi\mu_0\rho_s} \frac{\partial B_3^{\lambda*}}{\partial t} + \frac{B_3^{\varphi*}}{4\pi\mu_0\rho_s} \frac{\partial B_3^{\varphi*}}{\partial t} \right\rangle = \dots \quad (5-5f)$$

Note that the magnetic energy density equations are derived directly from the magnetic induction equations in which the electric field \underline{E} and the current density \underline{J} have been eliminated. Thus, quantities such as the Poynting vector $\underline{E} \times \underline{B}$ will not appear in the final energy equations. Also, the energy density equations involving available potential energy are

$$g \left(\frac{\partial \sigma_s}{\partial z} \right)^{-1} \frac{\langle \sigma_2' \rangle}{\sigma_s} \frac{\partial \langle \sigma_2' \rangle}{\partial t} = \dots \quad (5-5g)$$

$$g \left(\frac{\partial \sigma_s}{\partial z} \right)^{-1} \sigma_s^{-1} \langle \sigma_2'^* \frac{\partial \sigma_2'^*}{\partial t} \rangle = \dots \quad (5-5h)$$

The energy density equations are now multiplied by \int_0^D and integrated over a sphere of radius "a". The integrands of the various energy transformation integrals are not unique, but the integrals over the entire fluid region are. Integrating by parts and using the results of Starr and Gilman (1966) as a guide, we obtained a set of energy integrals. The following equations and boundary conditions were required for this step: The equations of mass and magnetic continuity, i.e. (3-21a) and (3-24a), the identity (2-43) governing magnetohydrostatic balance, the boundary condition that there are no singularities at the poles, and the boundary conditions (3-4) and (3-5) at $z=0, z_4$. Our results are consistent with the kinetic energy balance in spherical geometry for the nonmagnetic case which is given in Saltzman (1957).

The energy integrals appear on the right hand side of the energy balance equations (5-6a) through (5-8b):

$$\begin{aligned} \frac{\partial \langle KZ \rangle}{\partial t} = & \{ \langle KM \rangle \rightarrow \langle KZ \rangle \} + \{ \langle EKE \rangle \rightarrow \langle KZ \rangle \} - \{ \langle KZ \rangle \rightarrow \langle MZ \rangle \} \\ & - \{ \langle KZ \rangle \rightarrow \langle EME \rangle \} + \langle F_{KZ} \rangle + \langle KZ \downarrow \rangle \end{aligned} \quad (5-6a)$$

$$\begin{aligned} \frac{\partial \langle KM \rangle}{\partial t} = & - \{ \langle KM \rangle \rightarrow \langle KZ \rangle \} + \{ \langle EKE \rangle \rightarrow \langle KM \rangle \} - \{ \langle KM \rangle \rightarrow \langle MZ \rangle \} \\ & - \{ \langle KM \rangle \rightarrow \langle MM \rangle \} - \{ \langle KM \rangle \rightarrow \langle EME \rangle \} + \{ \langle ZPE \rangle \rightarrow \langle KM \rangle \} \\ & + \langle F_{KM} \rangle + \langle KM \downarrow \rangle \end{aligned} \quad (5-6b)$$

$$\begin{aligned}
\frac{\partial \langle EKE \rangle}{\partial t} &= -\{ \langle EKE \rangle \rightarrow \langle KZ \rangle \} - \{ \langle EKE \rangle \rightarrow \langle KM \rangle \} - \{ \langle EKE \rangle \rightarrow \langle MZ \rangle \} \\
&\quad - \{ \langle EKE \rangle \rightarrow \langle MM \rangle \} - \{ \langle EKE \rangle \rightarrow \langle EME \rangle \} + \{ \langle EPE \rangle \rightarrow \langle EKE \rangle \} \\
&\quad + \langle F_{EKE} \rangle + \langle EKE^\nu \rangle \qquad (5-6c)
\end{aligned}$$

$$\begin{aligned}
\frac{\partial \langle MZ \rangle}{\partial t} &= \{ \langle KZ \rangle \rightarrow \langle MZ \rangle \} + \{ \langle KM \rangle \rightarrow \langle MZ \rangle \} + \{ \langle EKE \rangle \rightarrow \langle MZ \rangle \} \\
&\quad + \langle O_{MZ} \rangle + \langle MZ^\nu \rangle \qquad (5-7a)
\end{aligned}$$

$$\frac{\partial \langle MM \rangle}{\partial t} = \{ \langle KM \rangle \rightarrow \langle MM \rangle \} + \{ \langle EKE \rangle \rightarrow \langle MM \rangle \} + \langle O_{MM} \rangle + \langle MM^\nu \rangle \quad (5-7b)$$

$$\begin{aligned}
\frac{\partial \langle EME \rangle}{\partial t} &= \{ \langle KZ \rangle \rightarrow \langle EME \rangle \} + \{ \langle KM \rangle \rightarrow \langle EME \rangle \} + \{ \langle EKE \rangle \rightarrow \langle EME \rangle \} \\
&\quad + \langle O_{EME} \rangle + \langle EME^\nu \rangle \qquad (5-7c)
\end{aligned}$$

$$\frac{\partial \langle ZPE \rangle}{\partial t} = -\{ \langle ZPE \rangle \rightarrow \langle KM \rangle \} - \{ \langle ZPE \rangle \rightarrow \langle EPE \rangle \} + \langle G_{ZPE} \rangle \quad (5-8a)$$

$$\frac{\partial \langle EPE \rangle}{\partial t} = -\left\{ \langle EPE \rangle \rightarrow \langle EKE \rangle \right\} + \left\{ \langle ZPE \rangle \rightarrow \langle EPE \rangle \right\} + \langle G_{EPE} \rangle \quad (5-8b)$$

These energy balance equations give the time rate of change of the various types of energy in the model.

Terms with curly brackets are energy transformation integrals. In order of appearance,

$$\begin{aligned} \left\{ \langle KM \rangle \rightarrow \langle KZ \rangle \right\} &= \rho_s D \int_{\sigma_s} \left[\left(2\mathcal{L} + \frac{\langle u_1 \rangle}{a \cos \varphi} \right) \langle u_1 \rangle \langle v_1 \rangle \right. \\ &\quad \left. + \left(2\mathcal{L} + \frac{\langle u_3 \rangle}{a \cos \varphi} \right) \langle u_3 \rangle \langle v_3 \rangle \right] \sin \varphi \, dS \end{aligned} \quad (5-9)$$

$$\begin{aligned} \left\{ \langle EKE \rangle \rightarrow \langle KEZ \rangle \right\} &= \rho_s D \int_{\sigma_s} a \cos \varphi \left[\langle u_1^* v_1^* \rangle \frac{1}{a} \frac{\partial}{\partial \varphi} \left(\frac{\langle u_1 \rangle}{a \cos \varphi} \right) + \langle u_3^* v_3^* \rangle \frac{1}{a} \frac{\partial}{\partial \varphi} \left(\frac{\langle u_3 \rangle}{a \cos \varphi} \right) \right] dS \\ &\quad + \rho_s D \int_{\sigma_s} \langle u_2^* w_2^* \rangle \frac{\langle u_3 - u_1 \rangle}{D} \, dS \end{aligned} \quad (5-10)$$

$$\begin{aligned} \left\{ \langle KZ \rangle \rightarrow \langle MZ \rangle \right\} &= \rho_s D \int_{\sigma_s} \frac{a \cos \varphi}{4\pi \mu_0 \rho_s} \left[\langle B_1^{\wedge} B_1^{\circ} \rangle \frac{1}{a} \frac{\partial}{\partial \varphi} \left(\frac{\langle u_1 \rangle}{a \cos \varphi} \right) + \langle B_3^{\wedge} B_3^{\circ} \rangle \frac{1}{a} \frac{\partial}{\partial \varphi} \left(\frac{\langle u_3 \rangle}{a \cos \varphi} \right) \right] dS \\ &\quad + \rho_s D \int_{\sigma_s} \frac{\langle B_2^{\wedge} B_2^{\circ} \rangle}{4\pi \mu_0 \rho_s} \frac{\langle u_3 - u_1 \rangle}{D} \, dS \end{aligned} \quad (5-11)$$

$$\begin{aligned} \left\{ \langle KZ \rangle \rightarrow \langle EME \rangle \right\} &= \rho_s D \int_{\sigma_s} \frac{a \cos \varphi}{4\pi \mu_0 \rho_s} \left[\langle B_1^{\wedge} B_1^{\circ*} \rangle \frac{1}{a} \frac{\partial}{\partial \varphi} \left(\frac{\langle u_1 \rangle}{a \cos \varphi} \right) + \langle B_3^{\wedge} B_3^{\circ*} \rangle \frac{1}{a} \frac{\partial}{\partial \varphi} \left(\frac{\langle u_3 \rangle}{a \cos \varphi} \right) \right] dS \\ &\quad + \rho_s D \int_{\sigma_s} \frac{\langle B_2^{\wedge} B_2^{\circ*} \rangle}{4\pi \mu_0 \rho_s} \frac{\langle u_3 - u_1 \rangle}{D} \, dS \end{aligned} \quad (5-12)$$

$$\begin{aligned}
 \{ \langle EKE \rangle \rightarrow \langle KM \rangle \} &= \rho_s D \int_{\sigma_s} \cos \omega \left[\frac{\langle v_1^{*2} \rangle}{a} \frac{\partial \langle v_1 \rangle}{\partial \omega (\cos \omega)} + \frac{\langle v_3^{*2} \rangle}{a} \frac{\partial \langle v_3 \rangle}{\partial \omega (\cos \omega)} \right] dS \\
 &- \rho_s D \int_{\sigma_s} \frac{\tan \omega}{a} \left[\langle v_1 \rangle \langle u_1^{*2} + v_1^{*2} \rangle + \langle v_3 \rangle \langle u_3^{*2} + v_3^{*2} \rangle \right] dS \\
 &+ \rho_s D \int_{\sigma_s} \langle v_2^* w_2^* \rangle \frac{\langle v_3 - v_1 \rangle}{D} dS \quad (5-13)
 \end{aligned}$$

$$\{ \langle KM \rangle \rightarrow \langle MZ \rangle \} = -\rho_s D \int_{\sigma_s} \frac{1}{4\pi\mu_0 \rho_s} \frac{\tan \omega}{a} \left[\langle B_1^\lambda \rangle^2 \langle v_1 \rangle + \langle B_3^\lambda \rangle^2 \langle v_3 \rangle \right] dS \quad (5-14)$$

$$\begin{aligned}
 \{ \langle KM \rangle \rightarrow \langle MM \rangle \} &= \rho_s D \int_{\sigma_s} \frac{1}{4\pi\mu_0 \rho_s} \left[\langle v_2 \rangle = 0 \langle B_2^3 \rangle - \langle w_2 \rangle \langle B_2^\omega \rangle \right] \left[-\frac{\langle B_3^\omega - B_1^\omega \rangle}{D} \right] dS \\
 &+ \rho_s D \int_{\sigma_s} \frac{\langle v_3 \rangle \langle B_4^3 \rangle}{4\pi\mu_0 \rho_s} \left[-\frac{\langle B_4^\omega - B_3^\omega \rangle}{D} \right] dS \quad (5-15)
 \end{aligned}$$

$$\begin{aligned}
 \{ \langle KM \rangle \rightarrow \langle EME \rangle \} &= -\rho_s D \int_{\sigma_s} \frac{a \cos \omega}{8\pi\mu_0 \rho_s} \left[\langle B_1^{\lambda*2} - B_1^{\omega*2} \rangle \frac{1}{a} \frac{\partial \langle v_1 \rangle}{\partial \omega (\cos \omega)} + \langle B_3^{\lambda*2} - B_3^{\omega*2} \rangle \frac{1}{a} \frac{\partial \langle v_3 \rangle}{\partial \omega (\cos \omega)} \right] dS \\
 &+ \rho_s D \int_{\sigma_s} \frac{\langle B_2^{\omega*} B_2^{3*} \rangle \langle v_3 - v_1 \rangle}{4\pi\mu_0 \rho_s} dS - \rho_s D \int_{\sigma_s} \left[\frac{\langle B_1^{\lambda*2} + B_1^{\omega*2} \rangle - \langle B_3^{\lambda*2} + B_3^{\omega*2} \rangle}{8\pi\mu_0 \rho_s} \right] \frac{\langle w_2 \rangle}{D} dS \quad (5-16)
 \end{aligned}$$

$$\{ \langle ZPE \rangle \rightarrow \langle KM \rangle \} = \rho_s D \int_{\sigma_s} g \sigma_s^{-1} \langle w_2 \rangle \langle \sigma_2' \rangle dS \quad (5-17)$$

$$\begin{aligned}
 \{ \langle EKE \rangle \rightarrow \langle MZ \rangle \} &= -\rho_s D \int_{\sigma_s} \frac{1}{4\pi\mu_0 \rho_s} \left[\langle u_2^* B_2^{3*} \rangle - \langle w_2^* B_2^{\lambda*} \rangle \right] \frac{\langle B_3^\lambda - B_1^\lambda \rangle}{D} dS \\
 &- \rho_s D \int_{\sigma_s} \frac{\langle u_3^* B_4^{3*} \rangle \langle B_4^\lambda - B_3^\lambda \rangle}{4\pi\mu_0 \rho_s} dS + \rho_s D \int_{\sigma_s} (4\pi\mu_0 \rho_s)^{-1} \frac{1}{a \cos \omega} \left[\langle v_1^* B_1^{\lambda*} - u_1^* B_1^{\omega*} \rangle \right. \\
 &\left. \cdot \frac{\partial \langle B_1^\lambda \rangle \cos \omega}{\partial \omega} + \langle v_3^* B_3^{\lambda*} - u_3^* B_3^{\omega*} \rangle \frac{\partial \langle B_3^\lambda \rangle \cos \omega}{\partial \omega} \right] dS \quad (5-18)
 \end{aligned}$$

$$\begin{aligned} \{ \langle EKE \rangle \rightarrow \langle MM \rangle \} &= \rho_s D \int_{\sigma_s} \frac{1}{4\pi\mu_0 \rho_s} \left[\langle v_2^* B_2^{\lambda*} \rangle - \langle w_2^* B_2^{\varphi*} \rangle \right] \left[- \frac{\langle B_3^{\varphi} - B_1^{\varphi} \rangle}{D} dS \right. \\ &+ \rho_s D \int_{\sigma_s} \frac{\langle v_3^* B_4^{\lambda*} \rangle}{4\pi\mu_0 \rho_s} \left[- \frac{\langle B_4^{\varphi} - B_3^{\varphi} \rangle}{D} \right] dS \end{aligned} \quad (5-19)$$

$$\begin{aligned} \{ \langle EKE \rangle \rightarrow \langle EME \rangle \} &= - \rho_s D \int_{\sigma_s} \frac{1}{4\pi\mu_0 \rho_s} \left\langle B_2^{\lambda} \left[u_2^* \frac{(B_3^{\lambda*} - B_1^{\lambda*})}{D} + v_2^* \frac{(B_3^{\varphi*} - B_1^{\varphi*})}{D} \right] \right. \\ &+ B_4^{\lambda} \left[u_3^* \frac{(B_4^{\lambda*} - B_3^{\lambda*})}{D} + v_3^* \frac{(B_4^{\varphi*} - B_3^{\varphi*})}{D} \right] \left. \right\rangle dS \\ &- \rho_s D \int_{\sigma_s} \frac{1}{4\pi\mu_0 \rho_s} \left\langle \nabla_H^2 \Psi_m^* (v_1^* B_1^{\lambda} - u_1^* B_1^{\varphi}) + \nabla_H^2 \Psi_m^* (v_3^* B_3^{\lambda} - u_3^* B_3^{\varphi}) \right\rangle dS \\ &+ \rho_s D \int_{\sigma_s} \frac{1}{4\pi\mu_0 \rho_s} \left\langle w_2^* \left[B_2^{\lambda} \frac{(B_3^{\lambda*} - B_1^{\lambda*})}{D} + B_2^{\varphi} \frac{(B_3^{\varphi*} - B_1^{\varphi*})}{D} \right] \right\rangle dS \end{aligned} \quad (5-20)$$

$$\{ \langle EPE \rangle \rightarrow \langle EKE \rangle \} = \rho_s D \int_{\sigma_s} g \sigma_s^{-1} \langle w_2^* \sigma_2^* \rangle dS \quad (5-21)$$

$$\{ \langle ZPE \rangle \rightarrow \langle EPE \rangle \} = - \rho_s D \int_{\sigma_s} g \left(\frac{\partial \ln \sigma_s}{\partial z} \right)^{-1} \sigma_s^{-2} \langle v_2^* \sigma_2^* \rangle \frac{1}{a} \frac{\partial \langle \sigma_2 \rangle}{\partial \omega} dS \quad (5-22)$$

The arrows denote the sign convention. Thus $\{ \langle ZPE \rangle \rightarrow \langle EPE \rangle \}$ would indicate a transformation of zonal into eddy available potential energy rather than vice versa. The energy transformation terms are named as such because they each appear with opposite signs in two energy balance equations.

For low Rossby number flows, the work done by the two

coriolis terms dominates in equation (5-9). Their sum, i.e.

$\rho_s D \int_{\sigma_s} 2\mathcal{N} \sin \varphi \langle v_z \rangle \langle u_z - u_1 \rangle dS$ does not vanish, unlike the net coriolis torque in the angular momentum balance. According to equation (5-10), the transport of angular momentum up the gradient of angular velocity results in a conversion of $\langle EKE \rangle$ into $\langle KE \rangle$. The last integral of (5-10) which contains the product of the vertical eddy Reynolds stress and the vertical shear of angular velocity cannot be neglected. The first and third integrals in (5-13) are analogous to the first two integrals in (5-10) with u replaced by v . Meanwhile, the second integral is associated with a curvature correction term introduced by the spherical geometry.

A given form of magnetic energy cannot be transformed directly into any other form of magnetic energy or into available potential energy, and conversely. But kinetic (magnetic) energy can be transformed into magnetic (kinetic) energy. In equation (5-11), the first integral is the previously mentioned Babcock term. The horizontal shear of the differential rotation stretches axisymmetric poloidal into axisymmetric toroidal magnetic fields. The second integral is analogous, but involves the vertical as opposed to the horizontal shear of angular velocity. Equation (5-12) resembles (5-11) except that eddy Maxwell stresses replace the axisymmetric Maxwell stresses. This equation may be also be compared to (5-10) which has eddy Reynolds stresses and opposite sign. Suppose that $\{ \langle EKE \rangle \rightarrow \langle KE \rangle \}$ were positive and that the Reynolds and Maxwell stresses had the same sign. The Maxwell stresses would then act as a magnetic brake upon the differential

rotation as noted by Starr and Gilman (1965b).

Equation (5-14) is similar in form to (5-9), neglecting the coriolis terms in the latter. Also, applying the mass continuity equation, (5-16) could be reduced to an integral expression analogous to (5-13).

The integrands of equations (5-18) and (5-19) involve $\langle \underline{V}^* \cdot \{ \underline{J} \times \underline{B}^* \} \rangle$ while that of (5-20) involves $\langle \underline{V}^* \cdot \underline{J}^* \times \underline{B}^* \rangle$. These terms may be interpreted as the work done by eddy fluid motions against the magnetic body force. Note that the integrals in (5-20) implicitly contain both double and triple eddy correlations. However, the triple correlations vanish, because our model contains only the two zonal wave numbers $n=0$ and $n=6$.

Available potential energy is converted to kinetic energy in (5-17) and (5-21) if fluid parcels systematically rise and cold parcels sink. Likewise, $\langle ZPE \rangle$ is transformed into $\langle EPE \rangle$ in (5-22) if heat is transported down the meridional temperature gradient.

The terms

$$\langle KZ^\downarrow \rangle = \int_{\sigma_s} \frac{\langle u_3 \rangle}{4\pi\mu_0} \left[\langle B_4^\lambda \rangle \langle B_4^z \rangle + \langle B_4^{\lambda*} B_4^{z*} \rangle \right] dS \quad (5-23a)$$

$$\langle KM^\downarrow \rangle = \int_{\sigma_s} \frac{1}{4\pi\mu_0} \left[\langle B_4^{\psi*} B_4^z \rangle \langle v_3 \rangle \right] dS \quad (5-23b)$$

$$\langle EKE^\downarrow \rangle = 0 \quad (5-23c)$$

$$\langle MZ^\downarrow \rangle = \int_{\sigma_s} \frac{1}{4\pi\mu_0} \left[\langle u_3^* B_4^z \rangle \langle B_4^\lambda \rangle \right] dS \quad (5-24a)$$

$$\langle MM^\dagger \rangle = \int_{\sigma_s} \frac{1}{4\pi\mu_0} \left[\langle v_3 \rangle \langle B_4^3 \rangle + \langle v_3^* B_4^{3*} \rangle \right] \langle B_4^4 \rangle dS \quad (5-24b)$$

$$\langle EME^\dagger \rangle = \int_{\sigma_s} \left[\frac{\langle u_3^* B_4^{\lambda*} + v_3^* B_4^{\mu*} \rangle \langle B_4^3 \rangle + \langle (u_3^* B_4^{\lambda*} + v_3^* B_4^{\mu*}) B_4^{3*} \rangle}{4\pi\mu_0} \right] dS \quad (5-24c)$$

represent energy fluxes of $\langle KZ \rangle$, $\langle KM \rangle$, $\langle EKE \rangle$, $\langle MZ \rangle$, $\langle MM \rangle$, and $\langle EME \rangle$ respectively, measured positive downwards, across the upper boundary $z=z_4$. All flux terms at the upper boundary which contain w_4 , as well as all fluxes at the lower boundary $z=0$, have been excluded due to the boundary conditions. Equations (5-23a) and (5-23b) represent the work done on the fluid at the upper boundary by the Maxwell stresses. Now $\langle B_4^\lambda \rangle = 0$, and from the discussion in section 4.2, $\langle B_4^{\lambda*} B_4^{3*} \rangle \sim \langle B_4^{\mu*} B_4^{3*} \rangle \sim 0$, suggesting that only $\langle MM^\dagger \rangle$ and $\langle EME^\dagger \rangle$ need be retained. But in the actual numerical computations, all the energy fluxes were negligible, although $\langle MM^\dagger \rangle$ and $\langle EME^\dagger \rangle$ were slightly larger than the others. Clearly, the dynamo is not maintained by a magnetic energy source in the non-conducting region $z \geq z_4$.

Zonal available potential energy is locally generated whenever $|\langle \sigma_2' \rangle / \sigma_*'| < 1$ by

$$\langle G_{EPE} \rangle = -\rho_s D \int_{\sigma_s} \frac{gK}{(\partial \ln \sigma_s / \partial z) \sigma_s^2} \left[\langle \sigma_2' \rangle \langle \sigma_2' - \sigma_*' \rangle \right] dS \quad (5-25a)$$

In contrast, the "generation" term

$$\langle G_{EPE} \rangle = -\rho_s D \int_{\sigma_s} \frac{gK}{(\partial \ln \sigma_s / \partial z) \sigma_s^2} \left[\langle \sigma_2'^{*2} \rangle \right] dS \quad (5-25b)$$

for eddy available potential energy is negative definite and hence represents an energy sink.

The frictional dissipation of $\langle KZ \rangle$, $\langle KM \rangle$, and $\langle EKE \rangle$ are given respectively by

$$\begin{aligned} \langle F_{KZ} \rangle &= -\rho_s D \int_{\sigma_s} \nu_{(3)} \left[\langle u_3 - u_1 \rangle^2 + 2 \langle u_1^2 \rangle \right] dS \\ &\quad + \rho_s D \int_{\sigma_s} \nu_{(H)} \left[\langle u_1 \rangle \Delta^\lambda (\langle u_1 \rangle, 0) + \langle u_3 \rangle \Delta^\lambda (\langle u_3 \rangle, 0) \right] dS \quad (5-26a) \end{aligned}$$

$$\begin{aligned} \langle F_{KM} \rangle &= -\rho_s D \int_{\sigma_s} \nu_{(3)} \left[\langle v_3 - v_1 \rangle^2 + 2 \langle v_1^2 \rangle \right] dS \\ &\quad + \rho_s D \int_{\sigma_s} \nu_{(H)} \left[\langle v_1 \rangle \Delta^\omega (0, \langle v_1 \rangle) + \langle v_3 \rangle \Delta^\omega (0, \langle v_3 \rangle) \right] dS \quad (5-26b) \end{aligned}$$

$$\begin{aligned} \langle F_{EKE} \rangle &= -\rho_s D \int_{\sigma_s} \nu_{(3)} \left[\langle (u_3^* - u_1^*)^2 \rangle + \langle (v_3^* - v_1^*)^2 \rangle + 2 \langle u_1^{*2} + v_1^{*2} \rangle \right] dS \\ &\quad + \rho_s D \int_{\sigma_s} \nu_{(H)} \left[\langle u_1^* (\Delta^\lambda (u_1^*, v_1^*) + v_1^* \Delta^\omega (u_1^*, v_1^*)) + u_3^* \Delta^\lambda (u_3^*, v_3^*) + v_3^* \Delta^\omega (u_3^*, v_3^*) \rangle \right] dS \quad (5-26c) \end{aligned}$$

and the ohmic dissipation of $\langle MZ \rangle$, $\langle MM \rangle$, and $\langle EME \rangle$ by

$$\begin{aligned} \langle O_{MZ} \rangle &= \frac{D}{4\pi\mu_0} \int_{\sigma_s} \eta_{(3)} \left[\langle B_1^\lambda \rangle \langle B_3^\lambda - B_1^\lambda \rangle + \langle B_3^\lambda \rangle \langle B_1^\lambda - 3B_3^\lambda + 2B_4^\lambda \rangle \right] dS \\ &\quad + \frac{D}{4\pi\mu_0} \int_{\sigma_s} \eta_{(H)} \left[\langle B_1^\lambda \rangle \Delta^\lambda (\langle B_1^\lambda \rangle, 0) + \langle B_3^\lambda \rangle \Delta^\lambda (\langle B_3^\lambda \rangle, 0) \right] dS \quad (5-27a) \end{aligned}$$

$$\begin{aligned} \langle O_{MM} \rangle &= \frac{D}{4\pi\mu_0} \int_{\sigma_s} \eta_{(3)} \left[\langle B_1^\omega \rangle \langle B_3^\omega - B_1^\omega \rangle + \langle B_3^\omega \rangle \langle B_1^\omega - 3B_3^\omega + 2B_4^\omega \rangle \right] dS \\ &\quad + \frac{D}{4\pi\mu_0} \int_{\sigma_s} \eta_{(H)} \left[\langle B_1^\omega \rangle \Delta^\omega (0, \langle B_1^\omega \rangle) + \langle B_3^\omega \rangle \Delta^\omega (0, \langle B_3^\omega \rangle) \right] dS \quad (5-27b) \end{aligned}$$

$$\begin{aligned}
 \langle O_{EME} \rangle = & \frac{D}{4\pi\mu_0} \int_{\sigma_s} \eta_{(3)} \left[\langle B_1^{\lambda*} (B_3^{\lambda*} - B_1^{\lambda*}) + B_3^{\lambda*} (B_1^{\lambda*} - 3B_3^{\lambda*} + 2B_4^{\lambda*}) + B_1^{\varphi*} (B_3^{\varphi*} - B_1^{\varphi*}) \right. \\
 & \left. + B_3^{\varphi*} (B_1^{\varphi*} - 3B_3^{\varphi*} + 2B_4^{\varphi*}) \right] dS + \frac{D}{4\pi\mu_0} \int_{\sigma_s} \eta_{(4)} \left[\langle B_1^{\lambda*} \Delta^\lambda (B_1^{\lambda*}, B_1^{\varphi*}) \right. \\
 & \left. + B_1^{\varphi*} \Delta^\varphi (B_1^{\lambda*}, B_1^{\varphi*}) + B_3^{\lambda*} \Delta^\lambda (B_3^{\lambda*}, B_3^{\varphi*}) + B_3^{\varphi*} \Delta^\varphi (B_3^{\lambda*}, B_3^{\varphi*}) \right] dS \quad (5-27c)
 \end{aligned}$$

Adding up the energy balance equations (5-6a) through (5-8b), the energy transformation integrals (5-9) through (5-22) cancel in pairs. Thus, neglecting the energy flux terms, we have the energy balance equation

$$\begin{aligned}
 \frac{\partial \langle \mathcal{E}_T \rangle}{\partial t} = & \langle G_{EPE} \rangle + \langle G_{EPE} \rangle + \langle F_{KZ} \rangle + \langle F_{KM} \rangle + \langle F_{EME} \rangle \\
 & + \langle O_{MZ} \rangle + \langle O_{MM} \rangle + \langle O_{EME} \rangle \quad (5-28)
 \end{aligned}$$

for the total energy

$$\begin{aligned}
 \langle \mathcal{E}_T \rangle = & \langle KZ \rangle + \langle KM \rangle + \langle EKE \rangle + \langle MZ \rangle + \langle MM \rangle \\
 & + \langle EME \rangle + \langle ZPE \rangle + \langle EPE \rangle \quad (5-29)
 \end{aligned}$$

The energy processes in our model are summarized in the energy diagrams of Fig. 5.1a and Fig. 5.1b, for the magnetic and non-magnetic cases respectively. In both figures the insignificant energy fluxes and the brackets $\langle \rangle$ are discarded to improve legibility.

Energy transformations are symbolized by arcs or straight line segments connecting any two dots (forms of energy). Arrows are drawn to indicate the sign of terms in the energy balance, (mostly dissipation and generation terms) if known a priori. All arrows are included in the diagrams constructed later for the two "production runs". Note how much more complicated Fig. 5.1a is of the two diagrams.

We were unable to prove any of the anti-dynamo theorems using the energy integrals as a starting point. However, it is still interesting to compare the energy diagrams in Fig. 5.2a and Fig. 5.2b for the toroidal motion² and axisymmetric anti-dynamo cases with Fig. 5.1a. It is perhaps more than coincidental that only Fig. 5.1a has closed, nonoverlapping paths (circuits) linking $\langle MZ \rangle$ and $\langle MM \rangle$. Such paths could exist in Fig. 5.2a and Fig. 5.2b if $\{ \langle KZ \rangle \rightarrow \langle MM \rangle \}$ were a valid energy transformation. But the kinetic energy of the axisymmetric toroidal motion is never delivered directly to the axisymmetric poloidal magnetic field.

An energy balance was also formulated for a model with continuous vertical variation. The appropriate integrals for the various energy forms, energy transformations, and boundary value fluxes are contained in Appendix C. There is an excellent correspondence between the two layer and continuous models. Thus the finite differencing scheme apparently introduces no spurious energy sources or sinks. On

²Available potential energy cannot be released in this case anyway, since $w=0$.

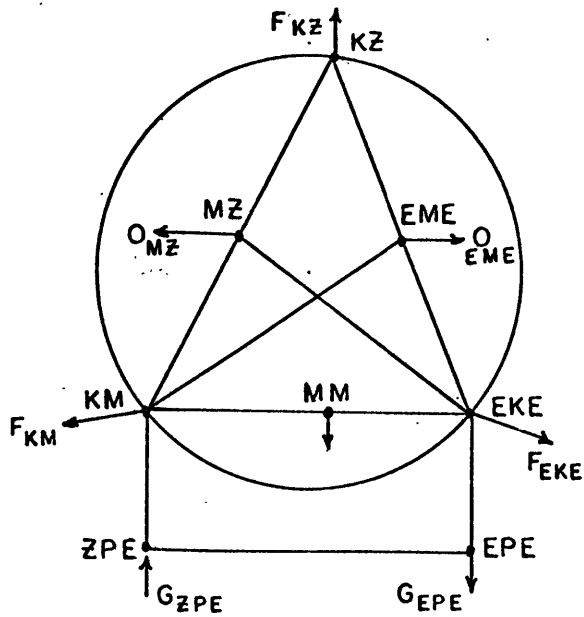


Fig. 5.1a. Energy diagram for the generalized magnetic case. The symbols are defined in the text.

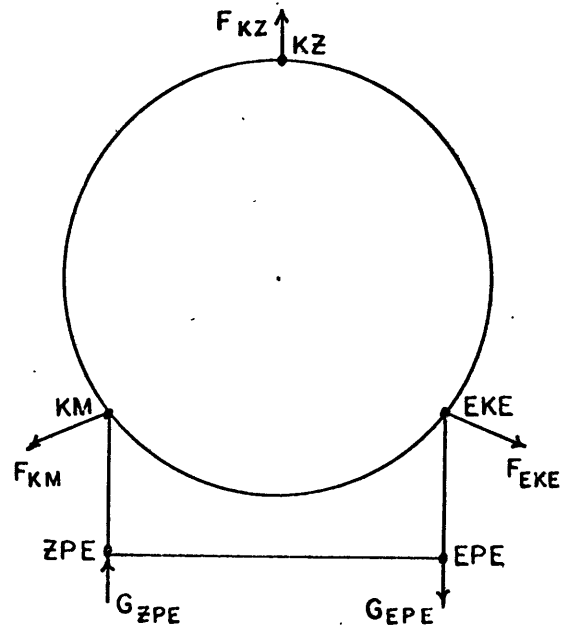


Fig. 5.1b. Energy diagram for the nonmagnetic case.

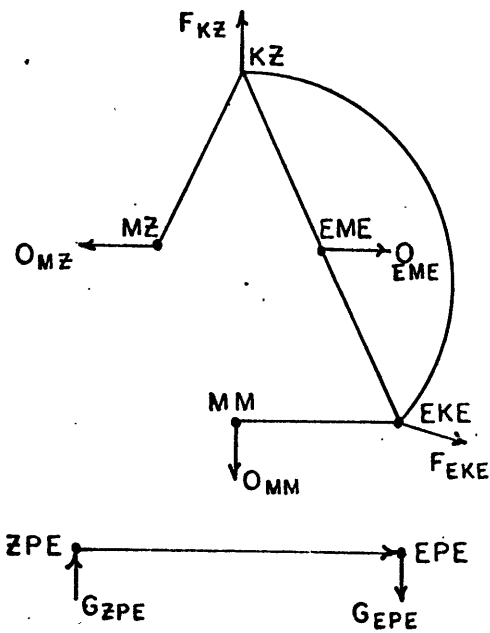


Fig. 5.2a. Energy diagram for toroidal motion anti-dynamo. Legend same as in Fig. 5.1a,b.

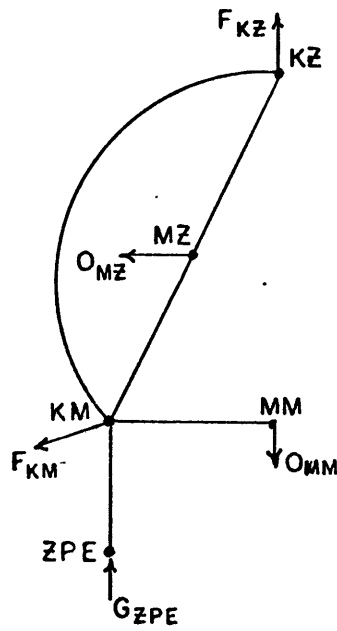


Fig. 5.2b. Energy diagram for axisymmetric anti-dynamo.

the basis of equation (5-28) and the correspondence between the two layer and continuous models, our model should be energetically consistent.

A numerical check of energetic consistency was also made over a short time interval for one of the "production runs". The instantaneous rates of change of the various forms of energy were computed (a) directly from equations (5-1a) through (5-3b) and then (b) from equations (5-6a) through (5-8b). As in all energy computations, trilinear terms were truncated only after the third factor was multiplied by the product of the first two factors. The integrals were conserved by the orthogonal truncation process. In any case, the percent difference between the results of method (a) and method (b) above was negligible.

We are now ready to discuss some numerical experiments with our model.

CHAPTER VI. NUMERICAL RESULTS

6.1. Introduction.

Computationally stable numerical solutions have been found. Only a limited number of "test" runs and two lengthy production runs could be made, however, due to the model's complexity and to the time scale of the solar magnetic cycle.

A model simulation of the earth's atmosphere is discussed in section 6.2, whereas section 6.3 lists parameters used in various solar test and production runs. Qualitative results on the relationship between angular velocity profiles and type of thermal forcing profile are presented in section 6.4. It is found that an equatorial jet can develop for certain simple Θ'_* profiles. Magnetic fields can significantly alter the jet.

In section 6.5, general circulation statistics are presented, mainly for both production runs. Magnetic fields greatly affect the angular momentum balance and nearly destroy the horizontal shear of the vertically averaged angular velocity profile. A crude determination is made of the Rossby-Hadley regime boundary for production run 2 (P.R. 2).

The dynamo maintenance aspects of the model are focused upon in sections 6.6 through 6.8. Magnetic fields apparently can be sustained by dynamo action if the magnetic Reynolds number R_m exceeds a certain critical value R_{mc} . We estimate that R_{mc} is somewhere around 250 for production run 2. The structure and evolution of magnetic field patterns are described, principally for the two production runs. Inferences about the irregular magnetic reversals are made from a study of the energetics.

Our attempt to reproduce the solar equatorial jet and features of the magnetic cycle simultaneously has been only partially successful. In P.R. 1 (P.R. 2), the equatorial acceleration at even the upper

level is much too weak (fairly realistic) while the characteristic time scale for magnetic reversals is reasonable (too rapid). The dimensions and amplitudes of our vertical magnetic eddies correspond roughly to those of the observed magnetic active regions of Bumba and Howard (1965b). At low latitudes, the magnetic eddies of production run 1 generally tilt in the same sense as the active regions for the first 12 years. Furthermore, the poleward transport of vertical eddy magnetic flux apparently leads to at least the first few poloidal magnetic field reversals. The model does not resolve sunspot scale phenomena.

6.2. Simulation of the Terrestrial Atmosphere — Test Run 1.

The nonmagnetic version of our model differs in many respects from Robert's (1966) more sophisticated primitive equation atmospheric model. Thus we did not attempt to reproduce his solutions. A simulation of the earth's atmosphere was still carried out though. The values of relevant dimensional and nondimensional parameters are given in Table 6.1. Most have been defined previously. We recall that $P_r = \nu_{(z)}/K = \frac{4}{D^2} \nu/K$ is the Prandtl number and Δt the time step. Two new parameters are the ratio γ of specific heats and the stability parameter $K_s = D \partial \ln \sigma_s / \partial z$. The precise definition of our thermal Rossby number is

$$R_{OT}^* = \frac{g(2D)}{(\pi/2) a \Omega} \frac{\Delta \theta_*}{\sigma_s} (2 \Omega \sin \varphi_* L_*)^{-1} \quad (6-1)$$

where $\theta'_*(\varphi_*) = 0$, $\Delta \theta_*$ is the difference between $\theta'_*(\varphi=0)$ and the nearest relative extremum of θ'_* and L_* is the corresponding meridional distance. Given R_{OT}^* and R_e , the eddy viscosity is then $\nu = \delta D |\Delta u_*| R_e^{-1}$, where $\Delta u_* = 2 \Omega \sin \varphi_* L_* R_{OT}^*$ is the externally imposed thermal wind.

Small random temperature eddies introduced initially were baroclinically unstable, i.e., Rossby-regime type flow developed. The

Table 6.1 Specified Parameters for the Earth and Sun

Parameter	Earth Value	Solar Value
ρ_s (gm/cm ³)	6.70×10^{-4}	3.88×10^{-4}
T_s (°K)	2.60×10^2	8.60×10^4
σ_s (°K)	2.84×10^2	1.03×10^5
g (cm/sec ²)	9.81×10^2	2.73×10^4
λ (sec ⁻¹)	7.27×10^{-5}	2.86×10^{-6}
R (ergs/gm deg)	2.87×10^6	1.50×10^8
a (cm)	6.36×10^8	6.80×10^{10}
S_H (cm)	7.60×10^5	4.72×10^8
λ_0 (cm)	1.00×10^8	1.50×10^{10}
D (cm)	3.80×10^5	2.36×10^8
Δt (sec)	2.70×10^3	4.39×10^4
\dot{V} (cm ² /sec)	1.56×10^5	variable
$\dot{V}_{(H)}$ (cm ² /sec)	0	variable
σ (cm ² /sec)	-	variable
$\sigma_{(H)}$ (cm ² /sec)	-	variable
K (sec ⁻¹)	1.08×10^{-6}	variable
σ'_* (°K)	$20(1-3\sin^2\theta)$	variable
\int	0.0038	0.016
P_r	1.00	1.00
K_s	0.10	0.0001
γ	7/5	5/3
R_e	6.67	variable
R_m	-	variable
R_{OT}^*	0.099	variable

numerical integrations were terminated after 72 rotations. The flow was then perhaps marginally quasi-steady, although rather noticeable fluctuations were still present. As the model appeared to simulate the earth's atmosphere in its gross aspects, we refocused our attention on the solar atmosphere. Later, a program was written for evaluating general circulation statistics of the two production runs stored on a history tape. A decision was then made to evaluate such statistics for some of the test runs. However, as they had not been permanently stored on tape, the data from the relevant computer printout had to be punched onto cards. Under these circumstances, data were punched for only a small number of rotations. But the computed statistics still should be fairly representative for test run 1.

The results for the earth's atmosphere case are illustrated in Fig. 6.1. The symmetry of the flow about the equator seems reasonable. The zonal wind cross section (Fig. 6.1a) shows a band of equatorial easterlies, a mid-latitude upper level jet, a positive vertical wind shear, and a very slight equatorward tilt with height of the jet axis. On the other hand, the jet is too far poleward and its strength is too weak by at least a factor of two. Lack of resolution is perhaps distorting the location and strength of the jet. Also, a flow at level 3 with energy density $\frac{1}{2} \rho_s \langle u_3^2 \rangle$ might be roughly 20% stronger if the Boussinesq approximation were relaxed and pressure coordinates adopted.

In Fig. 6.1b, the actual equator to pole potential temperature difference is $\sim 34^\circ \text{K}$ and the $\theta'_* \equiv \langle \theta'_* \rangle$ profile introduces no net heating of the model atmosphere. The meridional eddy heat transport in Fig. 6.1c has the correct sign, but again, the extrema are displaced too far poleward.

Figure 6.1d implies a direct meridional cell in each hemisphere

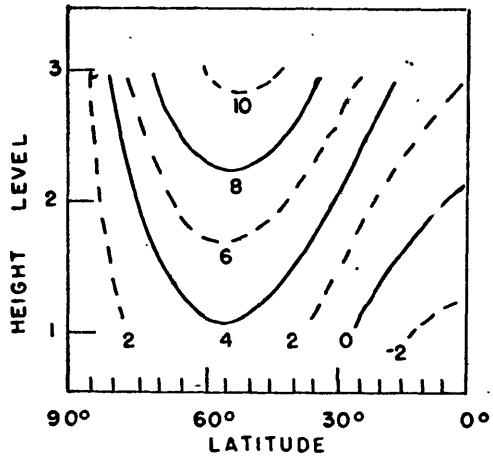
from the equator to about 40° and an indirect cell poleward. Perhaps the model is trying unsuccessfully to establish a three cell structure which requires $0 \leq m \leq 6$ minimum resolution. From figures 6.1d and 6.1e, one can infer the phase distortion of the coriolis torque term ($-2\Omega \sin \varphi \cdot \langle v_i \rangle \cos \varphi$) due to truncation. Fortunately, this term does not affect the "correctly truncated" angular momentum balance illustrated in Figure 6.1f. At each latitude, the frictional torque on the model atmosphere is almost completely balanced by the eddy horizontal angular momentum transport. The latitudinally integrated frictional torque is negligible.

Integrating the curves of Fig. 6.1f yields the "correctly truncated" eddy and axisymmetric angular momentum transports, which are everywhere poleward. But in the untruncated balance, the indirect meridional cell would produce a small equatorward axisymmetric transport. More resolution is evidently needed.

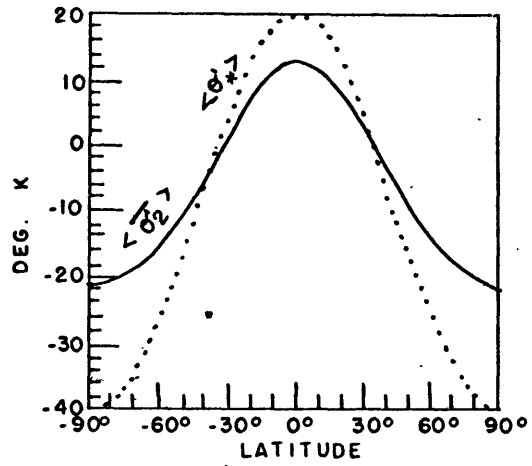
Fig. 6.1g contains the zonal and eddy vertical heat transports which have zero vertical convergence. But as they are directly proportional to the integrands of $\{\langle ZPE \rangle \rightarrow \langle KM \rangle\}$ and $\{\langle EPE \rangle \rightarrow \langle EKE \rangle\}$, these transports do help elucidate the energetics. Thus, the conversion of eddy available potential into eddy kinetic energy, i.e., $\{\langle EPE \rangle \rightarrow \langle EKE \rangle\} > 0$ is the more important process and occurs mainly in the 30° - 60° latitude belt. From figures 6.1b and 6.1c, one can infer that $\{\langle ZPE \rangle \rightarrow \langle EPE \rangle\} > 0$, while figures 6.1a and 6.1d suggest $\{\langle EKE \rangle \rightarrow \langle ZKE \rangle\} > 0$. Finally, since $|\langle \sigma_2' \rangle| < |\langle \sigma_*' \rangle|$ in Fig. 6.1b, $\langle G_{ZPE} \rangle > 0$ at virtually all latitudes.

6.3. Summary of Runs and Parameters for the Solar Model.

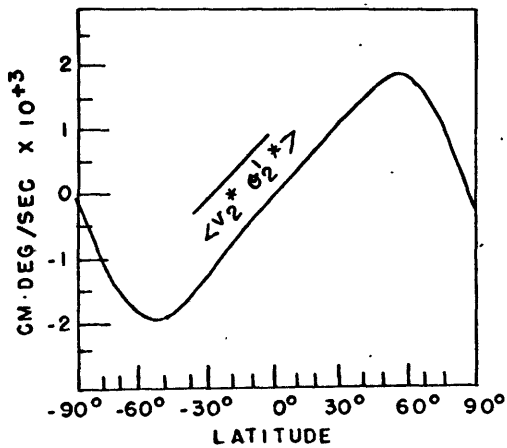
A number of relatively short numerical integrations designated as test runs were made for various purposes together with two long magnetic production runs. The values of relevant dimensional and nondimensional



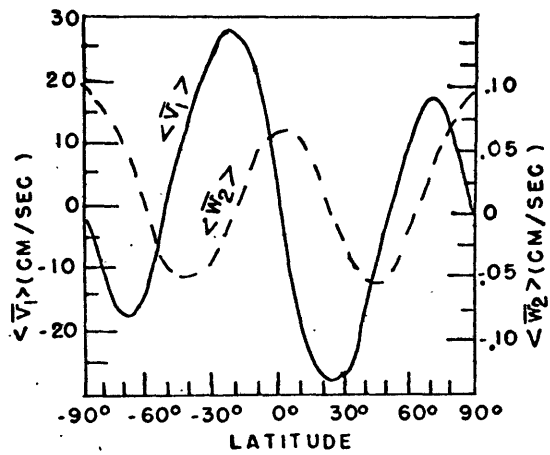
(a) Vertical-meridional cross section of zonal velocity. Contours in m/sec.



(b) Perturb. potential temp. and thermal forcing profiles.

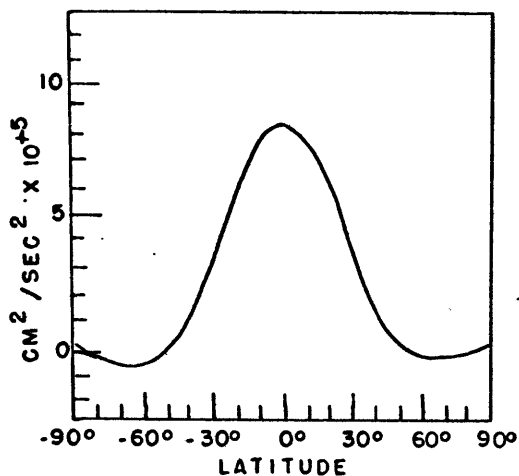


(c) Horizontal eddy heat transport.

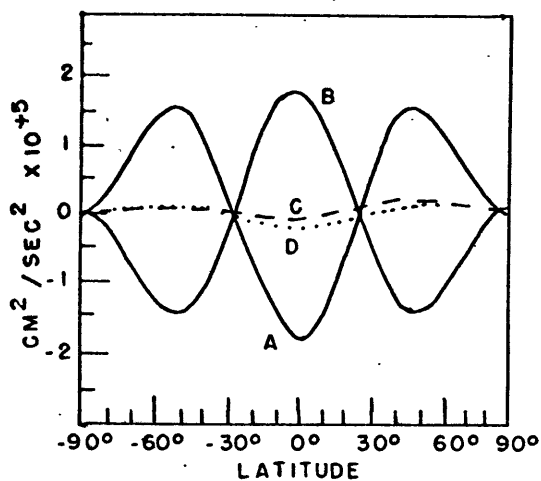


(d) Meridional circulation variables.

Fig. 6.1 General circulation statistics for terrestrial atmosphere test run.



(e) "Correctly truncated" coriolis torque.



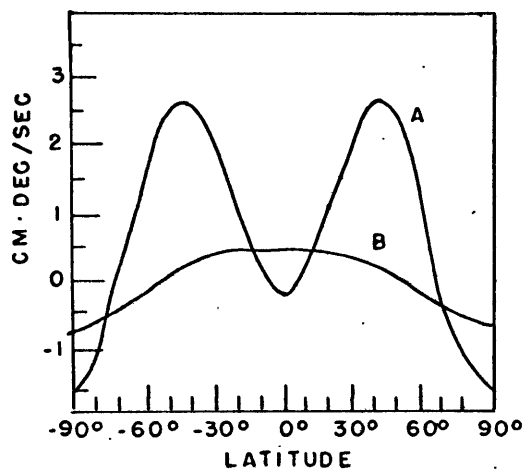
(f) Vertically averaged angular momentum balance.

A-converg. horiz. eddy transport.

B-frictional torque.

C-converg. horiz. axisym. transport.

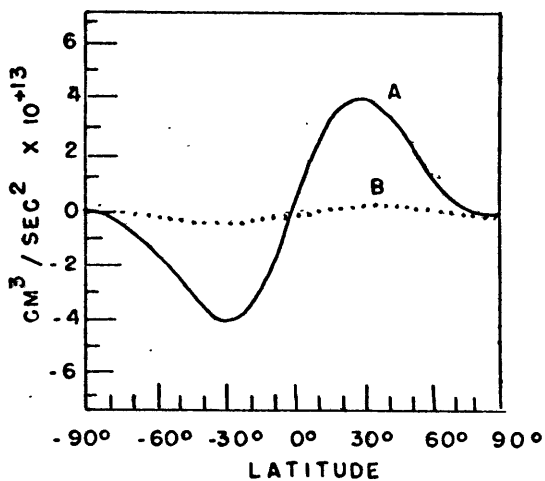
D-sum of A+B+C.



(g) Eddy and axisym. vert. heat transports.

A- $\langle w_2^* \theta_2^* \rangle$.

B- $\langle w_2 \rangle \langle \theta_2 \rangle$.



(h) Horiz. Reynolds stresses (vertical average).

A-eddy stress.

B-axisym. stress.

Fig. 6.1 continued

parameters held fixed throughout this study are given in Table 6.1. The values for ρ_s and T_s are based on a numerical stellar evolution model of Iben (1966). The ratio $\gamma = -5/3$ is appropriate to a fully ionized gas. The presence of helium (mass fraction ~ 0.1) is parameterized only by its contribution to the mean molecular weight. The rotation rate Ω of the lower boundary is the Greenwich convention value, 14.184 deg long/day, while g is very close to the currently accepted surface value of solar gravity.

Some test runs plus the two production runs are listed in Table 6.2, along with the values of the respective externally imposed variable parameters. Future reference is made to this table.

6.4. The Effects of Thermal Forcing Profile Type and Magnetic Fields upon the Angular Velocity Profile.

One objective was to find one or more time independent thermal forcing profiles $\sigma'_*(\varpi)$ associated with an equatorial jet. Five basic types of profiles were considered:

- (a) $\sigma_{*0} (1 - 3 \sin^2 \varpi), \sigma_{*0} > 0$
- (b) $\sigma_{*0} (1 - 3 \sin^2 \varpi), \sigma_{*0} < 0$
- (c) $\sigma_{*0} (1 - 10 \sin^2 \varpi + 35/3 \sin^4 \varpi), \sigma_{*0} > 0$
- (d) $\sigma_{*0} (1 - 10 \sin^2 \varpi + 35/3 \sin^4 \varpi), \sigma_{*0} < 0$
- (e) $\sigma_{*0} (1 - 5 \sin^2 \varpi + 10/3 \sin^4 \varpi), \sigma_{*0} > 0$

With the exception of (d), these profiles are illustrated in Fig. 6.2 for the quasi-normalized case $|\sigma_{*0}| = 1$. Profiles (a) and (b) are directly proportional to the Legendre polynomial P_2^0 ; (c) and (d) to P_4^0 . They are all even functions of latitude and contribute no net hemispheric heating.

Profile (a) corresponds to the warm equator-cold pole, i.e., terrestrial atmosphere case and (b) to the warm pole-cold equator case.

Table 6.2. Catalogue of Test Runs and Production Runs for Solar Model.

Name	R_{OT}^*	R_e	R_m	$\sigma_*' \text{ (}^\circ K)$	$V \text{ (cm}^2/\text{sec)}$	$V_{(H)} \text{ (cm}^2/\text{sec)}$	$\sigma_{(H)} \text{ (cm}^2/\text{sec)}$
test run 2	-0.143	6.67	-	$-10.23(1-10\sin^2\varphi + \frac{35}{3}\sin^4\varphi)$	3.42×10^9	0	0
test run 3	0.157	2	-	$24(1-10\sin^2\varphi + \frac{35}{3}\sin^4\varphi)$	3.91×10^{10}	0	0
test runs 4	variable	variable	-	$\sigma_{*0}(1-10\sin^2\varphi + \frac{35}{3}\sin^4\varphi)$ with $\sigma_{*0} > 0$, variable	variable	0	0
test run 5	0.077	20	-,100	$20(1-5\sin^2\varphi + \frac{10}{3}\sin^4\varphi)$	2.85×10^9	0	0
test run 6	0.116	5	-,100	$\frac{100}{3}(1-3\sin^2\varphi)$	3.04×10^{10}	0	0
test run 7	0.157	20	-,100	$24(1-10\sin^2\varphi + \frac{35}{3}\sin^4\varphi)$	3.91×10^9	0	0
P.R. 1	0.116	30	-,150	$30(1-5\sin^2\varphi + \frac{10}{3}\sin^4\varphi)$	2.85×10^9	6.52×10^{12}	6.52×10^{12}
test run 8	0.116	30	150	$30(1-5\sin^2\varphi + \frac{10}{3}\sin^4\varphi)$	2.85×10^9	6.52×10^{12}	6.52×10^{12}
test run 9	0.116	25	-	$\frac{100}{3}(1-3\sin^2\varphi)$	6.07×10^9	6.52×10^{12}	6.52×10^{12}
test run 10	-0.052	10	200	$-15(1-3\sin^2\varphi)$	6.84×10^9	6.52×10^{12}	6.52×10^{12}
test run 11	-0.087	20	-,100	$-25(1-3\sin^2\varphi)$	5.70×10^9	6.52×10^{12}	6.52×10^{12}
test run 12	-0.121	25	variable	$-35(1-3\sin^2\varphi)$	6.38×10^9	6.52×10^{12}	6.52×10^{12}
test runs 13	-0.121	25	-,500	$-35(1-3\sin^2\varphi)$	6.38×10^9	6.52×10^{12}	3.26×10^{11}
test runs 14	variable	variable	-	$\sigma_{*0}(1-3\sin^2\varphi)$ with $\sigma_{*0} < 0$, variable	variable	9.78×10^{12}	-
P.R. 2	-0.121	20	-,375	$-35(1-3\sin^2\varphi)$	7.66×10^9	9.78×10^{12}	4.89×10^{12}

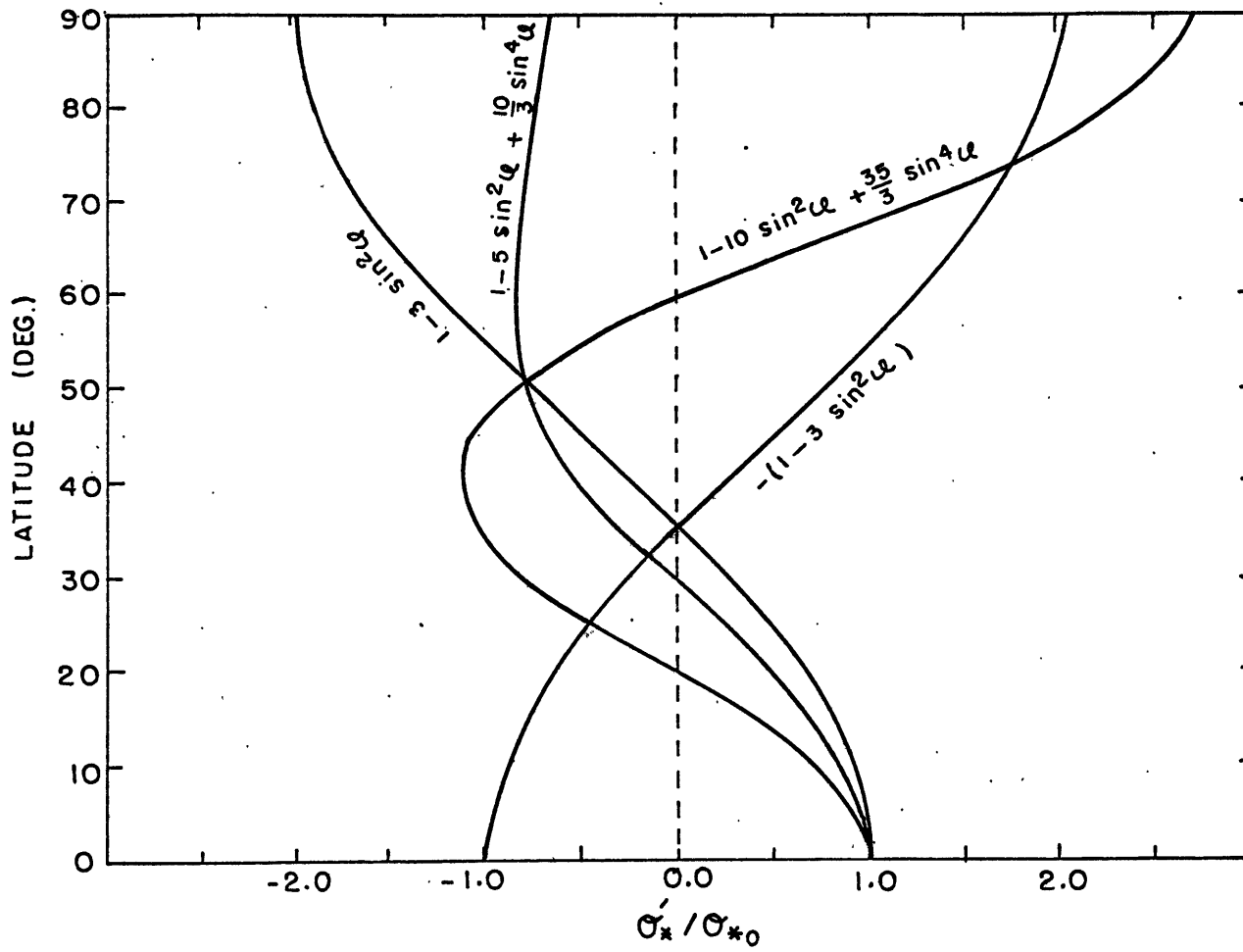


Fig. 6.2. Four types of thermal forcing profiles. These profiles have been quasi-normalized.

Thermal profiles (c) and (e) are intermediate between (a) and (b).

Extrapolation of Fultz's (1959) experimental results for a rotating dishpan would suggest that profiles (b) and (c) are the most promising. In fact, Fultz (1959) recognized a possible analogy between his experiments and certain aspects of the solar equatorial acceleration problem. Of course, the sun and our model have spherical geometry and lack sidewall boundaries, unlike the dishpan.

The chief difference between profiles (a) and (e) is that (e) begins to flatten at a lower latitude. Since (a) gave a mid-latitude jet in section 6.2, neither (a) nor (e) would seem too realistic for the sun, at least in the nonmagnetic case. Profile (d) represents a mid-latitude heat source. Higher resolution profiles would be more ad hoc and could not be resolved by our model anyway.

Table 6.3 summarizes our findings. Included is a qualitative description of the horizontal and vertical gradients of the time-zonal averaged absolute angular velocity

$$\bar{\omega}_{abs} = \omega + \sum_{m=0} \bar{\omega}_m \sin^m \varphi \quad (6-2)$$

and zonal wind

$$\langle \bar{u} \rangle = (\bar{\omega}_{abs} - \omega) a \cos \varphi \quad (6-3)$$

for each σ'_* profile. Secondly, the nonmagnetic (nm) and magnetic (m) cases may be compared in Table 6.3 for each σ'_* profile except (d). Thirdly, figures 6.8a, 6.3a, and 6.4a illustrate $\bar{\omega}_{abs}$ profiles in the magnetic and nonmagnetic cases for σ'_* profiles (b), (c), and (e), respectively. Corresponding potential temperature and σ'_* profiles appear in figures 6.8b, 6.3b, and 6.4b.

Table 6.3. Qualitative Effects of the σ_* Profile on Velocity Shear for Nonmagnetic and Magnetic Cases.

	$\sigma_{*0}(1-3\sin^2\varphi)$ $\sigma_{*0} > 0$ (a)	$\sigma_{*0}(1-3\sin^2\varphi)$ $\sigma_{*0} < 0$ (b)	$\sigma_{*0}(1-10\sin^2\varphi+35/3\sin^4\varphi)$ $\sigma_{*0} > 0$ (c)	$\sigma_{*0}(1-10\sin^2\varphi+35/3\sin^4\varphi)$ $\sigma_{*0} < 0$ (d)	$\sigma_{*0}(1-5\sin^2\varphi+10/3\sin^4\varphi)$ $\sigma_{*0} > 0$ (e)
$\partial \bar{u}_{abs} / \partial z$ lower lat. nm m	+ still +	- -	+ +	- -	+ +
$\partial \bar{u}_{abs} / \partial z$ higher lat. nm m	+ still +	- -	- -	+ -	+ +
$\partial \bar{u}_{abs} / \partial \varphi$ levels 2 and 3 nm m	+ generally +, but weaker	-, strength comparable to solar obs. Lv.2: mostly -, but weak. Lv.3: -, weaker, but still agrees qualitatively with obs.	-, strength comparable to solar obs. Lv.2: -, statistical residual. Lv.3: -, but weak	+ -	+ Lv.2: a very weak statistical residual. Lv.3: mostly -, but rather weak
upper level relative winds nm m	westerlies at all lat., jet at 50°-55° westerlies at all lat., mid-latitude jet usually	easterlies at all lat. For data sample of 5, jet at 50°-55° easterlies at all lat., jet at ~44°	quasi-steady westerly jet at equator, weaker easterly jet at 65° these jets are no longer permanent features	easterly jet at equator, weaker westerly jet at 60°-65°	westerlies at all lat. For data sample of 5, jet at 40°-45° westerlies at all lat., max. at equator.
lower level relative winds nm m	weak westerlies at higher latitudes, weak easterlies at lower latitudes still true	weak westerlies (easterlies) at low (high) latitudes weak easterlies (westerlies) at low (high) latitudes	easter. at low lat. wester. at high lat. these winds are no longer permanent features	weak easter. (westerlies) at low (high) latitudes still true	westerlies at higher latitudes, easterlies at lower latitudes still true
data source nm m	test run 6: quasi-steady, weak eddies. test run 9: strong eddies test run 6	mainly P.R. 2, but also test runs 9, 10, 11, 12, 13, 14 mainly P.R. 2, but also test run 12	test runs 3, 4, 7. Hadley and quasi-steady Rossby regimes. test run 7	test run 2 Hadley regime no magnetic runs made	test run 5, P.R. 1, other test runs in Rossby regime mainly P.R. 1

In equation (6-2), the spectral coefficient $\bar{\mathcal{N}}_2$ is a measure of the horizontal shear averaged over both hemispheres, while $\mathcal{N} + \bar{\mathcal{N}}_0$ is the rotation rate at the equator. From Newton and Nunn's formula, i.e., equation (1-1), $\mathcal{N} + \bar{\mathcal{N}}_0 = 14.38$ whereas $\bar{\mathcal{N}}_2 = -2.77$ degrees longitude per sidereal day, for the sun. In comparisons with solar observations, level 3 may be more appropriate, being closer to the visible surface, but level 2 is more representative of conditions in the model fluid as a whole.

Case (a): $\sigma_*' = \sigma_{*0}(1 - 3\sin^2\alpha), \sigma_{*0} > 0$.

The latitude distribution of relative winds and the signs of the horizontal and vertical gradients of absolute angular velocity are similar to those for the earth's atmosphere test run, i.e., there is no equatorial jet. Apparently, the horizontal shear of $\bar{\mathcal{N}}_{abs}$ decreases, but remains positive for the magnetic case. A shear reversal for a considerably larger value of R_m cannot be ruled out though.

Case (b): $\sigma_*' = \sigma_{*0}(1 - 3\sin^2\alpha), \sigma_{*0} < 0$.

This case is one of the two most successful. The horizontal shear $\bar{\mathcal{N}}_2$ is negative. From the nonmagnetic angular velocity profiles for production run 2 (P.R. 2), i.e., curves B and D in Fig. 6.8a, the ratios of computed to observed negative shears at levels 2 and 3 are respectively 1.1 and 1.7. The asymmetry of curve B between hemispheres might disappear with more data. The rates of rotation at the equator at levels 2 and 3 are 14.26 and 14.03 deg/day.

Other features for the nonmagnetic case which cannot be compared with solar observations include the following. First the vertical shear of $\bar{\mathcal{N}}_{abs}$ is everywhere negative, but strongest at high latitudes. Second, in the rotating reference frame, easterlies prevail except for a low latitude band of westerlies at levels 1 and 2. The upper level easterly

jet is centered at latitude 50° - 55° .

One indirect check of our model is Fultz's (1959) rotating dishpan experiments previously mentioned. Heating the center of the dishpan and cooling the rim produced an easterly regime at the top surface and a predominance of anticyclones over cyclones for $R_{OT}^* = -0.10$. An easterly jet was located between the rim and center. In a laboratory coordinate system, \bar{n}_{abs} would decrease from the rim to the easterly jet maximum rather than all the way to the center. This discrepancy between our model and the dishpan could be due to the different geometries and/or to the absence of an \mathcal{N}_4 harmonic in our model. Westerlies prevailed near the rim adjacent to the bottom of the dishpan.

When we introduce magnetic fields, the horizontal shear at both levels remains negative but decreases. In P.R. 2, the vertical shear remains negative and grows $\sim 20\%$ stronger. This is consistent with the strengthening of the potential temperature gradient. Energetically, the generation of $\langle ZPE \rangle$ also increases. The growth of strong magnetic fields characterized by $\alpha^2 \sim \mathcal{O}(1)$, rather than premature termination of the non-magnetic runs, is apparently responsible. In general, the magnetic model solutions are not quasi-steady as discussed later. The asymmetry in the magnetic curves in Fig. 6.8a is also probably a real model effect.

Case (c): $\underline{\alpha_*' = \alpha_* (1 - 10 \sin^2 \varrho + 35/3 \sin^4 \varrho)}, \alpha_* > 0$.

This is another successful run. Quasi-steady solutions were obtained for the nonmagnetic case. As for case (b), the horizontal shear of \bar{n}_{abs} is negative from equator to pole. From the nonmagnetic angular velocity profiles for test run 7 in Fig. 6.3a, the ratios of computed to observed negative shears at levels 2 and 3 are respectively 0.89 and 1.98. Meanwhile, the equatorial rotation rates at these levels are 15.43 and 16.79

deg/day. In contrast to case (b), the vertical shear of $\bar{\mathcal{N}}_{abs}$ is positive at low latitudes, as expected. An upper level westerly jet is now centered at the equator and easterlies are found at high latitudes. The streamlines of the relative velocity field at level 2 are illustrated in Fig. 6.21. Their tilt implies an equatorward angular momentum transport by eddy motions, which, with a little help from the surface frictional torque, completely balances the poleward transport by axisymmetric motions.

Fultz (1959) accidentally introduced heating in between profiles (b) and (c). This occurred when the center of the dishpan was heated and the rim not simultaneously cooled, because some heat was conducted along the bottom to the rim. At the top surface, the observed flow patterns and eddy transports were similar to the center heating-rim cooling case except for a narrow band of westerlies near the rim. These observations lend credence to our findings above.

For test run 7, \mathcal{N}_2 is weaker at level 3 but usually negative, in the magnetic as compared to the nonmagnetic case. In contrast, at level 2, \mathcal{N}_2 is a small negative statistical remnant. In fact, curve A of Fig. 6.3a shows an excursion into the $\mathcal{N}_2 > 0$ regime. The profiles in Fig. 6.3 for the magnetic case are not very representative, being based on a data sequence covering 10 rotations at intervals of two rotations. The qualitative difference in $\partial \bar{\mathcal{N}}_{abs} / \partial z$ between the magnetic and nonmagnetic cases is again consistent with the change in $\langle \bar{\theta}' \rangle$ in Fig. 6.3b. A magnetic production run for case (c) would be highly desirable, particularly if more resolution could be added to the model.

Case (d): $\sigma_*' = \sigma_* (1 - 10 \sin^2 \alpha + 35/3 \sin^4 \alpha), \sigma_* < 0.$

The results are nearly opposite to those for case (c) according to Table 6.3. Profile (d) seems incapable of reproducing the solar equator-

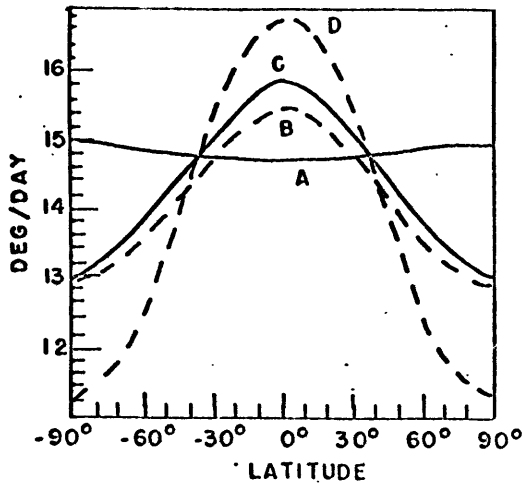


Fig. 6.3(a). Absolute angular veloc. $\bar{\mathcal{N}}_{abs}$ profiles for test run 7. A-level 2, magnetic. B-level 2, nonmagnetic. C-level 3, magnetic. D-level 3, nonmagnetic.

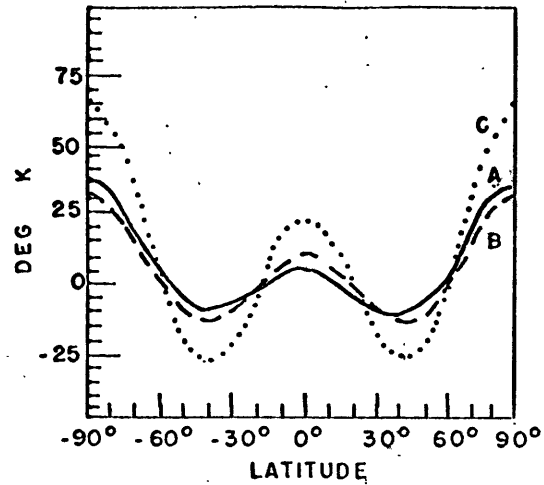


Fig. 6.3(b). Perturb. potential temperature and thermal forcing profiles for test run 7. A- $\langle \sigma_2' \rangle$, magnetic. B- $\langle \sigma_2' \rangle$, nonmagnetic. C- $\langle \sigma_*' \rangle$.

ial jet, at least for the nonmagnetic case.

Case (e): $\sigma_*' = \sigma_{*0} (1 - 5 \sin^2 \omega + 10/3 \sin^4 \omega)$, $\sigma_{*0} > 0$

The nonmagnetic solutions are rather similar to those for case (a), with the following exceptions. At level 3, $\bar{\mathcal{N}}_2$ is now weaker than at level 2, but still positive. This is consistent with thermal wind considerations and the kinematic constraints upon the spectral coefficients of $\bar{\mathcal{N}}_{abs}$ in equation (6-2). In any case, the westerly jet maximum is still at level 3, and its more equatorward position coincides with a similar displacement of the maximum gradient of σ_*' and $\langle \sigma_2' \rangle$ in Fig. 6.4b.

The introduction of dynamo-maintained magnetic fields significantly alters the situation in P.R. 1. The horizontal shear $\bar{\mathcal{N}}_2$ becomes negative at level 3, but is small by a factor of six compared to observations. Meanwhile at level 2, $\bar{\mathcal{N}}_2$ is only a very weak statistical residual, as seen in Fig. 6.4a. At level 3, the $\bar{\mathcal{N}}_{abs}$ profile is about 20% asymmetric about the equator. Meanwhile, the vertical shear of $\bar{\mathcal{N}}_{abs}$ remains

positive, (increasing a bit at the pole) along with the equator to pole temperature difference. This increase seems to be associated with the development of strong magnetic fields characterized by $\bar{a}^2 \sim \sigma(1)$.

Comparisons between Model Results and Solar Observations

In the nonmagnetic case, σ_* profiles (b) and (c) give results in best qualitative agreement with observations of the solar differential rotation. With the addition of magnetic fields, the value of $\bar{\lambda}_2$ is still of the correct order of magnitude at level 3, e.g., $\bar{\lambda}_2 = -2.08$ deg/day for P.R. 2. But at level 2, $\bar{\lambda}_2$ is only 23% of the observed value for P.R. 2 and <10% for test run 7. Case (e) gives interesting results for the magnetic case, but the negative shear is weak by a factor of nearly six at level 3 where $\bar{\lambda}_2 = -0.49$ and negligible at level 2. The horizontal angular velocity profiles for magnetic production runs 1 and 2 may be compared visually with Newton and Nunn's (1951) observed profile in figures 6.5 and 6.9. By varying λ and σ_{*0} respectively, $\bar{\lambda}_{2b5}(\varphi=0)$ for cases (a) through (e) and $\bar{\lambda}_2$ for nonmagnetic cases (b) and (c) probably could be tuned at either level 2 or level 3 to the observed solar values.

If the baroclinic hypothesis is to be plausible, the model horizontal temperature difference should not exceed $\sim 40^\circ\text{K}$. But the maximum differences in $\langle \overline{\sigma'_2} \rangle$ are respectively 90°K and 45°K for case (b) and case (c), while both gradients are about equal, due to the finer structure of σ_*' profile (c). From equation (2-50) and Table 6.1, the temperature range is about 85% of the potential temperature range. Thus the temperature differences are too large by a factor $F, 1 < F < 2$.

There are however some mitigating circumstances. First, for the nonmagnetic case, σ_{*0} could be conditionally decreased by nearly a factor of two for either profile (b) or (c). The condition is that $\bar{\lambda}_2$ at level

3 (as opposed to level 2) be used in computing the ratio of model to observed shear. Second, the thicker the baroclinic layer, the smaller the required horizontal (potential) temperature difference, e.g., $\Delta \theta_* < 10^\circ K$ if $2D \sim \sigma(R_{cz}) \sim 0.15 R_\odot$. The baroclinic layer could be considerably thicker than we have assumed. Third, it is not perfectly clear that the observations of temperature on "horizontal surfaces" are really surfaces of constant geopotential, or that horizontal temperature differences are not larger beneath the solar surface. Of course, the latter two arguments for not discarding the baroclinic approach are based on our ignorance rather than knowledge of the sun.

In the magnetic case, the value of $\bar{\mathcal{N}}_2$ at level 3 is weaker by a factor of two, but still agrees qualitatively with observations for σ_*^t profile (b). Also, the thermal forcing appears to maintain the vertical shear of $\bar{\mathcal{N}}_{abs}$. However $\bar{\mathcal{N}}_2$ at level 2 is too weak. By decreasing R_m , the Alfvén number would possibly increase. Magnetic fields would then have less impact upon the $\bar{\mathcal{N}}_{abs}$ profile and thus σ_{*0} could be decreased.

In principle, one could infer characteristics of the horizontal temperature structure from observations of $\partial \mathcal{N}_{abs} / \partial z$. For our baroclinic model at least, a thermal wind relation is clearly operative. The $\partial \mathcal{N}_{abs} / \partial z$ data cited by Bumba (1967) is for a fluid layer only 200 km thick located near the equator. Although case (c) fits this data better than case (b) within the context of the baroclinic hypothesis, the data sample is probably too small to conclude that (c) is the better profile.

Reliability of the Results.

In the experiments, R_{σ}^* and R_e were not held exactly fixed

while σ_*' was varied, as can be seen from Table 6.2. Some of the test runs involved served dual purposes and our main objective was to make one or more production runs, before using up our allotted computer time. However, the qualitative angular velocity results of Table 6.3 appeared to hold up over the ranges (if any) of R_{OT}^* and/or R_e encountered for given σ_*' . (Magnetic runs were restricted to the Rossby regime.)

An error was discovered in magnetic test runs 5,6, and 7 and later corrected in run 7, but the qualitative magnetic results for σ_*' profile (c) in Table 6.3 remained intact. The effect of the error upon test run 6 was not assessed, but the magnetic results for σ_*' profile (a) seem plausible.

The sample size used to compute the time averaged curves of figures 6.3, 6.4, and 6.8 were small except for the magnetic case curves of Fig. 6.4 (P.R. 1) and Fig. 6.8 (P.R. 2). Thus the first group of curves depart somewhat from the long term time average. They should still be qualitatively correct, though. Of the nonmagnetic curves, those of figure 6.3 are the most accurate due to the quasi-steady nature of the solutions for nonmagnetic test run 7. Subjective scrutiny of the computer printout of the angular velocity, confirmed the qualitative results of Table 6.3.

Increased resolution would probably cause some modifications of the results, especially for the magnetic case. Therefore runs with more resolution would clearly be desirable. But at least the indirect qualitative confirmation of our nonmagnetic solutions for σ_*' profiles (b) and (c) by Fultz's (1959) dishpan experiments is encouraging.

6.5. General Circulation Statistics for Production Runs 1 and 2.

Enough computer time was available for two extended magnetic production runs. Thermal forcing profiles (b) and (e) were selected for P.R. 1

and P.R. 2, respectively. The other promising profile, i.e., (c), is an intermediate case. Since the fourth order harmonic is considerably more dominant in this profile than in (e), the resolution difficulties could be more acute. The angular velocity and potential temperature profiles for P.R. 1 and P.R. 2 already have been discussed. The other statistics include the $\langle \overline{v_1} \rangle$ and $\langle \overline{w_2} \rangle$ velocity fields in meridional planes, the horizontal eddy heat transport, the vertical eddy and axisymmetric heat transports, the vertically averaged angular momentum balance, and the Reynolds and Maxwell stresses.

The time averaged statistics are based on many values (700 at intervals of one solar rotation) for the magnetic case, but on only 5 for the nonmagnetic case. From this standpoint, more confidence could be placed in statistics for the magnetic case, while comparisons between the magnetic and nonmagnetic cases should be regarded as qualitative. Of course, in a broader sense, all the results are crude, since the model resolution is so low.

6.5.1. Production Run 1. $(\sigma'_* = 30(1 - 5 \sin^2 \varphi + 10/3 \sin^4 \varphi)^\circ \text{K})$

The statistics for P.R. 1 are illustrated in figures 6.4, 6.5, 6.6, and 6.7. Tables 6.1 and 6.2 may be consulted for the values of the relevant parameters. Figures 6.4c and 6.4d imply that the mean meridional circulation consists of a direct cell at low latitudes and an indirect cell at high latitudes¹ (poleward of 45°). The circulation pattern is very similar to the one discussed in section 6.2 for the terrestrial atmosphere case. For the magnetic case, the direct cell is somewhat stronger and the

¹Perhaps the term quasi-indirect is more appropriate in view of the (weak) relative minimum in $\langle \overline{\sigma'_2} \rangle$ at latitude 70° , for the nonmagnetic case.

indirect cell somewhat weaker than for the nonmagnetic case. The maximum value of $\langle \overline{v_1} \rangle$ is roughly 9 m/sec at $\varrho = 25^\circ$, which does not contradict Ward's (1964) results. (i.e., his confidence limits are larger).

The horizontal eddy heat transport depicted in Fig. 6.4g is computed by truncating the true scalar $\frac{1}{a \cos \varrho} \frac{\partial}{\partial \varrho} (\langle \overline{v_2^* \theta_2'^*} \rangle \cos \varrho)$, integrating, dividing by $\cos^2 \varrho$, and finally multiplying by $\cos \varrho$. Meanwhile, $\langle \overline{w_2^* \theta_2'^*} \rangle$ and $\langle \overline{w_2} \rangle \langle \overline{\theta_2'} \rangle$ are truncated directly. For the nonmagnetic case, the three heat transport curves resemble those of figures 6.1g and 6.1h. The curve remains positive (negative) above latitude 70°N (70°S), due perhaps to the low model resolution.

There is a fairly dramatic change in heat transports for the magnetic case. The horizontal eddy heat transport and vertical eddy heat transport are greatly reduced at mid-latitudes, while the vertical axisymmetric heat transport is somewhat enhanced at low latitudes. Thus the energy conversions $\{ \langle \text{ZPE} \rangle \rightarrow \langle \text{EPE} \rangle \}^2$ and $\{ \langle \text{EPE} \rangle \rightarrow \langle \text{EKE} \rangle \}$ are smaller, whereas $\{ \langle \text{ZPE} \rangle \rightarrow \langle \text{KM} \rangle \}$ is larger. According to Gilman's (1967) linearized normal mode analysis of a quasi-heliostrophic model, baroclinic instability is totally suppressed if $a^2 < 4$. The critical value a_{CRIT}^2 is apparently somewhat lower in our primitive equation model. But usually, $a^2 > a_{\text{CRIT}}^2$ since significant but not total suppression of baroclinic instability occurs. Plots of w_2 and $\frac{B}{H_2}$ suggest that vertical motion eddies w_2^* are strongest where the axisymmetric toroidal magnetic field $\langle B_2^\lambda \rangle$ is locally weak. (See later discussion.)

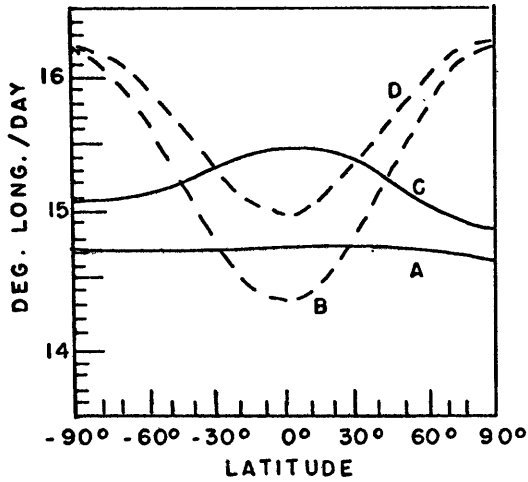
The nonmagnetic "correctly truncated" angular momentum balance (per unit mass) for P.R. 1 is illustrated in Fig. 6.4e. Curves A and B represent the convergences of the horizontal eddy transport and meridional

²This conversion would be weaker except for the stronger meridional gradient of $\langle \theta' \rangle$.

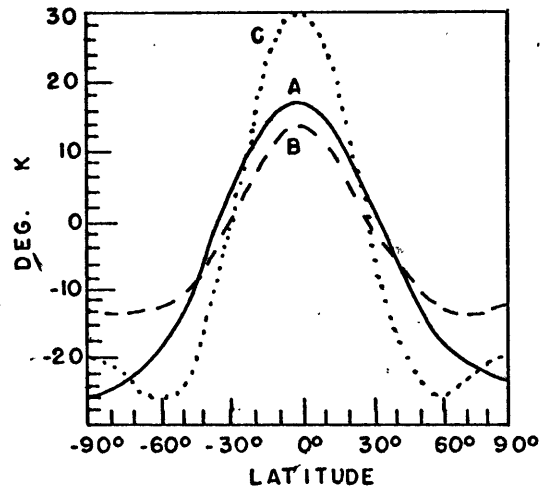
transport of angular momentum, respectively. Integration of these curves leads to the actual angular momentum transports of Fig. 6.4f. Both the eddies and the axisymmetric meridional cells transport angular momentum from low to high latitudes. The equatorward transport by the indirect meridional cell has been smoothed out by truncation. The eddy transport is stronger by a factor of 2.5 and reaches a maximum at 30° - 35° latitude. The two transports are approximately balanced by the total frictional torque. (Fig. 6.4e, curve C). The slight imbalance (curve D) is a manifestation of the small data sample.

Concerning the total frictional torque, an anisotropic eddy viscosity has been included to help selectively damp the higher harmonics. The horizontal eddy viscosity has a characteristic decay time of the lowest order mode of $\sim O(20)$ years. As the horizontal viscous dissipation term contributes only $\sim 10\%$ to the total frictional torque, the latter is essentially the torque exerted on the fluid by the rigidly rotating lower boundary.

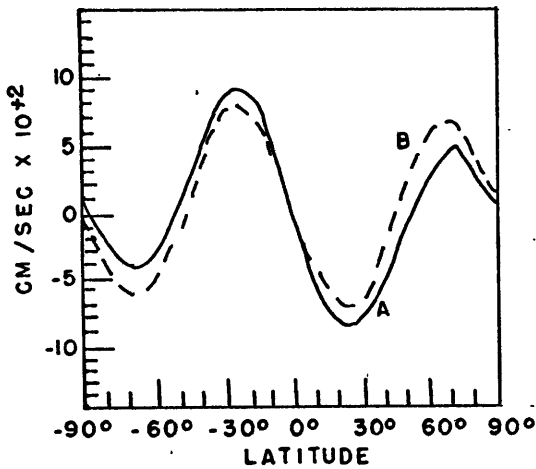
Figure 6.6 contains the "correctly truncated" angular momentum balance for the magnetic case. The convergence of eddy and axisymmetric transports of angular momentum are still negative at low latitudes and positive poleward of 25° - 30° latitude. However, with the partial suppression of baroclinic instability by the magnetic fields, the horizontal eddy transport is reduced by nearly a factor of five as seen from figures 6.4f and 6.7. Moreover, the eddies still transport angular momentum away from the equator. Thus with or without magnetic fields, the horizontal eddy transport for P.R. 1 is completely contrary to Ward's (1964) observational findings. The horizontal axisymmetric transport is little changed



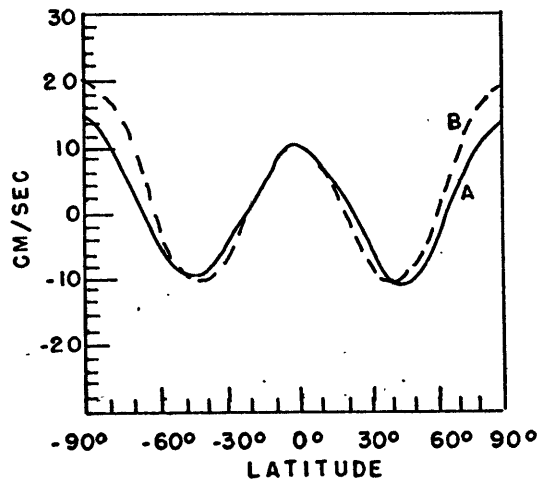
(a) Absolute angular velocity $\bar{\mathcal{N}}_{abs}$.
 A-level 2, magnetic.
 B-level 2, nonmagnetic.
 C-level 3, magnetic.
 D-level 3, nonmagnetic.



(b) Perturb. potential temp. and thermal forcing profiles.
 A- $\langle \theta_2' \rangle$, magnetic.
 B- $\langle \theta_2' \rangle$, nonmagnetic.
 C- $\langle \theta_*' \rangle$.

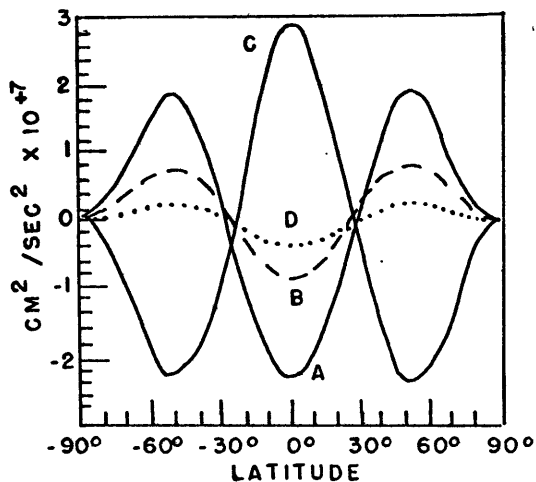


(c) Meridional velocity $\langle \bar{v}_1 \rangle$.
 A-magnetic; B-nonmagnetic.

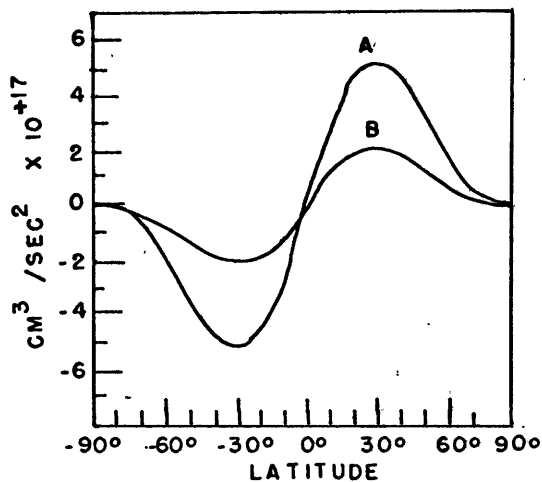


(d) Vertical velocity $\langle \bar{w}_2 \rangle$.
 A-magnetic; B-nonmagnetic.

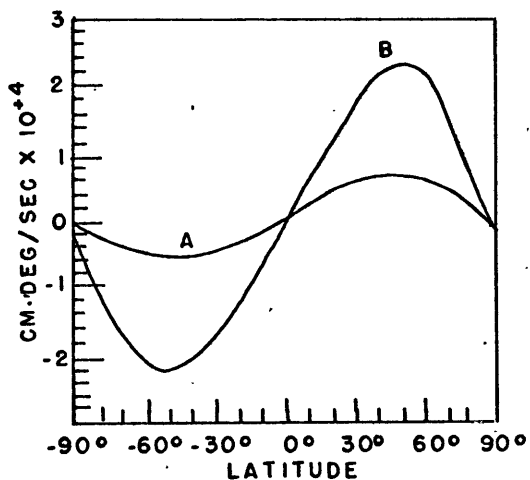
Fig. 6.4. Some general circulation statistics for P.R. 1.



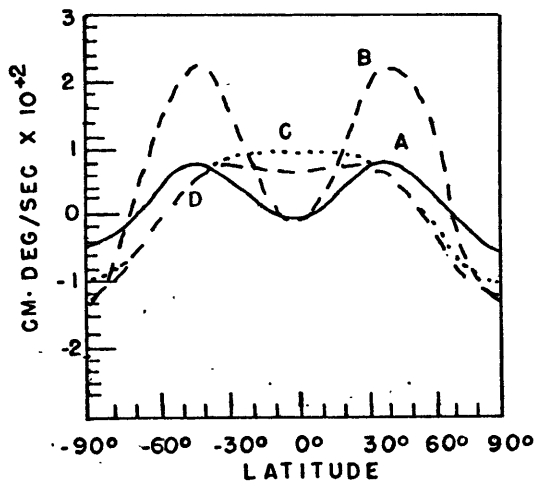
(e) Nonmagnetic angular momentum balance (vertical average).
 A-converg. horiz. eddy transport.
 B-converg. horiz. axisym. transport.
 C-frictional torque.
 D-sum of A+B+C.



(f) Horiz. Reynolds stresses (vertical average).
 A- eddy stress.
 B-axisym. stress.



(g) Horiz. eddy heat transport.
 A- $\langle v_2^* \theta_2'^* \rangle$, magnetic.
 B- $\langle v_2^* \theta_2'^* \rangle$, nonmagnetic.



(h) Vert. eddy and axisym. heat transp.
 A- $\langle w_2^* \theta_2'^* \rangle$, magnetic.
 B- $\langle w_2^* \theta_2'^* \rangle$, nonmagnetic.
 C- $\langle w_2 \rangle \langle \theta_2' \rangle$, magnetic.
 D- $\langle w_2 \rangle \langle \theta_2' \rangle$, nonmagnetic.

Fig. 6.4. continued.

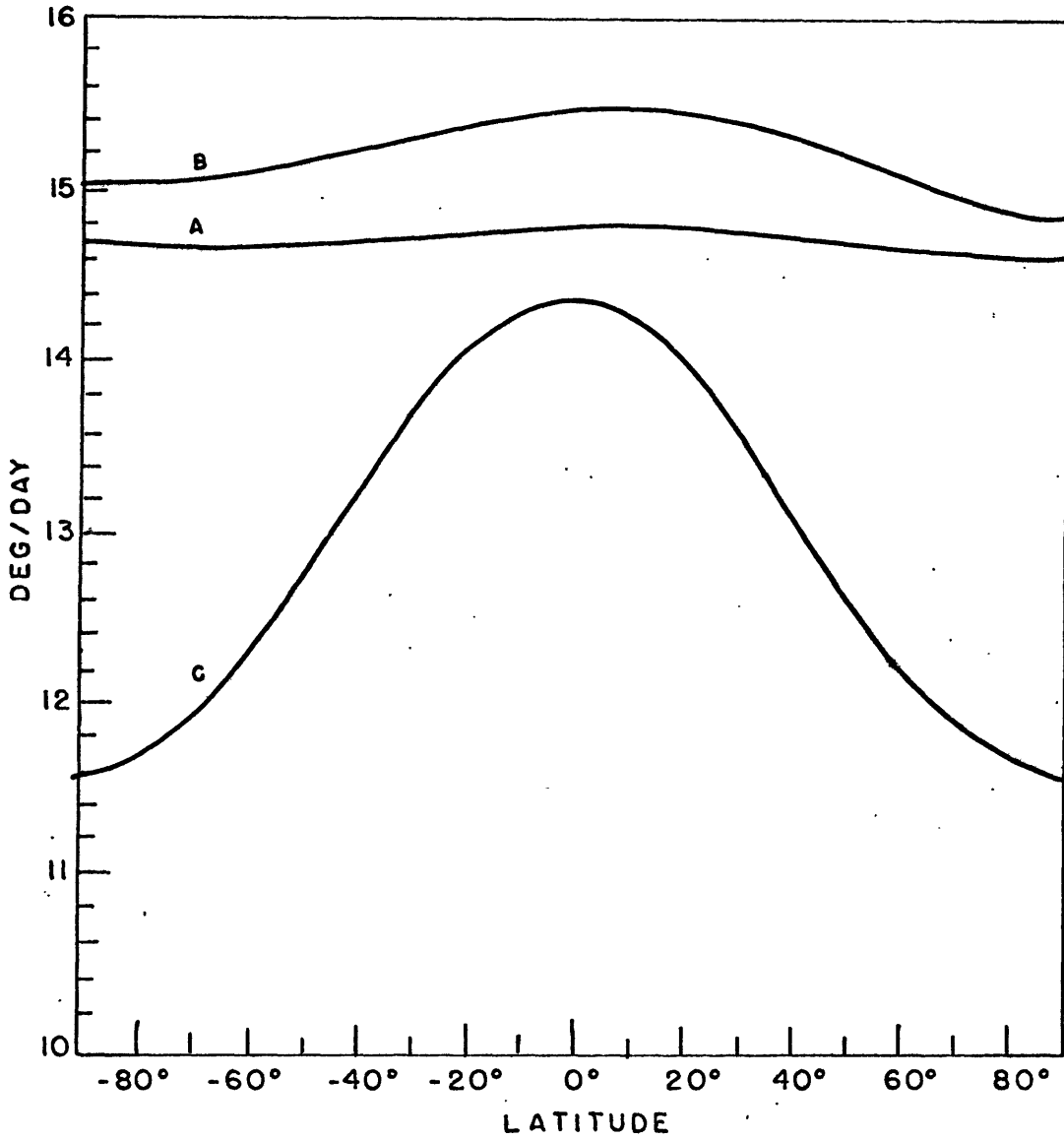


Fig. 6.5. Comparison of absolute angular velocity profiles of magnetic P.R. 1 with observations.

A- $\bar{\mathcal{N}}_{abs}$ at level 2.

B- $\bar{\mathcal{N}}_{abs}$ at level 3.

C-Newton and Nunn's (1951) observed profile.

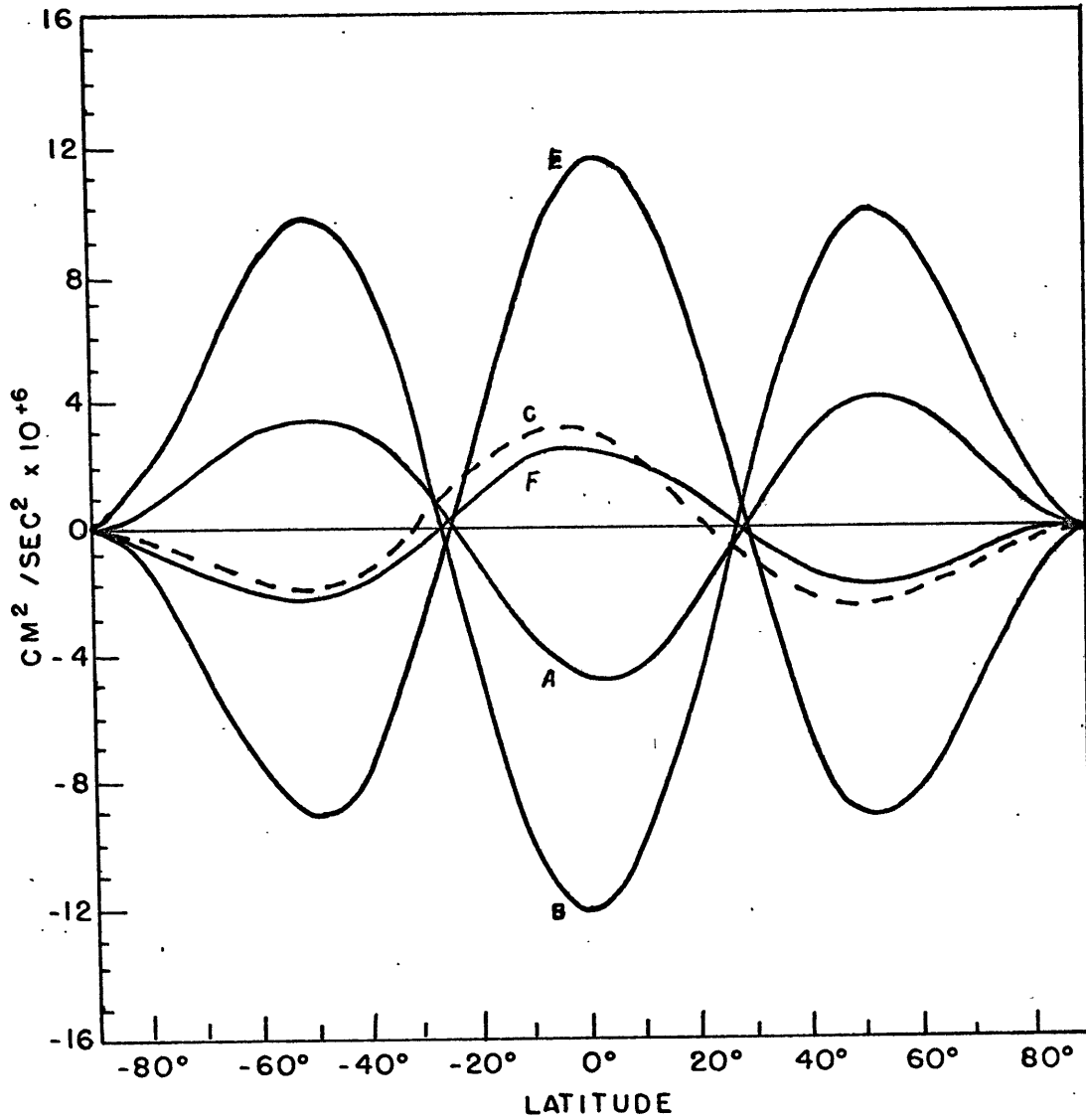


Fig. 6.6. Vertically averaged angular momentum balance of magnetic P.R. 1.

- A-convergence of horizontal eddy transport (Reynolds stress).
- B-convergence of horizontal axisymmetric transport (Reynolds stress).
- C-total frictional torque.
- E-divergence of horizontal axisymmetric Maxwell stress.
- F-divergence of horizontal eddy Maxwell stress.

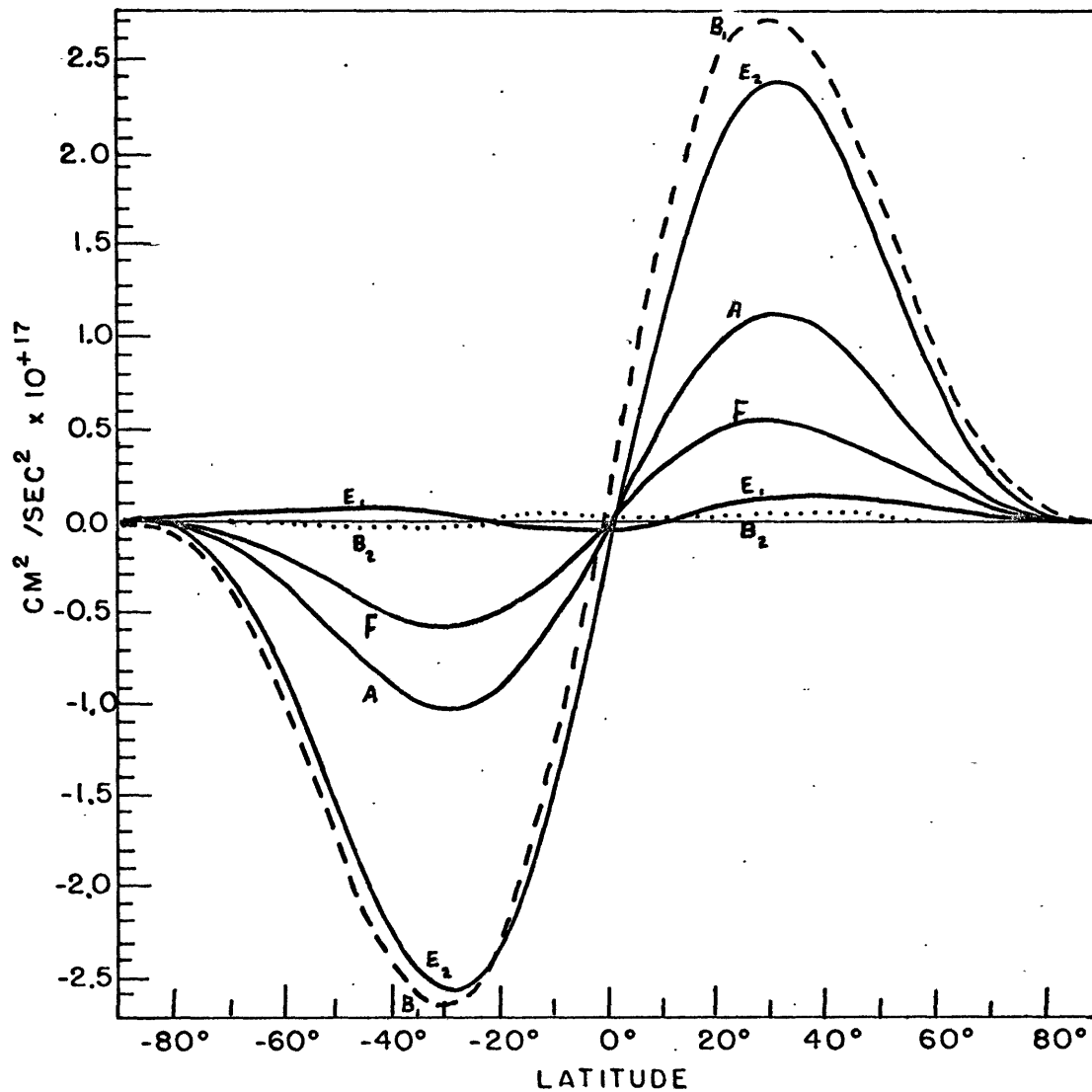


Fig. 6.7. Vertically averaged horizontal Reynolds stresses and Maxwell stresses of magnetic P.R. 1.

- A-eddy Reynolds stress.
- B₁-stationary axisymmetric Reynolds stress.
- B₂-fluctuating axisymmetric Reynolds stress.
- E₁-stationary axisymmetric Maxwell stress.
- E₂-fluctuating axisymmetric Maxwell stress.
- F-eddy Maxwell stress.

(only ~20% larger) from the nonmagnetic case but is now the dominant transport mechanism. The frictional torque term in the angular momentum balance (curve C) is much smaller in the magnetic case. But it is similar in shape to its nonmagnetic case counterpart except for a 5° phase shift.

Two new terms are the divergence of the horizontal eddy Maxwell stress (curve F) and the divergence of the horizontal axisymmetric Maxwell stress (curve E). The latter is the second largest term in the angular momentum balance and almost balances the convergence of the axisymmetric transport. This is not inconsistent with the drastic change, i.e., almost total destruction of $\bar{\mathcal{N}}_2$ at level 2. The eddy magnetic term is half the size of the corresponding eddy transport term but of opposite sign. It gives almost an identical contribution as the frictional torque term.

The Maxwell stresses are obtained by integrating the two terms above. They have the same sign as the Reynolds stresses³, as indicated in Fig. 6.7. Here, the axisymmetric stresses have each been split up into two parts, i.e., (1) a product of time-zonal means and (2) a time averaged product of two time eddies of zonal quantities. Note that the steady axisymmetric Reynolds stress (curve B₁) is much larger than its unsteady counterpart (curve B₂). Conversely, the steady axisymmetric Maxwell stress (curve E₁) is negligible compared to the unsteady axisymmetric Maxwell stress (curve E₂), which is not unreasonable for a reversing dynamo.

Typical propagation speeds of disturbances are roughly $+15^\circ$ longitude (i.e., 1/4 wavelength) per rotation, in both the nonmagnetic and magnetic cases. This value is comparable in order of magnitude to the westerly zonal current. The β effect is evidently weak since $\eta = 6$ and

³At level 2, the total horizontal Maxwell and Reynolds stresses are respectively $+\frac{1}{2}(4\pi\mu_0\bar{g}_z)^{-1}(B_1^A B_1^u + B_3^A B_3^u)a \cdot \cos u$ and $+\frac{1}{2}(u_1 v_1 + u_3 v_3)a \cdot \cos u$, according to our sign convention. The factor $a \cdot \cos u$ is really the torque arm length.

$m \geq 2$, generally speaking, for the wave disturbances.

6.5.2. Production Run 2. ($\sigma'_* = -35(1-3\sin^2\varphi)^\circ K$).

General circulation statistics are summarized in figures 6.8, 6.9, 6.10, and 6.11. See tables 6.1 and 6.2 for values of parameters for production run 2. Again the axisymmetric circulation in meridional planes depicted in Fig. 6.8c and Fig. 6.8d contains both a direct and an indirect cell. But the indirect cell is relatively weaker and is confined closer to the pole for this run. The circulation of the northern hemisphere extends about 5° into the southern hemisphere in the magnetic case. But the main change which occurs after the magnetic fields have been introduced is an increase in strength of the circulation. This is not inconsistent with the increased temperature gradient in Fig. 6.8b. Once more, the development of strong magnetic fields, and not the premature termination of the nonmagnetic runs probably is the cause. At any rate, the direct cell is about 50% stronger in the magnetic case, and both the direct and indirect cells are in phase with their nonmagnetic counterparts. The maximum values of $\langle \overline{v} \rangle$ for the nonmagnetic and magnetic case are respectively 14 and 21 m/sec, at about 25° - 30° latitude. The latter value just falls outside of Ward's (1964) confidence limits on $\langle \overline{v} \rangle$.

Baroclinic instability is rather noticeably suppressed at mid-latitudes by magnetic fields, as was found to occur in production run 1. One change though in P.R. 2 is that the axisymmetric vertical heat transport becomes positive at all latitudes in the magnetic case. Fig. 6.8h indicates that $\{ \langle ZPE \rangle \rightarrow \langle KM \rangle \}$ will be \sim as large as $\{ \langle EPE \rangle \rightarrow \langle EKE \rangle \}$. Another change from P.R. 1 for both the nonmagnetic and magnetic cases is that the horizontal eddy heat transport is now equatorward, which is no surprise.

In P.R. 2, the decay time for horizontal viscous dissipation (of the lowest order mode) is 15 years. As in P.R. 1, the horizontal dissipation contributes only $\sim 10\%$ to the total frictional torque.

The "correctly truncated" angular momentum balance for nonmagnetic P.R. 2 is illustrated in Fig. 6.8e and the horizontal transports (Reynolds stresses) in Fig. 6.8f. In the rotating coordinate system, the winds are easterly except for a low latitude band of westerlies at level 1 and level 2. Hence, according to figures 6.8e and 6.8f, the horizontal eddies are maintaining the mid-latitude easterly jet whereas the total frictional torque and axisymmetric meridional circulation work to destroy it. The poleward transport of easterly (i.e., negative) angular momentum by the horizontal eddies is equivalent to an equatorward transport of westerly (i.e., positive) angular momentum. The "correctly truncated" eddy Reynolds stress reaches maximum values at $\pm 25^\circ$, is roughly three times larger than the axisymmetric Reynolds stress, and is of opposite sign. Figure 6.8 was constructed from a small amount of data, as indicated previously. This may explain the imbalance (curve D).

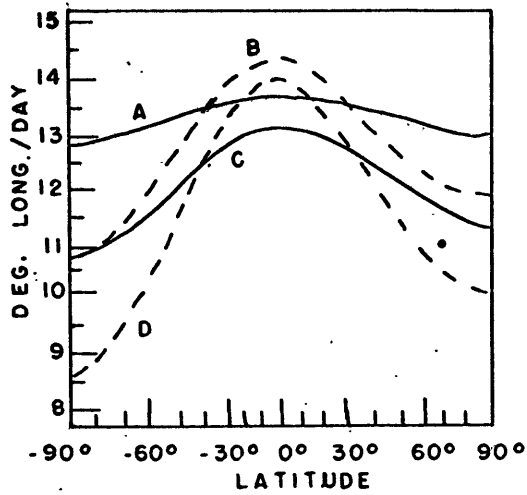
Incidentally, Fultz (1959) observed horizontal eddies between the rim and the center of his upper level easterly jet (discussed earlier), which were tilted in the same sense as ours. Moreover, the required angular momentum transport was accomplished predominantly by these eddies.

The horizontal axisymmetric transport overshadows the horizontal eddy transport of angular momentum in magnetic P.R. 2. But the phases of both terms are not changed much from the nonmagnetic case. The reduction of the eddy Reynolds stress by a factor of five is again attributed to the partial suppression of baroclinic instability by magnetic fields. The axisymmetric Reynolds stress increases by about a factor of two which is

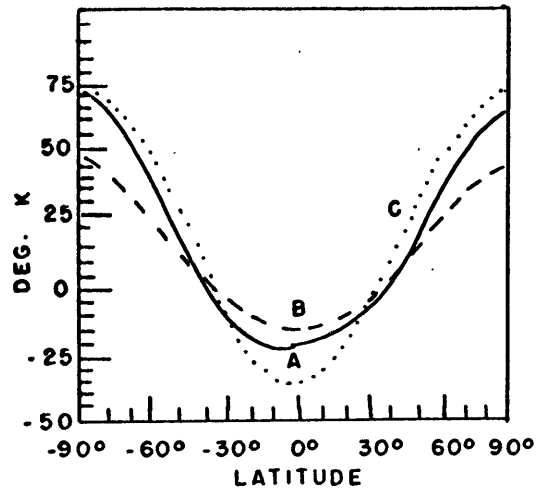
somewhat more than the increase in strength of the axisymmetric meridional circulation. This extra increase may reflect the greater relative dominance of the direct cell in the magnetic case.

A peculiar phenomenon in the magnetic case is the reversal of the regions of easterlies and westerlies at level 1. This may be analogous to the reversal of the shear of $\bar{\mathcal{N}}_{abs}$ in P.R. 1 after large amplitude magnetic fields were generated. (No programming errors were found.) Due to the wind reversal, the frictional torque helps maintain rather than destroy the mid-latitude easterly jet, as if the differential rotation were partly friction-driven. The torque is considerably weaker in magnitude though than in the nonmagnetic case. The phenomenon is apparently a reaction to a magnetic drive. Kippenhahn's (1963) analysis is probably inapplicable even though we have $V_{(H)} > V$, because his circulation is frictionally-driven in the nonmagnetic case and is not characterized by $R_e \gg 1$. It remains to be seen if the above result would hold up in a model with greater horizontal (and vertical) resolution.

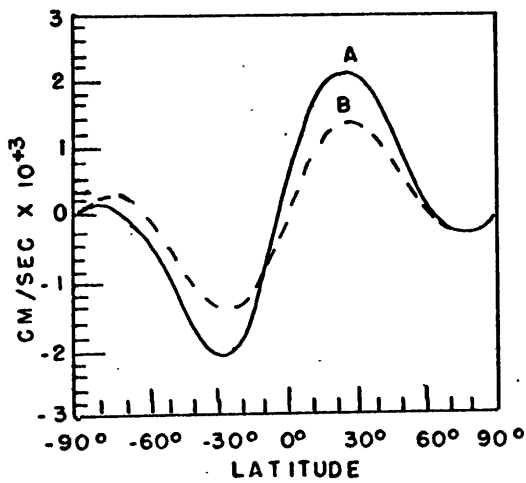
The convergence of the horizontal axisymmetric transport is now the largest sink of westerly (easterly) angular momentum near (far from) the equator. It is opposed by three terms: (1) the frictional torque, (2) the convergence of the horizontal eddy transport, and (3) the divergence of the eddy Maxwell stress. Of these, term (1) is a bit larger than (2) which in turn is roughly three times larger than (3). The divergence of the axisymmetric Maxwell stress is rather nonsymmetric about the equator. Secondly, it is smaller here relative to the convergence of the axisymmetric Reynolds stress, than in P.R. 1. These two terms tend to oppose each other, but they work together at some latitudes. The sum of terms displayed in Fig.



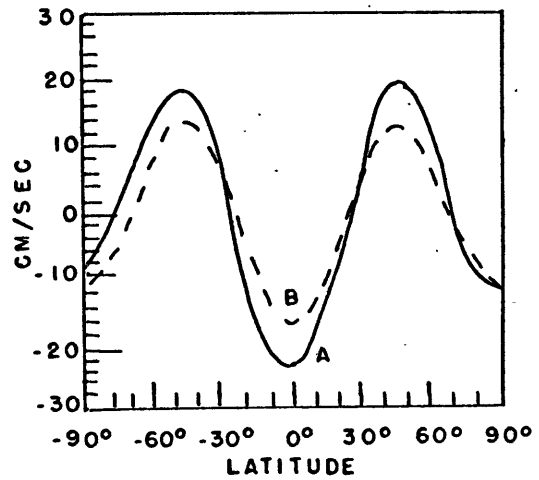
(a) Absolute angular velocity \bar{n}_{abs}
 A-level 2, magnetic.
 B-level 2, nonmagnetic.
 C-level 3, magnetic.
 D-level 3, nonmagnetic.



(b) Perturb. potential temp. and thermal forcing profiles.
 A- $\langle \theta_2' \rangle$, magnetic.
 B- $\langle \theta_2' \rangle$, nonmagnetic.
 C- $\langle \theta_x' \rangle$.

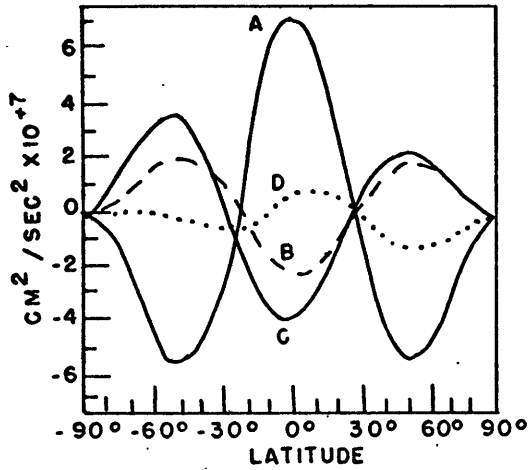


(c) Meridional velocity $\langle \bar{v}_1 \rangle$.
 A-magnetic; B-nonmagnetic.

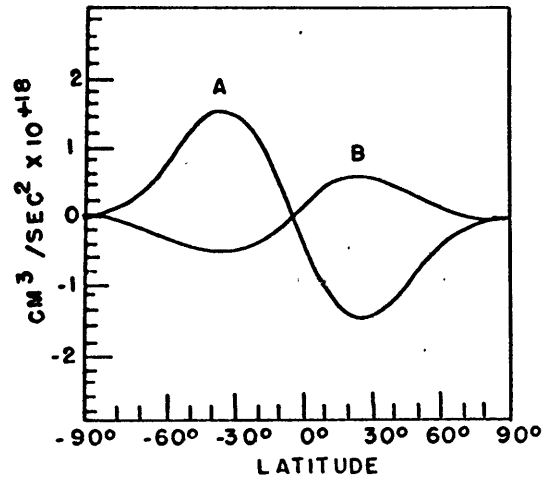


(d) Vertical velocity $\langle \bar{w}_2 \rangle$.
 A-magnetic; B-nonmagnetic.

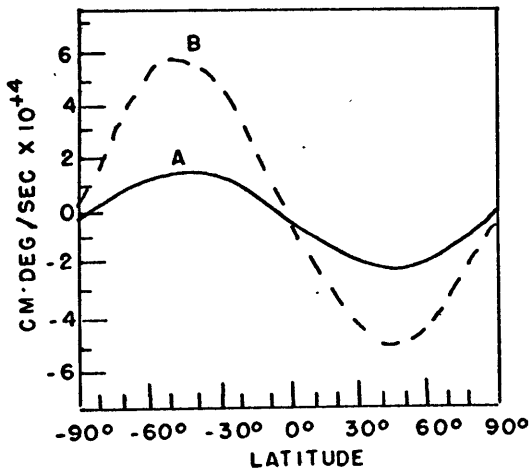
Fig. 6.8. Some general circulation statistics for P.R. 2.



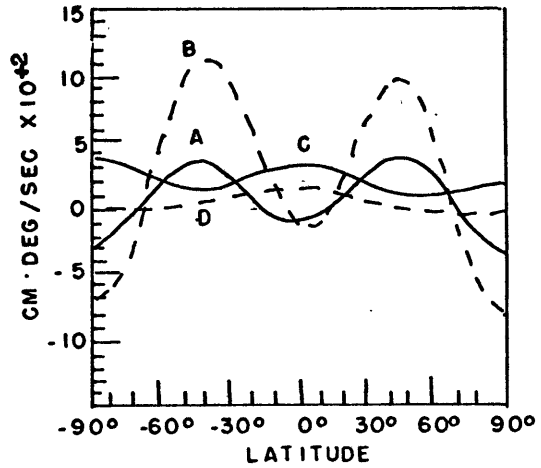
(e) Nonmagnetic angular momentum balance (vertical average).
 A-converg. horiz. eddy transport.
 B-converg. horiz. axisym. transport.
 C-frictional torque.
 D-sum of A+B+C.



(f) Horiz. Reynolds stresses (vertical average).
 A-eddy stress.
 B-axisym. stress.



(g) Horiz. eddy heat transport.
 A- $\langle V_2^* \sigma_2'^* \rangle$, magnetic.
 B- $\langle V_2^* \sigma_2'^* \rangle$, nonmagnetic.



(h) Vert. eddy and axisym. heat transp.
 A- $\langle w_2^* \sigma_2'^* \rangle$, magnetic.
 B- $\langle w_2^* \sigma_2'^* \rangle$, nonmagnetic.
 C- $\langle w_2 \rangle \langle \sigma_2' \rangle$, magnetic.
 D- $\langle w_2 \rangle \langle \sigma_2' \rangle$, nonmagnetic.

Fig. 6.8. continued.

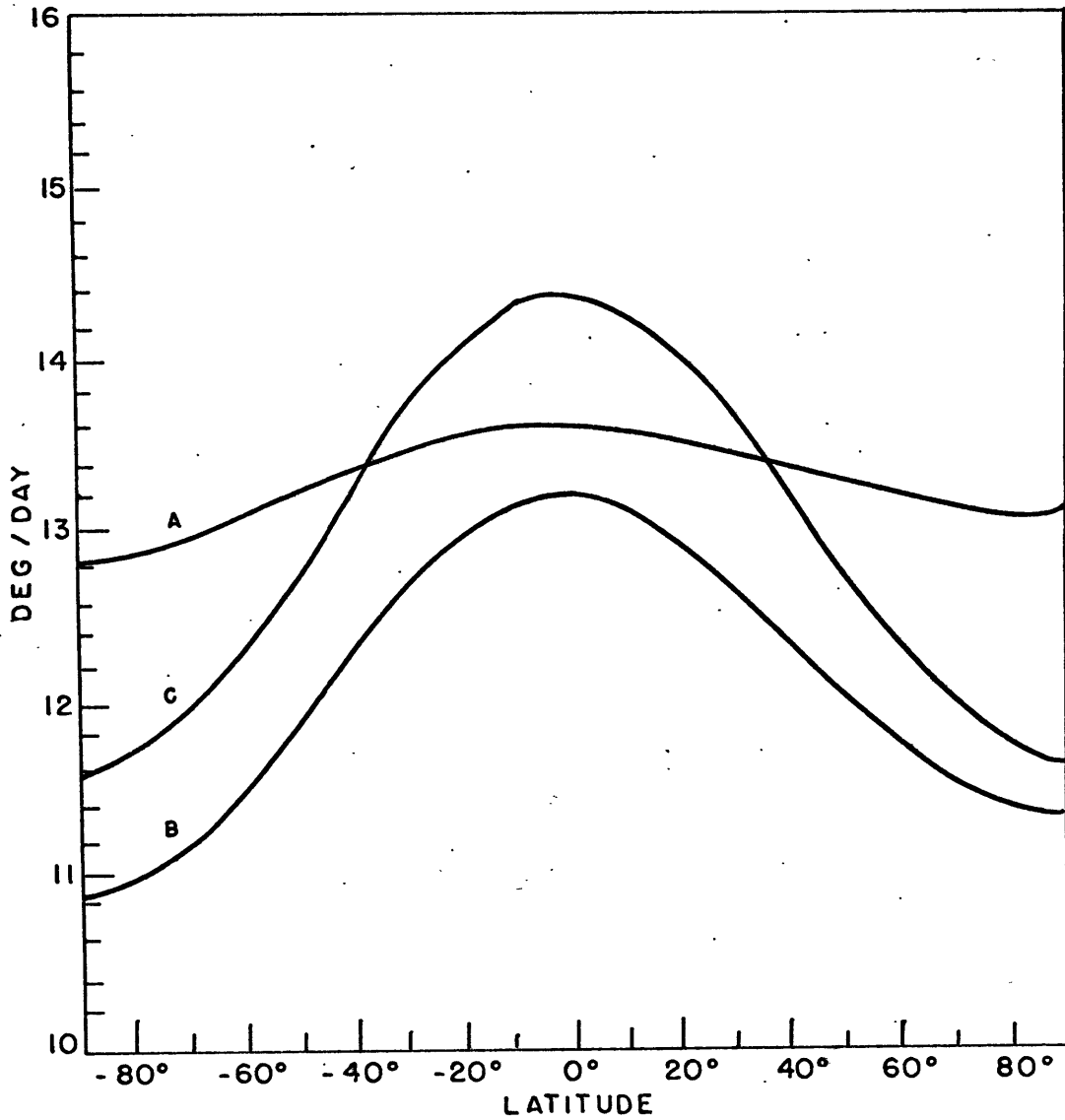


Fig. 6.9. Comparison of absolute angular velocity profiles of magnetic P.R. 2 with observations.

A- \bar{n}_{abs} at level 2.

B- \bar{n}_{abs} at level 3.

C-Newton and Nunn's (1951) observed profile.

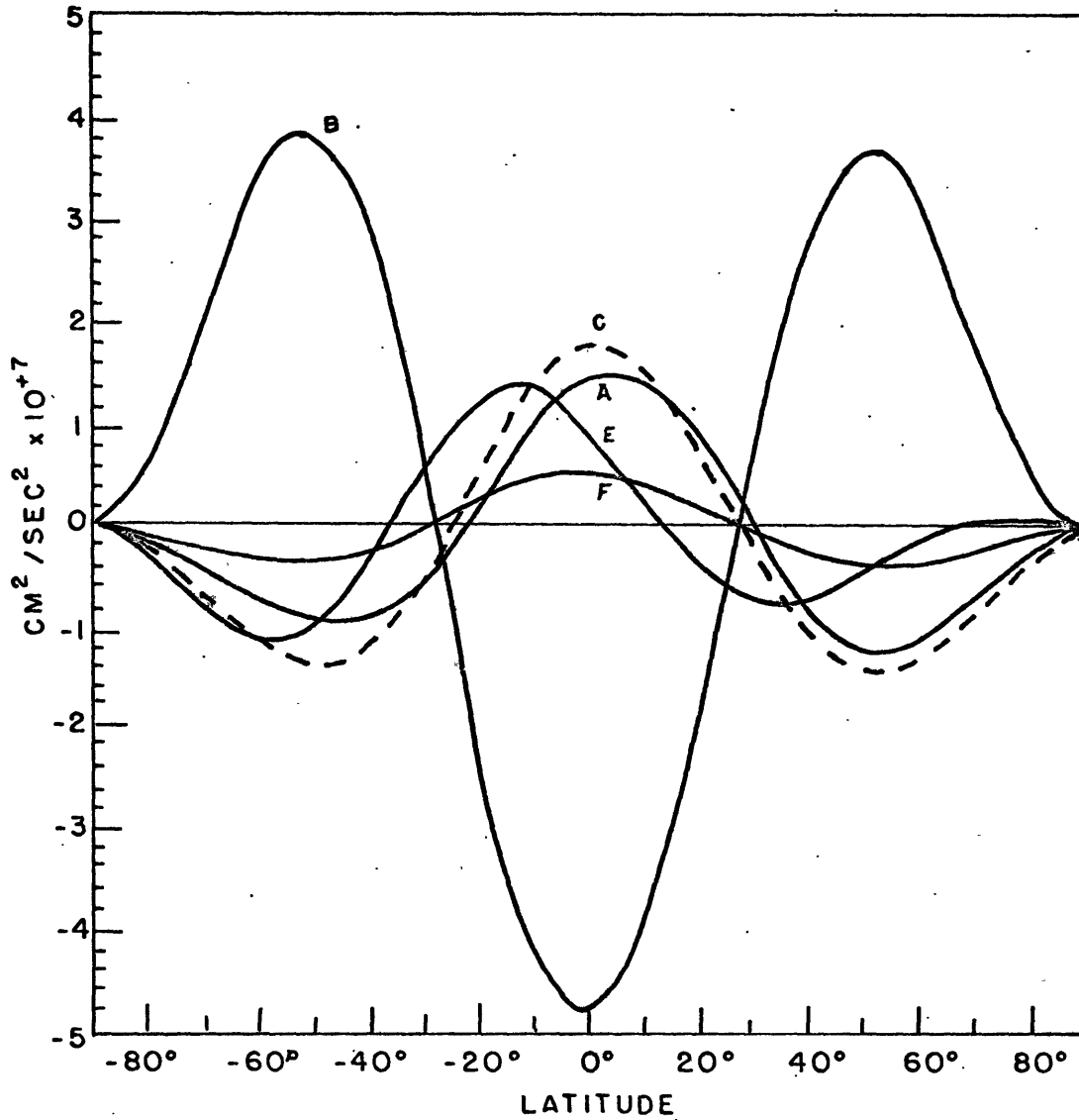


Fig. 6.10. Vertically averaged angular momentum balance of magnetic P.R. 2.

- A-convergence of horizontal eddy transport (Reynolds stress).
- B-convergence of horizontal axisymmetric transport (Reynolds stress).
- C-total frictional torque.
- E-divergence of horizontal axisymmetric Maxwell stress.
- F-divergence of horizontal eddy Maxwell stress.

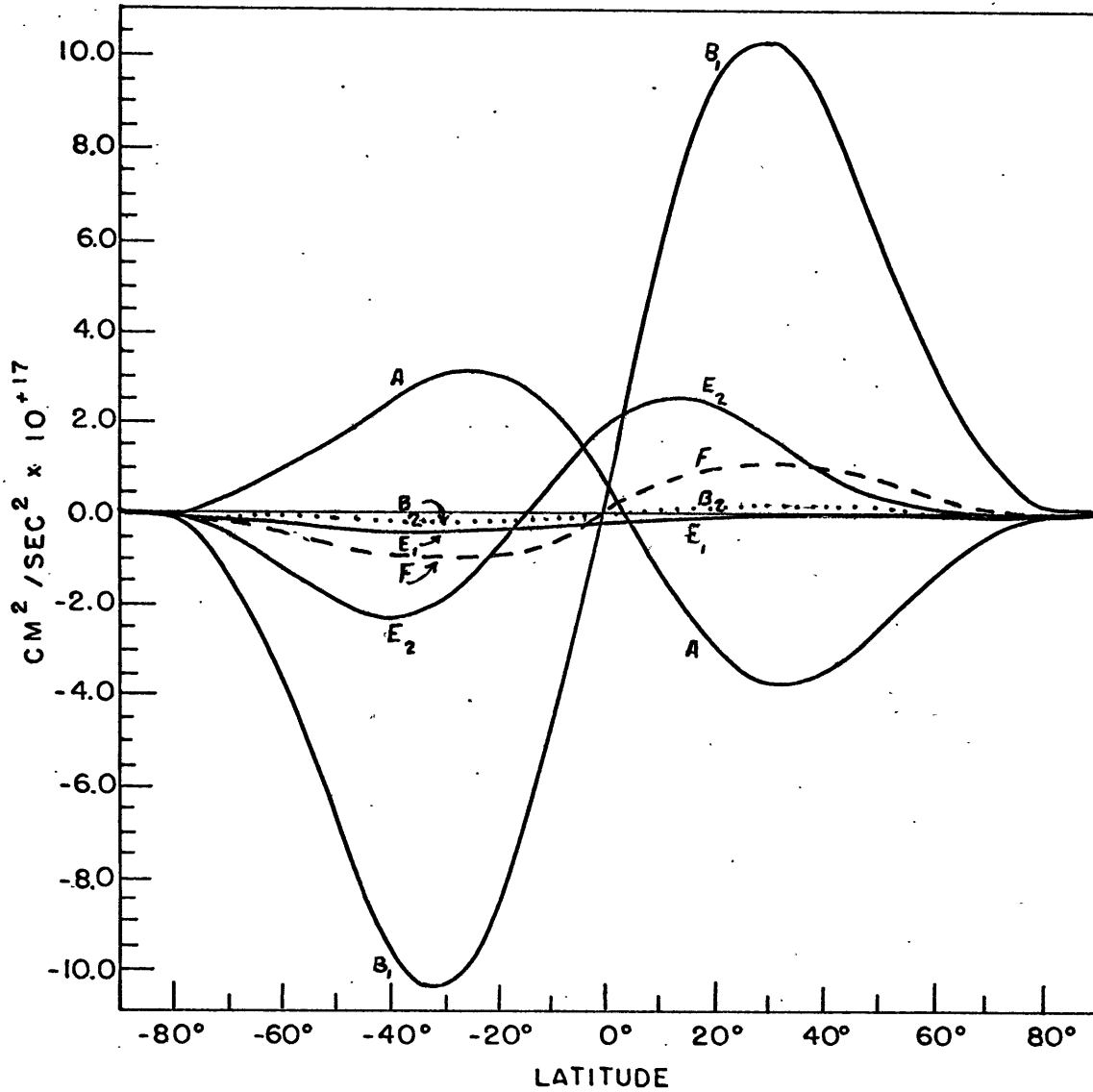


Fig. 6.11. Vertically averaged horizontal Reynolds stresses and Maxwell stresses of magnetic P.R. 2.

- A -eddy Reynolds stress.
- B₁-stationary axisymmetric Reynolds stress.
- B₂-fluctuating axisymmetric Reynolds stress.
- E₁-stationary axisymmetric Maxwell stress.
- E₂-fluctuating axisymmetric Maxwell stress.
- F -eddy Maxwell stress.

6.10 is negligible compared to the magnitude of the individual terms, and thus a long term "correctly truncated" angular momentum balance exists for P.R. 2. A similar balance is achieved in Fig. 6.6 for P.R. 1.

The Reynolds stresses and Maxwell stresses themselves are illustrated in Fig. 6.11 for magnetic P.R. 2. The nonfluctuating axisymmetric Maxwell stress and the oscillating axisymmetric Reynolds stress are again smallest. The two largest terms are the nonfluctuating axisymmetric Reynolds stress and the eddy Reynolds stress, respectively. The horizontal eddy Reynolds and Maxwell stresses now have opposite signs (cf. Fig. 6.7).

Typical propagation speeds of disturbances are about -30° longitude (i.e., $1/2$ wavelength) per rotation. This value is \sim twice as large as for P.R. 1 and is comparable to the magnitude of the easterly zonal current.

Comparison with Observations.

Ward's (1964) covariances in units of $(\text{deg}/\text{day})^2$ from his Table 7 may be compared to our horizontal eddy transports by multiplying his values by $-\left(\frac{2\pi a}{360}\right)\left(\frac{2\pi a \cos \varphi}{360}\right)(8.64 \times 10^4)^{-2}(a \cos \varphi)$. Of interest here is the north-south average for the 20° - 30° latitude belt for 1935-1944. For Ward's cases with no cutoff, moderate cutoff and severe cutoff, the converted values are -2.1×10^{18} , -1.3×10^{18} , and $-3.2 \times 10^{17} \text{ cm}^3/\text{sec}^2$, respectively. At latitude 25° , where the maximum eddy transport of the model occurs, we obtain -1.6×10^{18} and $-3.6 \times 10^{17} \text{ cm}^3/\text{sec}^2$, respectively, for nonmagnetic P.R. 2 and magnetic P.R. 2. Thus our values fall within the range of Ward's at 25° , and agreement is attained to within an order of magnitude. From the standpoint of horizontal shears and horizontal eddy transports of angular momentum, P.R. 2 is more realistic than P.R. 1. The

reversal of the horizontal shear of \bar{N}_{abs} in P.R. 1 by magnetic effects is interesting however.

The Rossby-Hadley Regime Boundary for P.R. 2.

By varying σ_{*0} and R_e , and keeping all other parameters the same as for P.R. 2, a crude determination of the Rossby-Hadley regime boundary can be made for that run. The results for the nonmagnetic case are presented in Fig. 6.12. The relevant group of experiments comprises test run 14 in Table 6.2.

In Fig. 6.12, $\log_{10}(R_e^2/\sigma_{*0}^2)$ and σ_{*0} are logical dimensional coordinates, since σ_{*0} and R_e were the quantities actually varied. However, they may be converted to the more standard nondimensional coordinates $\log_{10} T_a$ and R_{OT}^* , respectively where

$$T_a = f^2 (2D)^4 / v^2 \tag{6-4a}$$

defines the Taylor number.

Now $v = D^2 L^{-1} |\Delta u_*| R_e^{-1}$, where $\Delta u_* = 2\Omega \sin \varphi_* L_* R_{OT}^*$
 $= 169D \Delta \sigma_* / (4\pi a \Omega \sigma_s)$ from equation (6-1), and $f = 2\Omega \sin \varphi_*$.
 But for P.R. 2, $\Delta \sigma_* = 3\sigma_{*0}$ and $\sin \varphi_* = 1/\sqrt{3}$. Making the necessary substitutions, $T_a = C (R_e^2/\sigma_{*0}^2)$ where $C = (4/3)\pi^2 (a\Omega^2/9) \delta^{-2} (\sigma_{*0}/\Delta \sigma_*)^2 \sigma_s^2$.
 During the above experiments, $C \sim 2.6 \times 10^4 (\text{°K})^2$ is held fixed.

Hence the abscissa in Fig. 6.12 may be transformed to

$$\log_{10} T_a = \log_{10} [C (R_e^2/\sigma_{*0}^2)] \tag{6-4b}$$

Similarly, in the definition (6-1) of R_{OT}^* , all parameters are held fixed except $\Delta \sigma_* = 3\sigma_{*0}$, so that R_{OT}^* is linearly proportional to σ_{*0} .

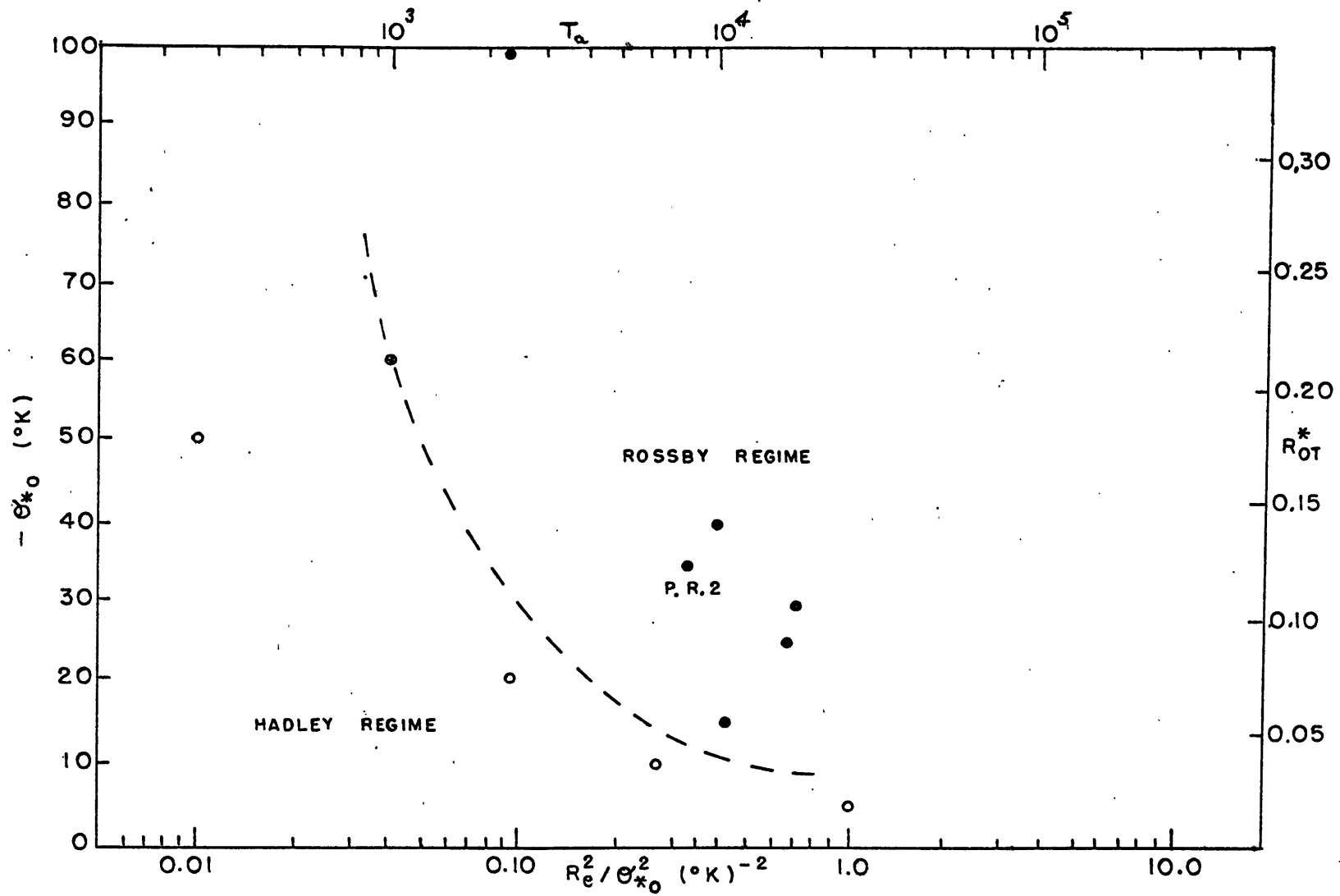


Fig. 6.12. Crude determination of the Rossby regime-Hadley regime boundary for nonmagnetic P.R. 2
The dashed curve is only speculative.

In Fig. 6.12, a dashed line separates the Rossby and Hadley regimes. This boundary is obviously only speculative, especially near the top of the diagram, considering that it is based upon only 11 points. A similar diagram for the profile $\sigma_{*0} (1 - 10 \sin^2 \alpha + 35/3 \sin^4 \alpha)$ is not included because only 6 points were obtained from test runs 2, 3, and 7 (see Table 6.2). However, as in Fig. 6.12, the Rossby and Hadley regimes seem to be separated.

In Fig. 6.12, the eddies are quite weak for the solution symbolized by the black circle closest to the dashed line (this circle is also the lowest black circle). The solutions corresponding to the white dot inside the Hadley regime and situated farthest from the dashed line converge to axisymmetric-steady state the most rapidly. There is one point on the dashed line. Here, the solutions show little tendency to converge to a steady state configuration after ~ 50 rotations; the initial eddy perturbations neither seem to grow nor die out. Finally we note that within a particular regime (Rossby or Hadley) the solutions at the various points differ from each other.

Not enough computer time remained to determine how magnetic fields would affect the Rossby-Hadley regime boundary. We would not expect dynamo solutions in the Hadley regime of Fig. 6.12 however, since magnetic fields seem to suppress baroclinic instability and since axisymmetric dynamos are impossible.

6.6. The Search for Dynamo Solutions.

We recall from Chapter III that each magnetic run was preceded by an analogous nonmagnetic run in the Rossby regime. The latter was terminated after large amplitude eddy disturbances and self-consistent (but not necessarily quasi-steady) axisymmetric flow patterns appeared, e.g.,

after ~ 2000 time steps.

Small, random toroidal magnetic field eddies were then inserted, such that $a^2 \sim O(10^5)$. Typically a^2 remained of $O(10^5)$ or increased slightly during the next 10 rotations (the adjustment phase) irrespective of whether R_m was supercritical. Now if $R_m < R_{mc}$, then a^2 continued to increase, i.e., the magnetic fields decayed to zero. Based on a small number of runs, the rate of decay seemed slower for the smaller values of $R_{mc} - R_m$.

In contrast, if $R_m > R_{mc}$, the magnetic fields grew (a^2 decreased) after the initial adjustment phase for all runs with resolution $0 \leq m \leq 4$, $n = 0, 6$. A typical generation phase lasted for ~ 40 to 60 rotations before giving way to the dynamo maintenance phase. Here a^2 oscillated about its time-averaged value $\overline{a^2}$. Approximate equipartition of kinetic and magnetic energy occurred for both production runs, but $\overline{a^2}$ had somewhat different values for each. For example, $\overline{a^2}$ was slightly less than unity for P.R. 2, but between 2.0 and 2.5 for P.R. 1.

According to Table 6.2, $R_m = 150$ and $R_e = 30$, giving a value of 5 for the magnetic Prandtl number P_{rm} , while $R_{OT}^* = 0.116$ for P.R.1. The horizontal Reynolds and magnetic Reynolds numbers may be defined by

$$R_{e(H)} = R_e (a/D)^2 (\nu/\nu_{(H)}) \quad \text{and} \quad R_{m(H)} = R_m (a/D)^2 (\sigma/\sigma_{(H)})$$

For P.R. 1, $R_{e(H)} = R_{m(H)} = 1090$, which is large compared to R_e and R_m .

Dynamo action occurred for this run, but not for another run in which

$$R_m = 125, R_e = 25, R_{OT}^* = -0.121, R_{e(H)} = R_{m(H)} \sim 907, \text{ and } \sigma_*' = -35(1 - 3 \sin^2 \varphi)$$

The most significant difference in parameters between the two runs was the σ_*' profile. Setting $R_m = 250$, a^2 first grew from $O(10^5)$ to $O(10^6)$, then decreased, leveling off at $O(10^5)$. Thus R_{mc} is close to 250 for a run similar to P.R. 2. Two

other attempts with $R_m = 375$ and $R_m = 500$ (and other parameters similar to those in P.R. 2) succeeded in generating large amplitude magnetic fields. The above runs plus another with higher resolution are summarized in Table 6.4.

We speculate from the data of Table 6.4 that R_m could be affected by the structure of the velocity field (in the nonmagnetic case) associated with Θ_{*o}' . (We are implicitly assuming here that R_{mc} is not a rapidly varying function of R_e or R_{or}^* .) It is not unreasonable that certain velocity profiles could be more favorable than others to the induction of magnetic fields.

Table 6.4. Dynamo Behavior for Different Runs.

Profile	R_{or}^*	R_e	$R_{e(H)}$	R_m	$R_{m(H)}$	Resol.	Dynamo Action	$\overline{a^2}$
(e), $\Theta_{*o} = 30$	0.116	30	1090	150	1090	$0 \leq m \leq 4$	yes	$2 +$
(e), $\Theta_{*o} = 30$	0.116	30	1090	150	1090	$0 \leq m \leq 6$	yes, but weak	$\sim 1 \times 10^4$
(b), $\Theta_{*o} = -35$	-0.121	25	907	125	907	$0 \leq m \leq 4$	no	$\rightarrow \infty$
(b), $\Theta_{*o} = -35$	-0.121	25	907	250	907	$0 \leq m \leq 4$	marginal	$\sim 2 \times 10^5$
(b), $\Theta_{*o} = -35$	-0.121	25	605	375	1360	$0 \leq m \leq 4$	yes	$0.9 +$
(b), $\Theta_{*o} = -35$	-0.121	25	907	500	18140	$0 \leq m \leq 4$	yes	$0.7 -$

Secondly, Table 6.4 suggests that $\overline{a^2}$ decreases as $R_m - R_{mc}$ and $R_{m(H)}$ increase over the ranges of values considered. Perhaps $R_{mc} \sim 250$ would increase if $R_{m(H)}$ were decreased. The strong induction of poloidal magnetic fields for $R_m = 500$ is illustrated in Fig. 6.23. Note the large vertical eddy magnetic fields and the prominent regions of inflow

and outflow in the horizontal magnetic field. Had we been able to vary R_m from 250 to 375, it is possible that \bar{a}^2 could have been tuned to $O(10)$ or to $O(100)$ for example.

In test run 8, all the parameters were identical to the ones in P.R. 1 except that the resolution was increased to $0 \leq m \leq 6$, $n=0, 6$. The computer time per numerical integration was twice that for the old resolution. The run was terminated 114 rotations after insertion of the magnetic eddies. But \bar{a}^2 had decreased only from $O(10^5)$ to $O(10^4)$, 8×10^3 being the minimum value.

Although convergence is an important question, we lacked the computer resources to investigate it properly, and can only speculate on the interpretation of the above result. One possibility is that R_{mc} and even \bar{a}^2 increase with resolution over a finite range of resolution. Of course if R_m and \bar{a}^2 increased without bound, our model would not act as a true dynamo.

6.7. Basic Structure of the Magnetic Field Solutions.

The structure of the magnetic field solutions is described below, mainly for P.R. 1 and P.R. 2. Magnitudes of the vertical magnetic fields are approximately of the correct order of magnitude. The toroidal magnetic field is not persistently either an odd or even function of latitude. If the solar magnetic cycle is (partially) controlled by large scale processes, then our model results should correspond somewhat to the cycle's large scale aspects. Obviously, our model resolution is much too crude to simulate sunspot or smaller scale motions.

Loosely interpreting our vertical magnetic eddies as active regions, the generalized Hale polarity laws for leading (following) regions in opposing hemispheres are sometimes obeyed. But the following regions

are more intense than the leading regions. The tilt of the bipolar magnetic regions tends to be in the correct sense for only the first 12 years of P.R. 1 (especially at level 2) and not for P.R. 2. The level of magnetic activity differs between the two hemispheres, as is observed on the sun. The generalized Spörer law governing the equatorward migration of the mean latitude position of active region formation does not hold.

The most substantive result is that magnetic field reversals occur for both production runs. In P.R. 1, the time scale for the reversals is of the correct order of magnitude. Conversely, it is too short in P.R. 2. A detailed discussion of the reversal process is deferred until section 6.8.

6.7.1. Solutions for Production Run 1.

The evolution of the horizontal magnetic field \underline{B}_{H_2} is illustrated in Fig. 6.13 for P.R. 1. This figure, like most of the others of this section, was originally plotted on the NCAR DD80 device. Arrows point in the direction of the local horizontal magnetic field, at 5° increments of latitude and longitude. Also, they are subdivided into several standardized length-thickness categories to indicate the local horizontal field strength. The maximum field strength and the time relative to the introduction of the initial magnetic perturbations, are written at the bottom of each plot.

The sequence in Fig. 6.13 is for a 7.7 year epoch at intervals of 0.70 years (10 rotations). It begins at time $\mathcal{X} = 4.73$ years, not long after the completion of the generation phase. At first, toroidal (rotational) magnetic eddies are prominent. We recall that the initial magnetic field was of pure toroidal eddy type. Both the axisymmetric and eddy toroidal fields are antisymmetric about the equator for most of the sequence. After $\mathcal{X} = 5.42$ years, the eddy toroidal field is not too prominent. The

axisymmetric toroidal field at first contains a mixture of $\partial Y_4^0 / \partial \alpha$ and $\partial Y_2^0 / \partial \alpha$ toroidal vector spherical harmonics. Later, $\partial Y_2^0 / \partial \alpha$ is dominant. At 11.68 years an eddy disturbance affects only the northern hemispheric fields. Thereafter, the antisymmetry of the axisymmetric toroidal field basically disappears except for some short-lived recurrences. At $t = 26.96$ years, for example, B_{H_2} is symmetric about the equator as shown in Fig. 6.14b. We do not know the cause of the pronounced asymmetry of $\langle B_2^\lambda \rangle$ between the two hemispheres. No solar observations of $\langle B_2^\lambda \rangle$ are available as a guide, either. It would be interesting to investigate whether or not this asymmetry is related to either the strong magnetic feedback upon the flow or to the low model resolution.

The characteristic instantaneous peak strength of the axisymmetric toroidal field $\langle B_2^\lambda \rangle$ varies from under 500 to over 1500 gauss. Although these values are about half an order of magnitude larger than Babcock (1961) has suggested, no observations are available to substantiate Babcock's estimate. However, the local twisting of Babcock's flux ropes is supposed to generate small scale fields of sunspot amplitude, e.g., $\sim \mathcal{O}(2000 \text{ gauss})$. The magnitude of our toroidal fields could be reduced by over a factor of 2, if $\overline{a^2}$ were ~ 10 . A similar reduction would occur if ρ_s were set to $\sim 4 \times 10^{-5} \text{ gm/cm}^3$, which is closer to the photospheric density.

Figures 6.17a-6.17d show the v_{H_2} , w_2 , B_4^z , and B_2^z fields, respectively, at $t = 8.20$ years, for P.R. 1. The horizontal wind field is zonal and axisymmetric in character and the horizontal shear is very small. The vertical motion field has a little more character but basically reflects a dominant meridional circulation with two cells in each hemisphere. Occasionally, the eddy structure of w_2 is more prominent.

The B_4^z field reflects a nonvanishing horizontal divergence of

B_{H_2} and is perhaps more analogous than B_2^z to the surface vertical magnetic fields. We recall that the observed line of sight fields are a composite, over one solar rotation, of fields detected near the central meridian of the solar disk. The most direct comparison between our B_4^z (or B_2^z) fields and the observed line of sight fields can be made at low latitudes. Typical strengths of the B_2^z and B_4^z magnetic fields in P.R. 1 are both of $\mathcal{O}(5 \text{ gauss})$ in agreement with measurements made with moderate resolution magnetographs, B_2^z being somewhat stronger than B_4^z .

In Fig. 6.17c, the B_4^z contours equatorward of the closed contours tilt in the same sense although not so steeply as Bumba and Howard's (1965b) observed field patterns. However, B_4^z is quasi-axisymmetric, i.e. no regions of alternating polarity are found. In contrast, the eddies of B_2^z are more pronounced and there are adjacent regions of opposite polarity between latitudes -60° and $+60^\circ$. But disturbances of one polarity still dominate the regions of the opposite polarity in each hemisphere. At $\tau = 8.20$ years, the dominant polarity of the B_2^z eddies is positive in the southern hemisphere and negative in the northern hemisphere. Incidentally, the eddy structure of B_2^z differs in the two hemispheres. The dominant eddies of each hemisphere could be characterized as being of following polarity (i.e., opposite to the polarity at the pole).

The configurations of the B_2^z and B_4^z fields in Fig. 6.17 are not persistent, but are among the more typical ones. The magnetic eddies tend to tilt towards the equator as shown, especially at level 2, until $\tau \sim 12$ years. But Fig. 6.15 illustrates an example of magnetic eddies having an opposite and more pronounced tilt. There is still a predominance of one eddy polarity (i.e., of following type) over the other in each hemisphere. Also, the zonally averaged part of B_2^z has an octa-

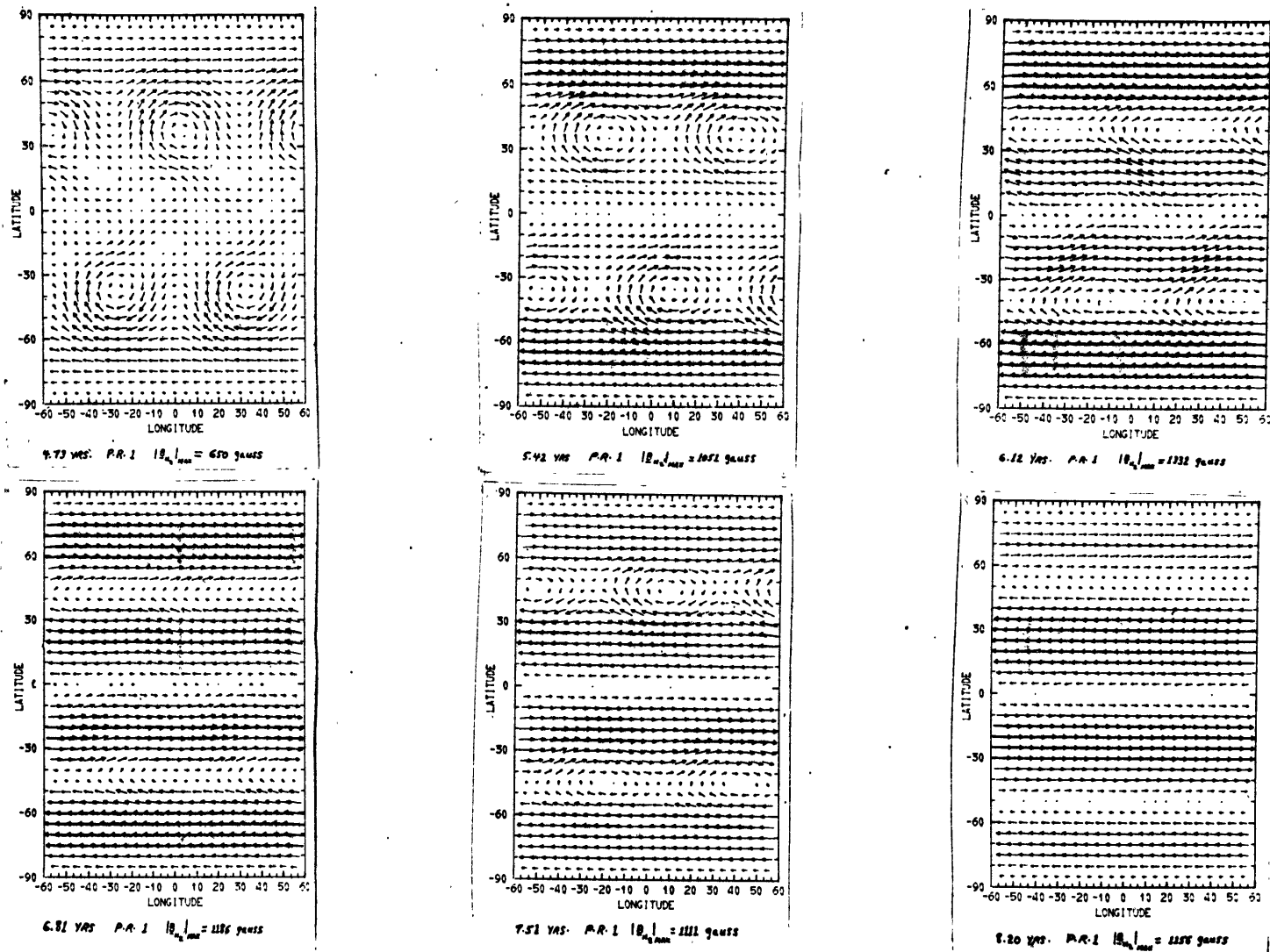
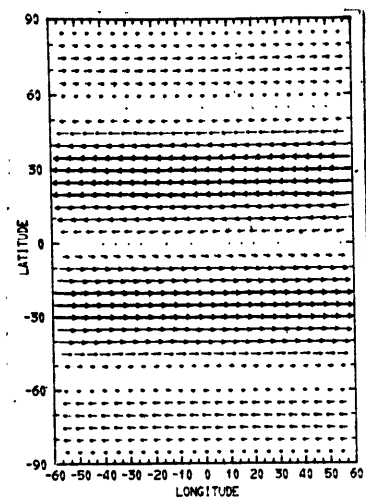
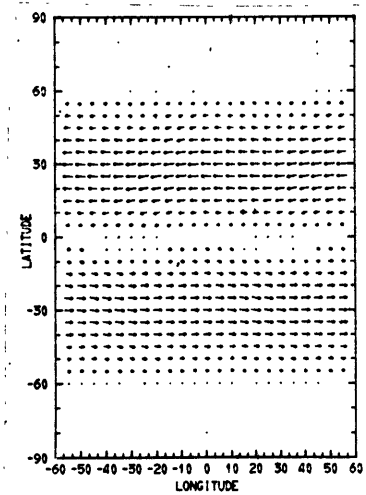


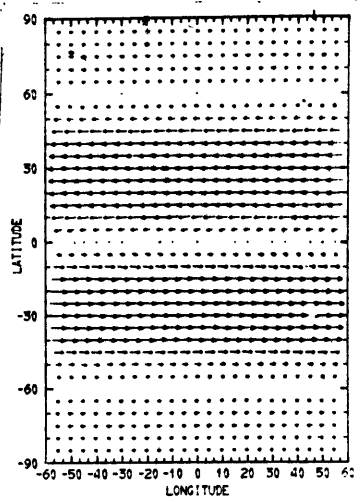
Fig. 6.13. Time evolution of horizontal magnetic field B_{H_2} for P.R. 1, at intervals of 10 solar rotations. Note the coherency in time of B_{H_2} . The antisymmetry about the equator of $\langle \theta_2^A \rangle$ disappeared later.



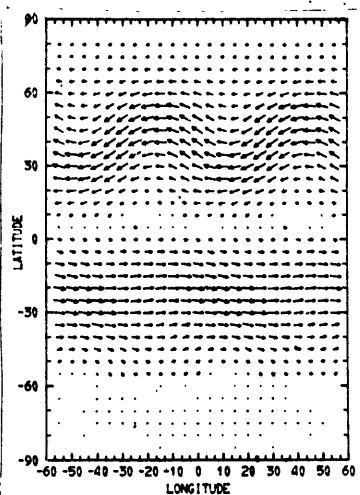
8.50 Yrs. $PR-1 |B_{\theta}|_{max} = 1096 \text{ gauss}$



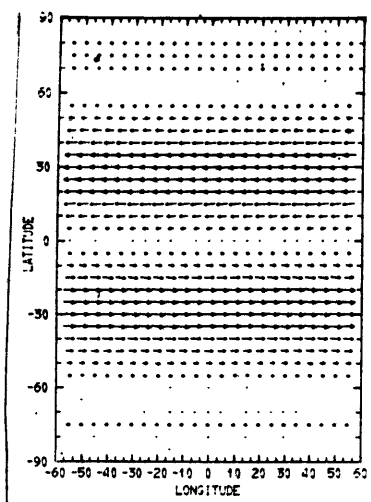
10.97 Yrs. $PR-1 |B_{\theta}|_{max} = 492 \text{ gauss}$



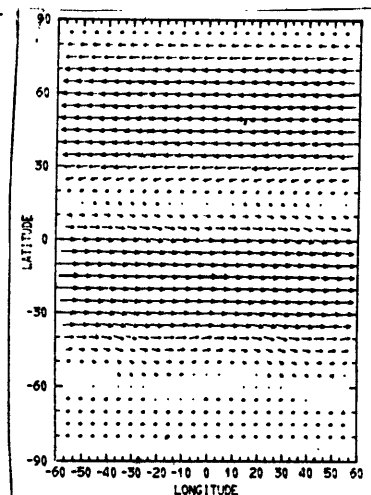
9.59 Yrs. $PR-1 |B_{\theta}|_{max} = 899 \text{ gauss}$



12.68 Yrs. $PR-1 |B_{\theta}|_{max} = 679 \text{ gauss}$



10.29 Yrs. $PR-1 |B_{\theta}|_{max} = 679 \text{ gauss}$



12.17 Yrs. $PR-1 |B_{\theta}|_{max} = 948 \text{ gauss}$

Fig. 6.13. continued.

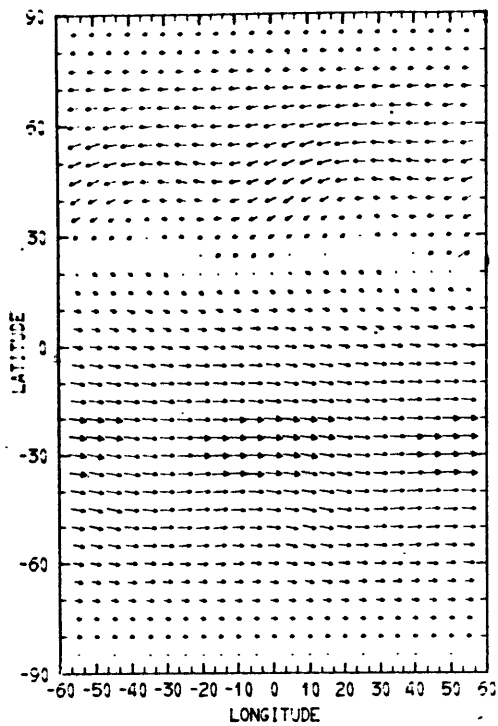


Fig. 6.14(a) B_{N_2} for P.R. 1 at $t=13.76$ yrs. $\langle B_2^A \rangle$ is not antisymmetric about equator.

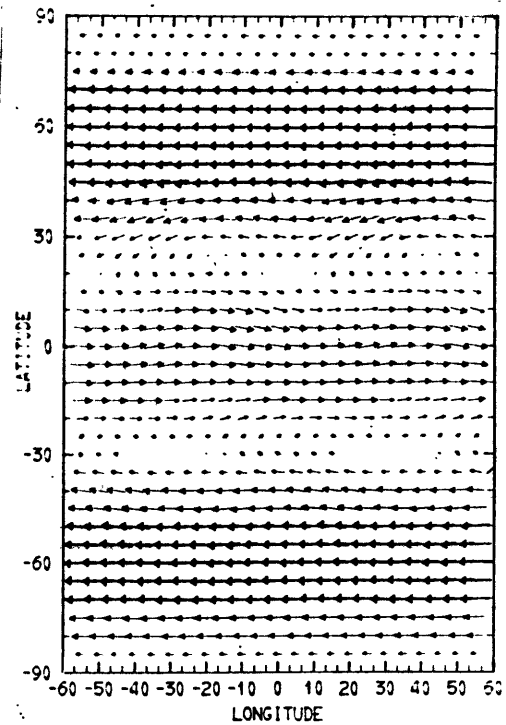


Fig. 6.14(b) B_{N_2} for P.R. 1 at $t=26.96$ yrs. $\langle B_2^A \rangle$ is symmetric here.

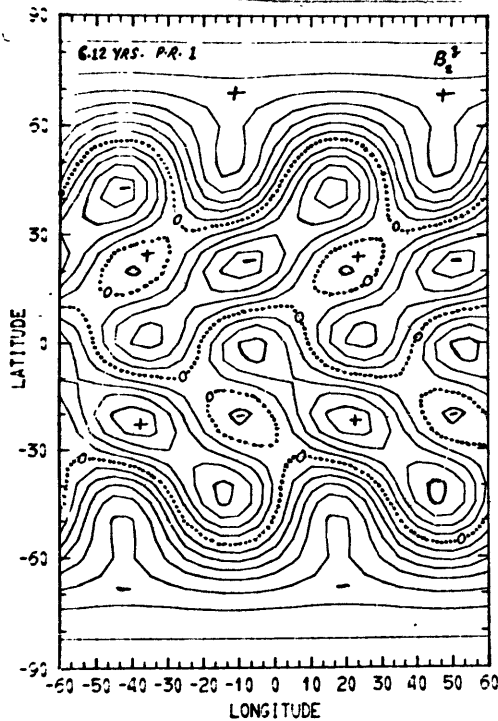


Fig. 6.15. B_2^z for P.R. 1 at $t=6.12$ yrs. Contour interval=1.0 gauss, range=-7.0 to +7.0 gauss. Magnetic patterns tilt in the wrong sense.

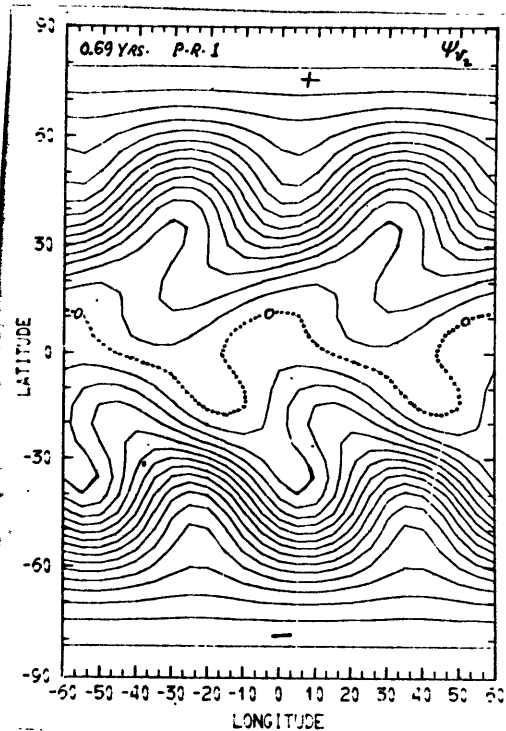
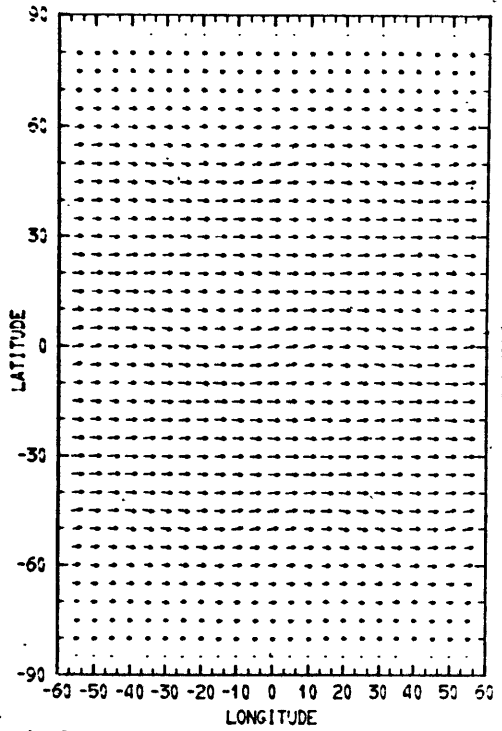
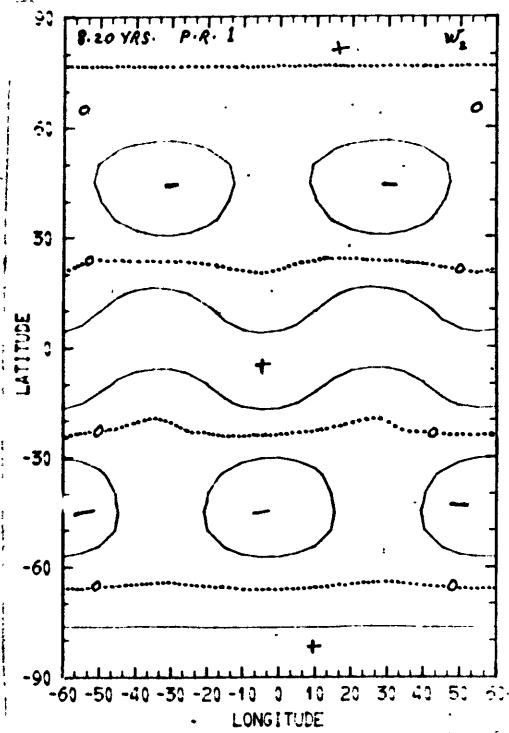


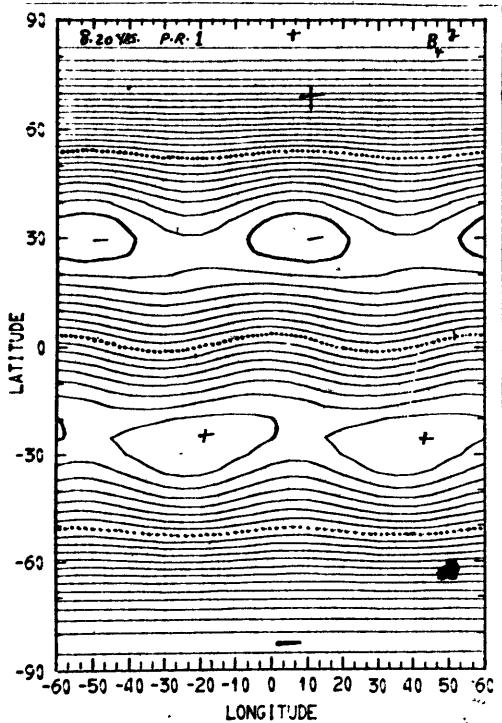
Fig. 6.16. Stream function Ψ_2 for P.R. 1. at $t=0.69$ yrs., i.e., before significant dynamo action occurs. Contour int.= 5.0×10^{13} cm²/sec. Eddies transport ang. mom. from low to mid-latitudes.



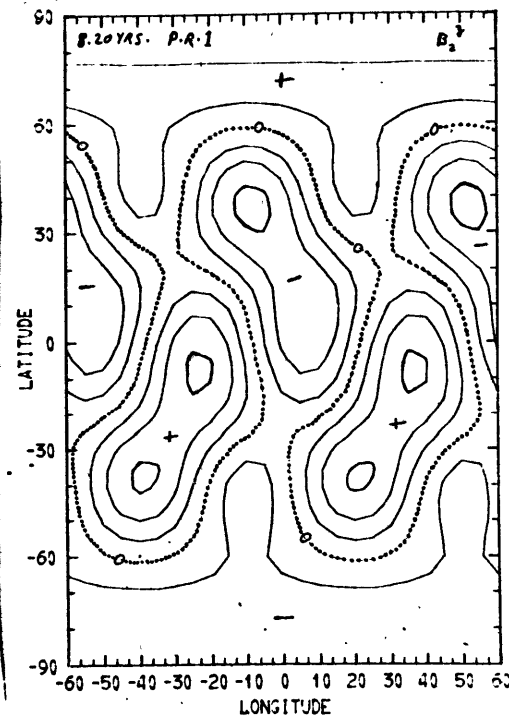
(a) Horiz. velocity V_{N_2} . $|V_{N_2}|_{MAX} = 7.12 \times 10^3$ cm/sec.



(b) Vert. velocity W_2 . Contour int.=10 cm/sec.



(c) Vert. mag. field B_4^3 . Contour int.=0.10 gauss, range=-1.30 to +1.60 gauss.



(d) Vert. mag. field B_2^3 . Contour int.=1.0 gauss, range=-3.0 to +3.0 gauss.

Fig. 6.17. Sample solutions for P.R. 1 at $t=8.20$ yrs.

pole configuration at $\tau = 6.12$ and 8.20 years. Sometimes the configuration is more dipole-like and at other times, is either an even function of latitude or a mixture of even and odd modes.

As stated in Chapter I, observed active magnetic regions of leading polarity tend to be located at lower latitudes and have stronger fields than regions of following polarity. However, the latter are more spread out in longitude. In addition, the leading (and following) polarity are opposite for the two hemispheres. Thus the $\langle B^{\lambda} \rangle$ pattern for the model should probably have five nodes between the two poles. But the highest odd number permitted by our resolution is three. Interpreting Fig. 6.15 and 6.17d, for example, in this light, a region of leading polarity is represented by the penetration of a region of following polarity into the opposite hemisphere. But the regions of following polarity are stronger. In this manner, the following regions could neutralize the polar field despite the constraints imposed by the resolution. We also note that our longitudinal resolution cannot simulate the "unipolar" and "ghost unipolar regions" characterized by $n \sim 1$ and $n \sim 2$.

6.7.2. Solutions for Production Run 2.

A 7.7 year evolutionary sequence of \underline{B}_{H_2} at ~ 0.70 year (10 rotation) intervals is illustrated in Fig. 6.18 for P.R. 2. The antisymmetric character of \underline{B}_{H_2} present at first in P.R. 1 seemed to be lacking in P.R. 2. The beginning of the time sequence is at 22.52 years. Note that the fluctuations are much more rapid in Fig. 6.18 than in Fig. 6.13. Nevertheless, some coherency is still present from one plot to the next in the sequence. Two reversals in the hemispheric average sign of $\langle B_2^{\lambda} \rangle$ occur in the northern hemisphere and one in the southern hemisphere between $\tau = 22.52$ and 30.16 years. The configuration of $\langle B_2^{\lambda} \rangle$ basically changes

from odd to even symmetry with respect to the equator. But more often than not, the hemispheric average $\langle B_2^\lambda \rangle$ fields for the two hemispheres are opposite in sign. Another feature is that for P.R. 2, the toroidal magnetic eddies are more prominent than for P.R. 1. But when and where the magnetic energy is large, it is predominantly in the $\langle B_2^\lambda \rangle$ field.

The peak magnitude of the instantaneous $\langle B_2^\lambda \rangle$ field is typically ~ 1000 gauss but occasionally may reach 2000 gauss.

Figures 6.19a-d contain the v_{H_3} , w_2 , B_4^z , and B_2^z fields, respectively, at $\tau = 24.60$ years. In Fig. 6.19a, note the mid-latitude easterly jet. Although the flow is predominantly zonal, the eddies are somewhat stronger than the arrow representation is capable of showing. The darker areas indicate that the eddies tilt NW-SE in the northern hemisphere. The vertical motion field has more eddy structure than in Fig. 6.17b. For example, vertical motions of opposite sign are juxtaposed at mid-latitudes.

The characteristic magnitudes of the vertical magnetic fields are ~ 10 to 20 gauss for B_2^z and ~ 1 to 2 gauss for B_4^z . Thus there is frequently an order of magnitude difference between B_2^z and B_4^z in P.R. 2, in contrast to the situation in P.R. 1. The values for B_2^z and B_4^z are in best agreement with observations taken during the active and inactive phases of the sunspot cycle, respectively.

The B_2^z and especially the B_4^z configurations in P.R. 2 often tilt in the incorrect sense. However at $\tau = 24.60$ years, the tilt of the B_2^z field in Fig. 6.19d is satisfactory. Even B_4^z manages to tilt in the correct sense at $\tau = 28.10$ years, but Fig. 6.20a is not really typical. Magnetic eddies of opposite polarity are somewhat more readily juxtaposed at level 4 in P.R. 2 than in P.R. 1. Regions of opposite polarity are still

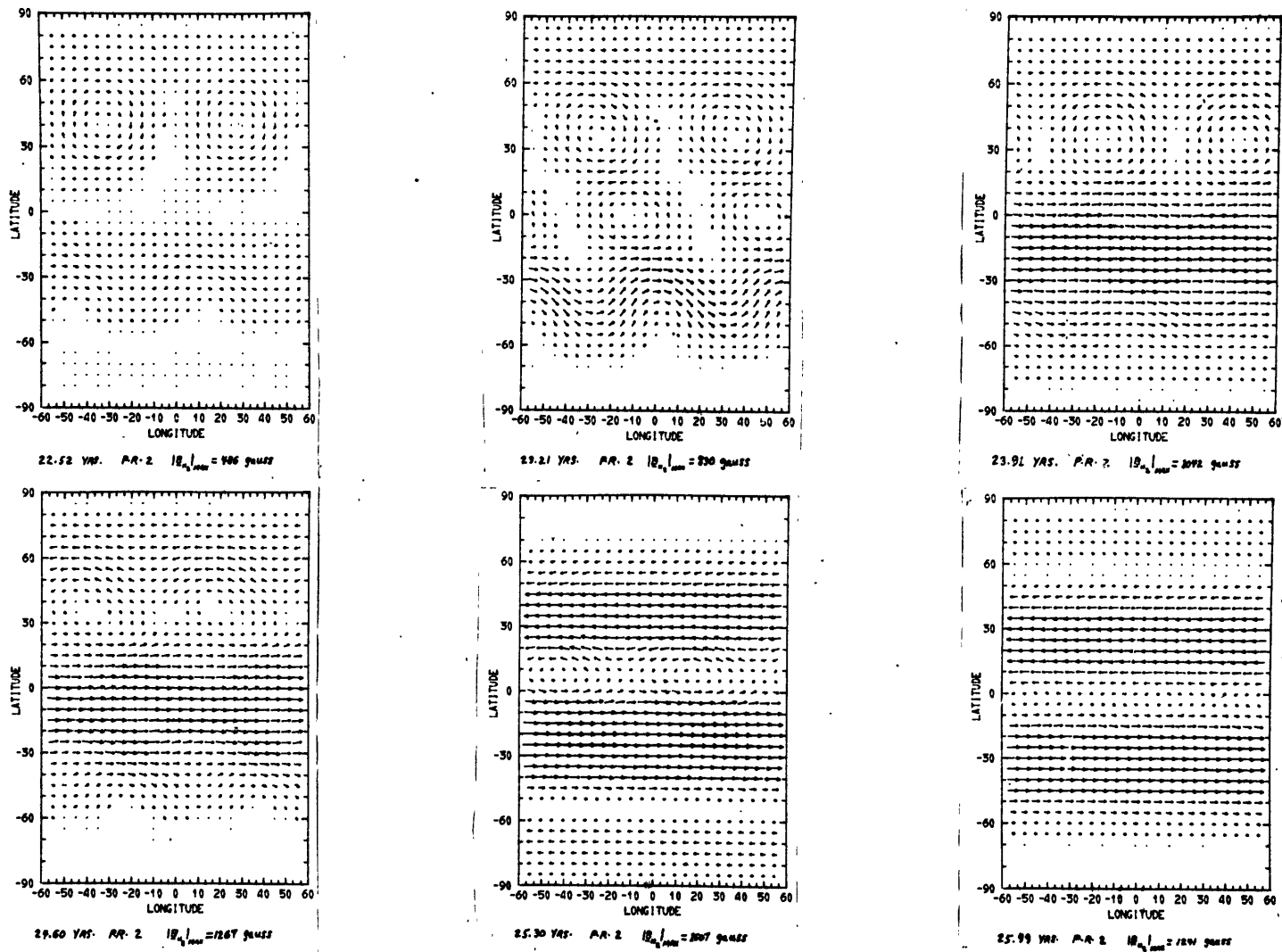
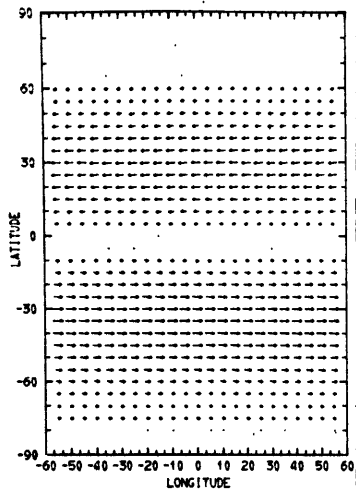
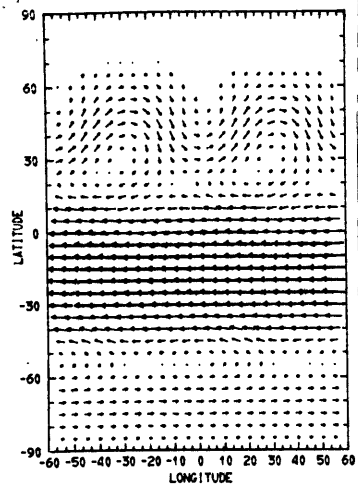


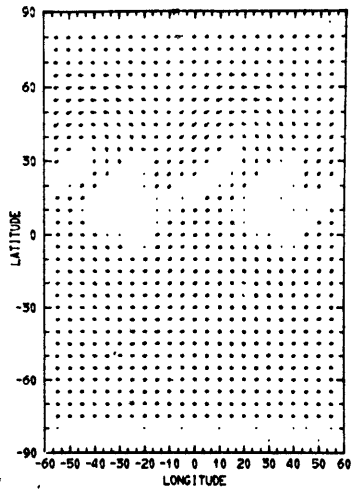
Fig. 6.18. Time evolution of horizontal magnetic field B_{H2} for P.R. 2 at intervals of 10 solar rotations. The fields are less coherent in time than those of Fig. 6.13.



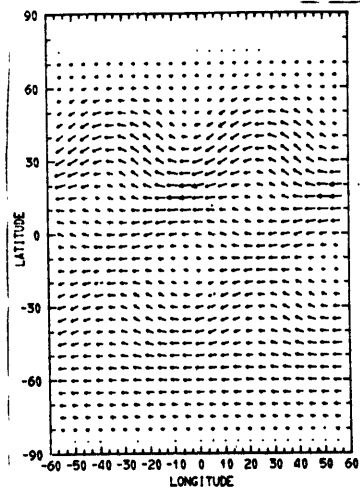
26.69 YRS. P.R. 2 $|B_{\theta}|_{max} = 779$ gauss



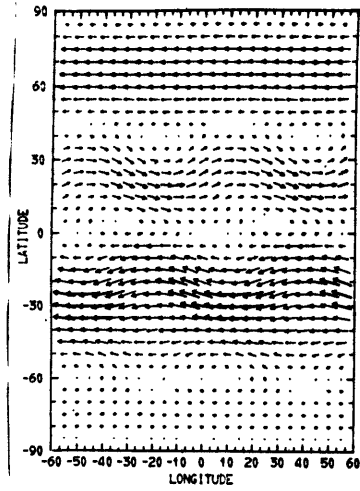
28.77 YRS. P.R. 2 $|B_{\theta}|_{max} = 2193$ gauss



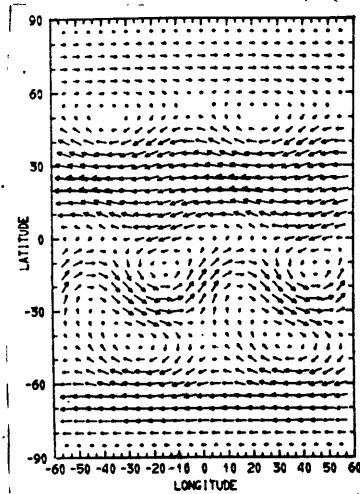
27.38 YRS. P.R. 2 $|B_{\theta}|_{max} = 927$ gauss



29.97 YRS. P.R. 2 $|B_{\theta}|_{max} = 973$ gauss

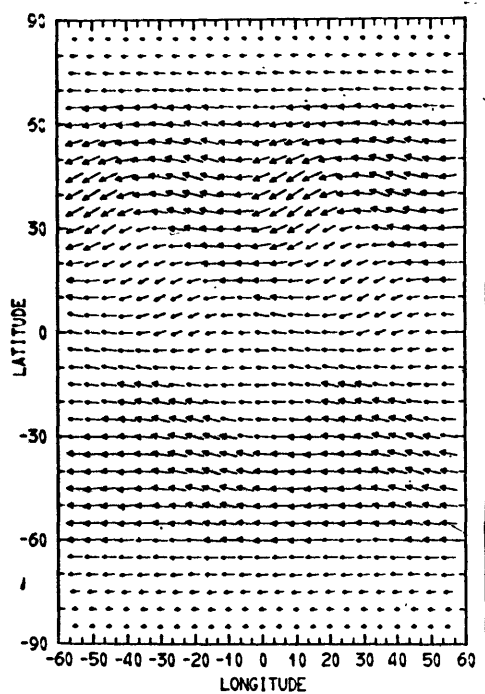


28.08 YRS. P.R. 2 $|B_{\theta}|_{max} = 1796$ gauss

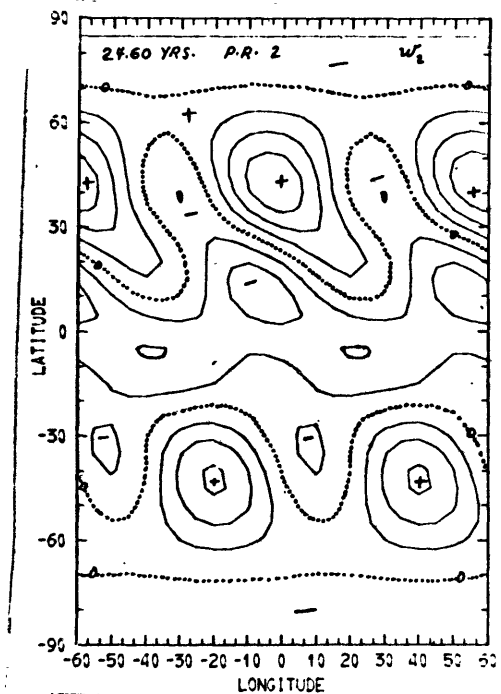


30.16 YRS. P.R. 2 $|B_{\theta}|_{max} = 2699$ gauss

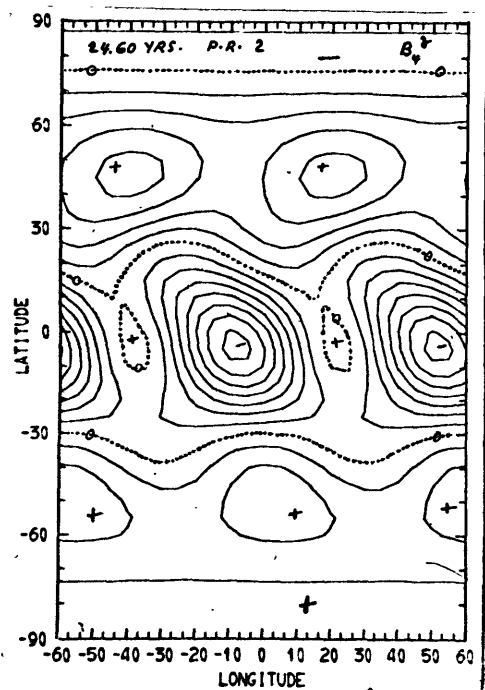
Fig. 6.18 continued.



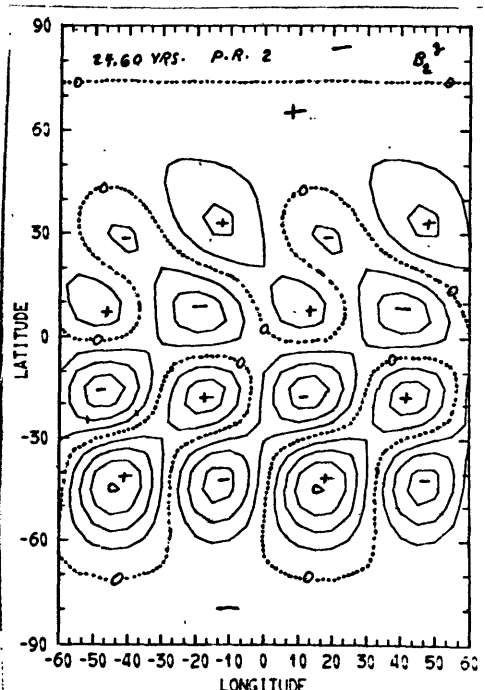
(a) Horiz. velocity $4Y_{H3}$.
 $|Y_{H3}|_{MAX} = 2.54 \times 10^4$ cm/sec.



(b) Vert. velocity w_2 . Contour
 int. = 20 cm/sec.

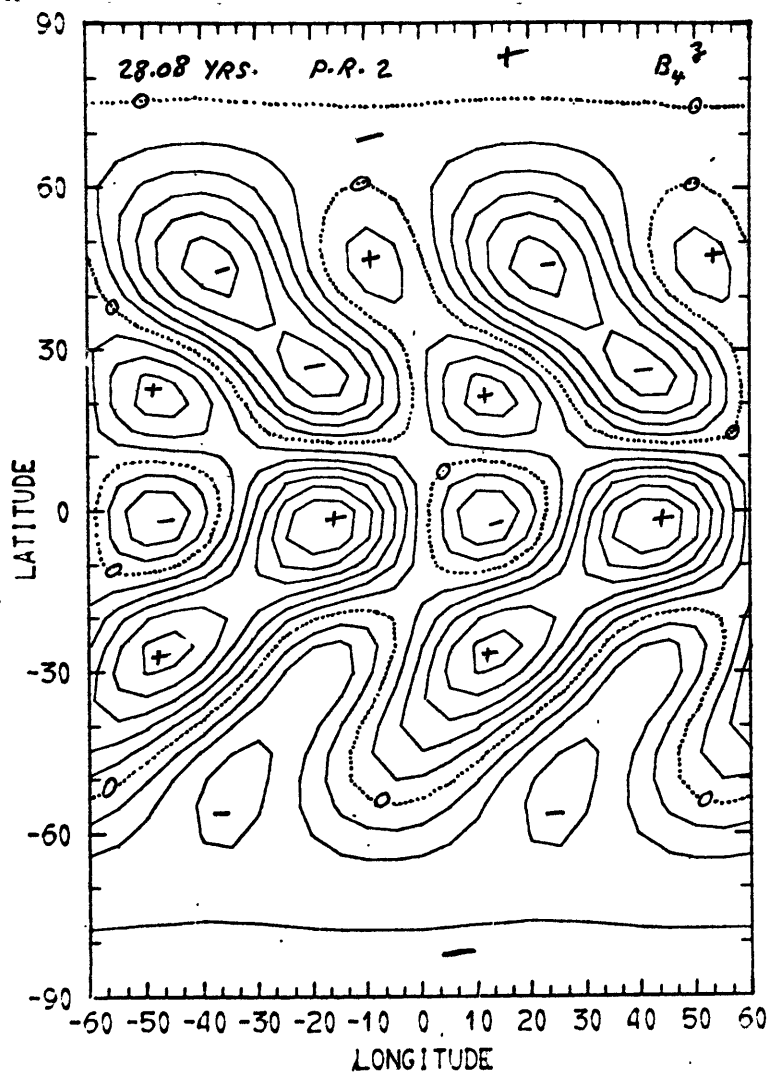


(c) Vert. mag. field B_+^y . Contour
 int. = 0.25 gauss, range = -1.75 to
 +1.00 gauss.

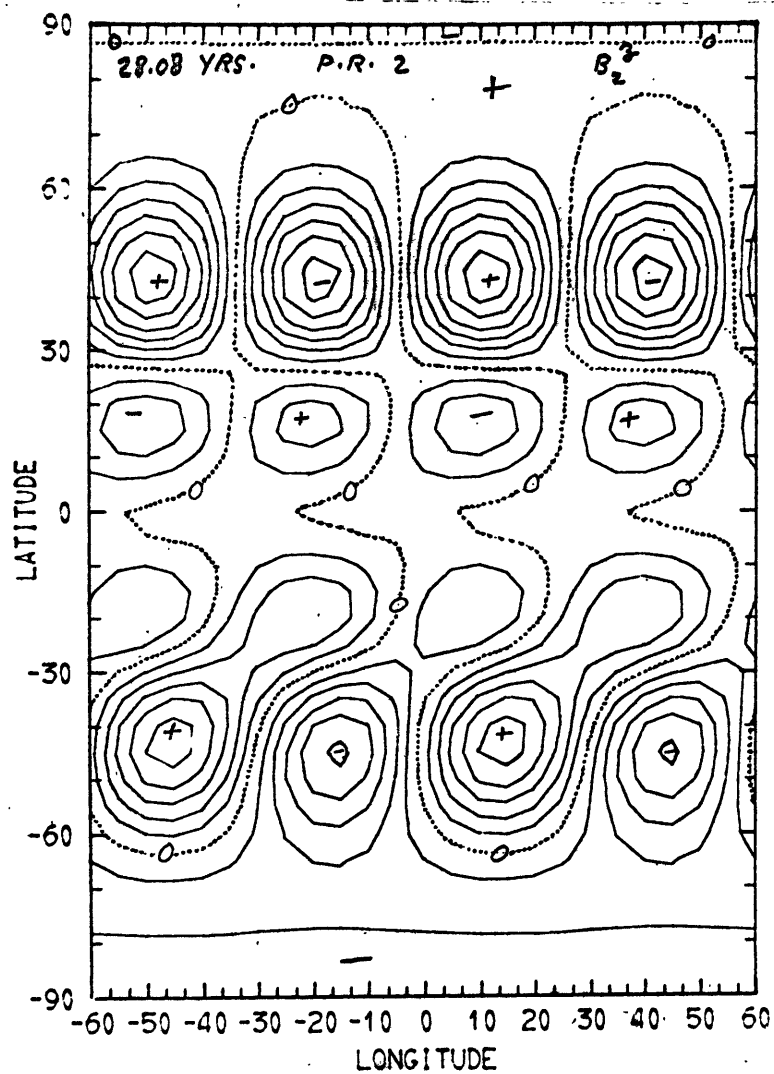


(d) Vert. mag. field B_2^y . Contour
 int. = 5.0 gauss, range = -15.0 to
 +20.0 gauss.

Fig. 6.19. Sample solutions for P.R. 2 at $t=24.60$ yrs.



(a) B_4^z . Contour int. = 0.25 gauss,
range = -1.25 to +1.50 gauss.



(b) B_2^z . Contour int. = 5.0 gauss,
range = -30.0 to +30.0 gauss.

Fig. 6.20. Vertical magnetic fields for P.R. 2 at $t=28.08$ yrs.

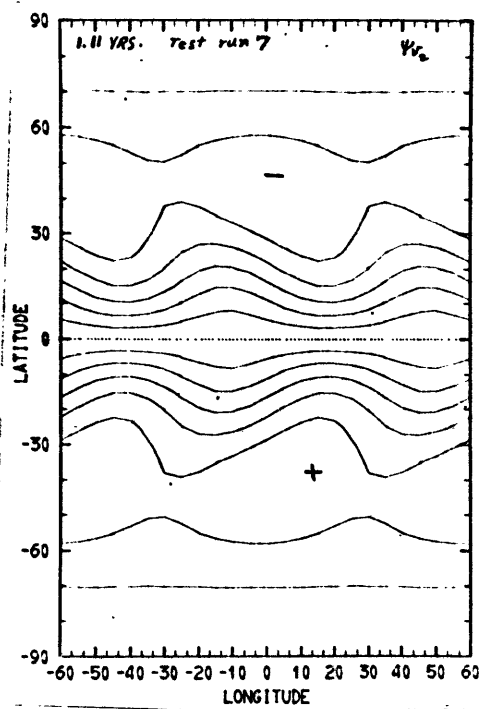


Fig. 6.21. Stream function Ψ_2 for test run 7 at $t=1.11$ yrs., i.e. before significant dynamo action occurs. Streamlines tilt in the desired sense.

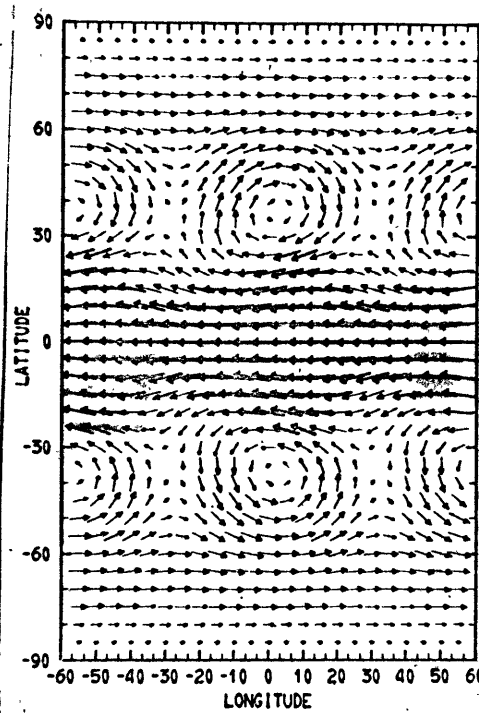


Fig. 6.22. Horiz. mag. field B_2^h for test run 7 at $t=3.89$ yrs. $\langle B_2^h \rangle$ is symmetric about the equator.

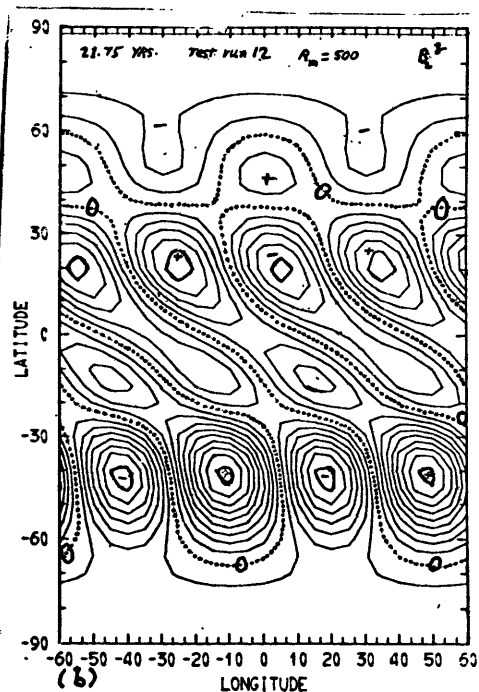
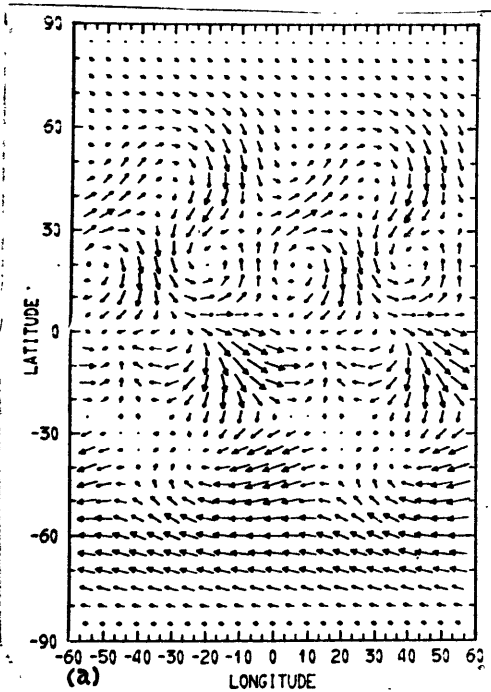


Fig. 6.23. Magnetic fields for test run 12 ($R_m=500$) at $t=21.75$ yrs.
 (a) - B_2^h . Note horiz. converg. and diverg. of field lines.
 (b) - B_2^v . Contour int.=5 gauss, range=-35 to +45 gauss, which is larger than in P.R. 2.

juxtaposed at level 2. The eddy activity can be stronger in one hemisphere than in the other, as indicated in Fig. 6.19d. Also, regions of leading and following polarity may be identified in figures 6.19c, 6.19d, and 6.20a. In the first two cases, the leader (or follower) regions in each hemisphere have the same polarity, in disagreement with one of the phenomenological laws of the sunspot cycle. There are three nodes for $\langle B_4^3 \rangle$ but four for $\langle B_2^3 \rangle$. Meanwhile, in Fig. 6.20a, the leader (or follower) regions of each hemisphere have opposite polarity and there are three nodes in the $\langle B_4^3 \rangle$ field.

6.8. Magnetic Field Reversals and Dynamo Maintenance.

6.8.1. Observations and Other Theories of Solar Magnetic Reversals.

The net polarity of the line of sight field was observed by Babcock to reverse sign near the sun's north pole during 1959 at sunspot maximum and possibly near the south pole about one year later. Babcock suggested that polar reversals were another manifestation of the solar magnetic sunspot cycle and that they should occur every 11 years on the average⁴. Using a low resolution magnetograph, Babcock did not find a zonally averaged line of sight field $\langle B^l \rangle$ in polar regions as strong as 1 gauss. In contrast, Severny (1964) reported field strengths ranging from ~ 2 gauss at $\varphi \sim +60^\circ$ to > 5 gauss at $\varphi \sim +78^\circ$, but again under 1 gauss in the south polar cap. These observations were based on 1963 and 1964 data obtained with a 9" arc resolution magnetograph and suggest that the solar reversals could be rather irregular.

Both the Babcock and Leighton models of the solar cycle, discussed

⁴Measurements of the sun's polar magnetic field made somewhat prior to the invention of the magnetograph around 1952 are of questionable validity but they indicate reversals around 1929, 1938, and 1948 which were approximately years of maximum sunspot activity.

in Chapter I, include quasi-regular reversals of the poloidal magnetic field. Similarly, Gilman(1969) obtains quasi-periodic reversals. His successive peaks have the same amplitude, provided $R_m / R_{mc} \lesssim 4/3$. In contrast, irregular reversals of the poloidal (as well as of the toroidal) magnetic field occur in our model. Considering the similarities between our dynamo model and Gilman's, one may wonder why our magnetic reversals are not quasi-periodic. Although we do not have the answer, it may be pointed out that our model is more complex. For example, it has 127 degrees as opposed to 18, includes both even and odd harmonics in the representation of each variable, and permits internal gravity waves. In fact, prior to the generation of magnetic fields, the flow had not yet (and might never have) reached a true quasi-steady state, especially in P.R. 2. Of course, in the final analysis, a good model should not necessarily yield irregular magnetic reversals, unless these are found to occur on the sun.

6.8.2. Simulation of Magnetic Reversals by our Model.

To illustrate our irregular magnetic reversals, a time history of the $\langle B_4^z \rangle$ magnetic field at both the north and south poles is displayed in Fig. 6.24 for P.R. 1 and in Fig. 6.25 for P.R. 2. Level 4 corresponds most nearly to the solar surface. On the other hand, a direct comparison with solar observations cannot be made. For example, the true radial field component near the pole could be stronger than the observed line of sight field $\langle B^l \rangle$. We note, however, that the larger weighting factor for $\langle B^u \rangle$ in the formula for $\langle B^l \rangle$ is partly offset by the fact that $\lim_{\omega \rightarrow \pm\pi/2} \langle B^u \rangle = 0$. Furthermore, if we assume that the magnetic fields are more intense beneath the surface, then a polarity reversal near the pole should affect both $\langle B^z \rangle$ and $\langle B^u \rangle$, and hence $\langle B^l \rangle$.

In P.R. 1, the first finite amplitude peak is very antisymmetric

about the equator. This is not true in P.R. 2. For both runs, we see that not all oscillations in $\langle B_4^3 \rangle$ are large enough to produce a polarity reversal. According to Fig. 6.24, six reversals at $Q = 90^\circ$ occur between $t=2$ years and $t=76$ years, in P.R. 1 at the pole. Another reversal also takes place at $t=79$ years, while the run was terminated at $t=84$ years. This gives an estimate for the mean reversal time of between 11 and 12 years, which agrees favorably with the postulated solar value. The pure dipole harmonic of $\langle B_4^3 \rangle$ experiences only five reversals, the minireversals at $t \sim 25$ and at $t \sim 31$ years in Fig. 6.24 being absent. There is a general tendency for the vertical field at the two poles to have opposite polarity⁵ and for their smoothed oscillations to be negatively correlated. In P.R. 1, $\langle B_4^3 \rangle$ is often, but not always unipolar at low latitudes, as previously mentioned. As the following polarity is predominant there, the hemispheric averaged $\langle B_4^3 \rangle$ field can be opposite in sign to the polar value. Although the reversals at the two poles are not synchronous, they usually occur within about one year of each other. The main exceptions are the 4 year lags associated with the two minireversals cited above. The strength of the peak $\langle B_4^3 \rangle$ fields near the pole is $\sim 4-5$ gauss, which is not inconsistent with Severny's values. Also the fields reach peak strength at the poles as in Fig. 6.28, and a peak at one pole can be stronger than the (corresponding) peak at the other pole. At level 2, the oscillations would be a bit more irregular, the reversals would occur between $1/2$ and 1 year earlier, and the peaks would be about twice as strong.

The situation for P.R. 2 is somewhat different. We estimate the mean reversal time to be between 1 and 2 years, i.e., presumably about a factor of 8 too small. The more rapid oscillations here as compared to

⁵The hemispheric averages of $\langle B_4^3 \rangle$ must be equal and opposite for the two hemispheres.

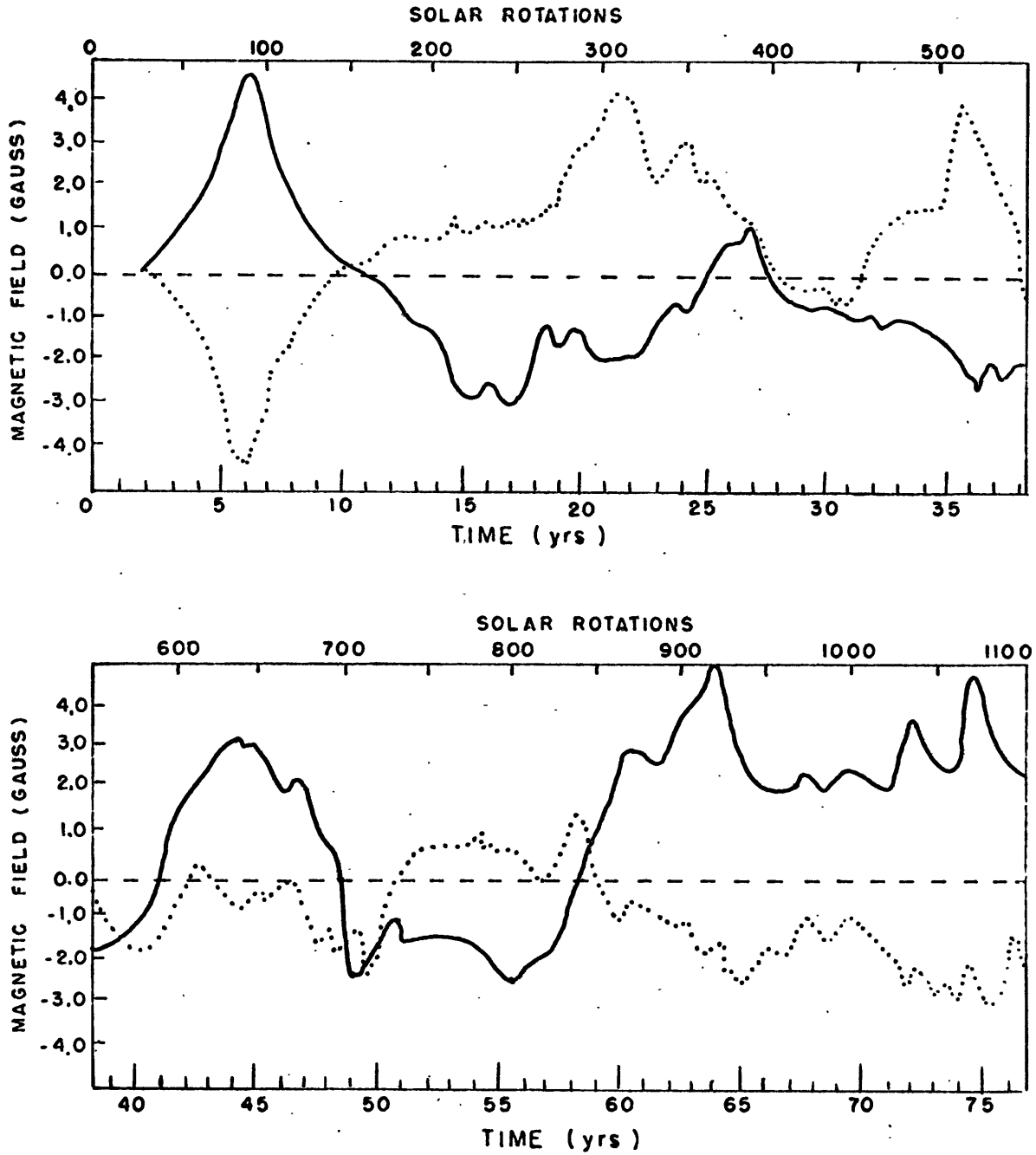


Fig. 6,24. Time reversal of polar magnetic fields for P.R. 1.

— = B_4^z ($\varrho = 90^\circ$); = B_4^z ($\varrho = -90^\circ$).

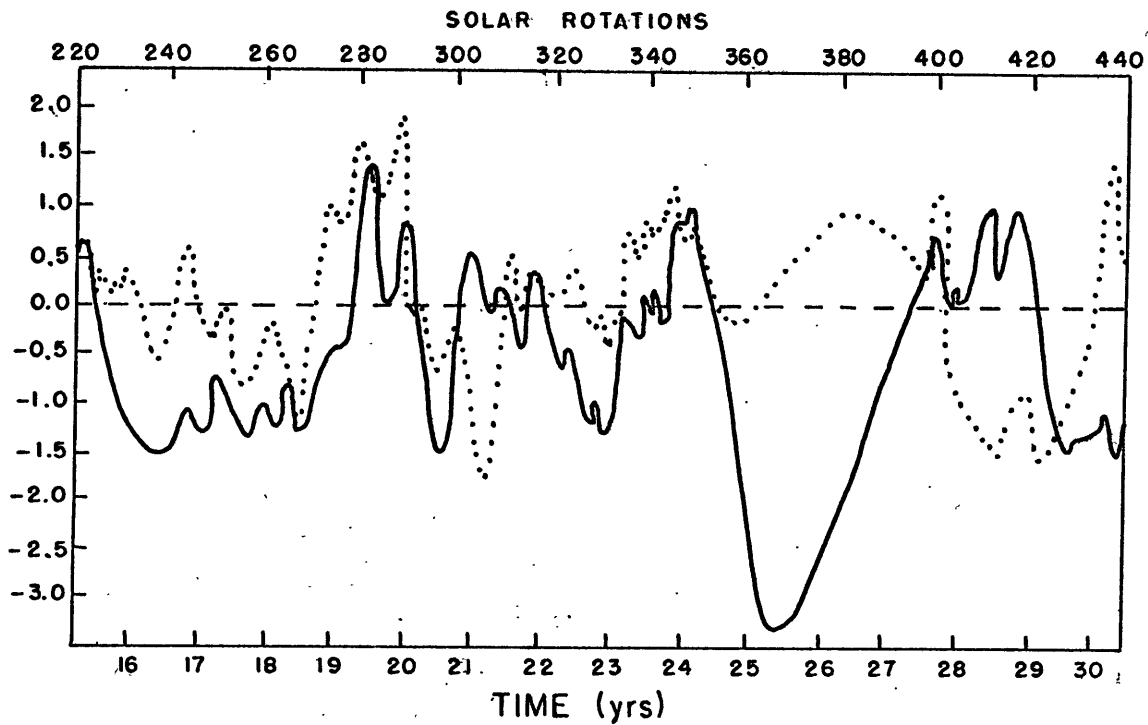
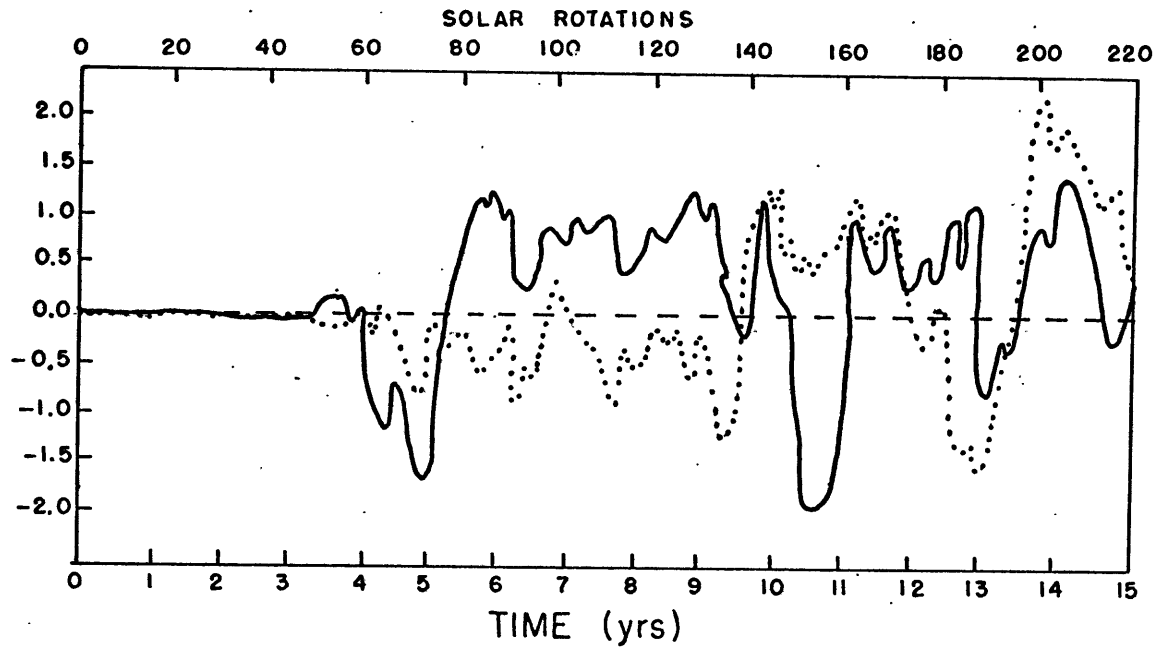


Fig. 6.25. Time reversal of polar magnetic fields, for P.R. 2. — = B_4^z ($\mathcal{L} = 90^\circ$); = B_4^z ($\mathcal{L} = -90^\circ$).

P.R. 1 may reflect the greater thermal forcing (vertical wind shear). We recall that the strength of the horizontal differential rotation at the upper boundary is more realistic in P.R. 2. While there is less tendency than in P.R. 1 for the sign of $\langle B_4^2 \rangle$ to be opposite at the two poles, the polar field is in general confined to a smaller polar cap. Finally, the peaks are much stronger and the oscillations noisier at level 2.

6.8.3. The Energetics of the Model and its Implications for Dynamo Maintenance.

An analysis of the energy integrals and energy transformation integrals of Chapter V helps clarify the physical processes of the model, including the maintenance of the dynamo. The Robert spectral method is applied in computing the above integrals, which are invariant under orthogonal truncation.

Some General Characteristics of the Energetics.

Energy diagrams corresponding to Fig. 5.1a are presented for P.R. 1 and P.R. 2 in Fig. 6.26 and Fig. 6.27, respectively. The time averaged values are based on roughly 35 years of data for P.R. 1 and on about 21 years of data for P.R. 2, time variations being more rapid for P.R. 2.

The energetics of both runs have many similarities. First, the energy input $\langle G_{EPE} \rangle$ is over three orders of magnitude smaller than the solar luminosity $L_0 \approx 3.9 \times 10^{33}$ ergs/sec. Thus only a small fraction of the outward going (convective plus radiative) energy flux would be required to drive the model. Second, the transformation $\{\langle ZPE \rangle \rightarrow \langle KM \rangle\}$ is not small compared to $\{\langle EPE \rangle \rightarrow \langle EKE \rangle\}$ in the magnetic case. We recall that the vertical heat transport curves of Fig. 6.4h and 6.8h implied $\{\langle EPE \rangle \rightarrow \langle EKE \rangle\}$ was dominant in the nonmagnetic case. Third, $\langle KM \rangle \lesssim O(10^{-2} \cdot \langle KZ \rangle)$ in P.R. 1 and $\langle KM \rangle$ is about 1.5 orders of magnitude smaller than $\langle KZ \rangle$ in P.R. 2,

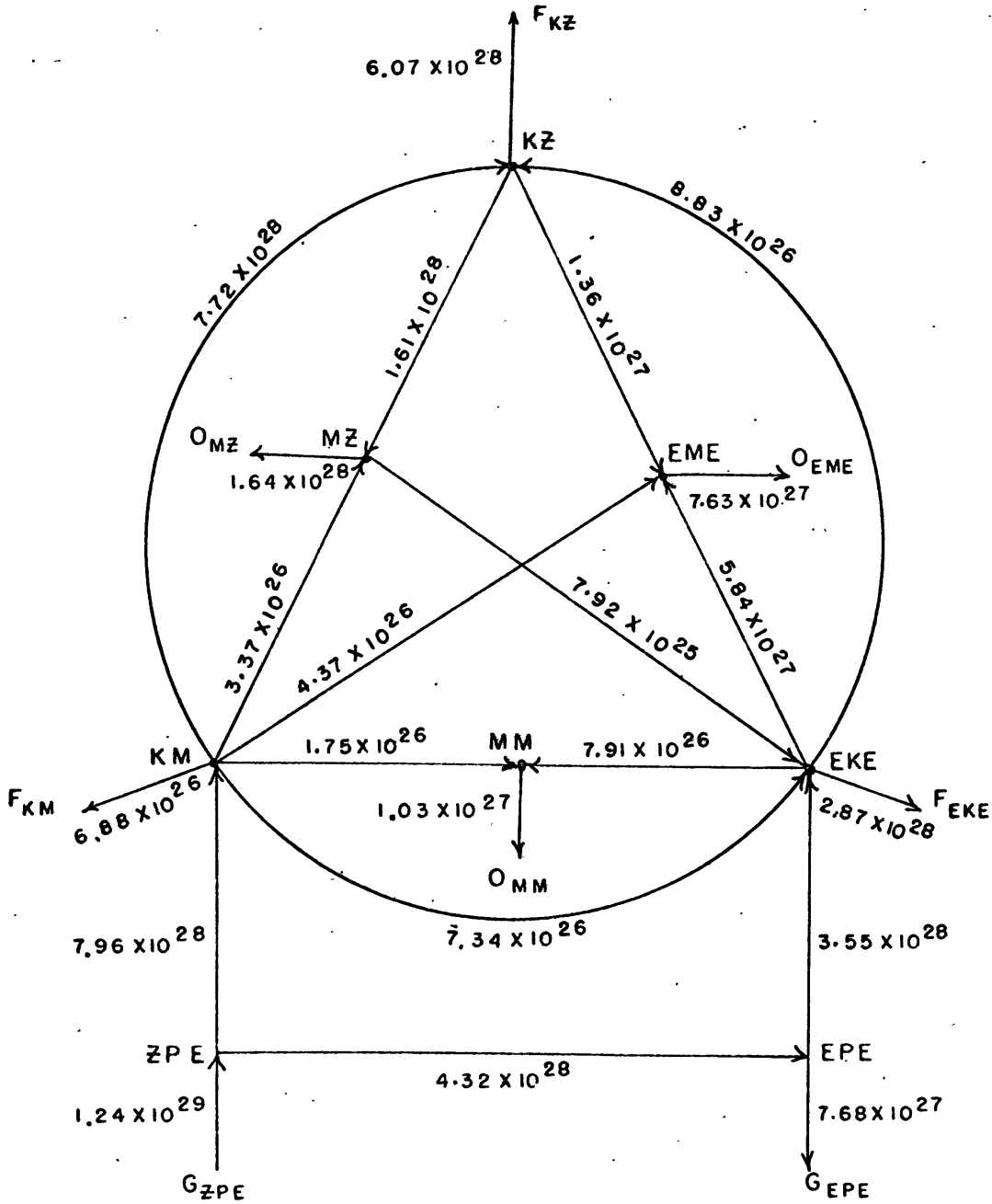


Fig. 6.26. Energy Diagram for magnetic P.R. 1. Units are in ergs/sec. Symbols are defined in text of Chapter V.

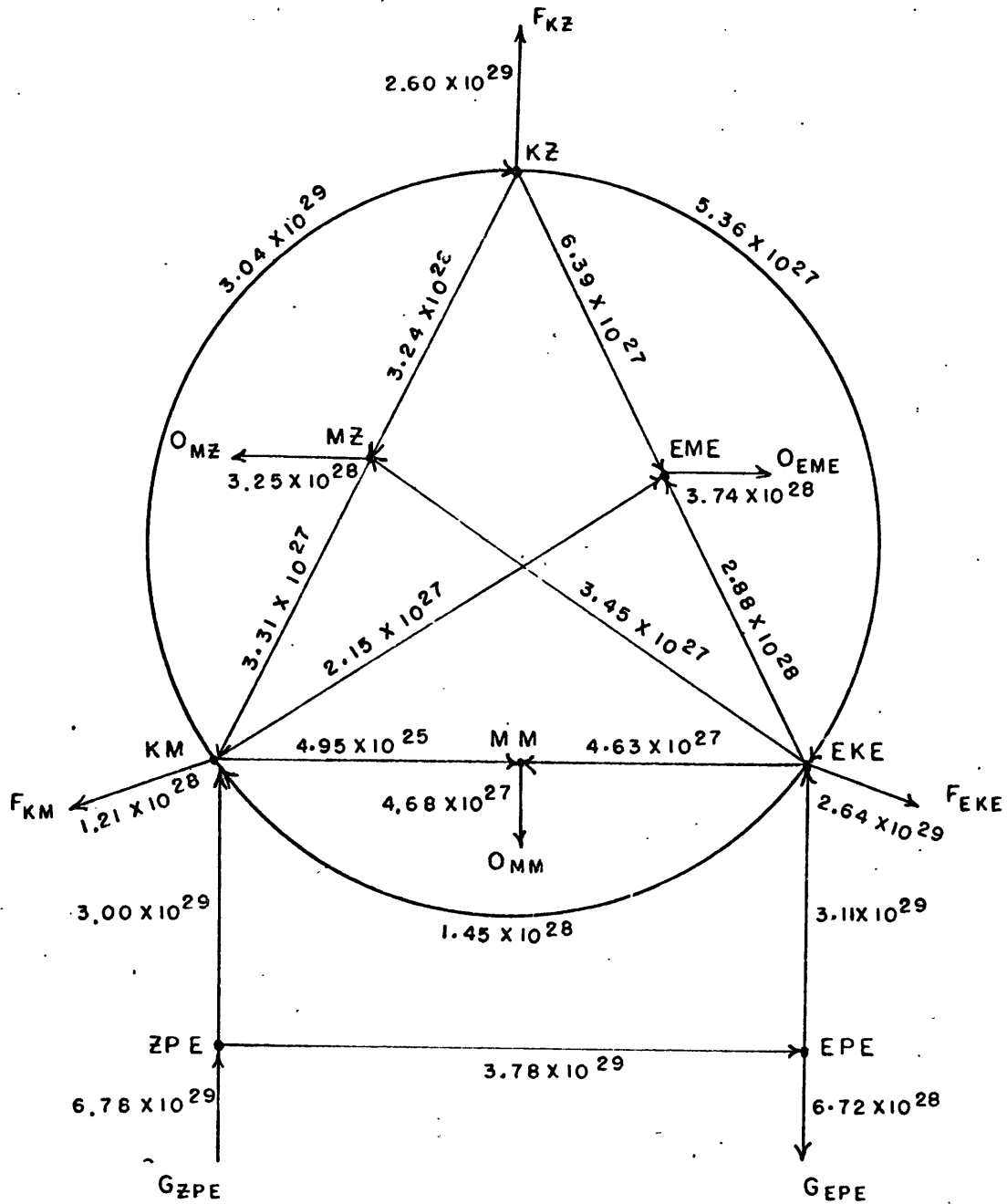


Fig. 6.27. Energy Diagram for magnetic P.R. 2. Units are in ergs/sec. Symbols are defined in text of Chapter V.

whereas $\langle MM \rangle$ is $\mathcal{O}(10^{-1} \cdot \langle MZ \rangle)$ in both runs. Thus, the (axisymmetric) magnetic field is less horizontally nondivergent than the (axisymmetric) velocity field. In Fig. 6.26, only $\sim 1\%$ of the energy input to $\langle KM \rangle$ is dissipated by friction, and most of the remainder is given up to axisymmetric toroidal motions. In contrast, a much greater fraction of the inputs to $\langle KZ \rangle$, $\langle MZ \rangle$, $\langle MM \rangle$, $\langle EKE \rangle$, and $\langle EME \rangle$ are dissipated. Fourth, $\langle EKE \rangle$ which might have been transformed into $\langle KZ \rangle$ in the nonmagnetic case, is transformed primarily into $\langle EME \rangle$ instead. Corresponding energy transformations in P.R. 1 and P.R. 2 have the same sign except for $\{ \langle EKE \rangle \rightarrow \langle KZ \rangle \}$, $\{ \langle EKE \rangle \rightarrow \langle KM \rangle \}$, and $\{ \langle EKE \rangle \rightarrow \langle MZ \rangle \}$, which are not dominant anyway.

One difference between P.R. 1 and P.R. 2 is that the energy levels, and rates of generation, transformation, and dissipation are about four times greater in the latter. We note that the thermal forcing was greater in P.R. 2.

Decomposing $\{ \langle EKE \rangle \rightarrow \langle KZ \rangle \}$, we find that the vertical shear term $\int_S D \int_{\sigma_s} \langle u_2^* w_2^* \rangle \frac{\langle u_2 - u_1 \rangle}{D} dS$ is somewhat more important than the horizontal shear term, especially in P.R. 1. This can perhaps be attributed to the inequality $\left| \frac{1}{a} \frac{\partial}{\partial \ell} \left(\frac{\langle u \rangle}{a \cos \varphi} \right) \right| < \frac{D}{L} \cdot \left| \frac{\partial}{\partial z} \left(\frac{\langle u \rangle}{a \cos \varphi} \right) \right|$. In magnetic P.R. 1 (P.R. 2), the horizontal eddies transport angular momentum down (up) the angular velocity gradient, the vertical eddies transport angular momentum up (down) the gradient, and $\{ \langle EKE \rangle \rightarrow \langle KZ \rangle \}$ is positive (negative). Recall that the equatorial jet in magnetic P.R. 2 appeared to be partly friction-driven. In both runs, $\{ \langle EKE \rangle \rightarrow \langle KZ \rangle \} + \{ \langle EKE \rangle \rightarrow \langle KM \rangle \} > 0$. Also, the coriolis term gives the largest contribution to $\{ \langle KM \rangle \rightarrow \langle KZ \rangle \}$, which may reflect the low model resolution. This term might have been smaller if an indirect cell had existed at mid-latitudes instead of at high latitudes.

Finally, the contribution to $\{\langle KM \rangle \rightarrow \langle KZ \rangle\}$ which involves axisymmetric Reynolds stresses is still larger than $\{\langle EKE \rangle \rightarrow \langle KZ \rangle\}$.

Production of Axisymmetric Toroidal Magnetic Fields

The transformation $\{\langle KZ \rangle \rightarrow \langle MZ \rangle\}$ represents the main source of energy for the axisymmetric toroidal field. It is related to the stretching of poloidal magnetic fields, by the differential rotation, into toroidal magnetic fields. All variables in this interaction are axisymmetric.

Further analysis of this transformation reveals that the vertical shear term $\int_{\sigma_5} \frac{D}{4\pi\mu_0} \langle B_2^\lambda \rangle \langle B_2^z \rangle \frac{\langle u_z - u_r \rangle}{D} dS$ is largest and is nearly always positive. This result is consistent with Leighton's (1969) results. In contrast, Babcock's (1961) scheme relied upon the horizontal shear term. Although that term was also important in Gilman's (1969) model, he expressly excluded the vertical shear term. We attribute the dominance of the vertical shear term in our model to the weakness of the average horizontally differential rotation.

In P.R. 1, the $\langle B_2^\lambda \rangle$ field at time $t-t'$ is strongly positively correlated with the $\langle B_2^z \rangle$ poloidal field at time t and with $\langle B_4^z \rangle$ at approximately time $t-t'$, where $t' \sim 10$ rotations. The strong correlation between $\langle B_2^\lambda \rangle$ and $\langle B_4^z \rangle$ at roughly zero time lag in P.R. 1 can be seen in Fig. 6.28. In P.R. 2, t' is even smaller and as shown in Fig. 6.29, the correlation between $\langle B_2^\lambda \rangle$ and $\langle B_4^z \rangle$ is negative. These differences are consistent with the more rapid time scale and the negative vertical shear of $\langle u \rangle$, respectively. But in both runs, the stretching of $\langle B_2^z \rangle$ fields into $\langle B_2^\lambda \rangle$ fields proceeds very rapidly.

Incidentally, oscillations in $\langle MZ \rangle$ lag behind those in $\langle MM \rangle$ by somewhat less than 90° on the average. This corresponds to a time lag

$t' \sim \mathcal{O}(10)$ rotations in P.R. 1 (shorter in P.R. 2).

We emphasize, however, that not all oscillations in $\langle MM \rangle$ are associated with a reversal of the polar poloidal magnetic field. Meanwhile, $\langle KZ \rangle$ lags a few rotations behind $\langle ZPE \rangle$ and between 90° and 180° (rather than 180°) behind $\langle MZ \rangle$. Although $\langle MM \rangle$ is generally larger than $\langle KM \rangle$, $\langle MM \rangle$ experiences considerably greater fluctuations.

The transformation $\{\langle EKE \rangle \rightarrow \langle MZ \rangle\}$ has a time averaged value only 10% as large as that of $\{\langle KZ \rangle \rightarrow \langle MZ \rangle\}$ in P.R. 2. The corresponding value in P.R. 1 is even relatively weaker and is negative. In both runs, $\{\langle EKE \rangle \rightarrow \langle MZ \rangle\}$ oscillates between positive and negative values. Lastly, $\{\langle KM \rangle \rightarrow \langle MZ \rangle\}$ has a negligible effect upon $\langle MZ \rangle$.

The leading term of $\{\langle EKE \rangle \rightarrow \langle MZ \rangle\}$ is

$$-\int_{\sigma_5} \frac{D}{4\pi\mu_0} \langle v_3^* B_3^{\lambda*} - u_3^* B_3^{\varphi*} \rangle \frac{1}{a \cos \varphi} \frac{\partial}{\partial \varphi} (-\langle B_3^\lambda \rangle \cos \varphi) dS.$$
 Those terms associated with the vertical shear of $\langle B^\lambda \rangle$ are smaller. In this connection, the

ratio of instantaneous horizontal to vertical shear of $\langle B^\lambda \rangle$ is not small, unlike the case for $\langle u \rangle$. Although the decomposition

$$\langle v_3^* B_3^{\lambda*} - u_3^* B_3^{\varphi*} \rangle = -\langle J_{\lambda, \varphi}(\psi_{v_3}^*, \psi_{m_3}^*) \rangle + \left[\nabla_H \psi_{v_3}^* \cdot \nabla_H \phi_{m_3}^* - \nabla_H \phi_{v_3}^* \cdot \nabla_H \psi_{m_3}^* + J_{\lambda, \varphi}(\phi_{m_3}^*, \phi_{v_3}^*) \right]$$

was not carried out, we speculate that $-\langle J_{\lambda, \varphi}(\psi_{v_3}^*, \psi_{m_3}^*) \rangle$ should be important since the toroidal components of \underline{B}_H and especially of \underline{v}_H are largest. This term has been referred to as a mixed stress by Gilman (1966) and may be interpreted as the advection of eddy toroidal magnetic flux by eddy toroidal motions. The nonvanishing of $J_{\lambda, \varphi}(\psi_{v_3}^*, \psi_{m_3}^*)$ implies that the magnetic and velocity streamlines are not in phase. This term contains no interaction with eddy poloidal fields. The last two terms inside the brackets do, but these interactions are evidently not very important in our model.

Maintenance and Reversals of Axisymmetric Poloidal Magnetic Fields.

According to Fig. 6.26 and Fig. 6.27, the energy transformation $\{ \langle EKE \rangle \rightarrow \langle MM \rangle \}$ is the primary source of axisymmetric poloidal magnetic energy. Axisymmetric poloidal magnetic fields may be directly regenerated via the transport of toroidal magnetic eddies by poloidal eddy motions. This involves the toroidal part of $B_2^{\omega*}$ in $\int_{\sigma_5} \frac{D}{4\pi\mu_0} \langle \omega_2^* B_2^{\omega*} \rangle \frac{\langle B_3^{\omega} - B_1^{\omega} \rangle}{D} dS$. The total integral oscillates between positive and negative values, its time averaged value being positive for P.R. 1 and negative for P.R. 2.

A more important term than the above integral, and hence than direct regenerative feedback, is the horizontal transport at level 2, i.e., $-\int_{\sigma_5} \frac{D}{4\pi\mu_0} \langle v_2^* B_2^{\beta*} \rangle \frac{\langle B_3^{\omega} - B_1^{\omega} \rangle}{D} dS$. The positive time averaged value of this integral is about a factor of five larger than that of the first and roughly 75% of its values are positive in P.R. 1. Meanwhile, the horizontal transport term involving $\langle v_3^* B_4^{\beta*} \rangle$ is small in comparison. Finally, $\{ \langle KM \rangle \rightarrow \langle MM \rangle \} \sim \int_{\sigma_5} \frac{D}{4\pi\mu_0} \langle \omega_2 \rangle \langle B_2^{\omega} \rangle \frac{\langle B_3^{\omega} - B_1^{\omega} \rangle}{D} dS$ is of comparable magnitude to its eddy counterpart in $\{ \langle EKE \rangle \rightarrow \langle MM \rangle \}$, but is not coupled to the toroidal magnetic field.

In the horizontal transport integral at level 2, $\langle v_2^* B_2^{\beta*} \rangle$ may be interpreted as the meridional transport of vertical magnetic eddies by toroidal eddy motions, since $\frac{v}{H_2}$ is purely toroidal. Gilman (1969) showed that the dominant term affecting his axisymmetric vertical magnetic field $\langle B^{\beta} \rangle$ (represented by a single harmonic) was a $\langle v^* B^{\beta*} \rangle$ eddy toroidal type transport term. Moreover, the quasi-periodic oscillation of $\langle B^{\beta} \rangle$ lagged that of $\langle v^* B^{\beta*} \rangle$ by $\sim 90^\circ$. In contrast, Leighton (1964, 1969) invoked a diffusion mechanism to account for polarity reversals of $\langle B^{\beta} \rangle$ at high latitudes. Finally, Babcock (1961), and Nakagawa and Swartztrauber (1969) invoked an axisymmetric poloidal transport term $\propto \langle v \rangle \langle B^{\beta} \rangle$.

Analysis of the energetics, including the time variation of the energy transformations affecting $\langle MM \rangle$, does not reveal which term (or terms) is responsible for the actual reversals of the polar $\langle B_2^3 \rangle$ or $\langle B_4^3 \rangle$ magnetic fields. This information could be obtained with the aid of the equations

$$\frac{\partial B_2^3}{\partial t} = -D \nabla_H \cdot \frac{\partial B_{H_1}}{\partial t} \equiv - \left(\underbrace{V_{H_2} \cdot \nabla_H B_2^3}_{(Ia)} + \underbrace{W_2 \frac{B_4^3}{2D}}_{(Ib)} \right) + \underbrace{B_{H_2} \cdot \nabla_H W_2}_{(II)} + \mathcal{H}_2 \quad (6-5a)$$

$$\frac{\partial B_4^3}{\partial t} = -D \nabla_H \cdot \left[\frac{\partial B_{H_1}}{\partial t} + \frac{\partial B_{H_2}}{\partial t} \right] \equiv - \underbrace{V_{H_3} \cdot \nabla_H B_4^3}_{(III)} - \underbrace{W_2 B_4^3 / D}_{(IV)} + \mathcal{H}_4 \quad (6-5b)$$

Here \mathcal{H}_2 and \mathcal{H}_4 represent ohmic dissipation, (I) — purely toroidal horizontal advection, (II) — horizontal twisting, and (III) — horizontal advection. Also, (IV) = 2 · (Ib) is best interpreted as a vertical twisting term. Note that no meridional transport $\langle V_2 \rangle \langle B_2^3 \rangle$ is possible at level 2, because $\langle V_2 \rangle = 0$. One could evaluate (6-5a) and (6-5b) from history tape data, once every rotation, say. This could be done in either the space domain (using the Robert method) or the spectral domain (using a spherical harmonic expansion). In this manner, the details of the reversals of $\langle B_2^3 \rangle$ and $\langle B_4^3 \rangle$ could be ascertained. Considering the lack of quasi-regularity and the greater number of interactions, the details of the reversals are apt to be more complex than in Gilman's model.

Regenerative Feedback of Poloidal Eddy Magnetic Fields.

If the direct regeneration of axisymmetric poloidal magnetic fields is relatively small on the average, as already implied, then eddy poloidal fields must be regenerated from toroidal fields. Energetically, the relevant transformations to be analyzed are $\{ \langle EKE \rangle \rightarrow \langle EME \rangle \}$, $\{ \langle KZ \rangle \rightarrow \langle EME \rangle \}$, and $\{ \langle KM \rangle \rightarrow \langle EME \rangle \}$. Of these, $\{ \langle EKE \rangle \rightarrow \langle EME \rangle \}$ is largest. Further analysis reveals that

$$-\int_{\sigma_s} \frac{D}{4\pi\mu_0} (\langle \nabla_H^2 \psi_{m_1}^* v_1^* \rangle \langle B_1^\lambda \rangle + \langle \nabla_H^2 \psi_{m_3}^* v_3^* \rangle \langle B_3^\lambda \rangle) dS$$
 and

$$\int_{\sigma_s} \frac{D \langle B_2^\lambda \rangle}{4\pi\mu_0} \langle w_2^* \frac{(B_3^{\lambda*} - B_3^{\lambda**})}{D} \rangle dS$$
 are respectively the first and second largest terms of $\{ \langle EKE \rangle \rightarrow \langle EME \rangle \}$. Both terms are generally positive in P.R. 1 and their ratio is ~ 5 . The remaining terms are individually 10% as large, but their sum virtually cancels. In P.R. 2, the second term is $\sim 50\%$ as large as the first. However, the first term is negative $\sim 30\%$ of the time. Meanwhile, the other terms are negligible. Incidentally, oscillations in $\langle EME \rangle$ and $\langle EKE \rangle$ are highly correlated in time, and $\langle EME \rangle$ lags behind $\langle EKE \rangle$, but by only one or two rotations.

From Fig. 6.26 and Fig. 6.27, $\{ \langle KZ \rangle \rightarrow \langle EME \rangle \} \sim 25\%$ of $\{ \langle EKE \rangle \rightarrow \langle EME \rangle \}$ and $\{ \langle KM \rangle \rightarrow \langle EME \rangle \} \sim 10\%$ of $\{ \langle EKE \rangle \rightarrow \langle EME \rangle \}$. The weak horizontal differential rotation is probably responsible.

Of course, what really interests us here is the eddy poloidal magnetic energy $\langle EME \rangle_P = \int_{\sigma_s} \frac{D}{8\pi\mu_0} (|\nabla_H \phi_{m_1}^*|^2 + |\nabla_H \phi_{m_3}^*|^2) dS = \langle EME \rangle - \langle EME \rangle_T$ where $\langle EME \rangle_T = \int_{\sigma_s} \frac{D}{8\pi\mu_0} (|\nabla_H \psi_{m_1}^*|^2 + |\nabla_H \psi_{m_3}^*|^2) dS$ is the eddy toroidal magnetic energy. We speculate that the twisting of axisymmetric toroidal magnetic fields by eddy vertical motions could be an important if not the dominant regenerative feedback of eddy poloidal magnetic fields. It is analogous to the mechanism found by Gilman (1969). Some heuristic arguments are given below in support of this view.

From the previous discussion, the three largest terms which build up $\langle EME \rangle$ are, in order of size,

$$\begin{aligned}
 & - \int_{\sigma_s} \frac{D}{4\pi\mu_0} (\langle \nabla_H^2 \psi_{m_1}^* v_1^* \rangle \langle B_1^\lambda \rangle + \langle \nabla_H^2 \psi_{m_3}^* v_3^* \rangle \langle B_3^\lambda \rangle) dS, \\
 & \int_{\sigma_s} \frac{D}{4\pi\mu_0} \langle B_2^\lambda \rangle \langle w_2^* \frac{(B_3^{\lambda*} - B_3^{\lambda**})}{D} \rangle dS \quad \text{and} \quad \int_{\sigma_s} \frac{D}{4\pi\mu_0} \langle B_2^{\lambda*} B_2^{\lambda**} \rangle \frac{\langle u_3 - u_1 \rangle}{D} dS.
 \end{aligned}$$

Now the third integral evidently builds up only $\langle EME \rangle_T$ since it lacks poloidal motions. Bullard and Gellman (1954) proved (for a somewhat different model) that such motions are required to regenerate poloidal magnetic

energy. In fact, the third integral represents the magnetic eddy analogue of the stretching of axisymmetric poloidal into toroidal fields by the vertical shear.

The second integral is probably smaller than the first, because the former contains only a poloidal velocity component whereas the latter involves a larger toroidal velocity V_T^* as well. However, the part of the first integral associated with V_T^* should affect only $\langle EME \rangle_T$. We also note that the first integral contains no poloidal magnetic field harmonics and that the poloidal magnetic field eddies in the second integral are presumably not much smaller than their toroidal counterparts. Hence the second integral could make at least a significant contribution to $\langle EME \rangle_P$. In this integral, w_2^* and $\langle B_2^1 \rangle$ can be traced back to the horizontal induction equations, while $B_3^1 - B_1^1$ is related to the factors $B_{H_1}^*$ and $B_{H_3}^*$ in the energy balance equation $\sum_{i=1,3} \langle B_{H_i}^* \cdot \frac{\partial B_{H_i}^*}{\partial x} \rangle$ for $\langle EME \rangle$.

6.8.4. Further Discussion of Dynamo Maintenance.

It was previously suggested that the development of strong magnetic fields characterized by $\overline{a^2} < O(10)$ partially suppressed baroclinic instability. This could come about, for example, by a reduction of w_2^* . In this connection, the vertical eddy motions are generally weakest in regions of strong axisymmetric toroidal magnetic fields in P.R. 1 and in P.R. 2, as illustrated in Fig. 6.30. There, the instantaneous untruncated standard deviation $\sigma_s(w_2(\varrho, t)) = \sqrt{\langle w_2^{*2} \rangle}$ of w_2 at latitude ϱ exceeds a specified value σ_{sc} inside the shaded regions. Although the values adopted for σ_{sc} are somewhat arbitrary, $\sigma_s(w_2(\varrho, t))$ usually would be greater than σ_{sc} in the nonmagnetic case, within the mid-latitude zones of maximum baroclinicity. The truncated values would be somewhat weaker due to smoothing effects. Another property (not illustrated) is the tendency for strong

centers of $\sigma_5^{\lambda}(w_2(\varrho, t-t''))$ and $\zeta_5^{\lambda}(B_2^{\lambda}(\varrho, t))$ to overlap, where the lag t'' is small, e.g., 3 solar rotations or less.

The above results, like the energetics analysis, suggest that the term $\frac{\langle B_2^{\lambda} \rangle}{a \cos \varrho} \frac{\partial w_2^*}{\partial \lambda}$ in equation (6-5a) could be important for the regenerative feedback of eddy (vertical) poloidal magnetic fields. The product is small if either $\langle B_2^{\lambda} \rangle$ is locally small or very large. In the latter case, w_2^* is small. The reduction of regenerative feedback ultimately imposes an upper bound on $\langle B_2^{\lambda} \rangle$. However, for a while, advection and vertical twisting of vertical magnetic fields can cause a local buildup of $\langle B_2^{\lambda} \rangle$ fields and hence of $\langle B_2^{\lambda} \rangle$ fields. There is no regenerative feedback term in equation (6-5b) involving toroidal fields.

Babcock (1961) cited two regenerative feedback mechanisms for the formation of sunspots, which apparently have a rather different physical basis than our feedback mechanism. More specifically, these are Parker's magnetic buoyancy of locally intense toroidal magnetic fields and Lundquist's magnetic loop instabilities in very strong toroidal flux ropes.

Recently, Leighton (1969) devised an axisymmetric magneto-kinematic model of the solar cycle (see Chapter I) in which the zonally averaged effects of sunspots are parameterized. Wherever the axisymmetric toroidal magnetic field exceeded a critical strength, he assumed that sunspots extracted magnetic flux from this field at a specified rate. If $\overline{a^2}$ could have been larger in our model, the vertical eddy motions would not be drastically suppressed when $\langle B_2^{\lambda} \rangle$ reached peak strength. Thus, in principle, maximum regenerative feedback could occur at that time even in a baroclinic hydromagnetic dynamo model.

6.8.5. Spörer's Law and Possibly Related Phenomena.

According to Spörer's law for sunspots, the zone of maximum

sunspot activity drifts equatorward during the course of each 11 year segment of the 22 year (double) sunspot cycle. The well known Maunder butterfly diagrams reflect this behavior. Spörer's law may also be generalized to include active regions in which the sunspots are imbedded.

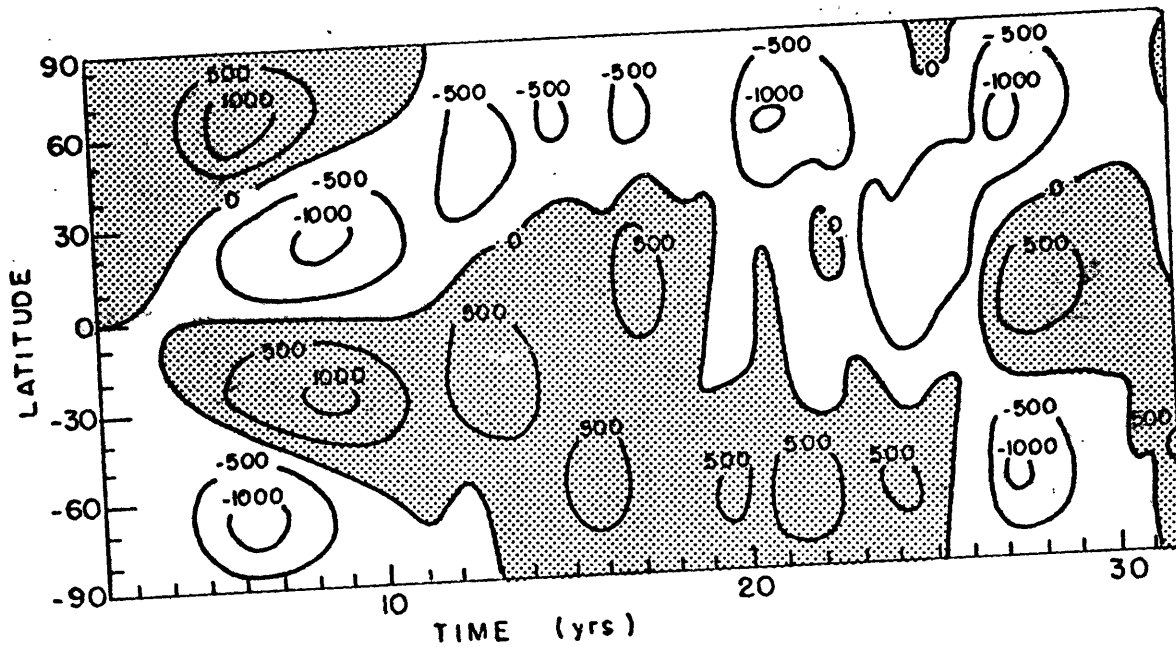
The most logical indices for magnetic activity in our model are the variance $\langle B_2^{3*2} \rangle$ of B_2^3 and $\langle B_4^{3*2} \rangle$ of B_4^3 . These variances are found to be considerably greater in one or the other hemisphere, at different times. On the other hand, maxima of $\langle B_2^{3*2} \rangle$ do not systematically drift equatorward or poleward in either run, just as is the case for maxima of $\langle w_2^{*2} \rangle$. An equatorward drift in the maxima of $\langle B_2^\lambda \rangle$ could possibly lead to such a drift in the maxima of $\langle B_2^{3*2} \rangle$, if $\langle w_2^{*2} \rangle$, which is inherently weaker at low latitudes, were not further weakened there by strong $\langle B_2^\lambda \rangle$ fields. Meanwhile, whereas $\langle B_4^{3*2} \rangle$ does not systematically drift either poleward or equatorward in P.R. 1, there is a vague suggestion of an equatorward drift in P.R. 2. But the variance is too small by an order of magnitude in both runs.

Leighton effectively takes the strength of $\langle B^3 \rangle$ as an index of magnetic activity in his axisymmetric magneto-kinematic model of the solar cycle. Despite the predominance of the leading polarity in bipolar magnetic regions, it is not entirely clear that $|KB^3|$ as opposed to $\langle B^{3*2} \rangle$ should be much larger there than at high latitudes, or is a good index of magnetic activity. At any rate, $|\langle B^3 \rangle|_{\max}$ drifts equatorward, followed by $|KB^\lambda|_{\max}$ in Leighton's model for the following two important cases: (a) observed horizontal differential rotation and zero vertical differential rotation; (b) observed horizontal differential rotation and a negative differential rotation proportional to $r \cdot \cos^8 \varphi$. But for his choice of amplitude of $\frac{\partial \omega}{\partial r}$, a positive vertical shear leads to a poleward drift. Note that $\partial \omega / \partial r$

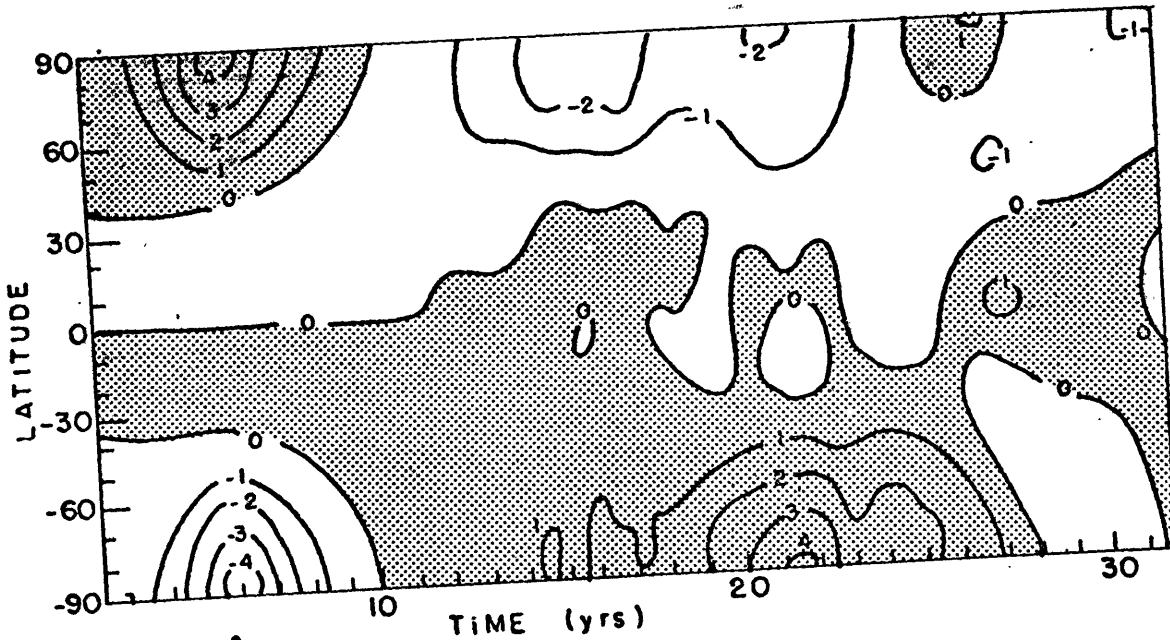
drops off very sharply with latitude.

Irrespective of the validity of Leighton's interpretation of his results, it is interesting to compare our migrations of $\langle B_2^1 \rangle$ and $\langle B_4^3 \rangle$ with his. We recall that these variables are well correlated in our model at close to zero time lag. Referring again to Fig. 6.28, we see that there is a tendency for poleward drifts in P.R. 1, especially during the first 13 years or so. Perhaps it is not a coincidence that the vertical differential rotation has a positive sign for this run. In other words, this may be an important determining factor in Leighton's model runs, and even more so in ours, since our horizontal differential rotation at level 2 is so weak. Fig. 6.29 depicts the situation for P.R. 2 in which the vertical shear of $\langle u \rangle$ is negative. Probably the most realistic interpretation is that magnetic regions of $\langle B_2^1 \rangle$ in the two hemispheres drift simultaneously, either northward or southward, and similarly for $\langle B_4^3 \rangle$. However, there is some suggestion of an equatorward drift of $\langle B_4^3 \rangle$, especially in the northern hemisphere. Making such an interpretation, some drifts overshoot the equator and some wings of the butterfly configuration are out of phase. More definitive equatorward drifts might occur in a higher resolution model with a stronger vertically averaged horizontal differential rotation. Incidentally, the magnetic related destabilization of the horizontal shear of $\langle u_2 \rangle$ is illustrated in Fig. 6.31 for P.R. 2. An analogous destabilization occurred in P.R. 1, except that the $\langle u_2 \rangle$ contours and the $\overline{a^2}$ curve were much smoother for this mid-latitude westerly jet case.

Another feature worthy of note in Fig. 6.28b is the drift of a zero line of $\langle B_4^3 \rangle$ towards each pole during the first reversal and towards the south pole during a minireversal in P.R. 1. Most drifts associated with reversals beyond $t=30$ years in P.R. 1 were also of this type.



(a) $\langle B_2^A \rangle$



(b) $\langle B_4^3 \rangle$

Fig. 6.28. Meridional-time cross section of axisymmetric toroidal and vertical magnetic fields for P.R. 1. Contours are in gauss. Regions of positive field are shaded.

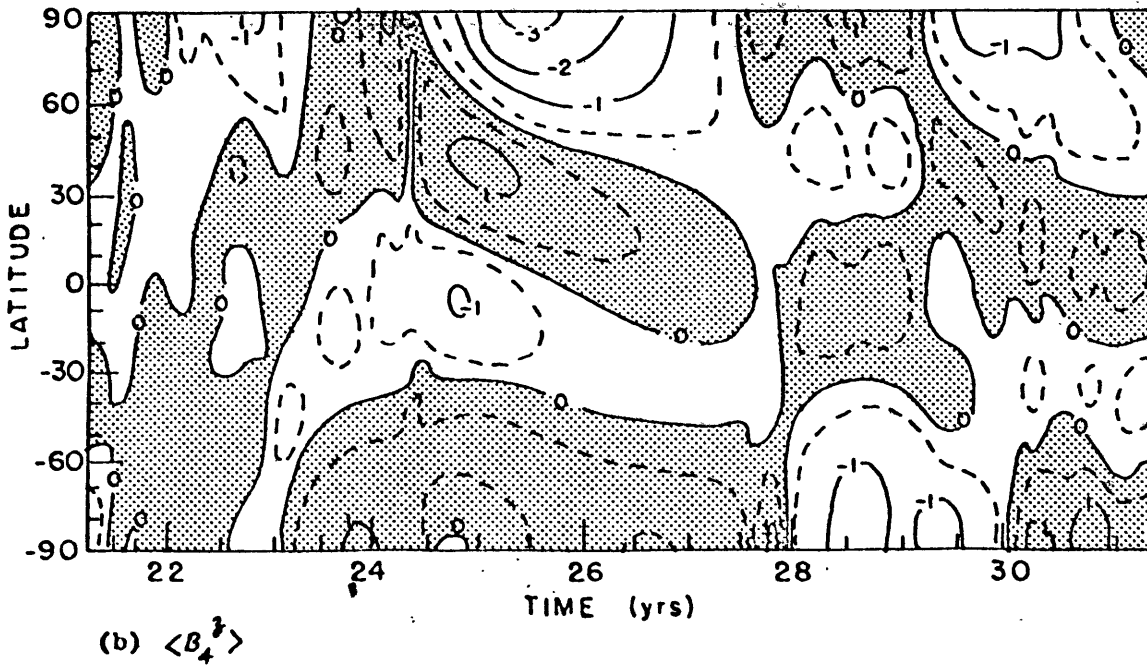
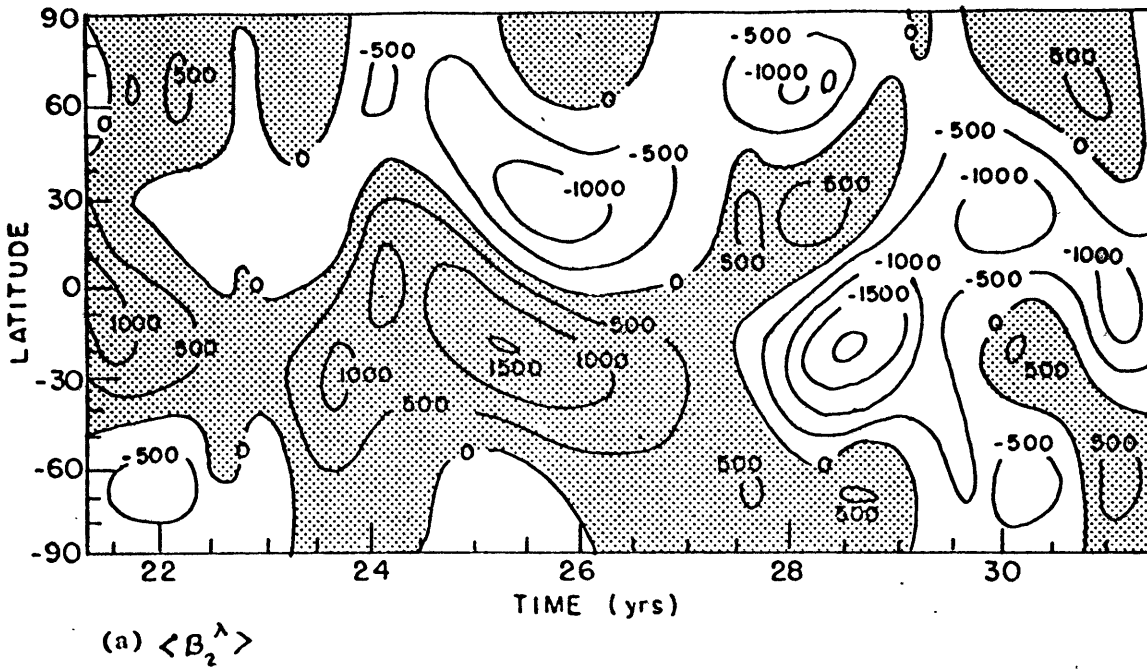


Fig. 6.29. Meridional-time cross section of axisymmetric toroidal and vertical magnetic fields for P.R. 2. Solid contours interval = 1 gauss, dashed contours = 0.4 gauss. Regions of positive field are shaded.

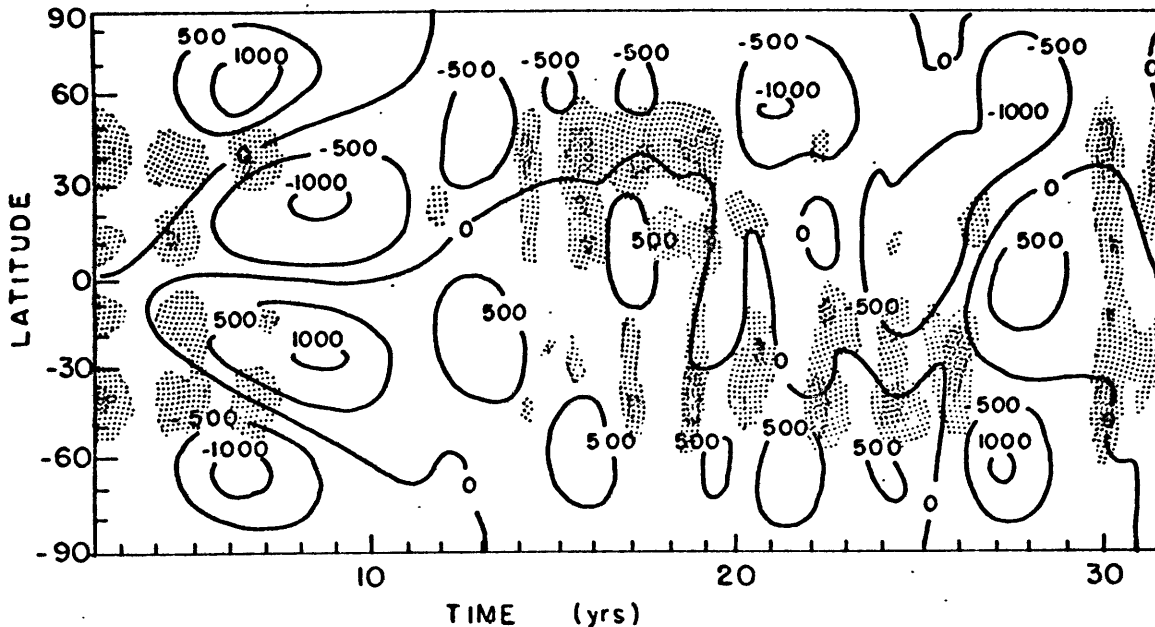


Fig. 6.30a. Superposition of regions of strong vertical eddy motions upon the meridional-time cross section of $\langle \beta_2^A \rangle$ of Fig. 6.28a for P.R. 1. The untruncated variance $\langle w_2^{*2} \rangle(u,t)$ exceeds 20 cm/sec and 40 cm/sec respectively, in lightly and darkly shaded regions.

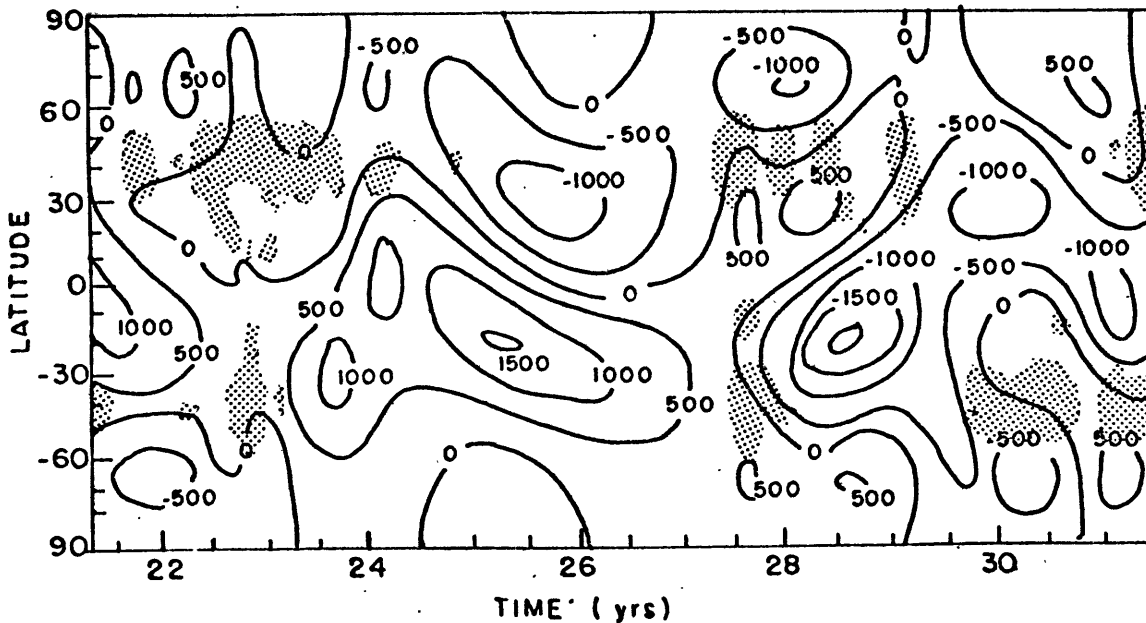


Fig. 6.30b. Superposition of regions of strong vertical eddy motions upon the meridional-time cross section of $\langle \beta_2^A \rangle$ of Fig. 6.29a for P.R. 2. The untruncated variance $\langle w_2^{*2} \rangle(u,t)$ exceeds 100 cm/sec in shaded regions.

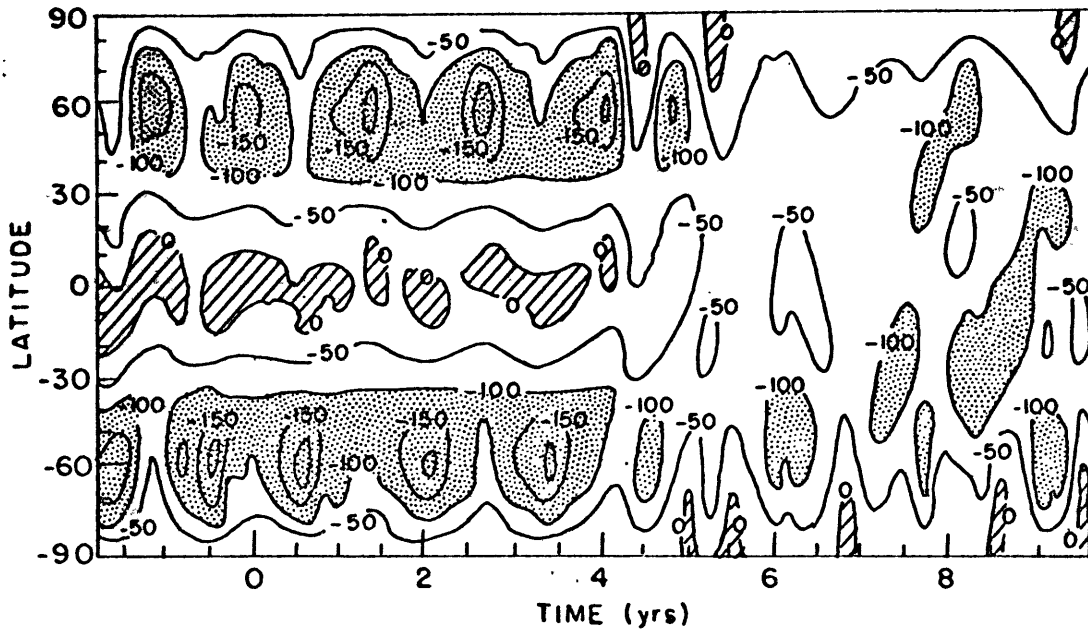


Fig. 6.31a. Meridional-time cross section of the vertically averaged zonal wind $\langle u_2 \rangle$ in P.R. 2. Contours are in m/sec. Hatched regions denote (weak) relative westerlies. Dotted regions denote relative easterlies stronger than 100 m/sec.

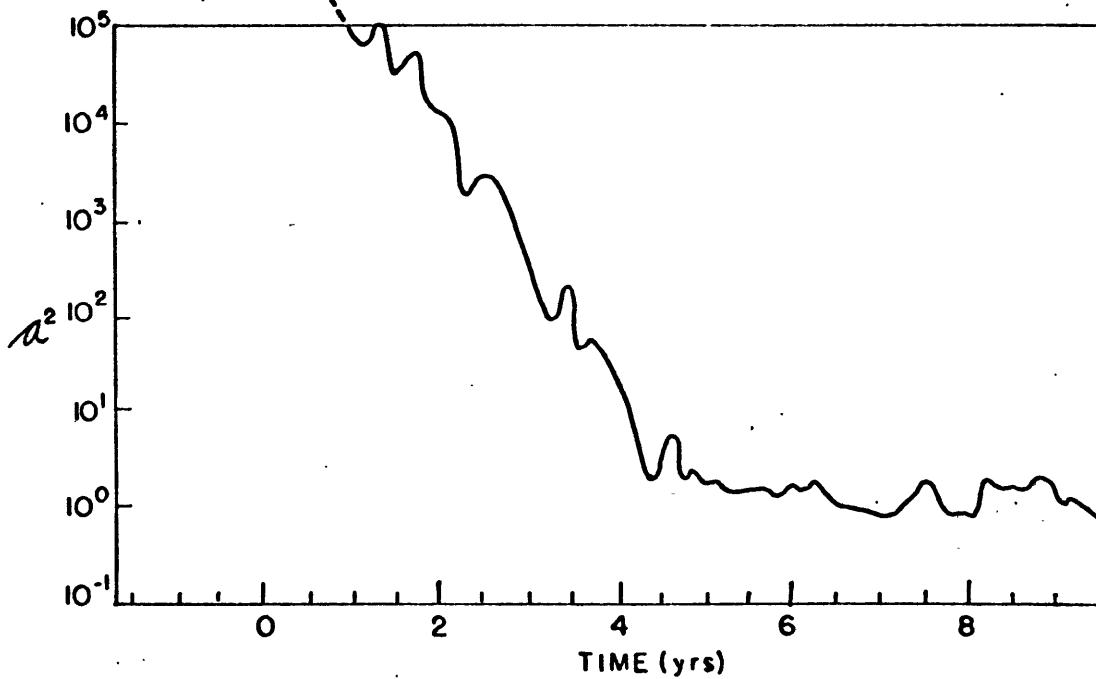


Fig. 6.31b. Time evolution of the square of the Alfvén number. The horizontal shear of $\langle u_2 \rangle$ in Fig. 6.30(a) breaks down to a large extent about the time that a^2 becomes smaller than $\sigma(10)$.

In Fig. 6.29b, there is evidence of slight recurving, but not enough, of the zero line of $\langle B_4^3 \rangle$ in polar regions. On the sun, the zero line of $\langle B^{\ell} \rangle$ usually delineates a solar quiescent prominence and both move poleward.

Finally, our zonally averaged vertical magnetic fields reach peak strength at the poles, not at lower latitudes. This is true for both runs. In contrast, the variance of B_2^3 (and of what there is of B_4^3) is generally confined to latitudes equatorward of $\pm 60^\circ$ in P.R. 1 and $\pm 50^\circ$ in P.R. 2. The magnetic eddies decay, of course, as $\cos^6 \varrho$, since $n=6$ is the only positive zonal wave number retained.

CHAPTER VII. CONCLUSIONS AND SUGGESTIONS FOR FUTURE RESEARCH

Although a primary objective was to test whether our baroclinic model is plausible for the sun, a definitive test would require considerably more model resolution than was currently feasible. Nevertheless, the results are encouraging in some respects, and indicate how to proceed numerically when faster computers are available.

In applying the model to the sun, we have attempted to (1) generate and sustain magnetic fields by dynamo action, (2) simulate the observed solar horizontal differential rotation and its maintenance, and (3) simulate the large scale features of the solar magnetic sunspot cycle including reversals of the polar poloidal magnetic field and phenomenological laws governing magnetic active regions.

We have demonstrated that magnetic fields can be generated and sustained by dynamo action. Whereas either $\bar{a}^2 \gtrsim \sigma(10^4)$ or $\bar{a}^2 < 3$ in our magnetic runs, intermediate values hopefully could be attained. This should be verified numerically, e.g., by inserting more resolution and/or by selecting a few values of R_m for P.R. 2 such that $250 < R_m < 325$ and estimating the steepness of the slope $-\partial\bar{a}^2/\partial R_m$. Our experiments did suggest that R_{mc} varies with the pre-established (nonmagnetic) flow pattern. The apparent increase of R_{mc} in the one run with higher resolution does not necessarily imply that R_{mc} would be unbounded in the limit of infinite resolution.

Modest success is claimed in the simulation of the solar equatorial jet in the nonmagnetic case. For two different thermal forcing profiles (i.e., (b) and (c)), a horizontal differential rotation of the required strength developed and was maintained by horizontal eddy transports.

Fultz's dishpan experiments and Ward's sunspot statistics lend credence to the above results, despite the low model resolution.

Future systematic Doppler measurements on different spectral lines could reveal information on $\partial \bar{n}_{abs} / \partial z$ (in the photosphere) which could favor one thermal forcing profile of (b) and (c) over the other. The large equator to pole temperature difference for profile (b) in P.R. 2 does not necessarily imply that the baroclinic hypothesis should be rejected. Thus, a smaller horizontal temperature difference which extended over a deeper layer could produce a vertical wind shear of the required magnitude.

One limitation of the model is that the highest permitted harmonic of \mathcal{N}_{abs} was \mathcal{N}_3 (cf. formulas 1-1) and (1-2)). Another possible limitation is that only two meridional cells per hemisphere could be resolved. Hence a qualitative confirmation of the above results with a higher resolution model would be recommended.

As a further improvement, the higher resolution nonmagnetic runs should be integrated for (up to) several hundred rotations before introducing the seed magnetic field. This would give the solutions a better opportunity to approach a quasi-steady state, if so inclined. Also, the general circulation statistics for the nonmagnetic case would be more representative.

In the magnetic runs with $\bar{a}^2 < 3$, the magnetic fields did not reverse the tilt of the streamline patterns or the sign of the eddy transport of angular momentum. Nevertheless, the magnetic feedback was very large and was associated with a somewhat stronger meridional circulation, partial suppression of baroclinic instability, reduced eddy transports, and a rapid conversion of eddy kinetic into eddy magnetic energy. Consequently, the pre-established zonal flow (barotropic mode) was also destabilized. It

remains to be seen whether the shear reversal at level 3 in P.R. 1 or at level 1 in P.R. 2 are real effects or are due to the low resolution. We also caution that the above results cannot be generalized throughout the range $\mathcal{O}(10^{-1}) \lesssim \overline{a^2} \lesssim \mathcal{O}(10^3)$. For $\overline{a^2} \sim \mathcal{O}(10^4)$, we verified that the magnetic feedback was negligible.

In Gilman's quasi-heliostrophic dynamo model, $\overline{a^2}$ remained of $\mathcal{O}(10)$ and the zonal velocity profile (barotropic mode) was not destabilized. Curiously enough, his toroidal magnetic fields could be produced from poloidal magnetic fields only by horizontal and not by vertical stretching. Thus, his model may have a built-in mechanism which our model lacks for increasing the lower bound on $\overline{a^2}$. In addition, his quasi-heliostrophic model excludes dynamically active axisymmetric Reynolds stresses, which were very important in our magnetic production runs.

Concerning the simulation of the solar magnetic cycle, the reversals in the poloidal magnetic field $\langle B_4^3 \rangle$ were encouraging. For P.R. 1, the mean reversal time was certainly of the correct order of magnitude, although the reversals were more irregular than is presumed to occur on the sun. The reversal time in P.R. 2 was much shorter. One possible cause is the stronger vertical wind shear, hence more rapid stretching of poloidal into toroidal field lines. Another is the more irregular character of the solutions in P.R. 2 as compared to P.R. 1 (or test run 7) in the nonmagnetic case. This could be related to the presence of a relative easterly mid latitude jet in P.R. 2. With less magnetic feedback ($\overline{a^2} \gg 1$), the motion field should remain relatively quasi-steady, at least for thermal forcing profile (c) and probably for (e). The result could be less irregular reversals with a proper time scale. Profile (c) is probably the more realistic since it yields a relative westerly equatorial jet in the

nonmagnetic case, which should persist in the magnetic case with $\overline{a^2} \gg 1$. One question mark is whether or not the positive vertical shear of $\langle u \rangle$ at low latitudes would be unfavorable to the equatorward migration of the zone of maximum magnetic activity.

From energetics considerations, some aspects of the dynamo maintenance were inferred. However, a more detailed analysis of the vertical magnetic induction equations (6-5a) and (6-5b) could further clarify the reversal process.

The model vertical magnetic fields were comparable in strength to the observed line of sight fields, except for the variance of β_4^3 . The intense magnetic feedback upon the flow could be reduced without weakening the vertical magnetic field strength by simultaneously increasing the vertical length scale D and, if possible, $\overline{a^2}$. Even with D five times larger, $\mathcal{J} < 0.20$.

Our vertical magnetic field patterns could be loosely interpreted as magnetic active regions. Also, asymmetry in magnetic activity between hemispheres was found. In other respects though, the simulation of the solar magnetic cycle was not too good. This may reflect deficiencies in the model other than the baroclinic drive. We speculate that the tilts of the β_4^3 eddy magnetic fields would be better in a run with $\overline{a^2} \gg 1$. In that case, the motions would essentially push the magnetic fields around and the magnetic field patterns could be stretched out by a differential rotation with more realistic horizontal shear.

The proper simulation of unipolar and ghost unipolar magnetic regions at higher latitudes requires the $n=1$ and $n=2$ harmonics. Also, to capture the detail of moderate resolution magnetograms (as in Fig. 1.1), much more resolution is a minimum requirement. Thirdly, with more resolution, e.g., $0 \leq n \leq 8$ and $0 \leq m \leq 8$, a meaningful comparison could be made

between our potential magnetic field above level 4 and the "observed" coronal magnetic field. The latter may be inferred from the observed coronal density structure since material flows along the magnetic field lines in the corona. Finally, a sector structure in the line of sight component of the model potential magnetic field, characterized by zonal wave number $n \sim 2$ could be looked for.

In short, when computationally feasible, runs should be made having (1) more horizontal resolution, e.g., $0 \leq n \leq 8$, $0 \leq m \leq 8$ and possibly more layers, (2) a larger vertical length scale D (holding $\sqrt{gD\kappa_s}$ fixed), and (3) a smaller value of $R_m - R_{mc}$. This would provide a more definitive test of the applicability of a baroclinic model to the sun. However, with $0 \leq n \leq 8$ and $0 \leq m \leq 8$ as the horizontal resolution, the number of harmonics would increase 10 fold and the computation time per time step ~ 100 fold. The other modifications would cause no loss of efficiency.

One could also try different initial conditions on the magnetic field. For example, a small axisymmetric dipole poloidal magnetic field could be specified instead of toroidal field perturbations at $t=0$, to see if the growth of antisymmetric harmonics of $\langle B^2 \rangle$ and $\langle B^1 \rangle$ were favored. Since the boundary conditions on \underline{V}_H were rather ad hoc, a comparison of results for various boundary conditions would also be useful. In particular, the condition at the top boundary that $\frac{\partial \underline{V}_H}{\partial z} = 0$ could be applied to the bottom boundary as well.

Kinematic dynamos (pseudo dynamos) have been studied numerically as a steady state (and/or axisymmetric) problem with the velocity field specified in a rather ad hoc manner. A somewhat new twist would be to choose a quasi-steady particular numerical solution of the nonmagnetic baroclinic model (if one could be found) as the known velocity field in the magnetic

induction equations. Physically, the magnetic solutions to the kinematic dynamo problem might be regarded as a sort of limiting case of hydromagnetic solutions with large $\overline{Q^2}$, assuming these exist. Computationally, of course, the kinematic dynamo problem is more tractable. Approximately a 30% savings of computer time would be gained for lengthy runs, reflecting a 30% reduction in the number of nonlinear terms to be evaluated. Even more importantly, a substantially longer time step could probably be used without the solutions becoming computationally unstable. Of physical interest is whether magnetic reversals would still be present, and if so, whether their character would remain basically unaltered from the hydromagnetic case. Although reversals occurred in Leighton's (1969) magneto-kinematic model, that model was not a true dynamo and the various phases of the cycle were helped along. We also note that P.H. Roberts (1967) speculated that in general, magnetic reversals might exist in only hydromagnetic type dynamos.

Future work may demonstrate the need for treating the motions and/or magnetic fields three-dimensionally. In principle, our Boussinesq model could be modified to treat large scale convection explicitly. The vertical hydromagnetic (or Lundquist) equations would have to be retained. As in the Rayleigh convection problem, the bottom boundary would be heated and the top boundary cooled. To eliminate the pressure, the $\hat{\mathcal{L}} \cdot \nabla \times$ and $\hat{\mathcal{L}} \cdot \nabla \times \nabla \times$ operators could be applied to the equations of motion (after first evaluating the right hand side), following Busse (1970). Computationally, the number of nonlinear multiplications in each equation would not be increased. However, at each level, there would be two more equations, and many more levels would be required. Thus, the convection version of the model is much more complicated than the original baroclinic version.

Finally, the question arises: What are the prospects for numerical prediction of the evolution of solar magnetic disturbances? As background, we recall that line of sight velocities and magnetic fields can be determined for photospheric (or chromospheric) lines at different levels. Thus, some vertical resolution is even possible. Also, the line of sight velocity or magnetic fields could be reduced to purely horizontal toroidal vector fields as a first approximation. In fact, a scheme (the method of characteristics) is being tested by H. Fischer on meteorological data. If the procedure worked on line of sight velocity as well as on line of sight magnetic field data (which is not as obvious)¹, then the magnetic flux equation

$$\partial \psi_m / \partial t = J_{\lambda, \omega}(\psi_r, \psi_m) \quad (7-1)$$

given by Gilman(1966) could be solved, in principle, for the magnetic stream function ψ_m . Finally, one could invert ψ_m to obtain a predicted line of sight field B^l . Since the characteristic time scale of $\mathcal{O}(1)$ solar rotation is considerably larger than a day, magnetic features might be predictable one solar rotation (~ 25 days) later. One drawback even here is that (for the present) data can be collected from only the visible solar disk. Over longer time intervals, the twisting terms $\frac{\langle B^u \rangle}{a} \frac{\partial \langle v_r \rangle}{\partial \omega} + \langle B^z \rangle \frac{\partial \langle v_\theta \rangle}{\partial \lambda}$, which equation (7-1) lacks, could be important on the sun.

It is doubtful that our model would be of much predictive value in the foreseeable future. First, it was designed for a subphotospheric layer. In applying it to a photospheric layer of fluid, some model assumptions would be violated. Second, the divergent parts of velocity and magnetic fields would have to be accurately known or balanced initially.

¹The magnetic fields were significantly less horizontally nondivergent than the velocity fields in our model and this might be true on the sun.

This is a formidable obstacle as neither of those fields is given by the above method of characteristics. Third, temperature measurements on horizontal (geopotential) surfaces have not yet been sufficiently perfected.

APPENDIX A. POLOIDAL AND TOROIDAL VECTOR
SPHERICAL HARMONICS

An arbitrary solenoidal, i.e. divergence-free, vector $(A^\lambda, A^\varphi, A^r)$ has the spectral decomposition

$$A^\lambda = \sum_{c,s} \sum_{n=0} \sum_{m=0} \left\{ -\frac{T_{m+n}^{n,(s)}}{r} \frac{\partial Y_{m+n}^{n,(s)}}{\partial \varphi} + \frac{1}{r \cos \varphi} \frac{\partial S_{m+n}^{n,(s)}}{\partial r} \frac{\partial Y_{m+n}^{n,(s)}}{\partial \lambda} \right\} \quad (\text{A-1a})$$

$$A^\varphi = \sum_{c,s} \sum_{n=0} \sum_{m=0} \left\{ \frac{T_{m+n}^{n,(s)}}{r \cos \varphi} \frac{\partial Y_{m+n}^{n,(s)}}{\partial \lambda} + \frac{1}{r} \frac{\partial S_{m+n}^{n,(s)}}{\partial r} \frac{\partial Y_{m+n}^{n,(s)}}{\partial \varphi} \right\} \quad (\text{A-1b})$$

$$A^r = \sum_{c,s} \sum_{n=0} \sum_{m=0} \left\{ \frac{(m+n)(m+n+1)}{r^2} S_{m+n}^{n,(s)} Y_{m+n}^{n,(s)} \right\} \quad (\text{A-1c})$$

In these formulae, $T_{m+n}^{n,(s)}(r)$, $S_{m+n}^{n,(s)}(r)$, and $Y_{m+n}^{n,(s)}(\lambda, \varphi)$ are respectively a cosine (or sine) toroidal spectral coefficient, poloidal spectral coefficient and ordinary spherical harmonic of degree $m+n$ and rank (i.e. zonal wave number) n . The c_s notation is the same as in Chapter III, section 4. Also, $Y_{m+n}^{n,c}$ and $Y_{m+n}^{n,s}$ are defined in equation (3-30). As usual λ, φ , and r denote the longitude, latitude and radius.

The contribution to A that involves toroidal coefficients can be expressed in terms of a horizontal stream function ψ_A . Similarly the contribution involving poloidal coefficients is related to a horizontal potential ϕ_A . We shall adhere to this usage of "toroidal" and "poloidal" throughout the text, as in equations (2-46) and (2-47), for example. We note that both V and B are solenoidal vectors in our model. In the special case that A is axisymmetric, the poloidal part of A is confined to meridional planes while the toroidal part of A is purely zonal.

An arbitrary solenoidal cosine (or sine) toroidal vector spherical harmonic has the representation

$$\left(-\frac{T_{m+n}^{n,(c)}}{r} \frac{\partial Y_{m+n}^{n,(c)}}{\partial \omega}, \frac{T_{m+n}^{n,(c)}}{r \cos \omega} \frac{\partial Y_{m+n}^{n,(c)}}{\partial \lambda}, 0 \right) \quad (\text{A-2a})$$

An arbitrary solenoidal cosine (or sine) poloidal vector spherical harmonic has the representation

$$\left(\frac{\partial S_{m+n}^{n,(c)}}{\partial r} \frac{1}{r \cos \omega} \frac{\partial Y_{m+n}^{n,(c)}}{\partial \lambda}, \frac{\partial S_{m+n}^{n,(c)}}{\partial r} \frac{1}{r} \frac{\partial Y_{m+n}^{n,(c)}}{\partial \omega}, S_{m+n}^{n,(c)} (m+n)(m+n+1) Y_{m+n}^{n,(c)} \right) \quad (\text{A-2b})$$

We may decompose the vector \underline{A} into a toroidal part \underline{A}_T and a poloidal part \underline{A}_P by summing equations (A-2a) and (A-2b) respectively, over n , m , and over both the cosine and sine harmonics. Finally, the thin spherical shell approximation can be made by replacing r by "a" dr by dz , and A^r by A^z in the above equations, as in chapter III.

APPENDIX B. PROGRAMMING THE NUMERICAL INTEGRATION

To simplify the debugging procedure, the basic program was split up into a driver program (program MAIN) and several subroutines. There is one version of MAIN for the nonmagnetic case and one for the magnetic case. Addition, scalar multiplication and $\frac{1}{a \cos \alpha} \frac{\partial}{\partial \lambda}$ differentiation are performed in program MAIN. Each of the other basic transformation algorithms is written as a subroutine. The transformed array of spectral coefficients is returned to the main program. If needed, the input array is also returned intact. Another group of subroutines carries out various other tasks.

To make our main program and subroutines as compatible as possible with a variety of computers, incremented indexing was employed exclusively¹.

For example, given the variable $\psi_1^+ = \sum_{c,s} \sum_m \sum_n (\hat{\psi}_1^+)^{n,c}_{m,s} R_m^n$, the spectral coefficient $(\hat{\psi}_1^+)^{n,c}_{m,s}$ is stored in location CYPl(n+1,m+1,1) of the 3x40x2 array CYPl for ψ_1^+ while $(\hat{\psi}_1^+)^{n,s}_{m,c}$ is stored in location CYPl(n+1,m+1,2).

Likewise, the values of the transformation coefficients $y_{m-1-2(I-1), m-1}^{n-1}$, $A_{m-1, m-1}^{n-1}$, and $A_{m-1, m-1-2(k-1)}^{n-1}$ (where $n, m, I \geq 1, k \geq 1$), are stored respectively in locations $y(n, m-2(I-1), m)$, $A(n, m, m)$ and in $A(n, m, m-2k+2)$. Finally the binomial coefficient $\frac{1}{2} b_{I-1}^{J-1} = \frac{1}{2} \frac{(-1)^{J-1} (I-1)!}{(I-J)! (J-1)!}$ is stored in BINOM(I, J), where $I \geq J \geq 1$.

Nonlinear multiplications originally required nearly 80% of the computation time. This value was reduced to about 50% by writing a specialized, more efficient subroutine MLTPLY. It is applicable provided the zonal wave number n has only two values, one of which is zero.

¹The computers we have used thus far accept the "zero" subscript.

APPENDIX C. ENERGY INTEGRALS FOR A CONTINUOUS, QUASI-BOUSSINESQ MODEL.

This appendix contains integrals of the various forms of energy, of energy transformations, and of energy fluxes. In the fluxes, all terms are formally retained even if they would vanish identically due to our choice of boundary conditions. These terms formally appear in the two layer model as well, but were omitted in Chapter V. Thermal forcing, frictional dissipation, and ohmic dissipation integrals are not included.

As in the text, the fluid is in vertical magnetohydrostatic balance and $\ln \theta = \ln \theta_s + \theta' / \theta_s$. Also $\partial \ln \theta_s / \partial z$ is still constant and the advection of potential temperature by poloidal motions is still neglected¹. Following Lorenz (1960b), our model could be extended to the case in which θ' is predicted at two levels, i.e. levels 1 and 3. Although the static stability would then be variable, the available potential energy could be defined in an energetically consistent manner.

The integrals in this appendix are valid for the quasi-Boussinesq case in which ρ_s varies with z , as well as for the Boussinesq case. Likewise, the integrals in Chapter V are also valid in the quasi-Boussinesq case except for (5-14). (cf. with (c.5-14)).

The labeling of equations corresponds to that in Chapter V.

¹On physical grounds, $(\partial \theta' / \partial z) / (\partial \theta_s / \partial z) \ll 1$ is possible for the sun.

Finally, $\int d\tau$ denotes a volume integral over the spherical shell bounded by $0 \leq z \leq z_4$.

The various energies are defined as follows:

$$\langle KZ \rangle = \int \rho_s \frac{\langle u \rangle^2}{2} d\tau \quad (C.5-1a)$$

$$\langle KM \rangle = \int \rho_s \frac{\langle v \rangle^2}{2} d\tau \quad (C.5-1b)$$

$$\langle EKE \rangle = \int \rho_s \frac{\langle u^{*2} + v^{*2} \rangle}{2} d\tau \quad (C.5-1c)$$

$$\langle MZ \rangle = \int \frac{\langle B^\lambda \rangle^2}{8\pi\mu_0} d\tau \quad (C.5-2a)$$

$$\langle MM \rangle = \int \frac{\langle B^\omega \rangle^2}{8\pi\mu_0} d\tau \quad (C.5-2b)$$

$$\langle EME \rangle = \int \frac{\langle B^{\lambda*2} + B^{\omega*2} \rangle}{8\pi\mu_0} d\tau \quad (C.5-2c)$$

$$\langle ZPE \rangle = \int \rho_s \frac{\langle \Theta \rangle^2}{2} d\tau \quad (C.5-3a)$$

$$\langle EPE \rangle = \int \rho_s \frac{\langle \Theta^{*2} \rangle}{2} d\tau \quad (C.5-3b)$$

where

$$\Theta = \sqrt{\frac{g}{(\partial \ln \sigma_s / \partial z)}} \frac{\sigma'}{\sigma_s} \quad (C.5-4)$$

The energy transformation integrals are:

$$\{ \langle KM \rangle \rightarrow \langle KZ \rangle \} = \int_S \rho (2\mathcal{L} + \frac{\langle u \rangle}{a \cos \omega}) \langle u \rangle \langle v \rangle \sin \omega \, d\tau \quad (\text{C.5-9})$$

$$\begin{aligned} \{ \langle EKE \rangle \rightarrow \langle KZ \rangle \} &= \int_S \rho \langle u^* v^* \rangle a \cos \omega \frac{1}{a} \frac{\partial}{\partial \omega} \left(\frac{\langle u \rangle}{a \cos \omega} \right) d\tau \\ &+ \int_S \rho \langle u^* w^* \rangle a \cos \omega \frac{\partial}{\partial z} \left(\frac{\langle u \rangle}{a \cos \omega} \right) d\tau \end{aligned} \quad (\text{C.5-10})$$

$$\begin{aligned} \{ \langle KZ \rangle \rightarrow \langle MZ \rangle \} &= \int \frac{a \cos \omega}{4\pi \mu_0} \langle B^A \rangle \langle B^W \rangle \frac{1}{a} \frac{\partial}{\partial \omega} \left(\frac{\langle u \rangle}{a \cos \omega} \right) d\tau \\ &+ \int \frac{a \cos \omega}{4\pi \mu_0} \langle B^A \rangle \langle B^B \rangle \frac{\partial}{\partial z} \left(\frac{\langle u \rangle}{a \cos \omega} \right) d\tau \end{aligned} \quad (\text{C.5-11})$$

$$\begin{aligned} \{ \langle KZ \rangle \rightarrow \langle EME \rangle \} &= \int \frac{a \cos \omega}{4\pi \mu_0} \langle B^{A*} B^{W*} \rangle \frac{1}{a} \frac{\partial}{\partial \omega} \left(\frac{\langle u \rangle}{a \cos \omega} \right) d\tau \\ &+ \int \frac{a \cos \omega}{4\pi \mu_0} \langle B^{A*} B^{B*} \rangle \frac{\partial}{\partial z} \left(\frac{\langle u \rangle}{a \cos \omega} \right) d\tau \end{aligned} \quad (\text{C.5-12})$$

$$\begin{aligned} \{ \langle EKE \rangle \rightarrow \langle KM \rangle \} &= \int_S \rho \langle v^* w^* \rangle \frac{\partial \langle v \rangle}{\partial z} d\tau + \int_S \rho \left[\langle v^{*2} \rangle \frac{1}{a} \frac{\partial \langle v \rangle}{\partial \omega} - \langle u^* \times v \rangle \frac{\tan \omega}{a} \right] d\tau \\ &= \int_S \rho \langle v^* w^* \rangle \frac{\partial \langle v \rangle}{\partial z} d\tau + \int_S \rho \left[\frac{\cos \omega}{a} \frac{\partial}{\partial \omega} \left(\frac{\langle v \rangle}{\cos \omega} \right) \langle v^{*2} \rangle \right. \\ &\quad \left. - \frac{\tan \omega}{a} \langle v \rangle \langle u^{*2} + v^{*2} \rangle \right] d\tau \end{aligned} \quad (\text{C.5-13})$$

$$\begin{aligned} \{ \langle KM \rangle \rightarrow \langle MZ \rangle \} &= - \int \frac{\langle B^A \rangle^2}{8\pi \mu_0} \left[\cos \omega \frac{1}{a} \frac{\partial}{\partial \omega} \left(\frac{\langle v \rangle}{\cos \omega} \right) + \frac{\partial \langle w \rangle}{\partial z} \right] d\tau \\ &= - \int \frac{\tan \omega}{4\pi \mu_0 a} \langle B^A \rangle^2 \langle v \rangle d\tau + \int \frac{1}{8\pi \mu_0} \frac{d\rho_S}{dz} \frac{\langle B^A \rangle^2 \langle w \rangle}{\rho_S} d\tau \end{aligned} \quad (\text{C.5-14})$$

$$\{ \langle KM \rangle \rightarrow \langle MM \rangle \} = \int \frac{1}{4\pi\mu_0} \left[\langle v \times B^z \rangle - \langle w \times B^{\theta} \rangle \right] \left[-\frac{\partial \langle B^z \rangle}{\partial z} \right] d\tau \quad (C.5-15)$$

$$\begin{aligned} \{ \langle KM \rangle \rightarrow \langle EME \rangle \} &= - \int \frac{a \cos \varphi}{8\pi\mu_0} \langle B^{\lambda^*2} - B^{\varphi^*2} \rangle \frac{1}{a} \frac{\partial}{\partial \varphi} \left(\frac{\langle v \rangle}{a \cos \varphi} \right) d\tau \\ &+ \int \frac{\langle B^{\varphi^*} B^z \rangle}{4\pi\mu_0} \frac{\partial \langle v \rangle}{\partial z} d\tau - \int \frac{\langle B^{\lambda^*2} + B^{\varphi^*2} \rangle}{8\pi\mu_0} \frac{\partial \langle w \rangle}{\partial z} d\tau \quad (C.5-16) \end{aligned}$$

$$\{ \langle ZPE \rangle \rightarrow \langle KM \rangle \} = \int \rho_s g \theta_s^{-1} \langle w \rangle \langle \theta' \rangle d\tau \quad (C.5-17)$$

$$\begin{aligned} \{ \langle EKE \rangle \rightarrow \langle MZ \rangle \} &= - \int \frac{\langle u^* B^z - w^* B^{\lambda} \rangle}{4\pi\mu_0} \frac{\partial \langle B^{\lambda} \rangle}{\partial z} d\tau \\ &+ \int \frac{\langle v^* B^{\lambda^*} - u^* B^{\varphi^*} \rangle}{4\pi\mu_0} \frac{1}{a \cos \varphi} \frac{\partial}{\partial \varphi} \left(\langle B^{\lambda} \rangle \cos \varphi \right) d\tau \quad (C.5-18) \end{aligned}$$

$$\{ \langle EKE \rangle \rightarrow \langle MM \rangle \} = \int \frac{\langle v^* B^z - w^* B^{\varphi} \rangle}{4\pi\mu_0} \left(-\frac{\partial \langle B^z \rangle}{\partial z} \right) d\tau \quad (C.5-19)$$

$$\begin{aligned} \{ \langle EKE \rangle \rightarrow \langle EME \rangle \} &= - \int \frac{1}{4\pi\mu_0} \left\langle \left(\hat{v}_H^* + w^* \hat{z} \right) \cdot \left[\left(\nabla \times B_H^* \right) \times \left(B_H + B^z \hat{z} \right) \right] \right\rangle d\tau \\ &- \int \frac{1}{4\pi\mu_0} \left\langle \left(\hat{v}_H^* + w^* \hat{z} \right) \cdot \left[\left(\nabla \times B_H^* \right) \times \left(B_H^* + B^z \hat{z} \right) \right] \right\rangle d\tau \quad (C.5-20) \end{aligned}$$

$$\{ \langle EPE \rangle \rightarrow \langle EKE \rangle \} = \int \rho_s g \theta_s^{-1} \langle w^* \theta'^* \rangle d\tau \quad (C.5-21)$$

$$\{ \langle ZPE \rangle \rightarrow \langle EPE \rangle \} = - \int \rho_s \langle v^* \Phi^* \rangle \frac{1}{a} \frac{\partial \langle \Phi \rangle}{\partial \varphi} d\tau \quad (C.5-22)$$

The boundary value integrals for energy flux into the region $0 \leq z \leq z_4$

are:

$$\begin{aligned} \langle KZ^\dagger \rangle &= \int_{\sigma_5} \left[\frac{1}{4\pi\mu_0} (\langle B^\lambda \rangle \langle B^{\lambda^*} \rangle + \langle B^{\lambda^*} B^{\lambda^*} \rangle) \langle u \rangle \right] \Big|_0^{z_4} dS \\ &\quad - \int_{\sigma_5} \left[\rho_s \frac{\langle u \rangle^2}{2} \langle w \rangle \right] \Big|_0^{z_4} dS - \int_{\sigma_5} \left[\rho_s \langle u^* w^* \rangle \langle u \rangle \right] \Big|_0^{z_4} dS \end{aligned} \quad (C.5-23a)$$

$$\begin{aligned} \langle KM^\dagger \rangle &= \int_{\sigma_5} \left[\frac{\langle B^{\lambda^*} B^{\lambda^*} \rangle}{4\pi\mu_0} \langle v \rangle \right] \Big|_0^{z_4} dS - \int_{\sigma_5} \left[\rho_s \left(\frac{\langle v \rangle^2}{2} \langle w \rangle + \langle v^* w^* \rangle \langle v \rangle \right) \right] \Big|_0^{z_4} dS \\ &\quad - \int_{\sigma_5} \left[\left(\langle P' \rangle + \frac{\langle B^\lambda \rangle^2}{8\pi\mu_0} + \frac{\langle B^{\lambda^* \lambda^*} + B^{\lambda^* \lambda^*} \rangle}{8\pi\mu_0} \right) \langle w \rangle \right] \Big|_0^{z_4} dS \end{aligned} \quad (C.5-23b)$$

$$\begin{aligned} \langle EKE^\dagger \rangle &= - \int_{\sigma_5} \left[\langle P'^* w^* \rangle \right] \Big|_0^{z_4} dS - \int_{\sigma_5} \left[\rho_s \frac{\langle u^{*2} + v^{*2} \rangle}{2} \langle w \rangle \right] \Big|_0^{z_4} dS \\ &\quad - \int_{\sigma_5} \left[\rho_s \left\langle \frac{(u^{*2} + v^{*2})}{2} w^* \right\rangle \right] \Big|_0^{z_4} dS \end{aligned} \quad (C.5-23c)$$

$$\begin{aligned} \langle MZ^\dagger \rangle &= \int_{\sigma_5} \left[\frac{1}{4\pi\mu_0} (\langle u^* B^{\lambda^*} \rangle - \langle w^* B^{\lambda^*} \rangle) \langle B^\lambda \rangle \right] \Big|_0^{z_4} dS \\ &\quad - \int_{\sigma_5} \left[\frac{\langle B^\lambda \rangle^2}{8\pi\mu_0} \langle w \rangle \right] \Big|_0^{z_4} dS \end{aligned} \quad (C.5-24a)$$

$$\begin{aligned} \langle MM^\dagger \rangle &= \int_{\sigma_5} \left[\frac{1}{4\pi\mu_0} (\langle v \rangle \langle B^{\lambda^*} \rangle - \langle w \rangle \langle B^{\lambda^*} \rangle) \langle B^{\lambda^*} \rangle \right] \Big|_0^{z_4} dS \\ &\quad + \int_{\sigma_5} \left[\frac{1}{4\pi\mu_0} (\langle v^* B^{\lambda^*} \rangle - \langle w^* B^{\lambda^*} \rangle) \langle B^{\lambda^*} \rangle \right] \Big|_0^{z_4} dS \end{aligned} \quad (C.5-24b)$$

$$\begin{aligned} \langle EME^\dagger \rangle &= \int_{\sigma_5} \left[\frac{1}{4\pi\mu_0} (\langle u^* B^{\lambda^*} + v^* B^{\lambda^*} \rangle \langle B^{\lambda^*} \rangle + \langle (u^* B^{\lambda^*} + v^* B^{\lambda^*}) B^{\lambda^*} \rangle) \right] \Big|_0^{z_4} dS \\ &\quad - \int_{\sigma_5} \left[\frac{1}{4\pi\mu_0} (\langle w^* B^{\lambda^*} \rangle \langle B^\lambda \rangle + \langle w^* B^{\lambda^*} \rangle \langle B^{\lambda^*} \rangle) \right] \Big|_0^{z_4} dS \\ &\quad - \int_{\sigma_5} \left[\frac{\langle B^{\lambda^* \lambda^*} + B^{\lambda^* \lambda^*} \rangle}{8\pi\mu_0} \langle w \rangle + \frac{\langle (B^{\lambda^* \lambda^*} + B^{\lambda^* \lambda^*}) w^* \rangle}{4\pi\mu_0} \right] \Big|_0^{z_4} dS \end{aligned} \quad (C.5-24c)$$

BIBLIOGRAPHY

- Abramowitz, M. and I. Stegun, ed., 1965: Handbook of Mathematical Functions, Dover Publications, Inc., New York, 798 p.
- Alfvén, H., 1965: Solar magnetic fields. (Only identification is the number HA26.3, 1965 on the manuscript.)
- Alfvén, H. and C.G. Fälthammar, 1963: Cosmical Electrodynamics, Fundamental Principals. Clarendon Press, Oxford.
- Allen, C.W., 1963: Astrophysical Quantities, 2nd ed., Univ. of London, Athlone Press, London, distr. U.S.A., Oxford Univ. Press, New York, 291 p.
- Arakawa, A., 1966: Computation design for long-term numerical integration of the equations of fluid motion: Two-dimensional incompressible flow. Part 1, Jour. of Computat. Phys. 1, 119-143.
- Babcock, H.D., 1961: The topology of the sun's magnetic field and the 22-year cycle. Ap. J. 133, 572-587.
- Backus, G.E., 1958: A class of self-sustaining dissipative spherical dynamos. Annals of Phys. 4, 372-447.
- Backus, G.E. and S. Chandrasekhar, 1956: On Cowling's Theorem on the impossibility of self-maintained axisymmetric homogeneous dynamos. Proc. of the Natl. Acad. of Sci. 42, 105-109.
- Baer, F., and G.W. Platzman, 1961: A procedure for numerical integration of the spectral vorticity equation. J. of Meteor. 18, 293-401.
- Baer, F. and T.J. Simons, 1968: Computational stability and time truncation of coupled nonlinear equations with exact solutions. Atmos. Sci. Paper No. 131, Dept. of Atmos. Sci., Colo. State Univ., Fort Collins, Colo.
- Beckers, J.M., 1960: Temperature variations on the sun with heliographic latitude. Bull. Astron. Inst. Neth. 15, 85-101.
- Bierman, L., 1958: Electromagnetic phenomenon in cosmical physics. A. U. Sympos. No. 6, Trans. I.A.U. 6, 248-255.
- Billings, D.E., 1966: A Guide to the Solar Corona. Academic Press, New York, 323 p.

- Bjerknes, V., 1926: Solar hydrodynamics. Ap. J. 64, 93..
- Braginskii, S.I., 1964: Self-excitation of a magnetic field during the motion of a highly conducting fluid. J. Exptl. Theoret. Phys. (U.S.S.R.) 47, 1084-1098. (Translated in Soviet Physics JETP 20, March 1965, 726-735.)
- Bryan, K., 1959: A numerical integration of certain features of the general circulation. Tellus 11, 163-174.
- Bullard, E. and H. Gellman, 1954: Homogeneous dynamos and terrestrial magnetism. Phil. Trans. Roy. Soc., Series A, 247, 213-278.
- Bumba, V., 1967: Observations of solar magnetic and velocity fields. Varenna, Italy, Scuola Internazionale di Fisica (Proc. of the International School of Physics), Enrico Fermi course XXXIX, Academic Press, New York and London, 77-123.
- Bumba, V. and R. Howard, 1965a: A study of the development of active regions on the sun. Ap. J. 141, 1492-1501.
- _____, 1965b: Large-scale distribution of solar magnetic fields. Ap. J. 141, 1502-1512.
- _____, 1965c: Solar magnetic fields. Science 149, 1331-1338.
- Bumba, V., R. Howard, M. Kopecky, and G.V. Kuklin, 1969: Some irregularities in the distribution of large-scale magnetic fields on the sun. Bull. Astr. Inst. Czechoslovakia 20, 18-21.
- Busse, F.H., 1970: Differential rotation in stellar convection zones. Ap. J. 159, 629-639.
- Chandrasekhar, S., 1953: The instability of a layer of fluid heated below and subject to Coriolis forces. Proc. Roy. Soc. (Ser. A.) 217, 306.
- _____, 1961: Hydrodynamic and Hydromagnetic Stability. Clarendon Press, Oxford.
- Charney, J.G., 1963: A note on large-scale motions in the tropics. J. A.S. 20, 607-609.
- Childress, S., 1969: A class of solutions of the magnetohydrodynamic dynamo problem. NATO Advanced Study Institute, The Application of Modern Physics to the Earth and Planetary Interiors. S.K. Runcorn, ed. A conference at Univ. of Newcastle upon Tyne, Engl., 1967. Wiley-Interscience, 629.

- Chu, B.-T., 1959: Thermodynamics of electrically conducting fluids. Phys. of Fluids 2, 473-484.
- Cocke, W.H., 1967: Alternate cause of the solar oblateness. Phys. Rev. Letters 19, 609-611.
- Cowling, T.G., 1934: The magnetic field of sunspots. Mon. Not. Roy. Astron. Soc. 94, 39-48.
- _____, 1957a: Magnetohydrodynamics. Interscience, New York, N.Y.
- _____, 1957b: The dynamo maintenance of steady magnetic fields. Quart. J. Mech. Appl. Math. 10, 129-136.
- Davies-Jones, R.P., 1969: The linear theory of thermal convection in horizontal plane couette flow. AFCRL-69-0382, Sci. Rep. No. 5, Univ. of Colorado, Boulder, Colo., Dr. P.A. Gilman, Principal Invest., 215 pp.
- Davies-Jones, R.P. and P.A. Gilman, 1970: Convection in a rotating annulus uniformly heated from below. NCAR MS 70-42, Advanced Study Program at Nation. Cent. for Atm. Res., Boulder, Colo. (To appear in JFM.)
- d'Azambuja, L. and A. d'Azambuja, 1948: Ann. Obs. Meudon 6, Fasc. 7.
- Deardorff, J.W., 1965: A numerical study of pseudo three-dimensional parallel plate convection. J.A.S. 22, 419-435.
- Dicke, R.H., 1964: The sun's rotation and relativity. Nature 202, 432-435.
- Dicke, R.H. and H.M. Goldenberg, 1967: Solar oblateness and general relativity. Phys. Rev. Letters 18, 313-316.
- Eddington, A.A., 1925: Circulating currents in rotating stars. Observatory 28, 285.
- Elsasser, W.M., 1950: The hydromagnetic equations. Phys. Rev. 79, 183.
- _____, 1956: Hydromagnetic dynamo theory. Rev. Mod. Phys. 28, 135-163.
- Fultz, D. et al., 1959: Studies of Thermal Convection in a Rotating Cylinder with some Implications for Large-Scale Atmospheric Motions. Meteorological Monographs, Vol. 4.
- Gibson, R.D., P.H. Roberts and S.Scott, 1969: The Bullard-Gellman dynamo. NATO Advanced Study Institute. The Application of Modern Physics to the Earth and Planetary Interiors, S.K. Runcorn, Ed. A conference at Univ. of Newcastle upon Tyne, 1967. Wiley Interscience, 577-602.
- Gille, J., 1967: Interferometric measurement of temperature gradient reversal in a layer of convecting air. J. Fluid Mech. 30, 371-384.

- Gilman, P.A., 1966: Hydromagnetic model for the solar general circulation. AFCRL-66-316. Scient. Rept. No. 1, Planet. Circ. Proj., V.P. Starr, Director, M.I.T., Dept. of Meteor., May, 1966.
- _____, 1967: Stability of baroclinic flows in a zonal magnetic field, Parts I, II, and III. J.A.S. 24, 101-143.
- _____, 1968: Thermally driven Rossby-mode dynamos. AFCRL-68-0501, Scient. Rept. No. 2, Dr. P.A. Gilman, Univ. of Colo., Boulder, Colo.
- _____, 1969: A Rossby-mode dynamo for the sun. Part I. Solar Phys. 8, 316-330, Part II. Solar Phys. 9, 3-18.
- Hart, A.B., 1956: Motions in the sun at photospheric level VI. Large scale motions in the equatorial region. M.N.R.A.S. 116, 38-55.
- Herring, J.P., 1964: Investigation of problems in thermal convection: Rigid boundaries. J.A.S. 21, 277-290.
- Herzenberg, A., 1958: Geomagnetic dynamos. Phil Trans. Roy. Soc. London, Series A, 250: 543-585.
- Howard, R. and J. Harvey, 1970: Spectroscopic determinations of solar rotation. Solar Phys. 12, 23-51.
- Iben, I., 1966: Computer output of numerical stellar model, for selected input parameters possibly applicable to the sun. Private communication.
- Inglis, D.R., 1955: Theories of the earth's magnetism. Rev. Mod. Phys. 27, 212-248.
- Jeffrey, A., 1966: Magnetohydrodynamics. Oliver and Boyd Ltd, London, England.
- Kippenhahn, R., 1963: Differential rotation in stars with convective envelopes. Ap. J. 317, 664-678.
- Krogdahl, W., 1944: Stellar rotation and large scale currents. Ap. J. 99, 191.
- Kubota, S., 1959: Surface spherical harmonics representations of the system of equations for analysis. Papers in Meteor. and Geophys. Met. Res. Inst. Tokyo 10, 145-166.
- Kuiper, G.P. (ed.), 1953: The Sun, Vol. I of the Solar System. Univ. of Chic. Press, Chicago, Ill.

- Kurihara, Y. and Holloway, J.L., 1967: Numerical integration of a nine-level global primitive equations model formulated by the box method. Mon. Wea. Rev. 95, 509-530.
- Leighton, R.B., 1959: Observations of solar magnetic fields in plage regions. Ap. J. 130, 366.
- _____, 1964: Transport of magnetic fields on the sun. Ap. J. 140, 1547-1562.
- _____, 1969: A magneto-kinematic model of the solar cycle. Ap. J. 156, 1-26.
- Lilly, D.K., 1965: On the computational stability of numerical solutions of time-dependent non-linear geophysical fluid dynamics problems. Mon. Wea. Rev. 93, 11-25.
- Livingston, W.C., 1966: Magnetic fields on the quiet sun. Scientific American, 215, No. 5, November, 54-62.
- _____, 1969: Solar rotation 1966-68. Solar Phys. 7, 146-148.
- Lorenz, E.N., 1955: Available potential energy and the maintenance of the general circulation. Tellus 7, 157-167.
- _____, 1960a: Maximum simplification of the dynamic equations. Tellus 12, 243-254.
- _____, 1960b: Energy and numerical weather prediction. Tellus 13, 364-373.
- _____, 1963: The mechanics of vacillation. J.A.S. 20, 448-464.
- _____, 1967: The Nature and Theory of the General Circulation of the Atmosphere. WMO, Geneva, Switz., 161 p.
- Loves, F.J. and I. Wilkinson, 1967: A laboratory self-exciting dynamo. NATO Advanced Study Institute on Planet. and Stellar Magnetism, Univ. of Newcastle upon Tyne, Apr. 1965, Magnetism and Cosmos, (ed: Hindmarsh, Loves, Roberts, and Runcorn), Oliver and Boyd, London, 121-125.
- Lundquist, S., 1952: Studies in magneto-hydrodynamics. Arkiv. for Fysik 15, 297-347.
- MacDonald, N.J., 1966: Methods of measuring solar and terrestrial relationships. Tellus 18, 13-17.

- Matsuno, T., 1966: Quasi-geostrophic motions in the equatorial area. J. of Meteor. Soc. Japan 44, 25-41.
- Mestel, L., 1967: Stellar magnetism. Varenna, Italy, Swola Internazionale di Fisica (Proc. of the International School of Physics), Enrico Fermi Course XXXIX, Academic Press, New York and London, 185-228.
- Nakagawa, Y. and S.K. Trehan, 1968: An axi-symmetric magnetic field with differential rotations in a spherical fluid shell. Ap. J. 151, 1111.
- Nakagawa, Y. and P. Swartrauber, 1969: The topology of an axisymmetric magnetic field of a differentially rotating sun. Ap. J. 155, 295-310.
- Newton, H.W. and M.L. Nunn, 1951: The sun's rotation period derived from sunspots and additional results, 1934-1944. Mon. Not. Roy. Astron. Soc. 111, 413.
- Nickel, G.H., 1966: Eddy Transport Maintenance of Solar Differential Rotation. Ph.D. thesis in Engineering - Applied Science in the Graduate Division of the Univ. of Calif., Davis, October 1966.
- _____, 1969: The maintenance of solar differential rotation by two-dimensional turbulence: A numerical model. Solar Phys. 10, 472-475.
- Parker, E.N., 1955a: The formation of sunspots from the solar toroidal field. Ap. J. 121, 491-507.
- _____, 1955b: Hydromagnetic dynamo models. Ap. J. 122, 293-314.
- Pedlosky, J., 1964: The stability of currents in the atmosphere and the ocean: Part I. J.A.S. 21, 342. Part II; J.A.S. 21, 342.
- Phillips, N.A., 1956: The general circulation of the atmosphere: a numerical experiment. Q.J.R.M.S. 82, 123-164.
- _____, 1959: An example of non-linear computational instability. The Atmosphere and the Sea in Motion. Rockefeller Institute Press in association with Oxford Univ. Press, New York, 501-504.
- _____, 1966: The equations of motion for a shallow rotating atmosphere and the "traditional approximation". J.A.S. 23, 626-628.
- Plaskett, H.H., 1962: Limb darkening and solar rotation. Mon. Not. Roy. Astron. Soc. 123, 541-561.
- Platzman, G.W., 1960: The spectral form of the vorticity equation. J. Meteor. 17, 635-644.
- Randers, G., 1942: On the rotation of stars with convective cores. Ap. J. 95, 454.

- Rikitake, T., 1958: Oscillations of a system of disk dynamos. Proc. Camb. Phil. Soc. 54, 89-105.
- _____, 1966: Electromagnetism and the Earth's Interior. Elsevier Publ. Co., New York, N.Y., 308 p.
- Robert, A.J., 1965: The behavior of planetary waves in an atmospheric model based on spherical harmonics. Arctic Meteor Research Group. Dept. of Meteor., McGill Univ., Montreal, Que., Canada, Publ. in Meteor. No. 77, 84 p.
- _____, 1966: The integration of a low order spectral form of the primitive meteorological equations. J. Meteor. Soc. Japan 44, 237-245.
- _____, 1970: Private communication.
- Roberts, P.H., 1967: Notes on the 1967 Summer Study Program in Geophysical Fluid Dynamics, Vol. 1, WHOI, Ref. No. 67-54, 212 p.
- _____, 1968: On the thermal instability of a rotating-fluid sphere containing heat sources. Phil. Trans. Roy. Soc. (Ser. A.) 263, 93.
- Roxburgh, I.W., 1967: Implications of the oblateness of the sun. Nature March 18, 1967, 1077-1078.
- _____, 1969: Lecture at Univ. of Colorado, Boulder, Colo.
- Saltzman, B., 1957: Equations governing the energetics of the larger scales of atmospheric turbulence in the domain of wave number. J. Meteor. 14, 513-523.
- Schwarzschild, M., 1958: Structure and Evolution of the Stars. Princeton Univ. Press, Princeton, N.J., 296 p.
- Severny, A.B., 1965: Solar magnetic fields. International Astronomical Union Transactions, Reports on Astronomy 12A (Invited discourses given at Univ. of Hamburg on Aug. 26, 1964), 755-772.
- Shercliff, J.D., 1965: A Textbook of Magnetohydrodynamics. Pergamon Press, London, 265 p.
- Shuman, F.G., 1957: Numerical methods in weather prediction: II. Smoothing and filtering. Mon. Wea. Rev. 85, 357-361.
- Silberman, I., 1954: Planetary waves in the atmosphere. J. Meteor. 11, 27-34.
- Simon, G.W. and R.B. Leighton, 1964: Velocity fields in the solar atmo-

sphere. III. Large scale motions, the chromospheric network, and magnetic fields. Ap. J. 140, 1120-1147.

Spitzer, L., 1967: Physics of Fully Ionized Gases. Second revised edition, Wiley-Interscience, publ., New York, 170 p.

Starr, V.P., 1968: Physics of Negative Viscosity Phenomena. McGraw-Hill, New York, 256 p.

Starr, V.P. and P.A. Gilman, 1965a: Energetics of the solar rotation. Ap. J. 141, 1119-1125.

_____, 1965b: On the structure and energetics of large scale hydromagnetic disturbances in the solar atmosphere. Tellus 17, 334-339.

_____, 1966: Hydromagnetic energy balance for the solar atmosphere. Pure and Appl. Geophys. 64, 145-155.

Stevenson, A.F., and S.J. Wolfson, 1966: Calculations on the dynamo problem of the earth's magnetic field. J.G.R. 71, 4496-4497.

Tough, J.G. and R.D. Gibson, 1969: The Braginskii dynamo. NATO Advanced Study Institute. The Application of Modern Physics to the Earth and Planetary Interiors. S.K. Runcorn, ed. A conference held at the Univ. of Newcastle upon Tyne, Engl., 1967. Wiley-Interscience, 555-560.

Veronis, G., 1966: Large amplitude Benard convection. J. Fluid Mech. 26, 49-68.

Ward, F., 1964: General circulation of the solar atmosphere from observational evidence. Pure and Appl. Geophys. 58, 157-186.

_____, 1965a: The general circulation of the solar atmosphere and the maintenance of the equatorial acceleration. Ap. J. 141, 534-537.

_____, 1965b: The effect of some systematic errors in the determination of the general circulation of the solar atmosphere. Pure and Appl. Geophys. 60, 126-128.

_____, 1966: Determination of the solar rotation rate from the motion of identifiable features. Ap. J. 145, 416-425.

Wasiutynski, J., 1946: Studies in hydrodynamics and structure of stars and planets. Astrophysica Norvegica 4, 27-31.

Weiss, N.O., 1964: Convection in the presence of restraints. Phil. Trans. Roy. Soc. A 256, 99-147.

Wilcox, J.M., 1966: Solar and interplanetary magnetic fields. Science 152, 161-166.

Wilcox, J.M. and R. Howard, 1970: Differential rotation of the photospheric magnetic field. Technical Report, ONR Contract N0014-69-A-0200-1016, Proj. NR 021 101 (submitted to Solar Phys.).

Williamson, D.L., 1969: A comparison of spherical grids for numerical integrations of atmospheric models. Ph.D. thesis, M.I.T., Dept. of Meteor., Cambridge, Mass. April 1969.

Zirin, H., 1966: The Solar Atmosphere. Blaisdell Publ. Co., Waltham, Mass. 502 p.

ACKNOWLEDGEMENTS

To Professor V.P. Starr, my advisor and teacher, I would like to express my deep appreciation and gratitude for his encouragement and valuable advice throughout the course of this investigation. Suggestions by Professor N.A. Phillips and Professor E.N. Lorenz also proved helpful. Dr. P.A. Gilman of N.C.A.R. has been keenly interested in this project and has offered his encouragement and advice. Dr. A.J. Robert of McGill University was happy to explain the details of his spectral harmonic scheme to me.

Some of the model data analysis was performed on the M.I.T. IBM-360 computer and a few short runs were made on Control Data Corporation's 6600 machine in Waltham, Mass. But most of the computations were made on the CDC-6600 at the National Center for Atmospheric Research in Boulder, Colorado. I am very appreciative for the 30 hours of free computer time given to me by N.C.A.R. In addition, the systems people and others associated with the N.C.A.R. computer facility were extremely helpful and kind. My special thanks go to Mrs. Jeanne Adams and Mr. Dave Robertson.

The thesis was typed by Misses Marion Morgan and Myna Gordon, and Mrs. Barbara Goodwin. Miss Myna Gordon, a devoted aunt who is a legal secretary in Chicago, insisted on typing two chapters during her vacation — "a labor of love", she called it. Mrs. Rachel Morton helped considerably in the writing of programs to display graphically the history tape data. Miss Isabelle Kole drafted most of the diagrams. Finally, despite the burdens that the writing of this thesis placed upon my parents and close friends, they offered much encouragement to me.

This work was funded under Air Force Contract No. F19628-69-C-0042 and National Science Foundation Grant No. GA-1310X. In addition, a Ford Foundation fellowship provided support during my first two years here.

BIOGRAPHICAL NOTE

The author was born in Chicago, Illinois on February 24, 1942. He was raised in Chicago and attended Von Steuben High School there. He studied at the University of Chicago from 1960 to 1964 and received a B.S. degree in geophysics in 1964. The author has been enrolled as a graduate student in meteorology at M.I.T. since September of 1964.